

Distribution Agreement

In presenting this thesis or dissertation as a partial fulfillment of the requirements for an advanced degree from Emory University, I hereby grant to Emory University and its agents the non-exclusive license to archive, make accessible, and display my thesis or dissertation in whole or in part in all forms of media, now or hereafter known, including display on the world wide web. I understand that I may select some access restrictions as part of the online submission of this thesis or dissertation. I retain all ownership rights to the copyright of the thesis or dissertation. I also retain the right to use in future works (such as articles or books) all or part of this thesis or dissertation.

Signature:

Yuan Chang

Date

**An Approach to Generate Ultra-Robust and Highly Modular Molecular Tension
Probes and Thermo-Responsive Enzymatic Nanoreactors to Regulate Reaction Rate**

By

Yuan Chang

Doctor of Philosophy

Chemistry

Khalid Salaita
Advisor

David Lynn
Committee Member

Brian Dyer
Committee Member

Accepted:

Lisa A. Tedesco, Ph.D.
Dean of the James T. Laney School of Graduate Studies

Date

**An Approach to Generate Ultra-Robust and Highly Modular Molecular Tension
Probes and Thermo-Responsive Enzymatic Nanoreactors to Regulate Reaction Rate**

By

Yuan Chang

B.S. Shandong University, 2010

Advisor: Khalid Salaita, Ph.D.

An abstract of

A dissertation submitted to the Faculty of the

James T. Laney School of Graduate Studies of Emory University

in partial fulfillment of the requirements for the degree of

Doctor of Philosophy

in Chemistry

2017

Abstract

An Approach to Generate Ultra-Robust and Highly Modular Molecular Tension Probes and Thermo-Responsive Enzymatic Nanoreactors to Regulate Reaction Rate

Yuan Chang

Mechanical forces between cells and their extracellular matrix (ECM) are mediated by hundreds of different receptors. These biophysical interactions play fundamental roles in processes ranging from cellular development to tumor progression. However, mapping the spatial and temporal dynamics of tension among various receptor-ligand pairs remains a significant challenge. Chapter 1 of this dissertation gives a brief overview of the history of studying mechanical signal transduction and summarizes the state of the art techniques to answer long-standing questions. In Chapter 2, the development of a synthetic strategy to generate modular tension probes combining the native chemical ligation (NCL) reaction with solid phase peptide synthesis (SPPS) is described. In principle, this approach accommodates virtually any peptide or expressed protein amenable to NCL. A small library of tension probes displaying different ligands was generated for mapping integrin and cadherin tension. It was also a first demonstration of long-term (~3 days) molecular tension imaging.

In chapter 3, we describe the development of a thermo-responsive enzymatic nanoreactor that can regulate reaction rates by tuning the phase transition of a polymer hydrogel. Enzymes were embedded into hydrogel nanoparticles that are thermo-responsive. When the temperature is raised above the lower critical solution temperature (LCST) of the polymer, the water is expelled from the hydrogel, which dampens the enzymatic turnover rate. This approach provides a tool to modulate enzymatic reactions

using external stimuli and could significantly improve our ability to control chemical reactions on-demand.

**An Approach to Generate Ultra-Robust and Highly Modular Molecular Tension
Probes and Thermo-Responsive Enzymatic Nanoreactors to Regulate Reaction Rate**

By

Yuan Chang

B.S. Shandong University, 2010

Advisor: Khalid Salaita, Ph.D.

A dissertation submitted to the Faculty of the
James T. Laney School of Graduate Studies of Emory University
in partial fulfillment of the requirements for the degree of

Doctor of Philosophy

in Chemistry

2017

Acknowledgements

First and foremost, I would like to thank my advisor, Khalid Salaita, for being an impeccable advisor, an inspiring mentor, and an encouraging friend. It has been a great honor to become a member of the Salaita lab. His support and advice have taught me a valuable lesson of never giving up. Next, I would like to truly thank my committee members Dr. David Lynn and Dr. Lanny Liebeskind for their many years of crucial insight and supportive guidance regarding my research and future career. Special thanks to Dr. Brian Dyer for invaluable research advice during our collaboration and for graciously agreeing to be my thesis defense committee member. I also would like to thank Ann Dasher, Steve Krebs, and Fred Strobel for all the help I received from them. Next I would like to thank my labmates for their support and shared knowledge. Kevin Yehl, Daniel Stabley, Zheng Liu, and Weiwei Zheng have been my great mentors and confidantes. Yoshie Narui and Yun Zhang have been the people that I could always depend on for advice. Specially, I want to thank Jessica Petree, without whom, I could not imagine how I could go through all the hardships in graduate school. I would also like to thank all the other Salaita lab members and friends who have provided great help during my time at Emory – I value the happy memories with you all. Last but not the least, I want to thank my loving husband, James, whose unconditional support and encouragement have been the greatest gift through these years and whose kindness, wisdom, and maturity have influenced me to become a better person.

List of Frequently Used Abbreviations

Abbreviation	Full Name
AFM	atomic force microscopy
AuNP	gold nanoparticle
cRGD	cyclic arginine-glycine-aspartate
DLS	dynamic lighting scattering
ECM	extracellular matrix
EGF	epidermal growth factor
EGFR	epidermal growth factor receptor
FA	focal adhesion
FRET	fluorescence resonance energy transfer
GFP	enhanced green fluorescent protein
GOX	glucose oxidase
HPLC	high-performance liquid chromatography
HRP	horse radish peroxidase
K _d	dissociation constant
k _{off}	dissociation rate
LCST	lower critical solution temperature
MALDI	matrix-assisted laser desorption/ionization
MTFM	molecular tension-based fluorescence microscopy

NCL	native chemical ligation
NHS	N-hydroxysuccinimide
PEG	polyethylene glycol
pN	piconewton
pNIPAM	poly N-isopropylacrylamide
pNIPMAM	poly N-isopropylmethylacrylamide
QE	quenching efficiency
RICM	reflection interference contrast microscopy
SBS	sulfobetaine siloxane
SLB	supported lipid bilayer
SPPS	solid phase peptide synthesis
TEM	transmission electron microscopy
TIRF	total internal reflection fluorescence

Table of Contents

Chapter 1: Introduction of mechanotransduction and cell adhesion.....	16
1.1. Mechanotransduction in cell biology	17
1.2. Focal adhesion and mechanotransduction.....	19
1.3. RGD motif and synergy binding site on fibronectin	24
1.4. Other receptor systems	26
1.5. Methods for studying live cell mechanical properties	26
1.6. Current molecular-scale tension sensors	28
2.1.1 Genetically encoded tension sensors	29
2.1.2 Living-nonliving interface tension sensors	29
1.7. Outlook.....	32
Chapter 2: A General approach to generate ultra-robust and highly modular molecular tension probes	38
2.1 Motivation and designing the tension sensor	39
2.1.3 The mechanism of quantifying the tension signal	41
2.1.4 Design and synthesis of the tension sensor.....	49
2.1.5 Methods and material.....	54
2.1.6 Determination of quenching efficiency	57
2.2 Integrin tension lead to biotin-streptavidin dissociation	61
2.2.1 Experiment findings.....	61
2.2.2 Discussion	65
2.3 Design and synthesis of the covalent, ultra-stable tension sensor.....	69
2.3.1 Covalent linkage via click chemistry	69
2.3.2 Fluorophore selection.....	71
2.3.3 Design and synthesis of MTFM sensor	73

2.4	The development of zwitterionic silane to prevent non-specific interaction of cells and glass surfaces	81
2.4.1	Biofouling in bioscience studies	81
2.4.2	Methods to prevent biofouling.....	82
2.4.3	Zwitterionic SBS passivation method.....	83
2.4.4	Synthesis of SBS.....	84
2.4.5	Preparation of the glass surface	84
2.4.6	Materials and Methods.....	87
2.4.7	Surface crowding caused by passivation molecules	87
2.4.8	Comparison of SBS and traditional PEG passivation.....	88
2.5	Tension map of fibroblast cells	91
2.5.1	Determine the surface density of MTFM tension sensor.....	91
2.5.2	Determine the quenching efficiency of the MFTM sensor.....	94
2.5.3	Integrin tension fluorescent map.....	96
2.5.4	Verifying tension reversibility by actin inhibitors	97
2.5.5	Tension causing by integrin mediated focal adhesion	99
2.5.6	Quantification of tension.....	100
2.6	Long term tension signal analysis	107
2.7	Tension generated by binding fibronectin synergy ligand PHSRN	109
2.7.1	Fibronectin III 9 th and 10 th domain	109
2.7.2	The effect of synergy site in cell mechanics.....	109
2.8	Cell-cell adhesion through Cadherin.....	111
2.8.1	Tension map of cadherin.....	111
2.8.2	Antibody mapping of cadherin	111
2.9	Materials and Methods	114

2.9.1	Reagents	114
2.9.2	Peptide synthesis	115
2.9.3	HPLC	115
2.9.4	MALDI-TOF Mass spectroscopy	115
2.9.5	Cu-TBTA preparation.....	115
2.9.6	Fluorescence microscopy.....	115
2.9.7	Cell culture.....	116
2.9.8	Preparation of small unilamellar vesicles phospholipids.....	116
2.9.9	Assembly of supported lipid membranes.....	117
2.10	References	118
Chapter 3: Thermo-responsive enzymatic nanoreactor to regulate reaction rate		130
3.1.	Motivation and designing the thermo-regulated enzymatic nanoreactor.....	131
3.1.1	Introduction	131
3.1.2	Design and mechanism of the thermo-regulated nanoenzyme reactor.....	137
3.1.3	Thermoresponsive polymers.....	139
3.1.3.1	LCST	140
3.1.3.2	pNIPAM and pNIPMAM.....	141
3.1.3.3	Glucose oxidase and horse radish peroxidase	142
3.2.	Synthesis of enzymatic nanoreactors	144
3.2.1	Synthesis of polyNIPAM and polyNIPMAM nanoparticles with alkyne functional groups	144
3.2.2	Modification of nanoparticles with NHS ester functional groups.....	146
3.2.3	Characterization of nanoparticles	146
3.2.3.1	TEM	146
3.2.4	Conjugation of enzymes on the nanoparticles.....	147

3.2.4.1	Fluorescent modification of enzyme for quantification purpose	147
3.2.4.2	Covalent conjugation of enzymes	149
3.2.4.3	Fluorescent image of nanoactuators	149
3.2.4.4	Mapping the distribution of enzymes in the particle using 5nm gold...	150
3.2.5	Determination of the number of enzymes on the hydrogel particle by fluorescence	152
3.2.5.1	DLS analysis of particle volume transition with temperature.....	155
3.3.	Kinetics of enzymatic reaction actuation.....	156
3.3.1	Results and discussion	156
3.3.2	Real-time recording of enzymatic reaction inhibition.....	160
3.4.	Conclusion and outlook	161
3.5.	References.....	162
	Chapter 4: Summary and future directions	174
	Appendix.....	191

List of Figures

Figure 1.1 Focal adhesion assembly and mechanotransduction.....	5
Figure 1.2 Structure of the fibronectin fragment III7-10 as determined by X-ray crystallography of the recombinant protein fragment.....	10
Figure 1.3 FRET based surface molecular tension sensors.....	17
Figure 2.1 Design and mechanism of MTFM tension sensor.....	24
Figure 2.2 Tetrameric structure of streptavidin with 2 bound biotins.....	30
Figure 2.3 Application of MTFM tension sensor.....	31
Figure 2.4 Jablonski diagram illustrating the coupled transitions involved between the donor emission and acceptor absorbance in FRET.....	34
Figure 2.5 Quenching efficiency and Foster distance R_0 of the FRET pair Alexa 647 and Fluorescein.....	37
Figure 2.6 Foster distance R_0 calculation of the FRET pair Alexa 647 and Fluorescein.....	37
Figure 2.7 Plot of PEG extension z (nm) vs force (pN).....	39
Figure 2.8 Process and mechanism of SPPS.....	40
Figure 2.9 Mechanism of NCL.....	42
Figure 2.10 Synthesis of Biotin-MTFM sensor precursor.....	44
Figure 2.11 Synthesis of Biotin-MTFM sensor.....	46
Figure 2.12 Characterization of Biotin-MTFM sensor.....	47
Figure 2.13 General scheme of Biotin-PEG-cRGD sensor and the determination of Alexa 647-Fluorescein quenching efficiency.....	50
Figure 2.14 Fluorescence signal and loss in Fluorescein and Alexa 647 Channel	

.....	52
Figure 2.15 Fluorescence loss irreversible when treated with Latrunculin B	
.....	54
Figure 2.16 Fluorescence background under the cell.....	55
Figure 2.17 Copper copper catalyzed click chemistry.....	61
Figure 2.18 General schematic of the MTFM sensor.....	62
Figure 2.19 Strategy to generate the MTFM sensor.....	63
Figure 2.20 Synthesis and characterization of the MTFM sensor precursor.....	65
Figure 2.21 synthesis of cRGD thioester.....	67
Figure 2.22 synthesis and characterization of a library of α -thioester peptide	
Ligands.....	69
Figure 2.23 synthesis of cRGD thioester.....	70
Figure 2.24 synthesis of cRGD thioester.....	73
Figure 2.25 Modification of the glass coverslip.....	76
Figure 2.26 Surface crowding comparison between PEG and SBS passivation.....	79
Figure 2.27 Surface passivation comparison.....	81
Figure 2.28 Surface crowding comparison between PEG and SBS passivation.....	83
Figure 2.29 Determine quenching efficiency of MTFM sensor by	
Photobleaching.....	84
Figure 2.30 Fluorescence tension signals with fibril-like details at the cell protrusion	
leading edge.....	86
Figure 2.31 Dynamic tension signals.....	87
Figure 2.32 Chemical structure of Latrunculin B.....	88

Figure 2.33 Tension signal is actin dependent.....	89
Figure 2.34 Tension is integrin mediated.....	90
Figure 2.35 Tension mapping with PEG48 MTFM sensors.....	96
Figure 2.36 Long-term live cell mechano-imaging using TAMRA-Alexa 488 sensor.....	98
Figure 2.37 The role of RGD and PHSRN peptides in mediating integrin tension.....	100
Figure 2.38 The Cadherin tension map.....	102
Figure 2.39 Fluorescent tension signal after treatment with actin inhibitor.....	103
Figure 3.1 Phase transition associated with the LCST and UCST.....	123
Figure 3.2 (adapted form J. Mater. Chem., 2009,19, 3955-3961 and Nature Chemistry 9, 480–486 (2017)).....	126
Figure 3.3 Schematic representation of thermo-regulated nanoenzyme Reactor.....	129
Figure 3.4 Dehydration mechanism of polymer with LCST.....	130
Figure 3.5 Reaction of GOX and HRP in the nanoenzymes.....	133
Figure 3.6 The synthesis and modification of pNIPAM nanoparticles.....	135
Figure 3.7 TEM image with negative staining of pNIPAM nanoparticles.....	137
Figure 3.8 Absorption spectrum of Alexa 488 labeled GOx.....	138
Figure 3.9 Modification with pNIPAM nanoparticles with Alexa 488 labeled GOx.....	139
Figure 3.10 The fluorescence image of Alexa 488-GOX on PNIPAM Nanoparticles.....	140

Figure 3.11 The TEM image of streptavidin-bound biotinylated gold nanoparticles on pNIPAM particles.....	141
Figure 3.12 Determination of number of GOX enzymes on the NIPAM Nanoparticles.....	144
Figure 3.13 DLS size distribution of NIPAM nanoparticles.....	145
Figure 3.14 DLS phase transition curve of PNIPAM and PNIPMAM Particles.....	146
Figure 3.15 Kinetics of the GOx enzymatic reaction by monitoring ABTS ²⁻ using UV-Vis.....	148
Figure 3.16 Real-time heating and cooling of the thermoresponsive nanoparticle catalyzed relations.....	150
Figure 4.1 Photo-printing MTFM sensors on the glass coverslip with defined patterns.....	167

Chapter 1: Introduction of mechanotransduction and cell adhesion

Adapted from Jurchenko, C.; Chang, Y.; Narui, Y.; Salaita, K.S. Integrin-generated forces lead to streptavidin-biotin unbinding in cellular adhesions *Biophys. J.* 2014, 106, 1436-1446, and Chang, Y.; Liu, Z; Zhang, Y.; Galior, K.; Yang, J.; Salaita, K.S. A general approach for generating fluorescent probes to visualize piconewton forces at the cell surface *J. Am. Chem. Soc.* 2016, 138,2901-2904, used with permission.

1.1. Mechanotransduction in cell biology

Signal transduction is the process by which information, or signals, are transmitted as a series of molecular events within an organism or cell in order to ultimately produce a response.¹⁻³ An example of a signaling pathway includes ligand binding to its cognate receptor, which then initiates a cascade of biochemical events. In the process of signal transduction, a signal is transmitted in a living system as a series of molecular events, which ultimately result in a response. The changes elicited by ligand binding of a receptor give rise to a cascade of biochemical events along a signaling pathway. The ways through which chemical or biological molecules (proteins or nucleotides) regulate signaling pathways primarily depend on solution chemistry where enzyme activities, reaction rates and binding affinities impact cellular processes.⁴ There has been significant interest in studying the process by which cells detect mechanical cues and convert these into chemical signals and vice versa. Mechanotransduction is the term that describes this phenomenon. Initially, these studies were focused on the tissues or organs that are mechanically stressed such as muscles, bones, cartilages, and blood vessels. These tissues experience mechanical stress and respond by modulating gene expression and cell development. Sensory systems such as hair cells in the ear also undergo the process of transducing physical stimuli into biochemical responses.⁵ Mechanotransduction started to attract more attention in the 1950s, when Sanford and coworkers first discovered that cancer cells were able to proliferate in soft agar without anchorage while most non-cancerous cells were known to fail to grow in non-supportive culture conditions⁶. This was one of the first studies of mechanotransduction on the cellular level which provided an important experimental tool for cancer research. Other studies on the cellular level

have shown that the sensation of membrane tension could lead to important changes in cell mobility such as migrating and spreading.^{7,8} With the rapid advancement in molecular biology tools, as well as the exchange with multiple disciplines such as physics and materials and engineering, a considerable amount of effort has been directed toward understanding the molecular mechanisms of mechanotransduction. The techniques that are widely used in studying molecular mechanotransduction include protein engineering, atomic force microscopy (AFM), high resolution fluorescence microscopy, optical traps, and advanced materials.^{9–13}

It has been shown that at the molecular level, sensing of mechanical cues is based on protein conformational changes induced by forces such as the opening of membrane channels or altered affinities to binding other factors, leading to downstream pathways.¹⁴ The generation of mechanical tension is also based on the conformational changes of proteins. For example, cellular motility and contractility depend on the conformational change of the motor protein myosin, an ATPase that moves along actin filaments.¹⁵ In addition to physical forces, cells also react to the mechanical properties of the environment, including the extracellular matrix (ECM) and neighboring cells. The stiffness of the environment can also have a major impact on cancer biology and developmental cell biology.^{16,17} For example, stem cells are directed towards specific fates depending on stiffness of the substrate on which the cells are grown.¹⁷ Soft environments that are similar in mechanical properties to brain tissues are neurogenic, while rigid substrates mimicking the mechanical stiffness of bone tissues are osteogenic. The matrices that have a rigidity in between these two extremes match the mechanical properties of muscles and lead to a myogenic cell fate. As cells rely on

mechanotransduction signaling for normal function, many human pathologies are directly the result of impaired mechanics or mechanosensing. A commonly used example is loss of hearing caused by mutations in the genes that encode for mechanosensitive proteins. Anecdotally, tumors are often detected due to their different mechanical properties compared to normal tissue. Other examples of tissues that could potentially be affected by mechanotransduction malfunctions include bone, cartilage, the lung, the immune system, and the central nervous system (Table 1.1).

1.2. Focal adhesion and mechanotransduction

Extensive research has identified several molecular structures involved in cellular mechanotransduction. There is growing recognition that the dynamic interactions between cells with their microenvironment-ECM and with neighboring cells play a central role in cell motility, proliferation and fate.¹⁸ At the center of these interactions are primarily myosin motors generating forces on actin cytoskeleton connecting cell–cell or cell–matrix adhesions.¹⁹ A great amount of research has been dedicated to understanding the cellular and molecular mechanisms of cellular communication with the environment. Focal adhesions (FAs), discovered in the 1970s, are multi-protein assembles at the cell membrane that mechanically link the cellular cytoskeleton to the ECM.^{20–22} The FA is comprised of hundreds of different structural, signaling, and adaptor proteins. Of particular importance are the integrin transmembrane proteins which nucleate the formation of the FA and connect intracellular actin bundles and the ECM in many cell types transmitting chemical and mechanical signals in a bidirectional manner. Integrins bind to ECM proteins such as fibronectin, vitronectin, and collagen via short amino acid

sequences, such as the RGD motif found in fibronectin, laminin, or vitronectin, or the DGEA and GFOGER motifs found in collagen.²³ Integrins are heterodimer proteins which contain one α and one β subunit. Each subunit is in different forms and there are a total of 24 types of integrins though different combinations of these subunits. Different combination of integrins bind and associate with different extracellular ligands, and these combinations also have different distribution in varies cell types. For example, the most widely spread integrin, $\alpha 5 \beta 1$, binds mainly to fibronectin and proteinases. Whereas $\alpha \nu \beta 3$ mainly expressed in activated endothelial cells, melanoma, and glioblastoma cells interacts with a broader spectrum of ECM proteins.²⁴ Intracellularly, integrins bind to the

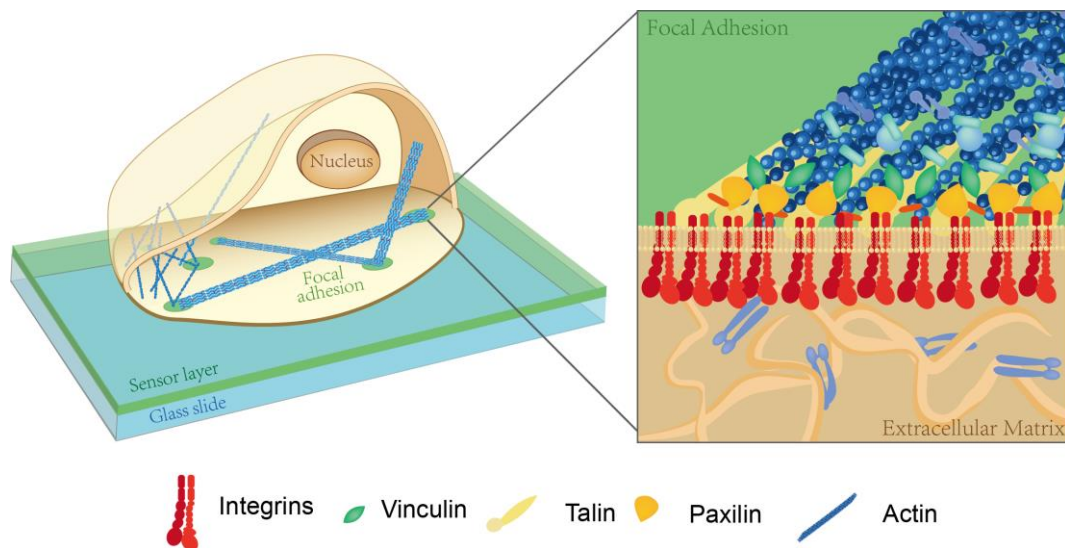


Figure 1.1 Focal adhesion assembly and mechanotransduction

Schematic showing how focal adhesions form the connection between ECM and cytoskeleton. Note that the FA is a multiprotein assembly with integrins at the core. The focal adhesions sense and transduce matrix rigidity and transmit tension from actin fibers to the ECM.

cytoskeleton via adapter proteins such as talin, α -actinin, filamin, vinculin, and tensin.¹⁸ Many other intracellular signaling proteins, such as focal adhesion kinase (FAK), also participate in the formation of the focal adhesions complex which altogether forms the foundation of mechanotransduction with ECM.

Evidence has shown that the above-mentioned myosin motor machinery is attached to FAs, and the mechanism of force generation has been described through the sliding filament theory and the swinging crossbridge model of myosin movement on actin filaments.^{25–27} The sliding filament theory is a model of muscle contraction that postulates that the actin filaments containing I-bands slide past the myosin-containing A-bands to generate force, whereas the swinging crossbridge model describes the ATP-dependent changes in the actin–myosin crossbridge angle that would cause the thin filaments to slide past myosin. These mechanisms form the basis for the generation of cellular tension. Tension generated by myosin is transmitted through actin filaments to the FAs, where it has been discovered that talin is involved in the linkage of actin to the integrin tail, and it is stretched under tension periodically. This process is described as a stick-slip mechanism.^{28–30} The actin binds to talin (‘stick’) and transmits tension to stretch it until the actin–talin bond ‘slips’ and talin refolds. The stretching permits the binding of vinculin to enhance the coupling to the actin cytoskeleton and reinforcement of the FA.

The complete cell force transmission started from the above mentioned focal adhesion complexes at the cell surface that physically link the ECM to the cytoskeleton. Furthermore, the cytoskeleton is coupled to the nucleus through nesprins and possibly other proteins on the outer nuclear membrane. Nesprins interact across the luminal space

with inner nuclear membrane proteins SUN1 and SUN2. These proteins are retained at the nuclear membrane by binding with other nuclear envelope proteins such as lamins and emerin.³¹

There are other proteins that are either within the nuclear architecture or interact with parts of the nucleus to facilitate coupling of the nucleus cytoskeleton with the ECM. Nuclear lamins use both activities, because they form stable nuclear complexes within the nucleus that can facilitate force transmission from the ECM to the nuclear interior by binding to DNA. Furthermore, another method to promote nuclear cytoskeletal coupling is through the binding of nuclear pore complexes by lamins and SUN proteins.

The cellular forces applied on these proteins are dependent on modifications of either cellular or extracellular structure and organization, which lead to fluctuations in the intracellular force transmission. These forces ultimately manifest as changes in mechanosensitive signaling. Therefore, the changes in intracellular force transmission through changes in extracellular or cellular structures can lead to altered molecular forces acting on these proteins, resulting in attenuated or increased mechanosensitive signals.

The extracellular changes include mechanical forces or deformations experienced by the tissue, or changes in ECM composition that affect its stiffness or biochemical properties.

Changes in cellular structures usually stem from inherited mutations in proteins that are part of the myosin tension generating machinery, the cytoskeletal network, the nuclear envelope and interior, and the FA complexes.³² Malfunction of these molecules can change the intracellular force distribution and thus interfere with mechanotransduction signaling. On the other hand, abnormality in cellular mechanosensors can also disturb mechanotransduction signaling when force distribution is normal. Malfunction in

mechanotransduction is involved in numerous diseases, including atherosclerosis, hypertension, osteoporosis, muscular dystrophy, myopathies, and cancer. For example, recent findings suggest that pathogenesis of glaucoma and axial myopia are caused by increased mechanical stress.³³ Glaucoma is a pathology characterized by elevated hydrostatic pressure within the ocular orbit. This results in altered biomechanics of the optic nerve head, which could then manifest as decreased vision or even overt blindness. Human eye tissues have been shown to be exquisitely sensitive to changes in intraocular pressure, with even minute changes leading to tissue deformation.³⁴ In another example, in Duchenne muscular dystrophy, forces generated in the sarcomeres in skeletal muscle cells are transmitted to the ECM through a protein complex that consists of dystrophin, which shields the cell membrane from excessive stress. However, gene mutations in the dystrophin gene disrupt force transmission between the cytoskeleton and the ECM, which leads to progressive muscle degeneration.³⁵ Table 1.1 lists diseases associated with

defects in mechanotransduction. Therefore, it is imperative to understand the molecular mechanisms of mechanotransduction.

Disease	Primary cells/tissues affected
Asthma and lung dysfunction	Endothelial cells and alveolar tissue
Axial myopia and glaucoma	Optic neurons and fibroblasts
Cancer	Multiple cell types and tissues
Deafness	Hair cells in the inner ear
Developmental disorders	Multiple cell types and tissues
Muscular dystrophies and cardiomyopathies	Myocytes, endothelial cells and fibroblasts
Osteoporosis	Osteoblasts
Polycystic kidney disease	Epithelial cells
Potential central nervous system disorders	Neurons
Potential immune system disorders	Leukocytes

Table 1.1 Diseases associated with defects in mechanotransduction

1.3. RGD motif and synergy binding site on fibronectin

One of the major ECM protein components, fibronectin, is the most well studied ECM proteins. Fibronectin is a dimeric glycoprotein and serves as a ligand for integrin $\alpha 5\beta 1$. Fibronectin requires tension to assemble into fibrils.^{36,37} Each subunit of fibronectin is composed of three homologous domains termed FNI, FNII, and FNIII. The Arg-Gly-Asp (RGD) sequence in FNIII domain 10 (FN10) is the crucial binding site for fibronectin receptors such as integrins (Figure 1.2). A synergy binding site required for binding integrin $\alpha 5\beta 1$ is located in FN9. The short amino acid sequence Pro-His-Ser-Arg-Asn (PHSRN) was reported to be crucial for the synergistic binding effect of integrins.³⁸ However, other literature has argued that the synergy site is solely a more extended

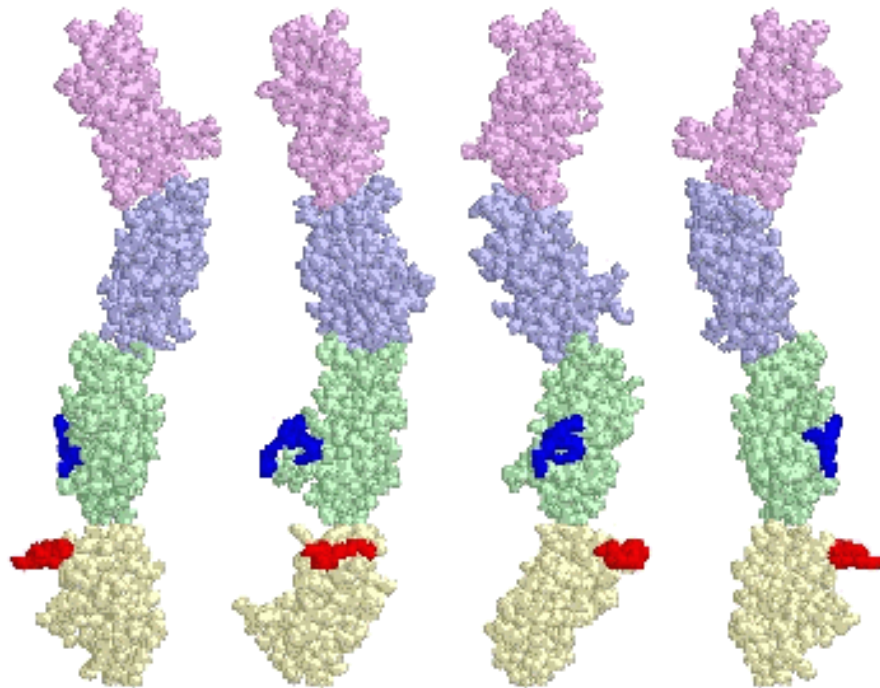


Figure 1.2 Structure of the fibronectin fragment III7-10 as determined by X-ray crystallography of the recombinant protein fragment

RGD highlighted in blue and PHSRN highlighted in red. Structure data were obtained from Leahy et al., 1996⁶⁸

surface of FN9 that is not involved with integrin binding events.^{39,40} An atomic force microscopy (AFM) measurements study shows that rupture force of PHSRN deletion mutants was less than that of the wild type and was not increased by activation, which suggests that integrin activation involved a cooperative interaction with both the RGD and synergy sites.⁴¹ Therefore, it would be interesting to further understand the role that the synergy binding site plays in mechanotransduction through integrin and fibronectin.

1.4. Other receptor systems

Cells sense and respond to physical cues externally from ECM and neighboring cells. At cell–cell contacts, cadherin adhesions are sites where cells mechanically communicate with neighboring cells and resist tugging forces from each other.⁴² Cadherin molecules play major roles in mechanical tension transmission and in the maintenance of tissue integrity. A role for cadherin in mechanotransduction has been hypothesized and directly tested using magnetic tweezers.⁴³ Stiffened adhesion contacts were observed between the cadherin-coated beads and the cells in response to repetitive twisting force. The stiffening increased with the magnitude of the applied force, which suggested the engagement of E-cadherin in homophilic interactions and in sensing force and triggering a cellular response that involves the actin cytoskeleton.

1.5. Methods for studying live cell mechanical properties

Presently, the field of research in mechanotransduction is advancing rapidly due to the integration of multiple disciplines, as well as to the development and application of better tools to measure physical parameters of protein function in cells. The use of elastic

silicone surfaces as substrates for cell spreading first showed that non-muscle cells can apply traction forces on their environment.⁴⁴ This pioneering force-sensing tool formed the basis for the development of traction force microscopy (TFM), which is the gold standard for measuring single cell mechanics. In its current form, TFM substrates are embedded with fluorescent beads and the movements of these beads are recorded and used to calculate the applied cellular forces on the substrate.⁴⁵ Meanwhile, incubating cells on μm -scale patterned ECM demonstrated that the geometry of the matrix is crucial for controlling cell growth and death.⁴⁶ In the 1990s, techniques that allow for the application of active and passive forces to cells and molecules were introduced and provided the means to elucidate details of the mechanosensing process.⁵

For example, magnetic tweezers have been used to manipulate the movement of magnetic beads coated with integrin receptor ligands to apply forces to cells directly and this was observed to lead to rapid strengthening of the cytoskeleton⁴⁷. Atomic force microscopy (AFM) was used in mechanics studies of muscle proteins titins.⁴⁸ Pulling force was applied to the large muscle protein titin by AFM tips and the results showed that titin could be mechanically unfolded to unravel its individual immunoglobulin-like domains. This behavior suggested the mechanism of muscle stabilization against stretching. AFM was also used to study the properties of intramolecular bonds between receptors and their ligands.⁴⁹

Another form of TFM employs pillar arrays made from elastic polymers with a range of varied dimensions and stiffness. In this type of force measurement, live cells are incubated on the pillar arrays and the displacement of the pillars is measured and used to determine cellular forces that were applied to the substrate.⁵⁰ The advantage of the pillar

array approach is that it precludes the need for finite element computational modeling and analysis.^{51,52} The major limitation of pillar array and conventional TFM is the limited spatial and temporal resolution. Also the force resolution of these methods is at the nanoNewton scale which is 1000 times greater than the pN forces applied by integrin receptors within FAs. Of course, single molecule forces spectroscopy methods, such as optical tweezers use a focused laser beam to control the movement of beads to provide lateral or axial forces onto cells and thus measure forces experienced by single molecules on cell surfaces.⁵³ This offers high force sensitivity but such single molecule methods are highly serial, interrogating one molecule at a time. Each tool has its own advantages in terms of sensitivity, detection limits, spatial resolution etc., and therefore each methods is suitable for specific applications. The ideal probes would provide the pN resolution inherent to single molecule force spectroscopy, but with the throughput of TFM or even conventional fluorescence microscopy. In following section and in Chapter 2, I will discuss the advent of molecular force probes to map cellular traction forces.

1.6. Current molecular-scale tension sensors

Over the past decade, new methods have been developed to address the need for measuring molecular-scale forces in living cells. The detection limit of temporal and spatial magnitudes have been largely improved by involving fluorescence microscopy to this field. Fluorescence resonance energy transfer (FRET) is a mechanism on which new methods have been based upon and can extend the measurement to light microscopy resolution ($\sim 10^2$ -10 nm). FRET-based tension sensors were developed, and forces that could produce stretching of specific proteins were sensed with this tool.⁵⁴⁻⁵⁹ These molecular tension sensors consist of two basic components. The first component is a

FRET pair of chromophores that acts as a spectroscopic ruler, and the second component is a spacer connecting the two chromophores. These fluorescence based molecular tension sensors could be generally categorized into two classes, 1) sensors that are genetically engineered and expressed within living cells 2) sensors that are anchored to a surface mimicking the interaction of cells and the ECM or neighboring cells.

2.1.1 Genetically encoded tension sensors

In the case of genetically encoded tension sensors, the fluorophore and linker are fluorescent proteins and elastin that are genetically inserted into a protein of interest inside the cell. In 2010, Grashoff et al. designed a tension sensor module (TSMoD) which contains fluorescent proteins mTFP1 and Venus as the FRET reporters and amino acid sequence derived from spider silk protein as the flexible linker.^{54,60} TSMoD was then genetically inserted into vinculin to observe tension during cell adhesion and migration by monitoring the fluorescence using fluorescence microscopy. An increase in tension across vinculin within FAs at the protruding edges of the cell indicated that vinculin was experiencing tension. The dynamic range of the TSMoD was calibrated using single-molecule fluorescence imaging coupled with optical tweezers. Therefore, an average force of 2.5 pN was reported as the calibration. Nowadays, the TSMoD module is being widely applied to by a variety of mechanotransduction related proteins to study forces and cellular signaling pathways. Examples include E-cadherin, VE-cadherin,^{61,62} and PECAM.⁶³

2.1.2 Living-nonliving interface tension sensors

Interface tension sensors that are immobilized to a solid support provide a means to investigate molecular forces between membrane receptors and ligands, as well as cell-cell

or cell-ECM adhesion interactions. These anchored tension probes also elucidate how signals are relayed from the extracellular surroundings to become intracellular chemical cascades. Specifically, our group reported the first immobilized molecular tension sensor specific to cell surface receptors, which was used to determine the binding force exerted by the epidermal growth factor receptor (EGFR) with its ligand (Figure 1.3).⁵⁷ This tension-sensing method was termed molecular tension fluorescence microscopy (MTFM).^{64,65} The first developed MTFM sensor consisted of a pair of fluorophore-quencher connected by a PEG linker. The linker was anchored to the surface of a glass coverslip through streptavidin-biotin binding. The fluorophore-quencher pair reports the tension input as a simple “turn on” fluorescent signal. The worm-like chain model was applied to the extension of the PEG polymer in order to calculate the dynamic range of the MTFM sensor. This model can convert the fluorescence signal and FRET efficiency into an estimated per ligand force value. However, these values represent the minimum average force applied per receptor, because of the ensemble nature of the FRET measurements, and this principle holds true for all MTFM sensors, including those that are genetically encoded into the systems.

Recently, we found that biotin-streptavidin-immobilized MTFM probes were dissociated due to integrin receptor forces.⁶⁴ This was unexpected because this association is described as the strongest non-covalent bond in nature. Given that integrins exert sufficient tension to dissociate the biotin-streptavidin bond, we next developed nanoparticle-based MTFM probes that employ thiol-gold binding for immobilization.⁶⁴ We chose this approach because gold-thiol binding is a facile method for sensor immobilization and in the same time avoids the need for a FRET quencher, since gold

nanoparticles are effective quenchers for organic molecule fluorophores. This type of MTFM sensor, developed by Liu et al.⁵⁵. A cyclic RGD ligand was modified onto a gold nanoparticle (AuNP) via a PEG linkage. As the AuNP in the probe serves as both the anchor and the quencher, this energy transfer mechanism was described as nanometal surface energy transfer (NSET). This mechanism differed from FRET-based sensors because the energy transfer efficiency has a $1/r^4$ relationship, whereas that of FRET-based sensors is dependent on the fluorophore-quencher distance, which has a relationship of $1/r^6$. Thus, the energy transfer efficiency for NSET-based probes provides a more linear regimen of fluorescence-distance responses. Furthermore, NSET demonstrates larger R_0 values, thus probing greater distances and providing higher efficiency. Nonetheless, thiolated ligands are known to dissociate from the Au surface within 24 hrs.⁶⁶ Ligand exchange is further exasperated in biological media containing $\sim 100 \mu\text{M}$ thiol bearing molecules.⁶⁷ Alternatively, Blakely and colleagues used amine-thiol heterobifunctional linkers to immobilize DNA tension probes. However, this crosslinking chemistry limits the choice of ligands to molecules lacking lysine and cysteine. Therefore, new bio-orthogonal approaches for covalent immobilization of molecular tension probes are needed.

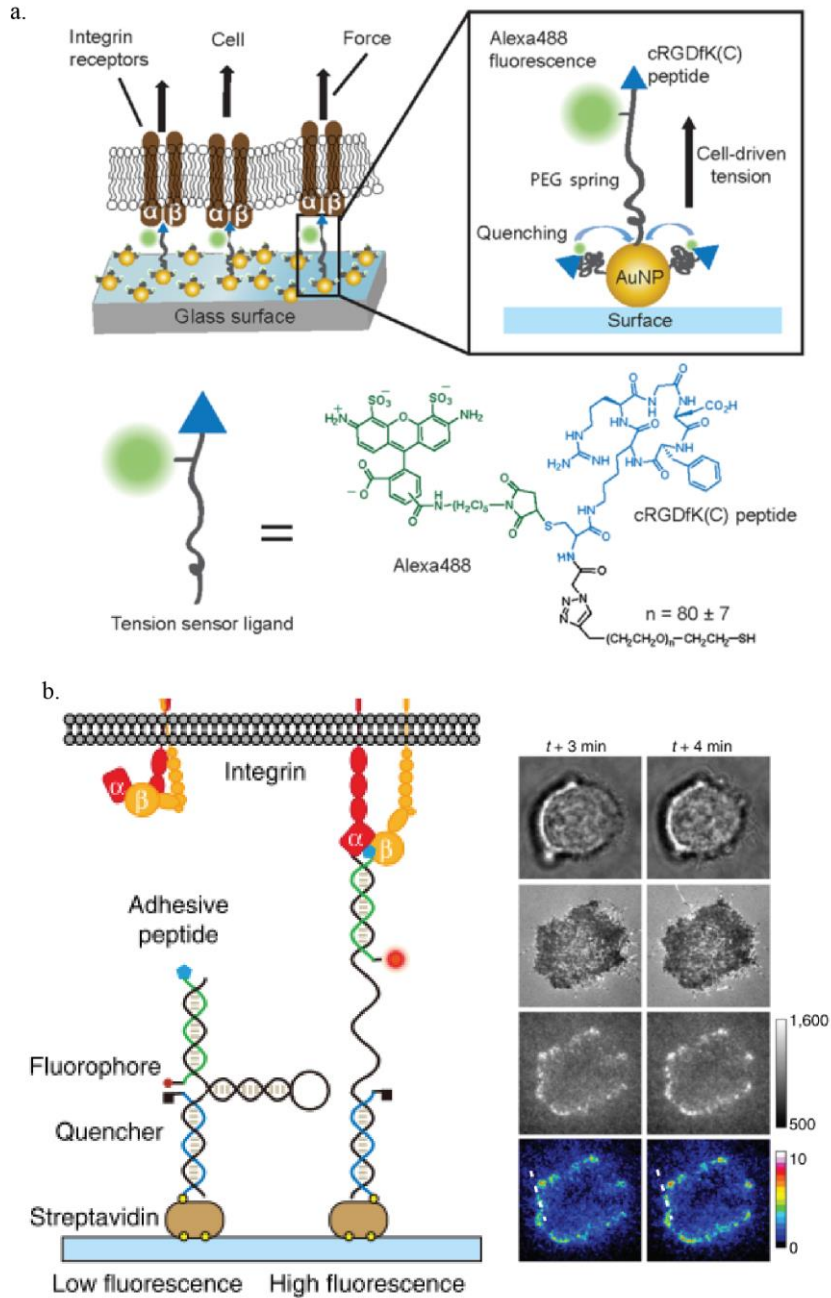


Figure 1.3 FRET based surface molecular tension sensors

PEG (a) and DNA (b) based molecular tension sensors. Figures are adapted from the original literatures a. (1) Liu, Y.; Yehl, K.; Narui, Y.; Salaita, K. J. Am. Chem. Soc. 2013, 135 (14), 5320–5323. b. Zhang, Y.; Ge, C.; Zhu, C.; Salaita, K. Nat. Commun. 2014, 5, 5167

1.7. Outlook

The work with the molecular tension sensors highlighted the importance of the role of protein assemblies in cellular mechanotransduction and raised further questions regarding how these assemblies contribute to cellular processes. There are still many questions yet to be answered regarding the role that mechanotransduction plays in living systems, and there are issues with these existing tools to be addressed. There are hundreds of signaling pathways with the potential for having sensitivity to physical inputs. To be able to efficiently study a wide range of target mechanical active molecules, a highly versatile sensor is needed for adaptation of these ligands. Long-lasting tools are needed to be able to monitor the cellular tension at a longer time scale as some of the biological activities entail. This requires the higher stability and biocompatibility of the tension sensors.

- (1) Bradshaw, R. A.; Dennis, E. A. *Handbook of cell signaling*, 2/e; 2010; Vol. 1–3.
- (2) Martin, G. S. *Cancer Cell* **2003**, 4 (3), 167–174.
- (3) Lai, E. C. *Development* **2004**, 131 (5), 965–973.
- (4) Eungdamrong, N. J.; Iyengar, R. *Biol. Cell* **2004**, 96 (5), 355–362.
- (5) Iskratsch, T.; Wolfenson, H.; Sheetz, M. P. *Nat. Rev. Mol. Cell Biol.* **2014**, 15 (12), 825–833.
- (6) SANFORD, K. K.; LIKELY, G. D.; EARLE, W. R. *J. Natl. Cancer Inst.* **1954**, 15 (2), 215–237.
- (7) Gauthier, N. C.; Fardin, M. A.; Roca-Cusachs, P.; Sheetz, M. P. *Proc. Natl. Acad. Sci.* **2011**, 108 (35), 14467–14472.
- (8) Sheetz, M. P.; Singer, S. J. *Proc. Natl. Acad. Sci.* **1974**, 71 (11), 4457–4461.
- (9) Liu, Z.; Tan, J. L.; Cohen, D. M.; Yang, M. T.; Sniadecki, N. J.; Alom, S.; Nelson, C. M.; Chen, C. S. **2010**.

- (10) Gardel, M. L.; Schneider, I. C.; Aratyn-Schaus, Y.; Waterman, C. M. *Annu. Rev. Cell Dev. Biol.* **2010**, *26* (1), 315–333.
- (11) Moy, V. T.; Florin, E. L.; Gaub, H. E. *Science (80-.)*. **1994**, *266* (5183), 257–259.
- (12) Shah, N. H.; Muir, T. W. *Chem. Sci.* **2014**, *5* (1), 446–461.
- (13) Borghi, N.; Sorokina, M.; Shcherbakova, O. G.; Weis, W. I.; Pruitt, B. L.; Nelson, W. J.; Dunn, A. R. *Proc. Natl. Acad. Sci. U. S. A.* **2012**, *109* (31), 12568–12573.
- (14) Schwarz, U. S.; Gardel, M. L. *J. Cell Sci.* **2012**, *125* (Pt 13), 3051–3060.
- (15) Spudich, J. A. *Nat. Rev. Mol. Cell Biol.* **2001**, *2* (5), 387–392.
- (16) Lochter, a; Bissell, M. J. *Semin. Cancer Biol.* **1995**, *6*, 165–173.
- (17) Engler, A. J.; Sen, S.; Sweeney, H. L.; Discher, D. E. *Cell* **2006**, *126* (4), 677–689.
- (18) Chen, C. S.; Tan, J.; Tien, J. *Annu. Rev. Biomed. Eng.* **2004**, *6*, 275–302.
- (19) Plotnikov, S. V.; Pasapera, A. M.; Sabass, B.; Waterman, C. M. *Cell* **2012**, *151* (7), 1513–1527.
- (20) CURTIS, A. S. *J. Cell Biol.* **1964**, *20*, 199–215.
- (21) Izzard, C. S.; Lochner, L. R. *J. Cell Sci.* **1976**, *21* (1), 129–159.
- (22) Abercrombie, M.; Heaysman, J. E. M.; Pegrum, S. M. *Exp. Cell Res.* **1970**, *62* (2–3), 389–398.
- (23) Hynes, R. O. *Cell*. 2002, pp 673–687.
- (24) Giancotti, F. G. *Science (80-.)*. **1999**, *285* (5430), 1028–1033.
- (25) Ludueña, M. A.; Wessells, N. K. *Dev. Biol.* **1973**, *30* (2), 427–440.
- (26) Kolega, J. *J. Cell Biol.* **1986**, *102* (4), 1400–1411.
- (27) LEVY, J. A.; DIAMENT, A. J.; SARAIVA, S. *Arq. Neuropsiquiatr.* **1960**, *18*, 259–264.

- (28) Hu, K.; Ji, L.; Applegate, K. T.; Danuser, G.; Waterman-Storer, C. M. *Science* (80- .). **2007**, *315* (5808), 111–115.
- (29) Aratyn-Schaus, Y.; Gardel, M. L. *Curr. Biol.* **2010**, *20* (13), 1143–1153.
- (30) del Rio, A.; Perez-Jimenez, R.; Liu, R.; Roca-Cusachs, P.; Fernandez, J. M.; Sheetz, M. P. *Science* **2009**, *323* (5914), 638–641.
- (31) Haque, F.; Lloyd, D. J.; Smallwood, D. T.; Dent, C. L.; Shanahan, C. M.; Fry, A. M.; Trembath, R. C.; Shackleton, S. *Mol. Cell. Biol.* **2006**, *26* (10), 3738–3751.
- (32) Jaalouk, D. E.; Lammerding, J. *Nat. Rev. Mol. Cell Biol.* **2009**, *10* (1), 63–73.
- (33) Tan, J. C. H. *Br. J. Ophthalmol.* **2006**, *90* (3), 383–388.
- (34) Johnstone, M. A. *J. Glaucoma* **2004**, *13* (5), 421–438.
- (35) Heydemann, A.; McNally, E. M. *Trends in Cardiovascular Medicine*. 2007, pp 55–59.
- (36) Zhong, C.; Chrzanowska-Wodnicka, M.; Brown, J.; Shaub, A.; Belkin, A. M.; Burridge, K. *J. Cell Biol.* **1998**, *141* (2), 539–551.
- (37) Wierzbicka-Patynowski, I.; Schwarzbauer, J. E. *J. Cell Sci.* **2003**, *116* (Pt 16), 3269–3276.
- (38) Aota, S.; Nomizu, M.; Yamada, K. M. *J. Biol. Chem.* **1994**, *269* (40), 24756–24761.
- (39) Kauf, A. C. W.; Hough, S. M.; Bowditch, R. D. *Biochemistry* **2001**, *40* (31), 9159–9166.
- (40) Redick, S. D. *J. Cell Biol.* **2000**, *149* (2), 521–527.
- (41) Li, F.; Redick, S. D.; Erickson, H. P.; Moy, V. T. *Biophys. J.* **2003**, *84* (2), 1252–1262.

- (42) le Duc, Q.; Shi, Q.; Blonk, I.; Sonnenberg, A.; Wang, N.; Leckband, D.; de Rooij, J. *J. Cell Biol.* **2010**, *189* (7), 1107–1115.
- (43) Le Duc, Q.; Shi, Q.; Blonk, I.; Sonnenberg, A.; Wang, N.; Leckband, D.; De Rooij, J. *J. Cell Biol.* **2010**, *189* (7), 1107–1115.
- (44) Harris, A.; Wild, P.; Stopak, D. *Science (80-.)*. **1980**, *208* (4440), 177–179.
- (45) Oliver, T.; Jacobson, K.; Dembo, M. *Cell Motil. Cytoskeleton* **1995**, *31* (3), 225–240.
- (46) Chen, C. S.; Mrksich, M.; Huang, S.; Whitesides, G. M.; Ingber, D. E. *Science (80-.)*. **1997**, *276* (5317), 1425–1428.
- (47) Wang, N.; Butler, J.; Ingber, D. *Science (80-.)*. **1993**, *260* (5111), 1124–1127.
- (48) Rief, M. *Science (80-.)*. **1997**, *276* (5315), 1109–1112.
- (49) Merkel, R.; Nassoy, P.; Leung, A.; Ritchie, K.; Evans, E. *Nature* **1999**, *397* (6714), 50–53.
- (50) Ghassemi, S.; Meacci, G.; Liu, S.; Gondarenko, A. A.; Mathur, A.; Roca-Cusachs, P.; Sheetz, M. P.; Hone, J. *Proc. Natl. Acad. Sci.* **2012**, *109* (14), 5328–5333.
- (51) Galbraith, C. G.; Sheetz, M. P. *Proc. Natl. Acad. Sci.* **1997**, *94* (17), 9114–9118.
- (52) Singhvi, R.; Kumar, A.; Lopez, G. P.; Stephanopoulos, G. N.; Wang, D. I.; Whitesides, G. M.; Ingber, D. E. *Science* **1994**, *264* (5159), 696–698.
- (53) Choquet, D.; Felsenfeld, D. P.; Sheetz, M. P. *Cell* **1997**, *88* (1), 39–48.
- (54) Grashoff, C.; Hoffman, B. D.; Brenner, M. D.; Zhou, R.; Parsons, M.; Yang, M. T.; McLean, M. a; Sligar, S. G.; Chen, C. S.; Ha, T.; Schwartz, M. a. *Nature* **2010**, *466* (7303), 263–266.
- (55) Liu, Y.; Yehl, K.; Narui, Y.; Salaita, K. *J. Am. Chem. Soc.* **2013**, *135* (14), 5320–

5323.

- (56) Meng, F.; Suchyna, T. M.; Sachs, F. *FEBS J.* **2008**, *275* (12), 3072–3087.
- (57) Stabley, D. R.; Jurchenko, C.; Marshall, S. S.; Salaita, K. S. *Nat. Methods* **2012**, *9* (1), 64–67.
- (58) Wang, X.; Ha, T. *Science* **2013**, *340* (6135), 991–994.
- (59) Zhang, Y.; Ge, C.; Zhu, C.; Salaita, K. *Nat. Commun.* **2014**, *5*, 5167.
- (60) Hoffman, B. D.; Grashoff, C.; Schwartz, M. a. *Nature* **2011**, *475* (7356), 316–323.
- (61) Borghi, N.; Sorokina, M.; Shcherbakova, O. G.; Weis, W. I.; Pruitt, B. L.; Nelson, W. J.; Dunn, A. R. *Proc. Natl. Acad. Sci. U. S. A.* **2012**, *109* (31), 12568–12573.
- (62) Cai, D.; Chen, S. C.; Prasad, M.; He, L.; Wang, X.; Choessel-Cadamuro, V.; Sawyer, J. K.; Danuser, G.; Montell, D. J. *Cell* **2014**, *157* (5), 1146–1159.
- (63) Conway, D. E.; Breckenridge, M. T.; Hinde, E.; Gratton, E.; Chen, C. S.; Schwartz, M. a. *Curr. Biol.* **2013**, *23* (11), 1024–1030.
- (64) Jurchenko, C.; Chang, Y.; Narui, Y.; Zhang, Y.; Salaita, K. S. *Biophys. J.* **2014**, *106* (7), 1436–1446.
- (65) Jurchenko, C.; Salaita, K. S. *Mol. Cell. Biol.* **2015**, *35* (15), 2570–2582.
- (66) Bhatt, N.; Huang, P. J. J.; Dave, N.; Liu, J. *Langmuir* **2011**, *27*, 6132–6137.
- (67) Mansoor, M. A.; Svardal, A. M.; Ueland, P. M. *Anal. Biochem.* **1992**, *200* (2), 218–229.
- (68) Leahy, D. J.; Aukhil, I.; Erickson, H. P. *Cell* **1996**, *84* (1), 155–164.

Chapter 2: A General approach to generate ultra-robust and highly modular molecular tension probes

Adapted from Jurchenko, C.; Chang, Y.; Narui, Y.; Salaita, K.S. Integrin-generated forces lead to streptavidin-biotin unbinding in cellular adhesions *Biophys. J.* 2014, 106, 1436-1446, and Chang, Y.; Liu, Z; Zhang, Y.; Galior, K.; Yang, J.; Salaita, K.S. A general approach for generating fluorescent probes to visualize piconewton forces at the cell surface *J. Am. Chem. Soc.* 2016, 138,2901-2904, used with permission.

2.1 Motivation and designing the tension sensor

To further elucidate the biophysical fundamentals of mechanotransduction, the design and development of a tool has spawned the following major challenges 1) the specificity to measure forces applied to a certain type of receptors on the cell surface; 2) the durability to enable monitoring the development of tensions over a long period of time (~days); 3) the versatility to accommodate a variety of cell membrane mechanotransduction receptors. To overcome the above-mentioned challenges, herein, we aimed to develop a modular molecular tension sensor capable of long-term measuring cellular tensions. Essentially, the sensor consists of a flexible linker that is conjugated to a biological ligand at one terminus and anchored onto a glass surface for immobilization. The ligand end and the surface end are functionalized with a fluorescent molecular pair (donor and acceptor) that undergoes Fluorescence Resonance Energy Transfer (FRET) mechanism⁶⁸. Cellular forces exerted on the ligand will extend the flexible linker from its relaxed conformational state and increase the distance between the FRET donor and acceptor, resulting in the increase of fluorescence

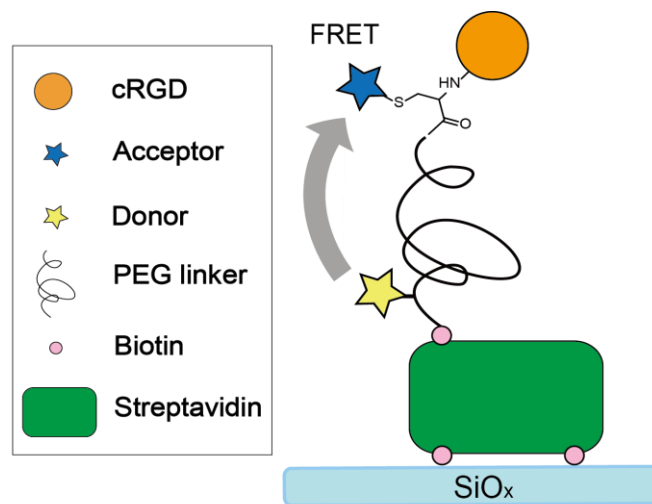


Figure 2.1 Design and mechanism of MTFM tension sensor

intensity and providing a signal to visualize mechanical tension transduced through specific receptor targets (Figure 2.1). To acquire and analyze the fluorescence signal, this approach only requires the use of a conventional fluorescence microscope which allows for non-invasive live cell imaging with high temporal and spatial resolution. The flexible linker in the MTFM tension sensor molecular sensor is comprised of a discrete polyethylene glycol (PEG) polymer because of its unique properties: biocompatibility, minimal non-specific interactions with other biomolecules and well-characterized and importantly reversible force-extension curves. One end of the PEG polymer was modified with a biotin group which is composed of an ureido ring fused with a tetrahydrothiophene ring. This small molecule has a high binding affinity for streptavidin, and this binding interaction is the strongest non-covalent biological interaction known, with a dissociation constant (K_D) in the order of $10^{-14}M$.⁶⁹ Each streptavidin is a tetramer and each subunit binds biotin with equal affinity (Figure 2.2 adapted from Protein Data Bank). The strong affinity for biotin and multi-valency allows for the attachment of multiple biomolecules to one another or onto a solid support. To break the streptavidin-biotin interaction, harsh conditions are needed, which usually result in the denaturation of the protein. The MTFM sensor construct is designed to bond to the biotinylated glass surface through biotin-streptavidin interaction. Thus, the streptavidin served

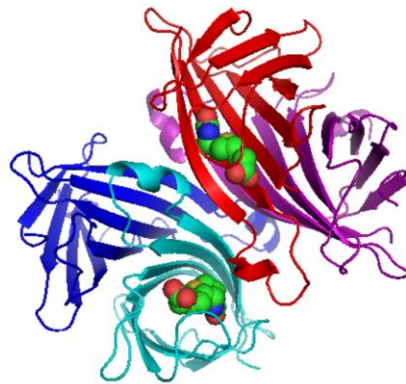


Figure 2.2 Tetrameric structure of streptavidin with 2 bound biotins

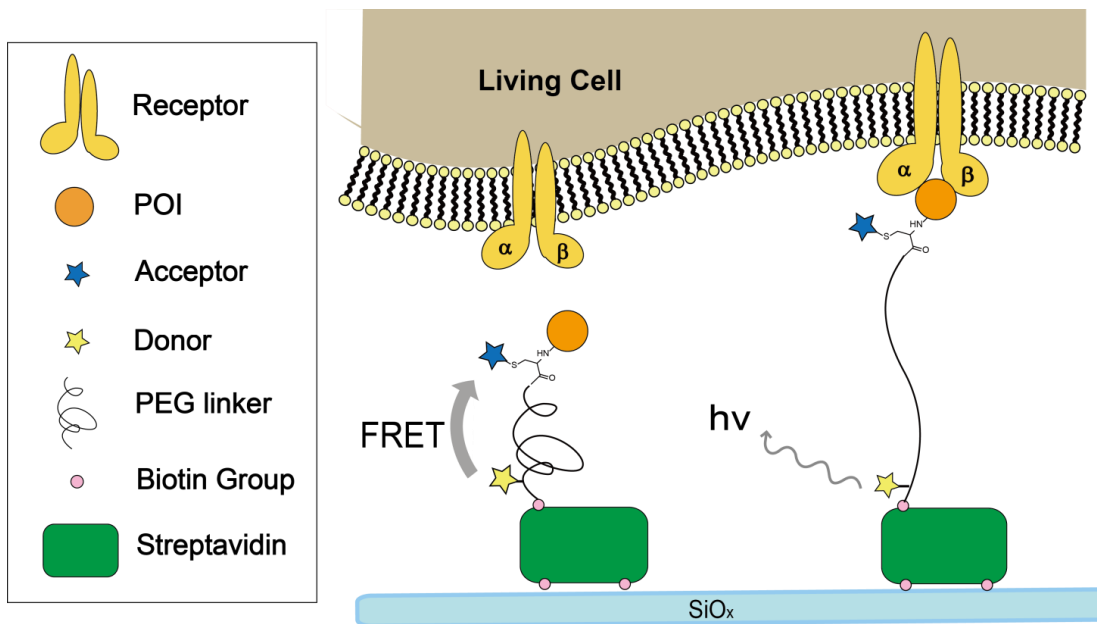


Figure 2.3 Application of MTFM tension sensor

as the glue to immobilize the sensor onto the surface. At the resting state of the MTFM sensor, FRET mechanism occurs between the spectrally matched fluorescence donor and acceptor when exciting the donor using laser. The energy was transferred to an acceptor chromophore through nonradioactive dipole–dipole coupling, therefore no emission of acceptor will be observed. Once a tension sensor is extended, the efficiency of the FRET is reduced inversely proportional to the sixth power of the distance between donor and acceptor. The minor change in distance will result in a drastic change in fluorescent intensity of the FRET donor. Therefore, an increase in donor fluorescence will be recorded by the fluorescence microscope as an indication of the tension at the according area.

2.1.3 The mechanism of quantifying the tension signal

The mechanism of quantifying the tension signal was based on the above-mentioned Fluorescence Resonance Energy Transfer (FRET) mechanism between the fluorescence

donor and acceptors, as well as the worm-like chain (WLC) model in polymer physics describing the behavior of semi-flexible polymers.

2.1.3.1 Fluorescence resonance energy transfer (FRET)

Fluorescence Resonance Energy Transfer (FRET) is first described in 1948 and is being used more and more in biomedical science research and drug discovery currently⁷⁰.

FRET relies on the distance-dependent transfer of energy from a donor molecule to an acceptor molecule (light-sensitive chromophores). The donor molecule is the dye or chromophore that initially absorbs the energy, and the acceptor is the chromophore to which the energy is subsequently transferred. The donor to acceptor energy transfer through FRET is a radiationless transmission of energy. This resonance interaction occurs over greater than interatomic distances, without conversion to thermal energy or molecular collision. The transfer of energy leads to a reduction in the donor's fluorescence intensity and excited state lifetime, and an increase in the acceptor's emission intensity. A pair of molecules that interact in such a manner that FRET occurs is often referred to as a donor/acceptor pair. Due to its sensitivity to distance, FRET has been used to investigate molecular interactions. The donor and acceptor molecules must be in close proximity to one another (typically 10-100 Å). There needs to be a spectrum overlap between the emission spectrum of the donor and the excitation spectrum of the donor. The degree to which the spectra overlap is referred to as the spectral overlap integral (J). It was demonstrated that the efficiency of the energy transfer (E) depends on the inverse sixth-distance between donor and acceptor (see Equation 1).

Eq 1.

$$E = \frac{R_0^6}{R_0^6 + r^6}$$

Where R_0 is the Förster distance at which 50% of the energy is transferred. And r is the actual distance between the FRET donor and acceptor. The distance at which energy transfer is 50% efficient is referred to as the Förster radius (R_0). The magnitude of the R_0 depends on the spectral overlap J of the donor and the acceptor. Förster distances ranging from 2 to 9 nm are most commonly used for biological studies of macromolecules. As a result, FRET is often applied as a spectroscopic ruler. The Förster distance (R_0) is dependent on the fluorescence quantum yield of the donor, the refractive index of the solution (n), the dipole angular orientation of each molecule (k^2), and the spectral overlap integral of the donor and acceptor (J). See Equation 2.

Eq 2.

$$R_0 = 978(n^{-4}fk^2J)\frac{1}{6}$$

The donor and acceptor molecules are different in most cases; therefore FRET can be detected by the fluorescence of the acceptor or by quenching of donor fluorescence. The donor probe is always a fluorescent dye molecule, and the acceptor could be a fluorescent dye whose absorption spectrum overlaps with the donor emission spectrum, or it could be a molecule that does not fluoresce but also absorbs the emission light from the donor.

These molecules are termed as fluorescence quencher molecules. For fluorescent molecules, when appropriately excited, its electrons jump from the ground state (S_0) to a higher vibrational level. Within picoseconds(ps), these electrons decay to the lowest vibrational levels (S_1) and eventually decay (within nanoseconds, ns) back to the S_0 state followed by the emission of a photon of light. (Figure 2.4) When required conditions for FRET are met (i.e. the proximity, the spectrum overlap) decay as donor fluorescence and

energy transfer to the acceptor will compete for the decay of excitation energy. When FRET occurs, the photon is not emitted by the donor, but rather the energy is transferred to the acceptor molecule, whose electrons then become excited. Consequently, the acceptor returns to the ground state S_0 and emits a photon (Figure 2.4).

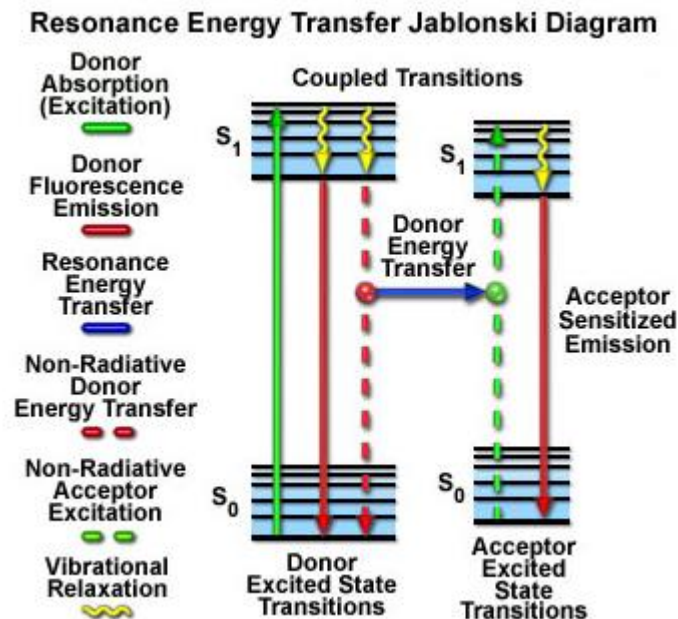


Figure 2.4 Jablonski diagram illustrating the coupled transitions involved between the donor emission and acceptor absorbance in FRET

(Adopted from Brian Herman and Victoria E. Centonze Frohlich - Department of Cellular and Structural Biology, University of Texas Health Science Center)

FRET can be detected and quantified in a number of different ways due to the effect of both a decrease in fluorescence of the donor and an increase in fluorescence of the acceptor. Therefore, the two signals could both be detected, and a ratio of the donor and acceptor could be determined.

Aside from the spectrum overlap, chemical stability and compatibility, high quantum yield, and low background fluorescence (autofluorescence), the high resistance against

photo-bleaching will also offer advantages in our molecular tension sensing application.

Autofluorescence is the natural fluorescence of biological structures such as mitochondria and lysosomes which usually emit at 30-450 nm range. The organic dyes Alexa 488, Alexa 647, Fluorescein, and Tetramethyl rhodamine (TAMRA) are generally chemically stable molecules that have a high quantum yield (~70%) and cover a wide emission range of spectrum from 480-650 nm. Background fluorescence is often reduced within this emission range.

There are a number of matters that need to be considered when designing a FRET experiment. The first is the matter of close proximity that will either be established or removed during the assay depending on the experimental design. The change in proximity will result in a change in signal that can be detected by fluorescence microscopy. Appropriate donor/acceptor pairs need to be designated by the following standards: 1) enough spectral overlap for efficient energy transfer, 2) have enough of a difference in spectrums as to be distinguishable from one another. Moreover, the choice of filters for fluorescent wavelength selection is critical to the success or failure of experimental detection of FRET. The excitation filter for the donor should allow for the exclusive excitation of the donor molecule, while minimize the direct excitation of the acceptor. Direct excitation of the acceptor molecule (acceptor bleed-through) can be accounted for using appropriate controls, however, large proportion of bleed-through will make it very difficult to interpret the experiment result. In most cases, the filters selected for donor excitation will minimize the excitation of the acceptor, while preserving sufficient excitation light for the donor.

Another important issue in regards to detection of FRET involves the absolute quantity of the donor molecules. FRET only occurs between the molecules that are in close proximity and interact with one another. When the quantity of donor and acceptor molecules that undergo FRET only occupies a small percentage, the most present molecules do not interact, in this case, and the actual amount of FRET activity may not be sufficient for detection.

FRET donor-acceptor pairs with separated excitation and emission spectra usually result in low overlap integral, although these pairs could have acceptable Förster distances. For example, Fluorescein emits maximally at 512 nm and Alexa 647 absorbs at 594 nm. The emission spectrum of fluorescein and absorption spectrum of Alexa 647 have a large separation. Herein, a measurement of Förster radius was determined by calculating the overlap integral using the following equations.⁷⁰ (Figure 2.5 and 2.6)

Eq.

$$R_0^6 = 8.82 \times 10^{-11} \cdot \frac{Q_0 \kappa^2 J}{n^4}$$

Eq.

$$J = \int f_D(\lambda) \epsilon_A(\lambda) \lambda^4 d\lambda$$

Where Q_0 is the fluorescence quantum yield of the donor in the absence of the acceptor, κ^2 is the dipole orientation factor, n is the refractive index of the medium, J is the spectral overlap integral, and R_0 = Förster radius, the distance at which the energy transfer efficiency is 50%. The R_0 of Fluorescein and Alexa 647 is calculated to be 5.27 nm, which suggests that large separation between pairs could have acceptable R_0 and it also

allows the measurement of acceptor emission as a result of FRET without interference from donor emission. In addition, these molecules can be linked directly and covalently to the two ends of the PEG polymer, allowing FRET to be used to assess the PEG extension upon force.

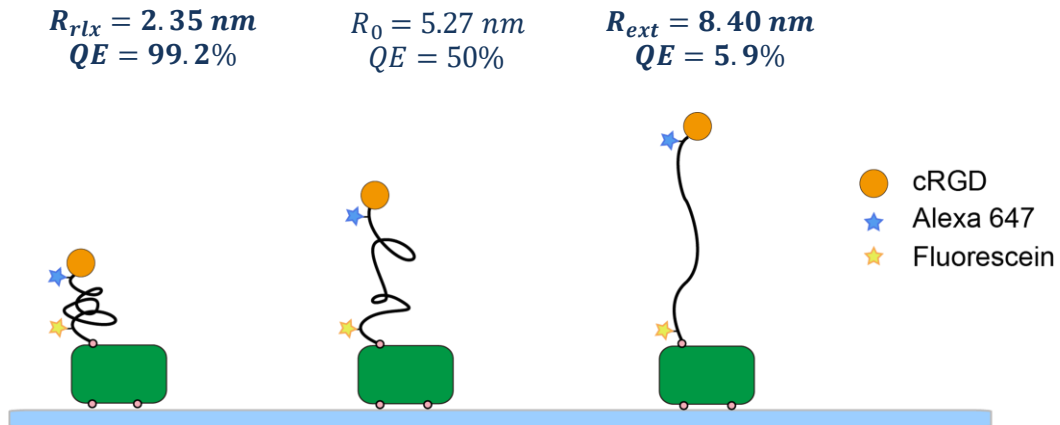


Figure 2.5 Quenching efficiency and Foster distance R_0 of the FRET pair Alexa 647 and Fluorescein

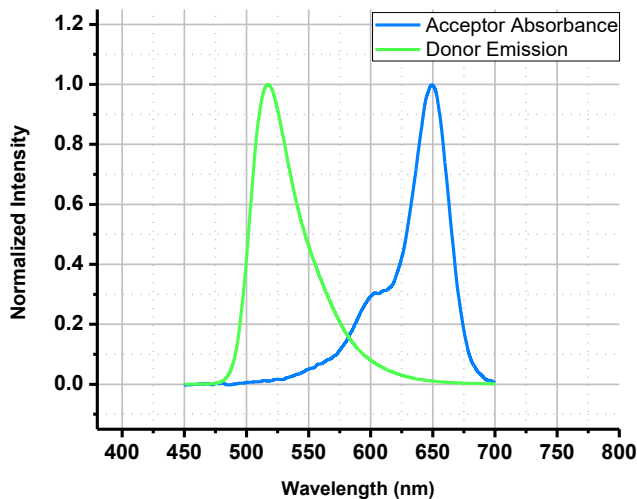


Figure 2.6 Foster distance R_0 calculation of the FRET pair Alexa 647 and Fluorescein

Considering the convenience in synthesis and purification, quantum yield as well as the appropriate Förster distance, we first chose Fluorescein and Alexa 647 as our FRET donor and acceptor.

2.1.3.2 Worm-Like Chain (WLC) Model

Many polymers, including biological molecules such as DNA and proteins, have an intrinsic elasticity. The Worm-Like Chain Model (WLC) is one of the simplest mathematics models used to describe the characteristic behavior of such semi-flexible polymers. It also successfully describes the elastic properties of a variety of biomolecules, such as ssDNA, dsDNA, RNA, and polypeptide chains⁷¹. An inextensible polymer driven by thermal fluctuations will tend to cluster in order to maximize its entropy. This behavior will result in an entropic force that is resistant to attempts to stretch the polymer to its full contour length. Therefore, the WLC model can incorporate a force along the z-direction as followed by Marko and Siggia⁷²:

Eq.

$$f = \frac{k_B T}{\xi} \left(\frac{1}{4 \left(1 - \frac{z}{L}\right)^2} - \frac{1}{4} + \frac{z}{L} \right),$$

Where r = experimental distance between donor and acceptor, T = temperature (310 K)
 ξ = persistence length of the polymer, L = contour length of the polymer, z = polymer extension, and k_B = Boltzmann constant (1.38×10^{-23} N·m/K).

The z , or polymer extension, specifically means the difference in length between the relaxed state and the extended state of the polymer under tension. A theoretical plot of

tension versus polymer extension specifically describing PEG polymer is shown in

Figure. 2.7. Note that PEG 24 is has better sensitivity at detecting tension within the 1-10

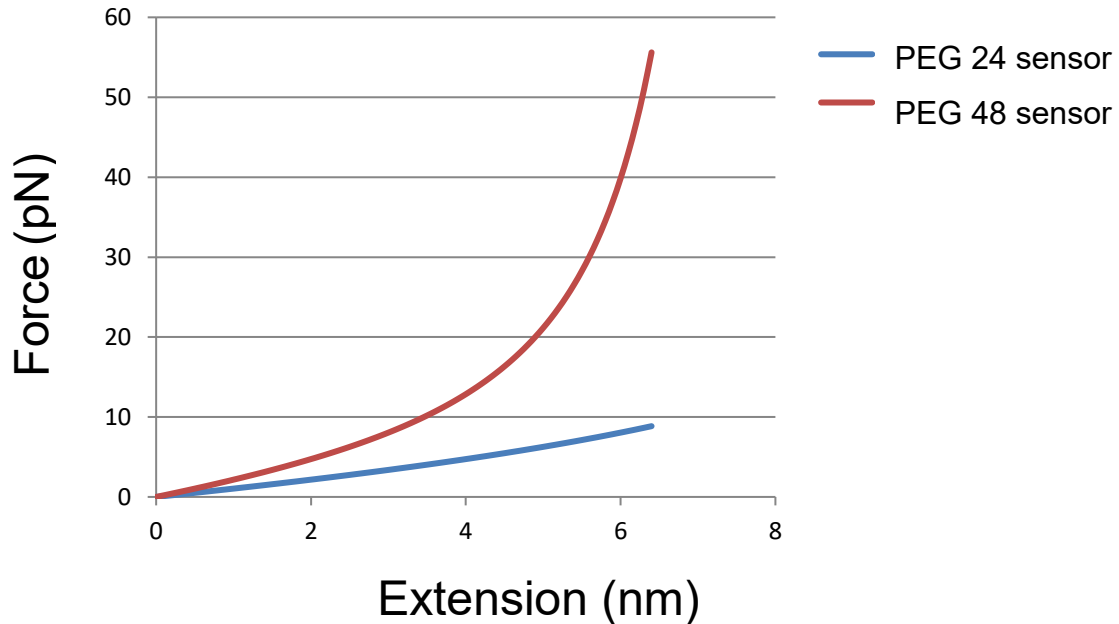


Figure 2.7 Plot of PEG extension z (nm) vs force (pN)

pN range, while PEG 48 has a dynamic range covering 8-30 pN.

2.1.4 Design and synthesis of the tension sensor

The synthesis of the MTFM sensor was split into two steps: the synthesis or recombinant production of the biological ligand and the solid phase synthesis of the MTFM sensor precursor. Solid Phase Peptide Synthesis (SPPS) was adopted in both parts due to its high yield, efficiency, modularity, and simple purification.

2.1.4.1 Solid Phase Peptide Synthesis

Solid Phase Peptide synthesis (SPPS) plays a central role in constructing the MTFM tension sensor. The second module of the synthesis of the MTFM sensor is used to construct the customized peptide/small protein ligand. SPPS is now the standard method for lab synthesis of peptides. SPPS allows for the synthesis of peptides that are difficult to express in bacteria such as peptides with modifications of backbones or peptides containing unnatural amino acids. The solid phase are sub-millimeter porous beads made with polymer and treated with functional units ('linkers'). The peptide chains can be covalently built on the beads through the linkers. The peptide remains covalently linked to the bead until the chemical cleavage from it by trifluoroacetic acid (TFA). During the process of SPPS, the liquid phase containing the amino acid and coupling reagent for each step of coupling is mixed with the solid phase beads. A filtration procedure is performed after each coupling

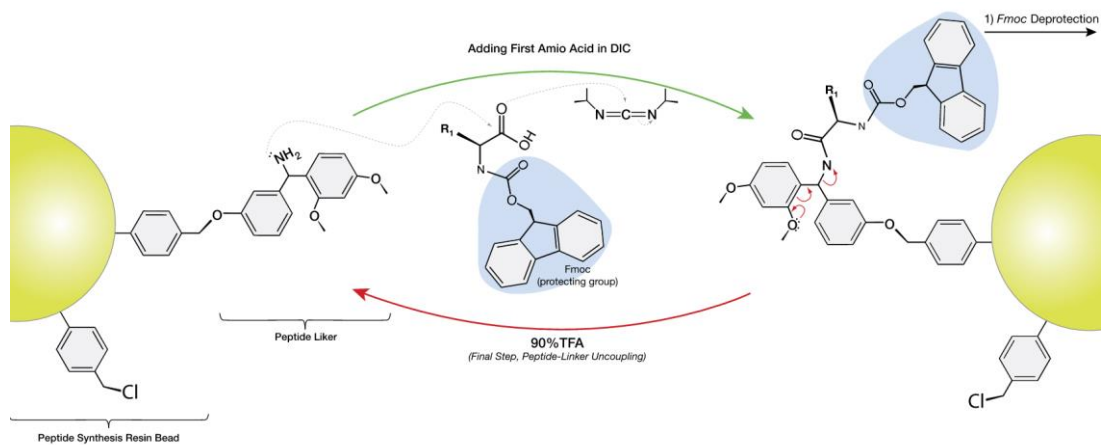


Figure 2.8 Process and mechanism of SPPS

Adapted from Dan Cojocari, Princess Margaret Cancer Centre, University of Toronto

step, and the liquid-phase unreacted amino acids, coupling reagents, and by-products can be flushed away while the peptide remains on the solid phase. The principle of SPPS is repeated cycles of deprotection-wash-coupling-wash (Figure 2.4, adapted from Dan Cojocari, Princess Margaret Cancer Centre, University of Toronto). After on-bead

deprotection, the freed N-terminal amine of a peptide/amino on solid-phase acid is coupled to the C-terminus of an amino acid (N-protected) in the liquid phase. This amino acid that was newly coupled on the solid phase is then deprotected, revealing a new N-terminal amine to which a further amino acid may be attached. The power of this technique is the ability to perform filtration/wash cycles after each reaction, thus removing excess reagent and byproducts with the growing peptide product remaining covalently attached to the solid phase. This avoids the significant loss of product during each purification step and gives extremely high yields in each step. Assuming a 99% yield of each coupling step, a 20-amino acid peptide would result in a ~80% final yield. SPPS proceeds in a C-terminal to N-terminal fashion. There are two major forms of SPPS: Fmoc-deprotection and Boc-deprotection. The N-termini of amino acid monomers is protected by either of these two protecting groups. Fmoc is base labile while Boc is acid labile. The side chains of the amino acids are usually protected by different protecting groups as well, and these protecting groups could be removed by the final TFA deprotection or other specific procedures.

Automated solid phase peptide synthesizers are available for both deprotection methods. However, many research groups choose to perform SPPS manually for specific reasons like flexibility or smaller scales. SPPS is faster, more efficient, and the purification is easier, and thus this method is widely used in chemistry and biochemistry labs. It is reported that peptides of up to of 50 amino acids were synthesized from the C-terminus to the N-terminus.

2.1.4.2 Native chemical ligation

Native chemical ligation was used as the key ligation step to join the synthetic tension probe and the biological ligand peptide. Comparably high efficiency, mild reaction condition, and biocompatibility have made native chemical ligation a widely-used method for preparing proteins from peptides by total or solid phase peptide synthesis. Wieland and coworkers first discovered the chemical foundation for this reaction by ligating two amino acids in 1953.⁷³ In 1994, Kent defined and developed "Native Chemical Ligation", as the first method for large unprotected peptide fragments ligation.⁷⁴ By enabling the fabrication of peptide fragments to proteins, this method provides complete atom-by-atom control over the covalent structure of the synthesized protein. Thus far, hundreds of proteins have been synthesized using native chemical ligation including those well over 100 amino acids in length. Examples are the variant of the erythropoiesis protein (166 amino acids) and the HIV-1 protease⁷⁵ (203 amino acid) and human glycoproteins⁷⁶ (containing glycosylated peptide Dipterucin ϵ).

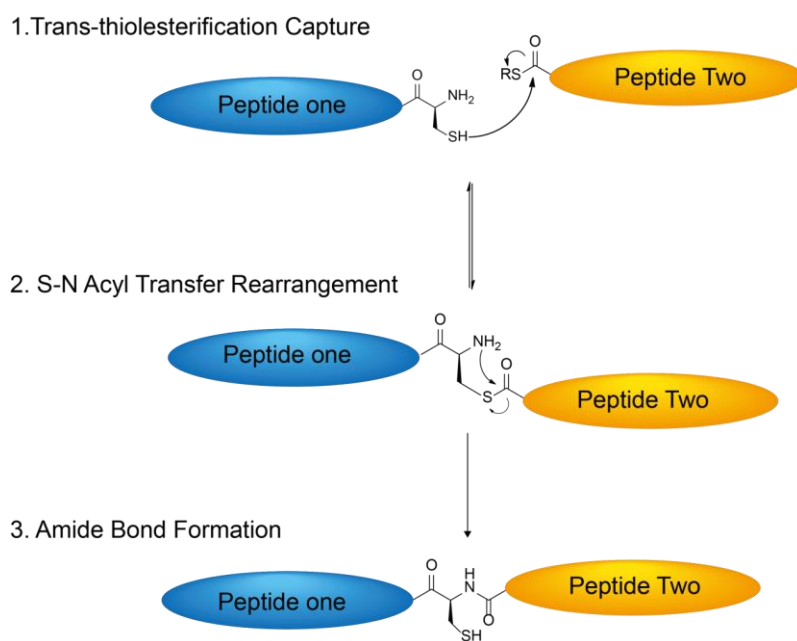


Figure 2.9 Mechanism of NCL

(aqueous conditions at neutral pH, room temperature)

Native chemical ligation involves the chemo-selective reaction of two unprotected peptides to give a single ligation product covalently linked by a native amide bond (Figure 2.5). This reaction occurs in aqueous solution at neutral pH. In the native chemical ligation reaction, the thiol group of an N-terminal cysteine residue of peptide A attacks the C-terminal thioester of peptide B in an aqueous buffer at neutral pH 7.0 and room temperature. This trans-thioesterification step is reversible and is chemo- and regio-selective leading to the formation of a thioester intermediate. An intramolecular S, N-acyl transfer occurs and rearranges the intermediate, resulting in the formation of a native amide bond at the ligation site (Figure 2.5). The ligating rate is partially dependent on the C-terminal amino acid in the peptide thioester: ligation at less sterically hindered C-terminal residues, such as Gly or Ala, proceeds more rapidly than ligation at hindered residues such as branched Ile- or Val. The reaction rate also depends on the nature of the thiol leaving group. Ligation with a highly activated 5-thio-2-nitrobenzoic acid thioester would proceed to completion within 10 min, whereas reaction with an alkyl thioester is very slow and can take up to days to reach completion. The rate-limiting step in native chemical ligation is the trans-thioesterification with the thiol group of the side chain of the N-terminal cysteine.

2.1.5 Methods and material

To measure mechanical tension across the integrin receptor, we synthesized and characterized an integrin-specific MTFM sensor. First, a cyclic Arg-Gly-Asp-D-Phe-Lys thiol ester peptide was selected to be the biological ligand to bind the cellular receptors. The RGD sequence is a common motif in the ECM protein fibronectin, which shows high affinity ($K_D \sim nM$) towards the $\alpha V\beta 3$ integrin receptor ($\alpha V\beta 3 \gg \alpha 5\beta 1, \alpha V\beta 5$). A cRGD thioester was custom synthesized based upon the solid phase synthesis of cyclic RGD derivatives reported by Xiao et al.⁷⁷ The resulting peptide thioester was then purified by RP-HPLC and characterized by MALDI-TOF MS (Figure A2.1).

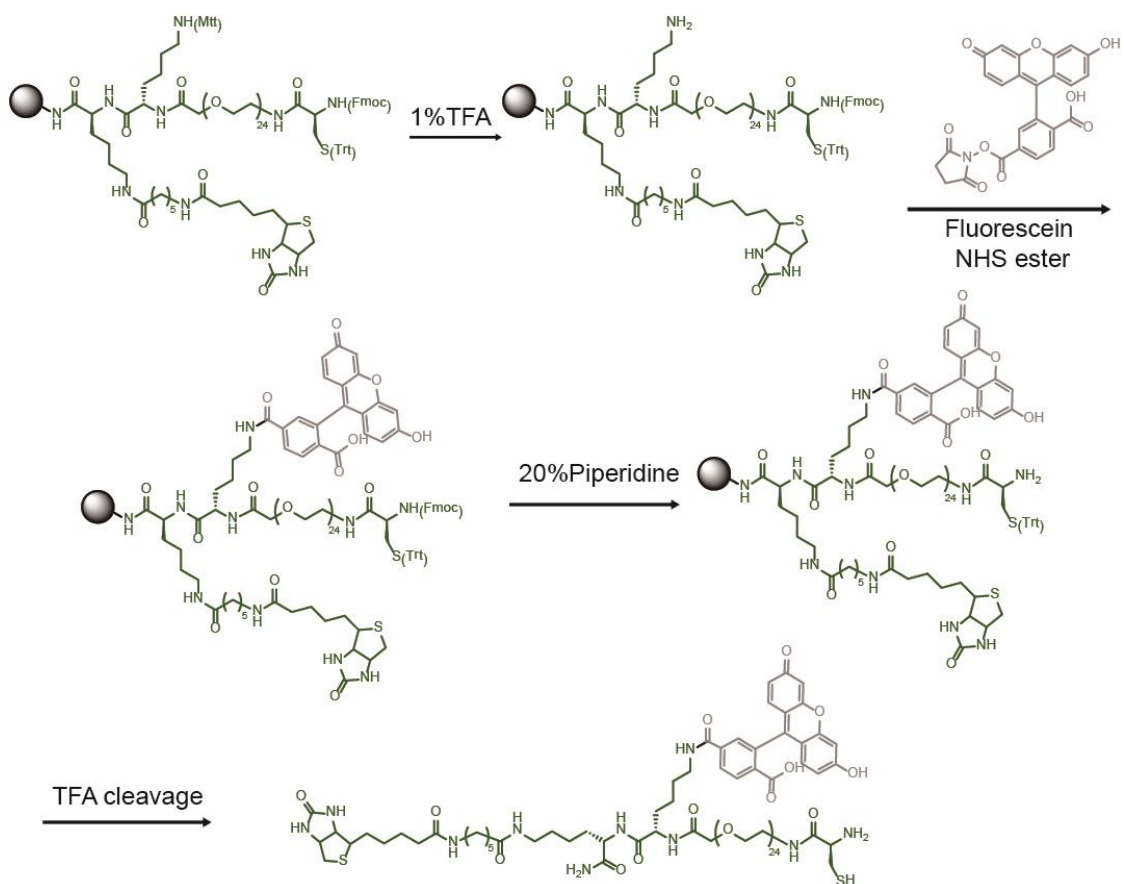


Figure 2.10 Synthesis of Biotin-MTFM sensor precursor

Second, a biotin-Fluorescein-PEG24-Cysteine sensor precursor was designed to accommodate the RGD thioester peptide using native chemical ligation (Figure 2.11). This precursor was generated using solid phase peptide synthesis and on-resin dye labeling. Fmoc-Lys(Biotin)-OH, Fmoc-Lys(mtt)-OH, Fmoc-PEG24-OH, and Fmoc-Cys(Trt)-OH were sequentially coupled onto the solid support using acid-amine chemistry and then the construct was treated using 1% TFA to remove the mtt group on the lysine. Next a fluorescein-NHS ester was added to the reaction and formed an amide bond with the lysine residue. The sensor was cleaved from the resin with 95% trifluoroacetic acid with triisopropylsilane as a scavenger. The final product was characterized by RP-HPLC and MALDI-TOF MS (Figure 2.12).

Conjugation of cRGD and sensor precursor was carried out to generate cRGDfK-Alexa 647-PEG24 fluorescein-biotin. Native chemical ligation was used by mixing 5 mM of 1 and 10 mM of 2 in 20 mM sodium Phosphate buffer (pH 7.5) containing 5 mM betaine and 30 mM sodium 2-mercaptoethanesulfonic acid (MPAA) (Figure 2.11). The reaction mixture was incubated for 24 h at room temperature to form compound 3. Finally, the Alexa 647-maleimide was coupled to the cysteine thiol group through Michael addition. The reaction mixture was incubated in DMF with N,N-diisopropylethylamine for 6 h. The product was then purified by RP-HPLC and analyzed by MALDI-TOF MS (Figure 2.11).

Importantly, this general strategy may be used for orthogonal and site-specific conjugation of a vast array of peptide and small molecule ligands, thus allowing one to investigate biophysical forces exerted by many receptors of interest, and this method bypasses the necessity of genetic engineering of target receptors.

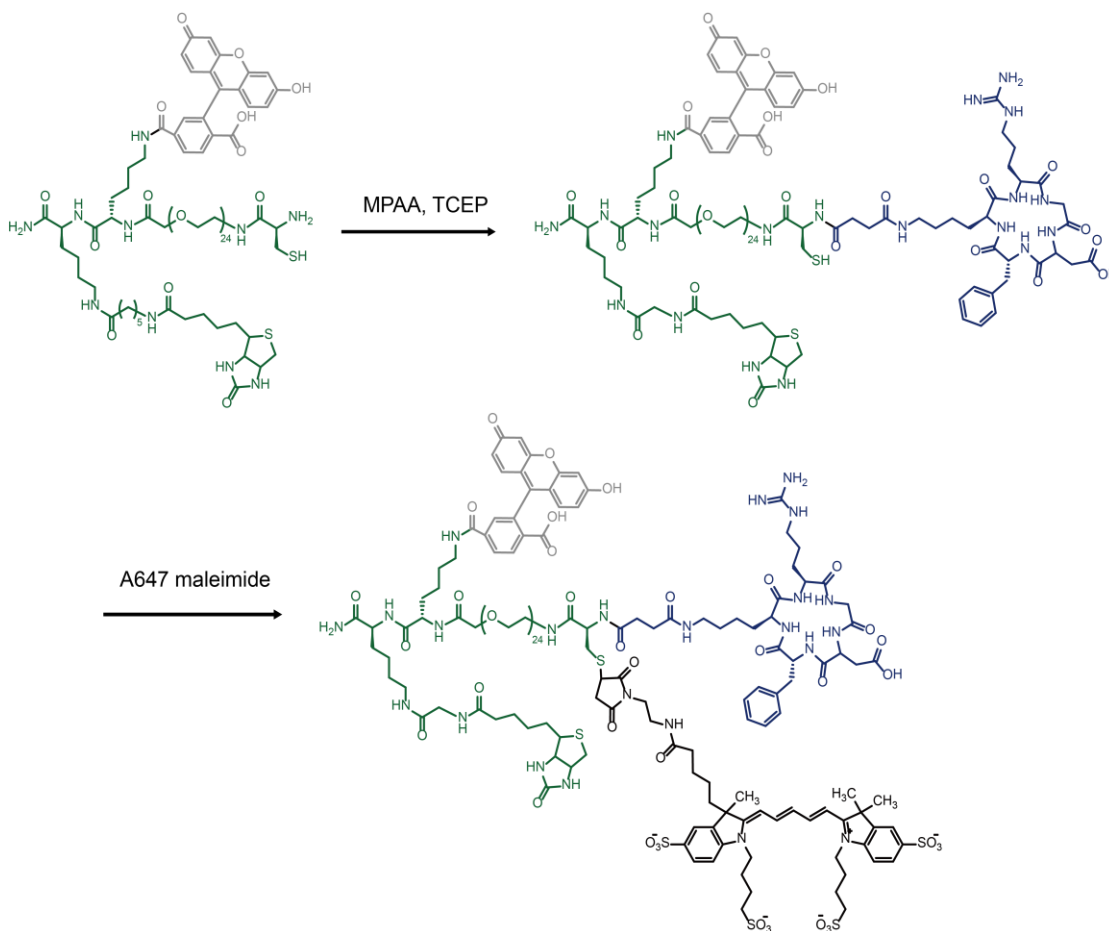


Figure 2.11 Synthesis of Biotin-MTFM sensor

Native chemical ligation between cRGD (shown in blue) thioester and sensor precursor (shown in green) followed by Michael addition of Alexa-647 maleimide (shown in black) to the Cysteine residue.

2.1.5.1 Reagents

Unless otherwise stated, all starting materials and reagents were purchased from Sigma-Aldrich (St. Louis, MO) and used without further purification. All buffers were made with Nanopure water (18.2 MU) and passed through a 0.2 μm filtration system.

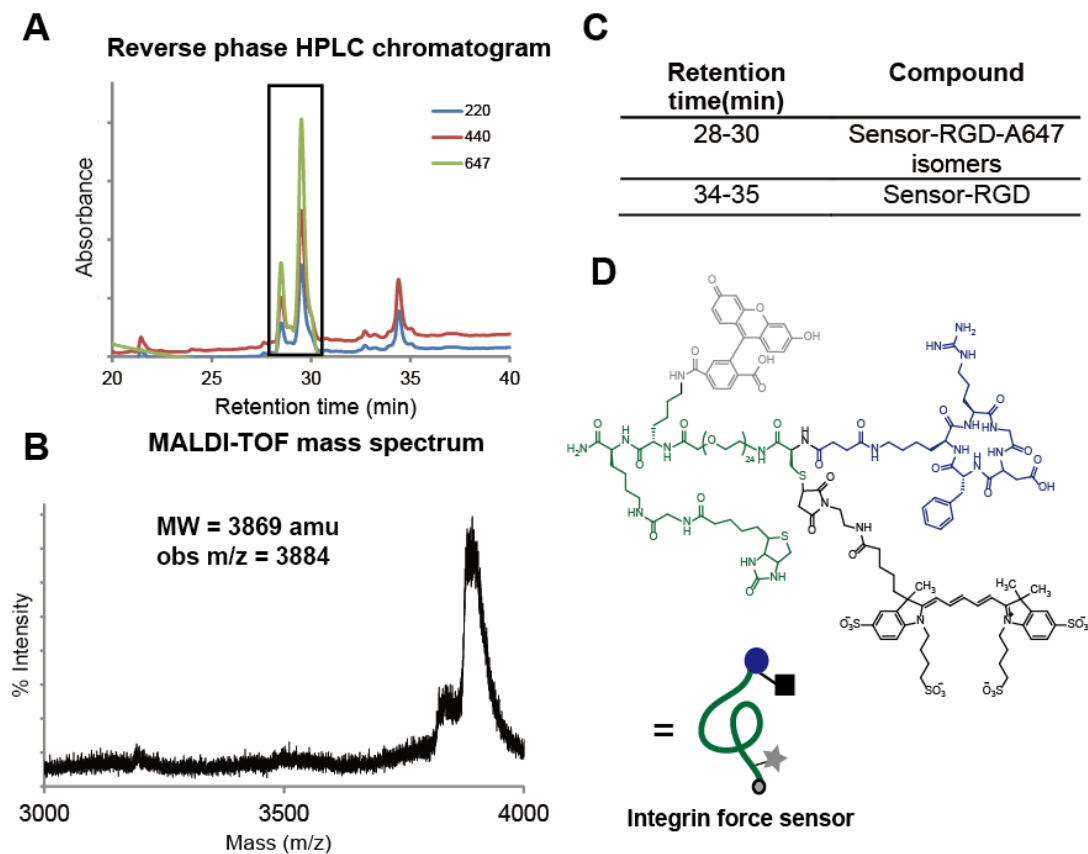


Figure 2.12 Characterization of Biotin-MTFM sensor

A. Reverse phase HPLC chromatography. The peak at 28-30min showing the overlap of the absorbance at 220nm, 440nm, and 647nm. B. MALDI-TOF mass spectrum showing the molecular mass of 3884 amu. C. Retention time of Sensor-RGD-A647 isomers and unreacted sensor-RGD construct. D. Chemical structure of Fluorescein-647-RGD MTFM sensor.

2.1.6 Determination of quenching efficiency

The general scheme of synthesizing the Biotin-Fluorescein-PEG24-Alexa 647-cRGD is shown in Figure 2.11 and 2.12. The MTFM sensors were modified on the glass slides along with the PEG passivation. The glass coverslips were passivated with 9-12 unit PEG oligomer to prevent non-specific binding of cells and other biomolecules. Passivation procedure followed the literature precedent published by Jurchenko et al.⁷⁸ Briefly, glass coverslips (25 mm diameter; VWR) were sonicated in Nanopure water (18.2 mΩ) for 10 min and then etched in piranha (a 3:1 mixture of sulfuric acid (Avantor Performance Materials) and 30% hydrogen peroxide (Sigma)) for 10 min (please take caution: piranha is extremely corrosive and may explode if exposed to organics). The glass coverslips were then washed six times in a beaker of Nanopure water (18.2 mΩ) and placed into three successive wash beakers containing EtOH (Decon Labs) and left in a final fourth beaker containing 1% (3-aminopropyl)triethoxysilane (APTES, Sigma) in EtOH for 1 h. The substrates were then immersed in the EtOH three times and subsequently rinsed with EtOH and dried under nitrogen. Substrates were then baked in an oven (~100 °C) for 10 min. After cooling, the samples were incubated with NHS-biotin (Thermo Fisher) at 2 mg/ml in DMSO (dimethyl sulfoxide, Sigma) overnight. Subsequently, the substrates were washed with EtOH and dried under nitrogen. The substrates were then washed with PBS (three 5 ml aliquots) and incubated with BSA (EMD Chemicals, 100 µg µl⁻¹, 30 min) and washed again with PBS (three 5 ml aliquots). Quencher labeled streptavidin was then added (1 µg ml⁻¹, 45 min, room temperature) followed by washing with PBS (three 5 ml aliquots) and incubating with the desired EGF construct (biotinylated linker and fluorophore labeled, 1 µg ml⁻¹, 45 min, room temperature). Substrates were then rinsed with a final wash of PBS (three 5 ml aliquots) and used within the same day. To verify

that surfaces were stable within the experimental time frame, a substrate, functionalized as described above, was imaged over two consecutive days. The fluorescence intensity of the surface did not change greatly within this time frame (Figure A2.9).

Next, the quenching efficiency of the FRET pair Fluorescein and Alexa 647 was determined by fluorescence microscopy. The MTFM sensor lacking the acceptor was also modified onto the glass slide and imaged under the same settings which served as the unquenched background (Fluorescence intensity I_D , quenching efficiency 0%). The surface with the MTFM sensor with the acceptor is considered as the quenched surface with a fluorescence intensity I_{DA} . The quenching efficiency is calculated using the following equation.

Eq.

$$E = 1 - \frac{I_{DA}}{I_D}$$

The initial quenching efficiency E of FRET pair Alexa 647 and Fluorescein in the MTFM tension sensor design (PEG24) is calculated to be 89.7%.

In optics, photobleaching is the photochemical change of a fluorophore molecule such that it permanently is unable to fluoresce. This is usually caused by cleavage of chemical bonds or non-specific reactions between the fluorophore and surrounding molecules such as oxygen.⁷⁹ Such irreversible modifications is caused by transition from a singlet state to the triplet state of the fluorophores, which do not fluoresce. Based on this optical property of the fluorophores, 647 nm laser was used to verify that there is energy transfer occurring between the acceptor Alexa 647 on the MTFM surface. The surface was exposed to the 647 nm laser for 3min for photobleaching, and a decrease in the acceptor channel Cy5 was observed. In the same time, an increase in the donor

channel FITC was also observed, which directly indicates the energy transfer between the donor and acceptor within the MTFM sensor on the glass slides (Figure 2.13).

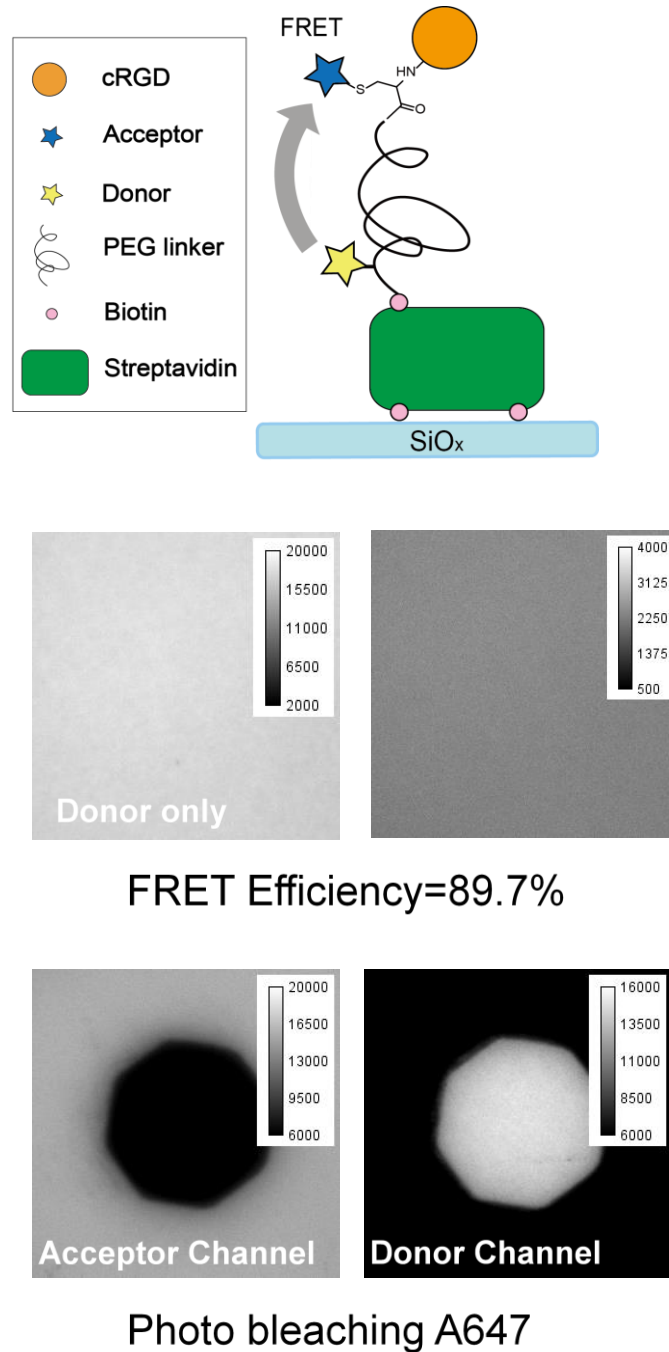


Figure 2.13 General scheme of Biotin-PEG-cRGD sensor and the determination of Alexa 647-Fluorescein quenching efficiency

2.2 *Integrin tension lead to biotin-streptavidin dissociation in cell adhesion*

2.2.1 Experiment findings

In initial experiments, we incubated HCC1143 immortalized breast cancer cells on surfaces that contained quencher modified streptavidin and the cRGDfK-A647-PEG23-Fluorescein-biotin peptide conjugate. Previously, our work has shown that cells do not engage or spread when streptavidin modified surfaces lack RGD or other cell adhesion ligands⁵⁷. Cells were incubated on the higher density peptide surfaces (4400 ± 370 streptavidin molecules/ μm^2) for ~60 min at 37 °C and 5% CO₂, and then imaged using brightfield reflection interference contrast microscopy (RICM), and conventional fluorescence microscopy. Unexpectedly, cells incubated on these surfaces generally revealed areas of reduced fluorescence in both the donor and the acceptor channels. In contrast to the donor-quencher system (Figure 2.14), some regions of a subset of cells displayed positive fluorescence signal in the donor channel, which typically correspond to the proximal side of the cell perimeter where the focal adhesion starts to form and protrude. The slight increase (~10%) in donor intensity is likely due to extension of the polymer, and this signal may be more readily observed due to the FRET sensitivity when the dyes are directly conjugated to the PEG chain, rather than randomly tagged to streptavidin. the perimeter of most cells was negative (Figure 2.14). This loss in fluorescence was also colocalized with vinculin, a focal adhesion marker.⁷⁸ This observation was also confirmed on cRGDfK(C)-A647-PEG23-biotin surfaces where the streptavidin was labeled with the quencher QSY21 where only loss of fluorescence at the cell perimeter was observed, indicating the removal of the sensor-PEG polymer. These observations suggest that the dark areas are not related to the presence of the quencher or to polymer conformation. In all cases, we observed a net reduction in fluorescence

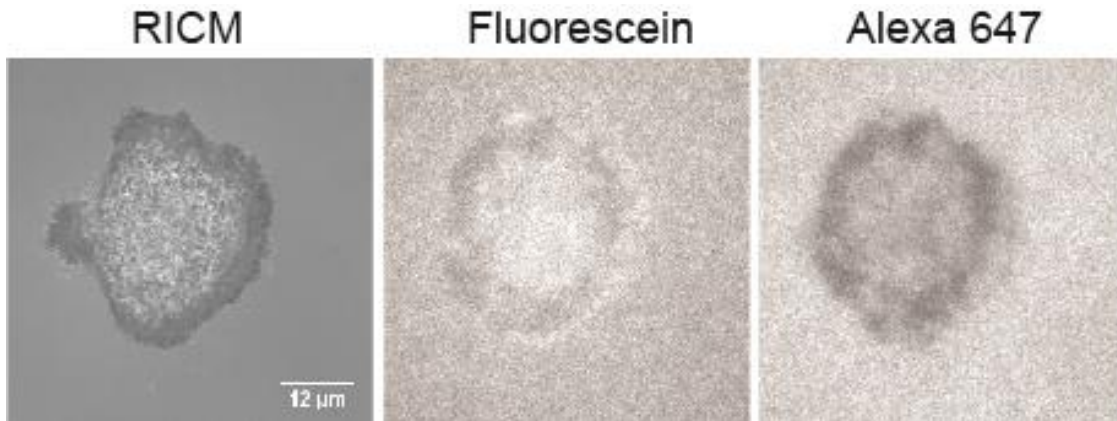


Figure 2.14 Fluorescence signal and loss in Fluorescein and Alexa 647 Channel

intensity at the edges of this epithelial cell type by the 60 min time point, thus suggesting biotin dissociation. This reduction could occur through dissociation of the streptavidin complex from the surface or dissociation of the biotinylated PEG tension probe from the immobilized streptavidin. Further experiments indicate that under these conditions, streptavidin remains immobilized, while the biotinylated PEG tension probes are dissociated from the surface (*vide infra*)⁷⁸. In some cases, fluorophores display spectral shifts and changes in quantum yield as a result of integrin receptor binding⁸⁰. To measure this contribution to the fluorescence emission intensity, we generated cRGDfK(C)-A647-PEG24 surfaces that were covalently attached to the substrate. We rationalized that changes to the dye emission intensity on these surfaces would be due to integrin binding. In these experiments, the mean fluorescence intensity of the surface under each cell showed a ~3% decrease when compared to the background. This decrease is uniform across the entire cell contact region. In contrast, streptavidin-biotin anchored ligands show a decrease of ~30 to 60% at the cell perimeter, which could be clearly visualized when fluorescence images were normalized and displayed as heat maps that represent the

fraction of MTFM ligand removed. The ligand loss appears to occur in regions that resemble focal adhesion contacts. The results indicate that the fluorescence decrease under cells incubated on surfaces with covalently tethered ligand is 10-20-fold lower than that observed on surfaces with ligand anchored by streptavidin-biotin attachment. Further evidence of biotin dissociation is revealed by the irreversible nature of the observed negative signal. Time-lapse images were collected from a single cell after 90 min of incubation on a streptavidin-biotin surface containing only the donor cRGDfK(C)-A647-PEG23-biotin conjugate. As the cell moves toward the right corner of the image and outside the field of view, the negative signal remains unchanged.⁷⁸ This experiment suggests that loss of donor intensity is irreversible. Controls using pharmacological inhibitors of f-actin and myosin show that biotin dissociation is dependent on the cytoskeleton. We found that cells pre-treated with the non-muscle myosin inhibitor blebbistatin for 15 min adhered to the surface, but completely failed to dissociate the streptavidin-anchored MTFM sensor. Cells treated with latrunculin B (LatB), an f-actin inhibitor, 30 min after adhering to a surface failed to show any reversibility in signal. Also, cells treated with soluble cRGD peptide dissociate from the surface but the negative signal remains despite the absence of the cell (Figure. 2.11). Taken together, these results unambiguously show that the majority of the signal decrease is due to irreversible, cytoskeleton-dependent, and focal-adhesion dependent biotin dissociation.

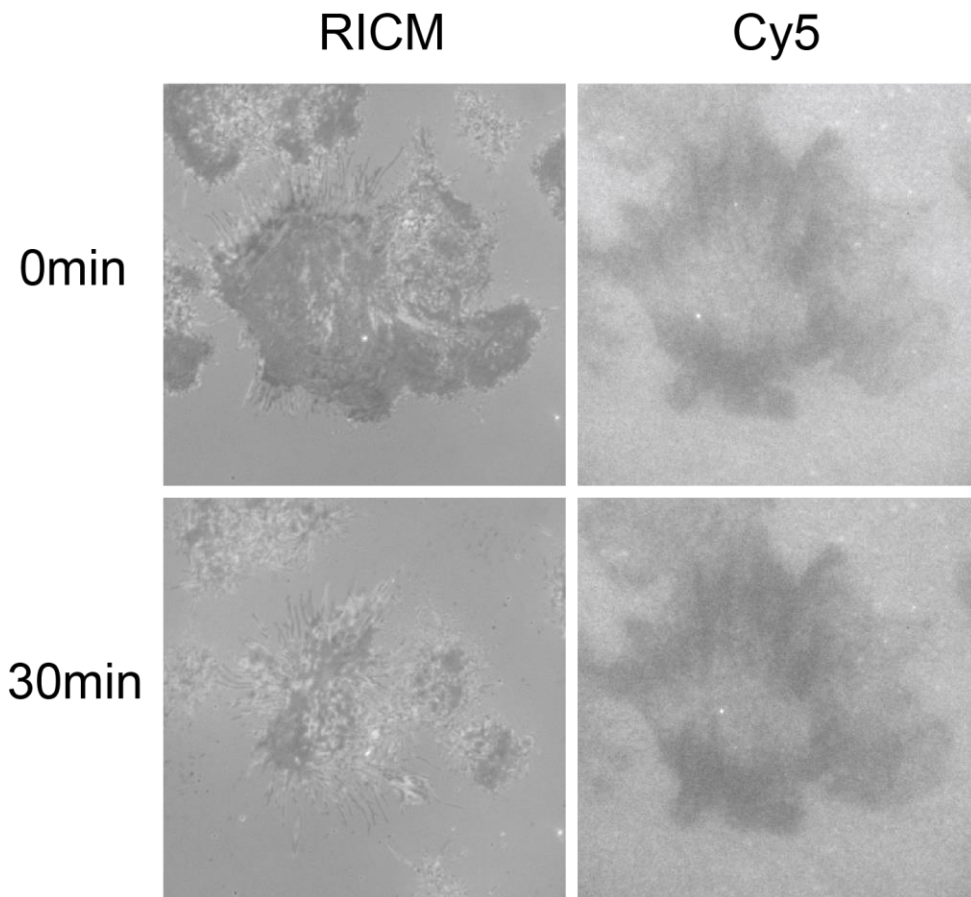


Figure 2.15 Fluorescence loss irreversible when treated with Latrunculin B

Cells incubating on the surface modified with MTFM sensor was treated with f-actin inhibitor Latrunculin B. After 30min incubation, cells started to detach from the coverslip due to the less efficient formation of f-actins. The fluorescence loss under the cell remains unchanged.

Furthermore, an MTFM sensor with an alkyne functional group in place of the biotin group is designed and synthesized to investigate the fluorescence loss of the biotin sensors. Instead, the glass coverslip is modified with an azide that reacts with an alkyne to form a triazole five membered ring. The procedure is described in Chang et al, 2015,⁸¹ where the covalent linkage secures the immobilization of the MTFM sensor on the

surface. Next, HCC cells are incubated on the surface for 60 min and imaged with a microscope.

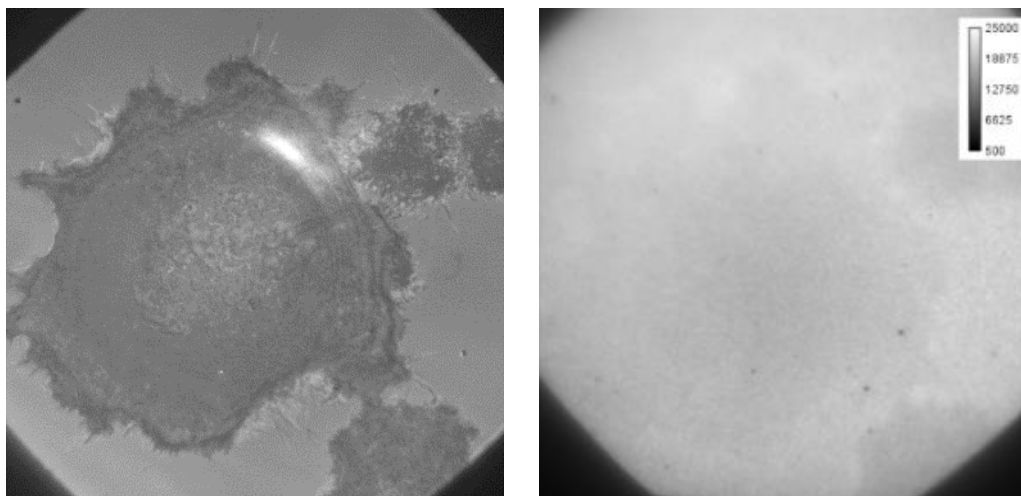


Figure 2.16 Fluorescence background under the cell

Cells were incubated on the surface modified with MTFM sensor covalent linked on the surface. No remarkable fluorescence loss was observed due to under the cell remains unchanged.

2.2.2 Discussion

Integrin driven biotin dissociation is unexpected given that the streptavidin-biotin interaction is often described as the strongest non-covalent association in nature with an absolute free energy of binding of ~ 18 kcal/mol^{11,82}. In support of this, experimentally measured rupture forces for streptavidin-biotin were reported at ~ 260 pN using atomic force microscopy¹¹. It should be noted, however, that rupture forces are dependent on the loading rate and temperature. For example, mean streptavidin-biotin rupture forces (at 25 °C) have been recorded at ~ 120 pN and ~ 200 pN at loading rates of 198, and 2300 pN/s, respectively⁸³. Given this remarkable stability, streptavidin-biotin association is

commonly used in the field of single molecule biophysics to measure the rupture force and bond lifetime between receptors and their ligands^{84,85}, including cell surface integrins and ligands derived from the ECM⁸⁶. It is of interest to note that one report described streptavidin-biotin dissociation at low force regimes (~5 pN), but this was shown to occur due to brief (μ s-ms) molecular encounters that do not allow the interaction to reach equilibrium^{49,87}. In our experiments, however, the biotin-tagged ligand is incubated with streptavidin for ~1 hr during MTFM sensor preparation and is therefore at, or near, equilibrium. The free energy binding of α v β 3 integrins with the linear GRGDSP peptide was measured at 3.10 kcal/mol⁸⁸. Accordingly, the single molecule rupture force for integrin-ligand associations have been reported in the range of ~40 to 90 pN depending on the loading rate, the type of ligand (using RGD peptides and various fibronectin fragments), the type of integrin receptor (α v β 3 or α 5 β 1), and the activation state (conformation) of the receptor^{41,89}. Therefore, literature precedence indicates that integrin-ligand interactions are more likely to dissociate under mechanical load when compared to streptavidin-biotin. Although the molecular mechanism of integrin-ligand bond strengthening is unknown, integrin clustering, focal adhesion maturation, and the formation of parallel and multivalent ligand-receptor bonds may contribute to increasing the effective lifetime of the integrin-ligand interaction⁹⁰. These supramolecular complexes only form at ECM-integrin interfaces that allow for clustering⁹¹. Therefore, single molecule force spectroscopy experiments performed on the surface of living cells are unable to recapitulate the ligand-receptor stabilization mechanisms that likely occur within focal adhesions. Consequently, the stabilization of integrin-ligand bonds over streptavidin-biotin may not be present in typical single molecule force

spectroscopy experiments. Because the cell membrane presents thousands of integrin receptors⁹² while the effective biotin concentration is fixed and negligible, integrin-ligand associations on the surface are more likely to be reversible than streptavidin-biotin interactions. Therefore, repeated integrin-ligand binding may contribute to the apparent enhancement of integrin-ligand affinity and force tolerance. Indeed, recent work reported the existence of low frequency (~ 0.1 Hz) traction force oscillations within focal adhesions¹⁹, and therefore, each tension probe may experience $\sim 4 \times 10^2$ cycles of tension within our experimental time frame of 1 h. To quantify the likelihood of streptavidin-biotin dissociation over integrin-ligand dissociation when the two bonds are in series, we used published values of k_{off} for both bonds^{93,94}, and applied the analysis developed by Neuert et al⁹⁵. Assuming that both bonds in the series have similar potential widths (Δx), we found that the probability of streptavidin-biotin dissociation under integrin-mediated tension is $\sim 2.8 \times 10^{-5}$. Thus, even if the tension probes were to experience hundreds of cycles of tension within 1 h, this likely generates only a small contribution ($<1\%$) to the observed enhancement in integrin-ligand affinity. In the situation where Δx of streptavidin-biotin is greater than that of the integrin-ligand bond (which is likely the case), the analysis becomes more complex, as the change in k_{off} becomes loading rate and force dependent. Nonetheless, in our case, the k_{off} values differ by orders of magnitude and will likely drive streptavidin-biotin survival over the weaker integrin-ligand association. Further evidence supporting our observation of enhanced integrin-ligand affinity comes from a recent report showing that focal adhesion formation requires integrin ligands that can withstand ~ 50 - 60 pN of tension (as defined by the rupture force under steady state tension over a duration of less than 2 sec)⁵⁸. Our own recent MTFM

work also shows that integrin receptors can apply at least 15 pN of tension within some focal adhesions⁹⁶. Therefore, integrin-ligand association must be sufficiently stabilized to withstand these large mechanical loads for extended durations, suggesting a mechanism of integrin-ligand affinity enhancement within functional cell adhesions. Interestingly, these reported magnitudes of tension are likely sufficient to dissociate streptavidin-biotin associations in our experiments. For example, based on the Bell model, loading rates of approximately 0.1 pN/s at 37 °C would lead to a mean streptavidin-biotin rupture force of ~57 pN^{83,97} and the average lifetime of streptavidin-biotin association is on the order of 10² sec when placed under 40 pN of constant tension⁸⁷. Therefore, it is feasible that biotin dissociates from streptavidin under the integrin-mediated tension; however, the enhanced stability of the integrin-ligand interaction remains unexpected and is likely related to focal adhesion formation.

In conclusion, we found that streptavidin-biotin tethered integrin ligand molecules dissociate from the surface due to cell-driven forces. This finding indicates that single molecule measurements almost certainly underestimate the stability of integrin-ligand interactions within functional focal adhesions. Many mechano-regulatory processes in the cell involve multi-protein complexes, and thus kinetic and thermodynamic parameters derived from single molecule techniques applied to individual ligand-receptor pairs may not accurately depict the biological context of the crowded cell environment.

Furthermore, we conclude that integrin-ligand tension is likely one to two orders of magnitude larger than had previously been estimated using microscopic averaging methods, such as traction force microscopy⁹⁸. This is significant because the streptavidin-biotin association is widely used to display small molecules and peptides to screen for

cues that trigger cell signaling pathways⁹⁹. Therefore, these results suggest that more robust immobilization strategies are needed to exclude the possibility of cell-based dissociation of surface ligands and remodeling of the surface, which may obscure results. MTFM is technically facile, but due to the unexpected dissociation of streptavidin-biotin, the signal presented by the sensor is not easily interpreted as an average force. Instead, it provides lower bound estimates of integrin-driven tension and this lower bound estimate vastly exceeds what has previously been predicted or reported. We anticipate that the next generation of covalently immobilized MTFM force probes will address existing gaps in our understanding of mechanotransduction pathways during cellular processes such as migration, mitosis, and wound healing.

2.3 Design and synthesis of the covalent, ultra-stable tension sensor

To address the biotin-streptavidin dissociation and to further elucidate the biophysical fundamentals of mechanotransduction, the design and development of a tool has spawned the following major challenges 1) the stability to sustain the cellular tension being exerted without being ruptured; 2) the durability to enable monitoring the development of tensions over a long period of time (~days); 3) the specificity to measure forces applied to a certain type of receptors on the cell surface; 4) the versatility to accommodate a variety of cell membrane mechanotransduction receptors. To overcome the above-mentioned challenges, herein, we aimed to develop a modular molecular tension sensor capable of long-term measurement of cellular tensions.

2.3.1 Covalent linkage via click chemistry

In replacement of biotin, an alkyne functional group was chosen to be the linkage between the surface and the MTFM sensor. The classic Copper-catalyzed click reaction is the reaction of an azide with an alkyne to form a 5-membered heteroatom ring: a Cu(I)-Catalyzed Azide-Alkyne Cycloaddition (CuAAC). This reaction offers a number of advantages for detecting cellular tensions in biological systems. First, lacking alkyne and azide functional groups in the living system granted the high specificity of CuAAC reaction which allows for minimum non-specific cross-reactions with the living systems and makes it easier to interpret the data. Second, the CuAAC reaction proceeds to completion within 10 min on glass surfaces in water/DMSO, and the high efficiency of the chemical reaction minimizes the exposure time of the sensor to the environment which might result in chemical degradation or photo bleaching of the MTFM sensor. Third, aside from the Cu(I), which will be rinsed off after the reaction, the functional

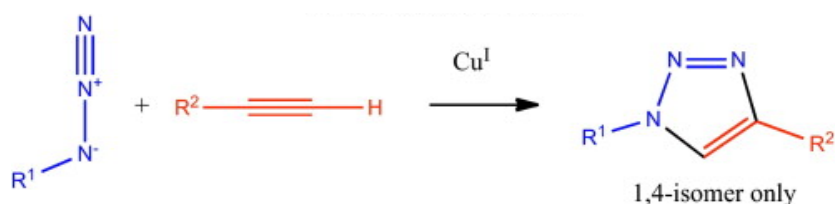


Figure 2.17 Copper copper catalyzed click chemistry

group azide and alkyne are both non-toxic and biocompatible. This property provides low adverse effects for living cells. In conclusion, bio-orthogonal copper-free click chemistry has provided rapid, biocompatible, and absolutely specific chemical reactions in cellular systems. Therefore it was chosen for the immobilization of the MTFM sensor to investigate cellular mechanotransduction.

2.3.2 Fluorophore selection

In previous experiments, fluorescein was selected to be the fluorescence donor in the MTFM sensor due to its chemical stability, minimal cost and spectrum separation with Alexa 647 acceptor. However, noteworthy photobleaching behavior was observed during the experiments which is caused by the oxygen-independent, proximity-induced triplet-triplet or triplet-ground state dye reactions of fluorescein during imaging.¹⁰⁰ This behavior made it very difficult to capture the tension signal since the photobleaching of the donor results in a decrease in donor fluorescence, which could be misinterpreted as less tension caused by less polymer extension or fewer quantity of activated integrin molecules as well. On the other hand, the emission of fluorescein covers the range of 480-530 nm, which overlaps with the autofluorescence of a number of biological structures such as mitochondria and lysosomes. This also will lead to the misinterpretation of tension signals. Furthermore, fluorescein is negatively charged under neutral pH, and the charge in some cases attracts the binding of other opposite charged molecules.

Therefore, Tetramethylrhodamine (TAMRA) was selected to replace the fluorescein as one of the FRET fluorophores and overcome the photobleaching and autofluorescence issues. TAMRA, with an absorption maxima at 544nm and emission maxima at 572 nm, are supplements to fluorescein, as they exhibit longer wavelength emission maxima, higher photo- and chemical- stability. Moreover, the molecule is zwitterionic which has better solubility in aqueous solutions in living system. The negative charge and the positive charge on the dye molecule avoid non-specific binding to other hydrophobic or opposite charged biomolecules. TAMRA can be used as either the FRET donor or the

Acceptor, since its spectra are in between red dyes (Alexa 647, Cy5) and blue dyes (Fluorescein, Alexa 488). Based on the quantum yield and optimal spectrum overlap, Alexa 488 and QSY9 was designated to be the FRET donor and quencher for TAMRA, respectively, in the tension investigation studies.

2.3.3 Design and synthesis of MTFM sensor

We overcome this challenge by developing a new class of stable and modular MTFM probes that is generated using solid phase peptide synthesis (SPPS) along with the NCL reaction (Figure.2.19). This approach allows one to site-specifically incorporate a ligand and a pair of chromophores, and it is compatible with virtually any peptide of interest. The molecular probes were covalently immobilized onto an azide-modified glass slide using standard CuAAC click reaction conditions to prevent the dissociation of the MTFM sensor.

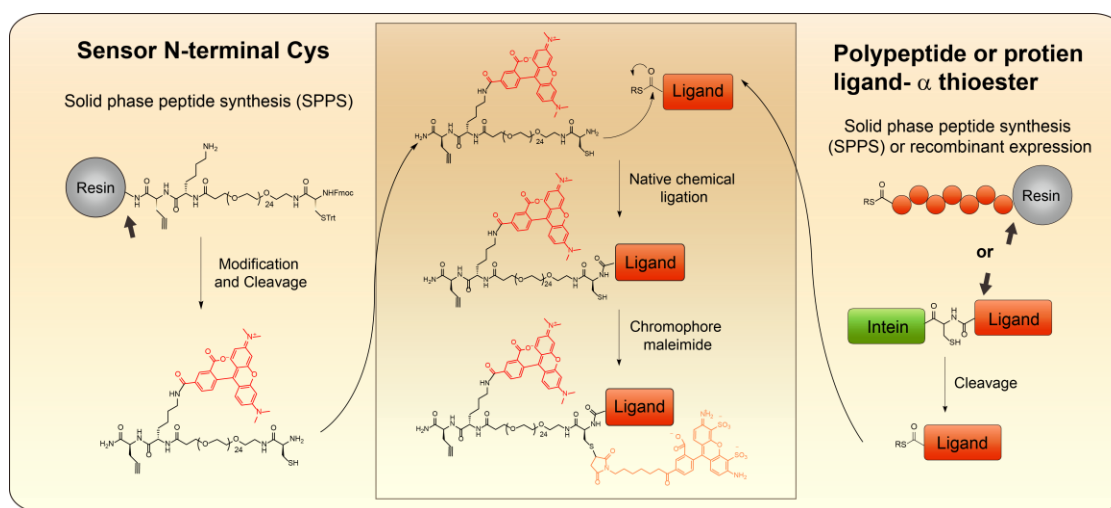


Figure 2.19 Strategy to generate the MTFM sensor

SPPS was used in generating both the MTFM sensor precursor and the biological ligands. After cleavage from the solid phase, the two parts of the MTFM sensor was ligated using Native Chemical ligation method to form a covalent native peptide bond linkage.

SPPS was used to generate a “spring” precursor of the MTFM sensor. The precursor is composed of a C-terminal alkyne-modified amino acid followed by lysine, discrete PEG24/PEG48, and terminated with an N-terminal cysteine. These Fmoc protected non-canonical amino acids are conjugated on the solid support sequentially using acid-amine chemistry to form a native amide bond. (Figure 2.19) Specifically, Fmoc-L-propargylglycine, Fmoc-Lys(Mtt)-OH, and Fmoc-PEG24-OH are coupled sequentially following the standard Fmoc peptide synthesis procedures in a syringe. The Mtt protecting group of the lysine is selectively deprotected with 1% trifluoroacetic acid (TFA) in CH₂Cl₂. Subsequently, the resin is then treated with excess TAMRA succinimidyl ester in DMF. After deprotecting the Fmoc-PEG24-OH with 20% piperidine in DMF, the Fmoc-Cys(Trt)-OH residue is coupled to the N-terminus of the peptide. After final Fmoc deprotection, the sensor is cleaved from the resin with 95% TFA with triisopropylsilane (TIS) as a scavenger. The synthesized construct was purified and characterized by a diode array detector-equipped HPLC and MALDI-TOF MS. Reverse phase HPLC chromatogram of the compound. The absorbance was measured at 560 nm. 1 ml fractions were collected as they eluted off the column (flow rate = 1 ml/min from 8% to 100% Acetonitrile/water). The peaks were characterized by MALDI-TOF MS and the final SPPS product 1 ($MW_{obs} = 1883.69$; $MW_{expected} = 1882.98$) was found to elute at 28-40 min. The yield of the product was >50%. After deprotection, the lysine was coupled to an NHS-ester modified tetramethylrhodamine (TAMRA) fluorophore. The peptide conjugate was then cleaved and purified using reverse phase HPLC (RP-HPLC) and verified using MALDI-TOF (Figure 2.20). Besides this strategy, a two-step synthesis was also developed and used for the synthesis of the

QSY9-TAMRA tension sensor. (Figure A2.2 and Figure A2.3) In this method, both QSY9 and TAMRA is conjugated to the sensor precursor via two amine functional groups on the backbone of the lysines at the two ends of the PEG spring. Deprotection of the first lysine occurs before the coupling of the second lysine. QSY9 succinimide ester

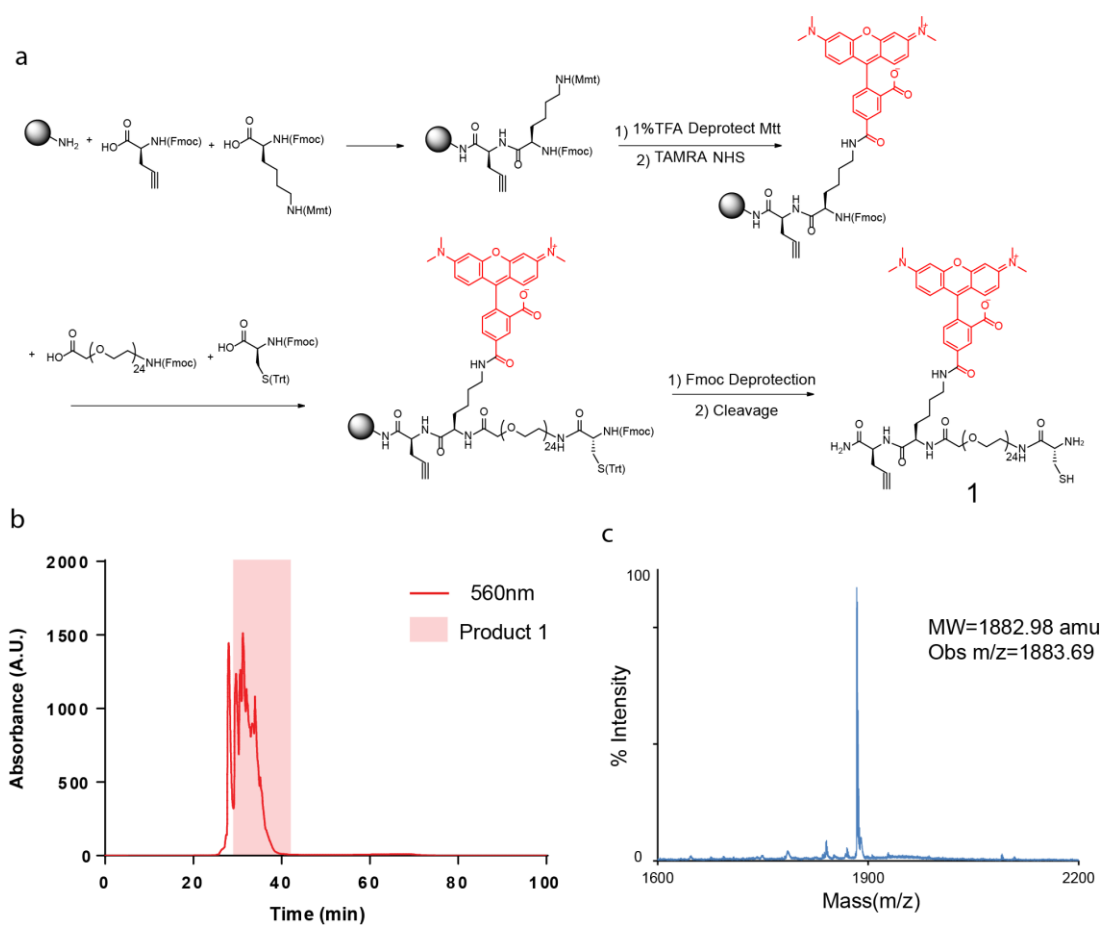


Figure 2.20 Synthesis and characterization of the MTFM sensor precursor

SPPS is used to generate a “spring” composed of a C-terminal alkyne-modified amino acid followed by lysine, discrete PEG24/PEG48, and terminated with an N-terminal cysteine, 1 (Scheme 1). The lysine was coupled to an NHS-ester modified tetramethylrhodamine (TAMRA) fluorophore. The peptide conjugate was then cleaved and purified using reverse phase HPLC (RP-HPLC) and verified using MALDI-TOF.

was then coupled to the amine residue. The second lysine in place of the Cysteine was then conjugated to the solid phase followed by the deprotection of the mmt group on the Gamma amine. The TAMRA was then conjugated to the second end of the PEG polymer. This synthetic strategy was illustrated in Figure 2.20.

SPPS was also used to generate a series of biological ligands that are able to bind and activate the receptors in the cell membrane. The synthesis of the cyclic-RGDfK thioester peptide was adapted from the protocol previously published by Xiao et al. Briefly, Asp(OAll), Gly, Arg(pbf), Lys(mtt) and D-Phe were coupled on a CEM Liberty Microwave Synthesizer (Matthews, NC) using standard solid-phase peptide synthesis procedures using Fmoc chemistry and Rink Amide resins. After synthesis of the protected linear peptide, the resins were transferred into a syringe. The C-terminal allyl ester protecting group was then removed by treatment with Pd(PPh₃)₄ in CHCl₃/AcOH/N-methylmorpholine 37:2:1 for 3h under a nitrogen atmosphere. The resin was washed carefully with DIPEA (5%) in DMF, and then the N-terminal Fmoc protecting group was removed by treatment with 20% piperidine in DMF. 5 equivalents of DEPBT and 2 equivalents of DIEA are then used to cyclize the peptide on resin. The cyclization reaction was carried out for 18 hours in DMF. Then, the Mtt protecting group of the lysine was selectively deprotected with 1% trifluoroacetic acid (TFA) in CH₂Cl₂. The lysine amine was subsequently acylated with succinic anhydride. Thioester formation was accomplished on-resin by addition of methyl 3-mercaptopropionate, 4-dimethylaminopyridine (DMAP), and N-hydroxybenzotriazole (HOBT) using N,N'-diisopropylcarbodiimide (DIC) as a coupling reagent. Cleavage from the resin and removal of the remaining protecting groups were accomplished using TFA with

triisopropylsilane (TIS) as a scavenger. The resulting peptide thioester, **2**, was precipitated from diethyl ether and purified by reversed phase HPLC. 1 ml fractions were collected as they eluted off the column (flow rate = 1 ml/min from 8% to 100% Acetonitrile/water). The yield of the product was >70%. The peptide was then characterized by HPLC and MALDI-TOF MS.

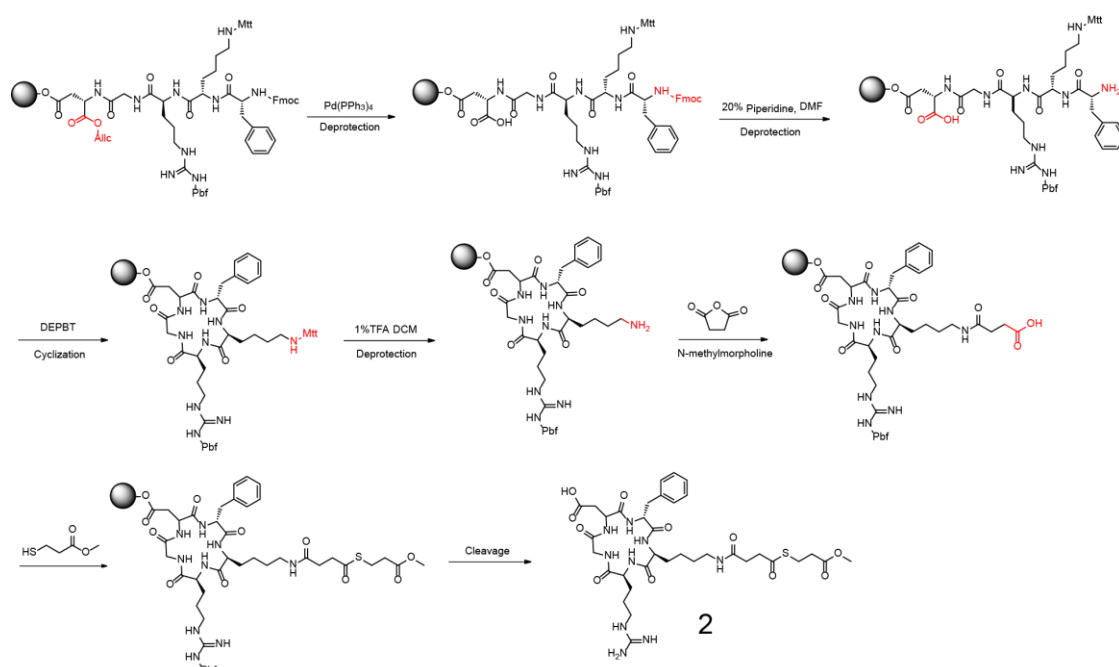


Figure 2.21 synthesis of cRGD thioester

SPPS is used to synthesize the cyclic RGD alpha thioester. The procedure was adapted from Xiao *et al.* The cyclization reaction was carried out on the solid support under the condition of 5 equivalents of DEPBT and 2 equivalents of DIEA for 18 hours in DMF. The peptide conjugate was then cleaved and purified using reverse phase HPLC (RP-HPLC) and verified using MALDI-TOF.

The SPPS synthesis method is also used to generate a library of α -thioester modified peptide ligands selected based on their specificity toward the integrin and cadherin

receptors. These peptide ligands recapitulate many of the cell responses in cell-cell and cell-ECM adhesions.^{101,102} These ligands included: 1) cyclic RGDfK (cRGDfK) and linear GRGDS peptides derived from the fibronectin-III repeat 10 (FN-III10), which primarily bind the $\alpha 5\beta 1$ and $\alpha v\beta 3$ integrins,¹⁰³ 2) the synergy site PHSRN derived from FN-III9, which is reported to increase cell adhesion when combined with the RGD sequence, 3) the PHSRN(SG)4RGDS peptide, which includes a spacer between the PHSRN and GRGDS peptides and better mimics the distance between the two binding domains in FN¹⁰⁴, and 4) the SHAVSS and LRAHAVDING peptides, which bind the E-cadherin and N-cadherin receptors, respectively.^{102,105} The synthesis of these peptide α -thioesters was based on SPPS. The peptide conjugate was then cleaved and purified using reverse phase HPLC (RP-HPLC) and verified using MALDI-TOF. (Figure.2.22)

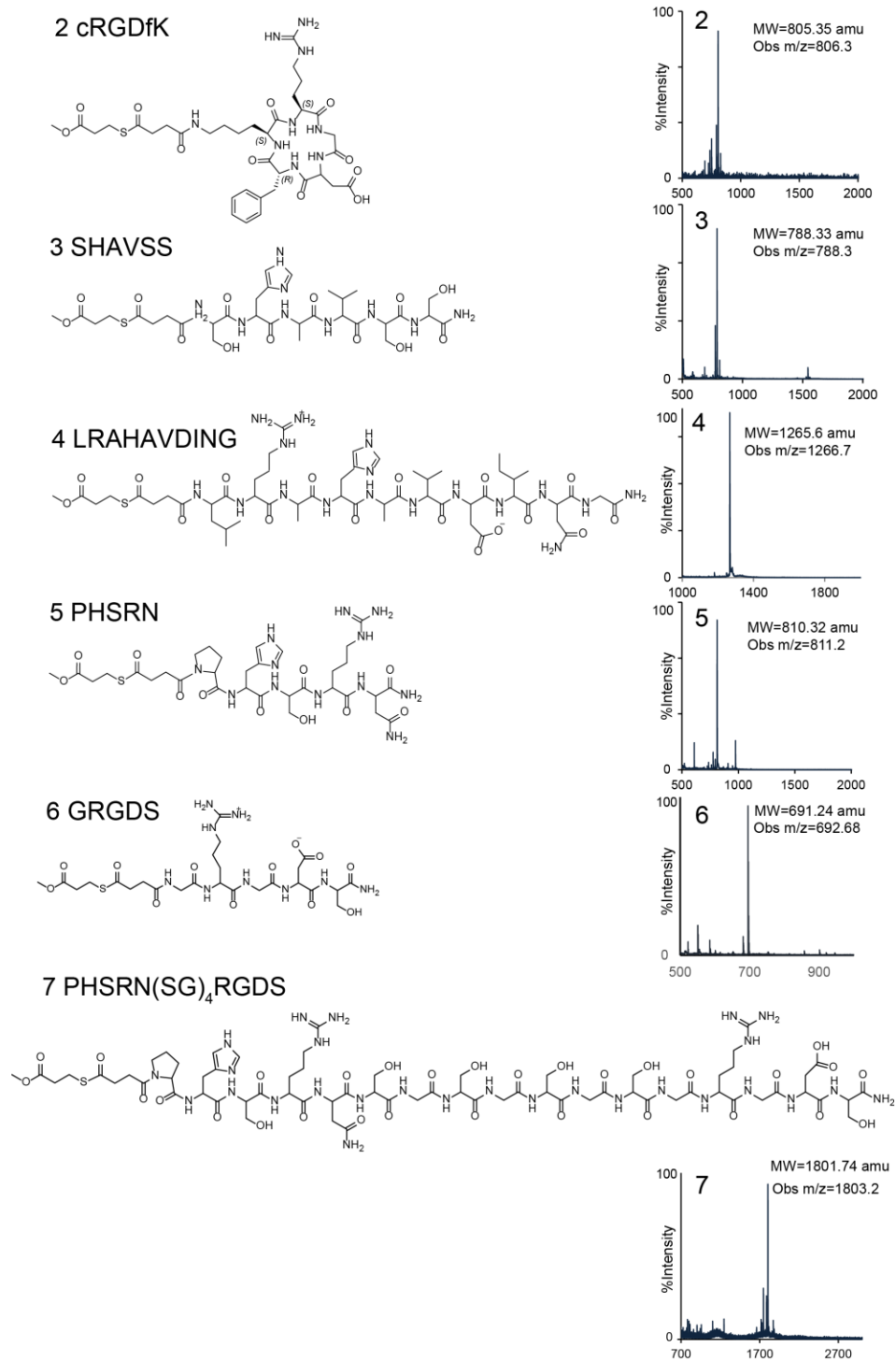


Figure 2.22 synthesis and characterization of a library of α -thioester peptide ligands

The following step involves the bioconjugation of the sensor precursor and the biological ligand cRGD thioester using Native chemical ligation at room temperature and neutral pH. The NCL reaction was carried out by mixing 1 (10 mM) with 5 mM peptide thioester (2-7) in 20 mM sodium phosphate buffer (pH 7.5) containing 5 mM betaine and 30 mM sodium 2-mercaptoethanesulfonic acid (MPAA). The reaction mixture was incubated for 24 hrs at room temperature. The thiol resulting from the NCL

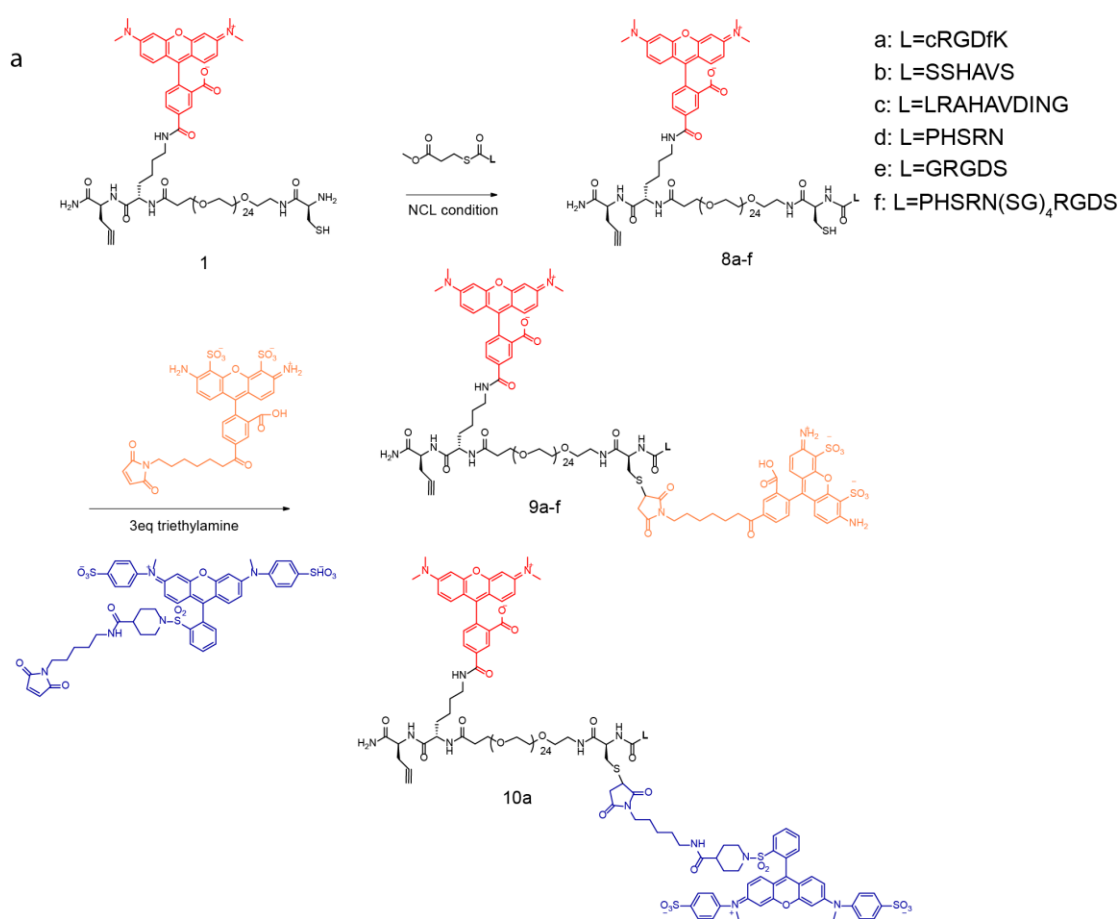


Figure 2.23 synthesis of cRGD thioester

Standard NCL conditions were used to couple the peptide to 1. The free thiol group inherent to the NCL reaction was used to site-specifically couple maleimide-modified dyes that take part in FRET with the TAMRA fluorophore.

reaction in 8a-d was subsequently coupled to a second dye/quencher via Michael addition. The reaction was carried out by mixing product 8a-d with Alexa 488 maleimide or QSY 9 maleimide (9a-f and 10a). The characterization (MALDI-TOF and HPLC) of the final product is shown in Figure A2.6.

2.4 *The development of zwitterionic silane to prevent non-specific interaction of cells and glass surfaces*

2.4.1 Biofouling in bioscience studies

At the living-nonliving interface, adsorption of protein or biofouling is a common unwanted issue and often leads to the loss of activity of biomaterial. Biofouling is a term used to describe the non-specific adsorption of proteins on artificial surfaces.¹⁰⁶ The causes of non-specific adsorption of protein are mainly attributed to three aspects: 1) the properties of the biomolecule, including structure, size, hydrophobicity, and distribution of charge and polarity; 2) the properties of the biomaterial surface, including charge, roughness, and state of surface energy; 3) environmental conditions such as pH, ionic strength, and temperature.¹⁰⁷ According to the literature, general correlations have been discussed that larger proteins tend to interact with surfaces because they can contact the surface at more sites.^{108,109} These biomolecules could affect the analysis of the target molecules in bioscience studies by contributing to the fluorescence background, and thus altering statistical analysis. In our application, when incubated on the glass coverslip, the cells tend to excrete extracellular matrix (ECM) proteins such as fibronectin and collagen to the environment such that they are able to adhere to the surrounding supports. The cell culture fetal bovine serum (FBS) is also rich in a variety of proteins such as globular protein, growth factors and bovine serum albumin. These proteins are prone to non-

specific binding to the glass coverslip surface. However, this nonspecific binding will interfere with the membrane receptors binding to the biological ligand on the MTFM sensor causing failure to function. Therefore, it is critical to develop methods to prevent this unwanted nonspecific binding of biomolecules to the surface.

2.4.2 Methods to prevent biofouling

The most widely used method to prevent nonspecific binding of biomolecules is via grafting the glass surface with polymers such as polyethylene glycol (PEG), or PEG derivatives, poly(vinyl alcohol), polyethyloxazoline, or poly(vinylpyrrolidone).¹¹⁰ Methods of using generic proteins such as bovine serum albumin (BSA) are also reported.¹¹¹ Although PEG surfaces typically are able to reject nonspecific adhesion of biomolecules, it is only effective at nano-molar (nM) concentrations, and its repulsive properties are diminished above 35°C. Moreover, in the presence of oxygen and some of the transition metal ions, the PEG polymer is prone to being oxidized.¹¹² Another disadvantage of PEG passivation is that the size of the hydrodynamic thickness will increase upon PEGylation. For example, Choi et al reported that they were unable to synthesize a PEGylated CdSe/ZnS quantum dot smaller than 10 nm.¹¹³ This is also critical to our application since the grafting of the PEG layer will increase the thickness of the surface, thus leading to extension of the MTFM sensor even without experiencing cellular force. This pre-extension of the MTFM sensor results in the removal of the FRET acceptor from the donor causing false positive signals and higher background fluorescence which will lower the sensitivity of the sensor. This effect will be investigated in later discussions. On the other hand, the protein-blocking method is even less effective in rejecting biomolecules.¹¹⁴

To maximize the interaction of the cell receptors with tension probes, we need to passivate the surface against non-specific binding of cell-generated ECM and serum proteins. Previously, PEG polymers were used for passivation in our experiments. However, we found that employing PEG polymers for passivation increased background signal and diminished sensitivity.

2.4.3 Zwitterionic SBS passivation method

To solve this problem, we tested the zwitterionic silane (3-(dimethyl-(3-(trimethoxysilyl)propyl)ammonio) propane-1-sulfonate), (SBS) (Figure 2.24).¹¹⁵ SBS is a type of zwitterionic silane molecule, which is the major component of most mammalian cell membrane surfaces. Zwitterions are known to be effective in reducing protein adsorption.¹¹⁶ Holmlin et al. reported that self-assembled monolayers of zwitterions were able to reject protein adsorption onto gold.¹¹⁷ Recently, Matsuura et al.¹¹⁸ and Jia et al.¹¹⁹ have both independently reported hydrophilic, aggregation resistant, gold and silica particles respectively grafted zwitterionic polymer on the surface. These colloid particles

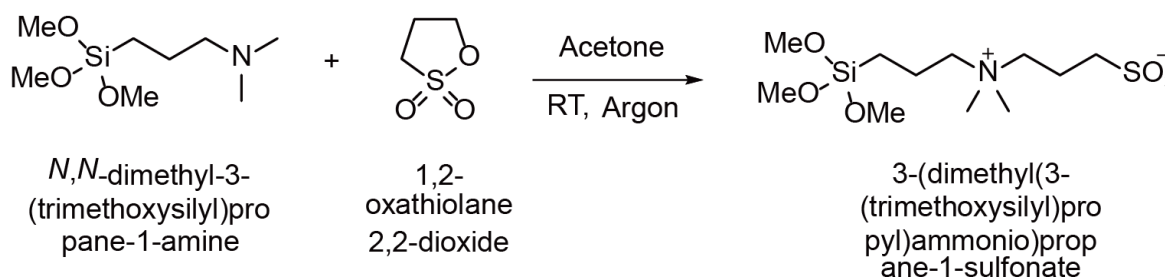


Figure 2.24 synthesis of cRGD thioester

7.5 g of (*N,N* dimethyl- 3-aminopropyl) trimethoxysilane was added to 4.45 g of propane sultone in 37 mL of acetone under N₂. The reaction was stirred vigorously for 6 hr. The white precipitate was collected by vacuum filtration and washed twice with acetone. The white solid was then dried and stored under Ar. The yield was > 90%.

showed a minor increase in size (around 1 nm) before and after coating with the zwitterion disulfide, and were stable in protein solutions and at high salt concentration with no evidence of protein adsorption. Therefore, the SBS was synthesized and tested for biomolecule passivation on the glass coverslip surfaces for the first time.

2.4.4 Synthesis of SBS

The synthesis of a small sulfo-betaine siloxane through straightforward aqueous siloxane chemistry is adapted from Estephan *et al.*¹¹⁵

7.5 g of (N,N dimethyl- 3-aminopropyl) trimethoxysilane was added to 4.45 g of propane sulfone in 37 mL of acetone under N₂. The reaction was stirred vigorously for 6 hr. The white precipitate was collected by vacuum filtration and washed twice with acetone. The white solid was then dried and stored under Ar. The yield was > 90%. Solution ¹H 300 MHz DMSO-6D and ¹³C CP/MAS solid state peak assignments and chemical shifts for the SBS are shown below. ¹H NMR (DMSO-6D, 300 MHz): δ 0.4-0.6 (B, t, 2H), 1.6-1.8(C, m, 2H), 1.9-2.0 (G, m, 2H), 2.4-2.5 (D, t, 2H), 3.0 (E, s, 6H), 3.1-3.3 (F, m, 2H), 3.3-3.4 (H, m, 2H), 3.5 (A, s, 9H). ¹³C NMR (MAS 15 KHz, 125.8 MHz): δ 49 (A), 13.8 (B), 2.78 (C), 59.25 (D, F), 58 (E), 16.55 (F), 46 (G). NMR spectrum can be found in Figure A2.4 and A2.5.

2.4.5 Preparation of the glass surface

The SBS passivation molecules are modified on the glass coverslip surface in the same time with the MTFM sensors. SBS is grafted on the surface through silane chemistry as well as a functional molecule 3-aminopropyltriethoxysilane (APTES) which provide amine (-NH₂) groups on the surface. The Amine groups were then converted to azide by coupling with a bifunctional small molecule azide N-hydroxysuccinimide (NHS-Azide)

(see Materials and Methods) through amine-succinimide reaction. Next, the sensors were added to the surface for immobilization through click chemistry.

First, glass coverslips (as described in Materials and Methods) were piranha-etched in order to produce a clean glass surface containing free terminal hydroxyl groups. A binary mixture of APTES and SBS at a molar ratio of 1: 50 was coupled to the hydroxyl surface groups of the glass coverslip to generate a surface presenting reactive amine and passivating zwitterion SBS. The reaction proceeded in methanol/water solution (methanol: water 1:4) overnight at 70°C. The glass coverslips were then cooled down to room temperature and washed with methanol and water four times. The last step was to dry the coverslip under a stream of N₂. These APTES and SBS modified glass coverslips can be stored in a sealed petri dish at room temperature for a week.

Before living cell experiment, the coverslips were taken out from the storage petri dish, and azide N-hydroxysuccinimide ester (NHS-Azide) was dissolved in DMSO in a concentration of 5 mM. This reaction proceeded for one hour at room temperature for coupling of the NHS-Azide to the free amines presented on the coverslip to generate an azide functionalized surface. Finally, the tension probes (Alkyne-Alexa 488-TAMRA/PEG24) were then covalently linked to the surface using copper-catalyzed Azide-Alkyne Huisgen cycloaddition. This was achieved by using a 50µL solution containing 0.1-5 µM alkyne-terminated tension probe, 5 mM Cu-TBTA, and 10 mM ascorbic acid in 1:1 DMSO:H₂O. The reaction was allowed to proceed between two azide-functionalized coverslips for 5 min. The preparation of Cu-TBTA is described in materials and methods.

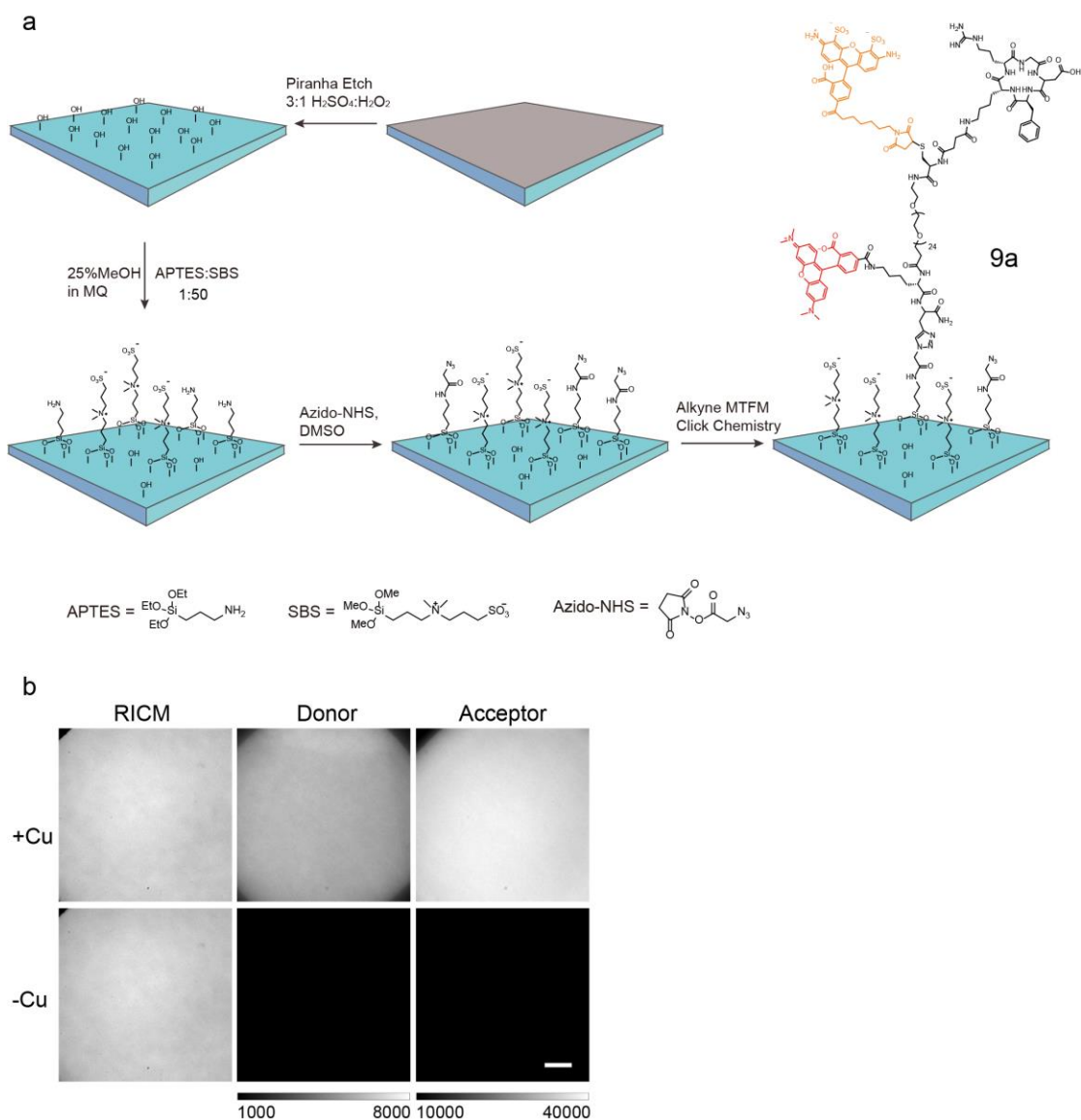


Figure 2.25 Modification of the glass coverslip

a) Procedure of functionalizing glass coverslips with SBS passivation and MTFM sensors.

The hydroxyl group was converted to Azide through coupling with NHS-Azide and the sensor was covalently linked to the surface using copper-catalyzed click chemistry. b) A solution with no Cu-TBTA was used to generate control samples, showing that the tension probe primarily bound the surface through the Cu-catalyzed click reaction. (Scale bar 10 μ m)

2.4.6 Materials and Methods.

To verify that the sensor presented on the glass surface was through covalent linkage by Copper assisted click chemistry, a solution with all the click chemistry reagents except Cu-TBTA catalyst was used to generate control samples. The two sample coverslips (Cu⁺ and Cu⁻) were rinsed off with methanol and DI water sequentially and were imaged using conventional microscopy. (Figure. 2.25) The Copper positive surfaces showed fluorescence in both the Donor and Acceptor channels, while the Copper negative surface showed minimal fluorescence under the same scale and exposure settings. This showed that the tension probe primarily bound the surface through the Cu-catalyzed click reaction.

2.4.7 Surface crowding caused by passivation molecules

Another concern is the above mentioned passivation molecule crowding issue given the importance of the molecular extension of the tension probes. We aimed to estimate the thickness of the passivation layer that is added to the surfaces when the surface was PEG passivated rather than SBS passivated. This was achieved by measuring mean inter-fluorophore distance using FRET mechanism. The FRET efficiency was measured using a TAMRA-PEG24-Fluorescein probe and reporting the acceptor-normalized donor intensity (Figure 2.26). The donor-acceptor distance was greater for the PEG2000 and PEG5000 surfaces in comparison to the SBS passivated surface. The mean inter-fluorophore distance for SBS surfaces was approximately 2.6 nm, which is in agreement with the predicted 2.4 nm distance based on the Flory model. The TAMRA-fluorescein distance increases by ~1 nm when the surface is passivated using PEG5000, which leads to a ~15% decrease in quenching efficiency. These results indicate that the PEG polymer

passivation (~2000 Da and ~5000 Da) leads to molecular crowding of the tension probe, thus placing it in a more extended conformation as compared to the samples prepared with SBS passivation. The extension of the tension probe upon passivation with PEG polymers is consistent with the literature showing that polymers with fixed grafting density and increasing molecular weight tend to increase crowding and the transition of polymers to more brush-like conformations.^{96,120} In contrast, the 1.3 nm length of the SBS was insufficient to crowd the tension probes. This feature of SBS passivation prevented the increased background signal and diminished sensitivity caused by long PEG polymer passivation.

2.4.8 Comparison of SBS and traditional PEG passivation

SBS provided enhanced passivation against cell adhesion in comparison to PEG polymers (Figure 2.27). 5w NIH 3T3 fibroblast cells were incubated on glass coverslips in FBS in DMEM medium supplemented with 10% FBS, L-glutamine, penicillin G and streptomycin (see method and materials) at 37 °C with 5% CO₂. At 20 min, 1h, 2.5h, and 24h time check points. Coverslips covalently modified with cRGD, SBS zwitterion, PEG2000 and PEG5000 were compared in parallel against surfaces with no passivation (in triplicates). Total cell counts in 800 μm² area were quantified by blind scorer. The observed cell attachment was as expected on the surface with no passivation and on

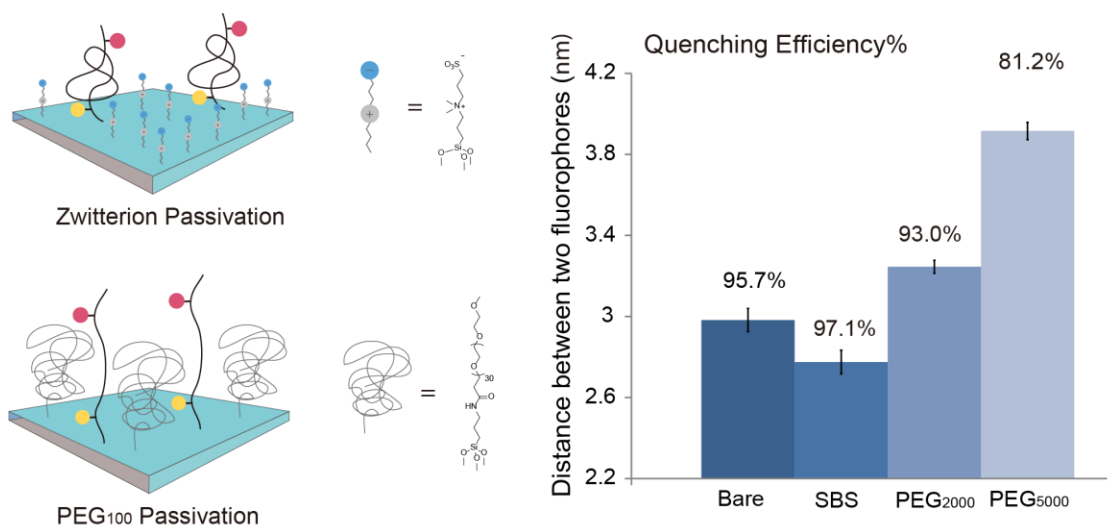


Figure 2.26 Surface crowding comparison between PEG and SBS passivation

The FRET efficiency was measured using a TAMRA-PEG₂₄-Fluorescein probe and reporting the acceptor-normalized donor intensity. The donor-acceptor distance was greater for the PEG₂₀₀₀ and PEG₅₀₀₀ surfaces in comparison to the SBS passivated surface. The mean inter-fluorophore distance for SBS surfaces was approximately 2.6 nm, which is in agreement with the predicted 2.4 nm distance based on the Flory model. The TAMRA-fluorescein distance increases by ~1 nm when the surface is passivated using PEG₅₀₀₀, which leads to a ~15% decrease in quenching efficiency.

surface with positive control cRGD, and cells reached 100% confluency over 24 hours. On the PEG (2000 and 5000) passivated surfaces, cell adhesion was rejected within one hour period of time. However, cell counts started to increase after the one hour time point. As expected, the PEG5000 surfaces showed superior passivation behavior than the PEG 2000 surfaces. This is in agreement with the hypothesis that longer PEG chain provides greater coverage on the surface resulting in better prevention of biofouling. In general, during the 24-hour experiment period, the PEG modified surfaces provided modest passivation against non-specific cell adhesion. In contrast, on the SBS surfaces there were no observable cell counts over the total time of experiments (24 hours). Therefore, SBS provides superior passivation against bio-fouling and concurrently improves probe sensitivity by reducing background signal. SBS passivation was used in all subsequent cell studies. This result represents the first demonstration of using SBS for cell culture and of SBS passivation outperforming that by PEG polymers, the most widely used reagent for passivation against biofouling.

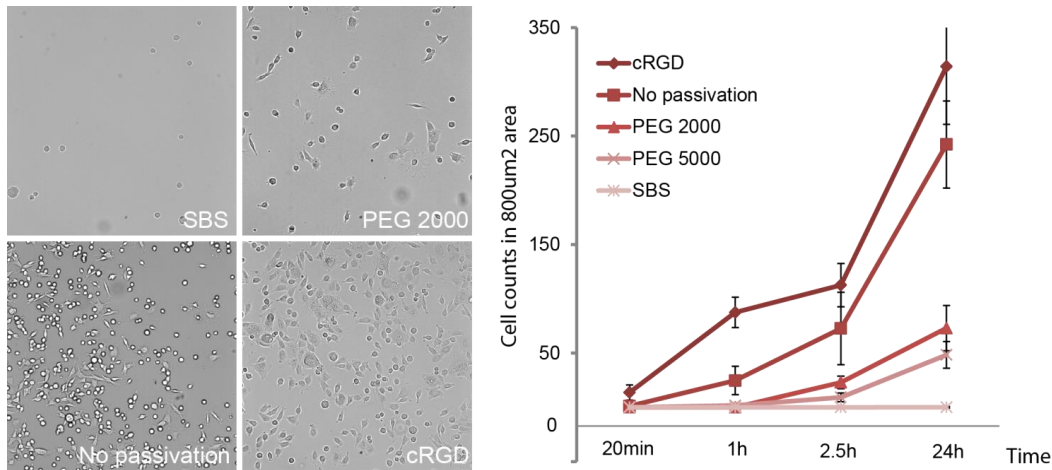


Figure 2.27 Surface passivation comparison

NIH 3T3 fibroblast cells were incubated on glass coverslips at 37°C. Cell counts were monitored at different time points. Brightfield images showing the cell attachment at time point 2.5 hours. Line graph showed the cell attachment over 24 hours

2.5 Tension map of fibroblast cells

2.5.1 Determine the surface density of MTFM tension sensor

It is imperative to inspect the quantity of MTFM sensors on the surface since the sensors presented on the surface has to simulate the density of the RGD motif in the ECM for the optimal biological function.¹²¹ However, routine fluorescence microscopy analysis of the absolute molecule surface density has been limited, without which only relative comparisons can be made.^{122,123} This is due to the difficulty to prepare appropriate calibration standards that relate measured fluorescence intensity to actual surface concentration. The surface density of the MTFM probes was determined using quantitative fluorescence microscopy with supported lipid bilayer standards.⁹¹ This is a

standard method to determine the density using supported lipid bilayers (SLB) developed by Galush et al. Supported lipid bilayers (SLBs) are popular models of cell membranes and they are easily created by several techniques. The SLBs are compositionally homogeneous,¹²⁴ and can contain a variety of labeling moieties across a broad range of densities (up to $10^4/\mu\text{m}^2$ or higher). These advantages allow SLBs to create large, uniform, fluorescent standards for fluorescence analysis in chemical and biological science.¹²⁵ Note that supported bilayers can self-assemble to a membrane thickness of $\sim 4\text{-}5\text{nm}$, thus making it easier to reproducibly make surfaces of chosen densities and at the same time avoid the need for further surface characterization. Although the spectral differences between lipid-bound and protein-bound fluorophores may initially seem to be difficult, these differences may be calibrated. A lipid-bound fluorophore roughly similar to that on the sample is preferably chosen in order to minimize the spectral difference. The 2D planar geometry of SLBs makes them well suited to microscopy focal plane. Therefore, this technique is best suited to the analysis of 2D sample geometries similar to planar-supported bilayers.

To quantify the grafting density of the MFTM sensors on the SBS passivated surfaces, supported bilayers for calibration standards containing rhodamine-DHPE mixed with DOPC were formed in glass-bottom 96 well plates. Fluorescence images showed calibration bilayers with increasing amounts of rhodamine-DHPE (scale bar = $10\mu\text{m}$). The fluorescence intensity of bilayers increases with increasing doping concentration (density) of rhodamine-DHPE. Each image corresponds to a single data point. In order to calibrate the fluorescence intensity of the tension probe against the lipid-conjugated rhodamine DHPE, we determined a scaling factor, F . To achieve this, the microscope was

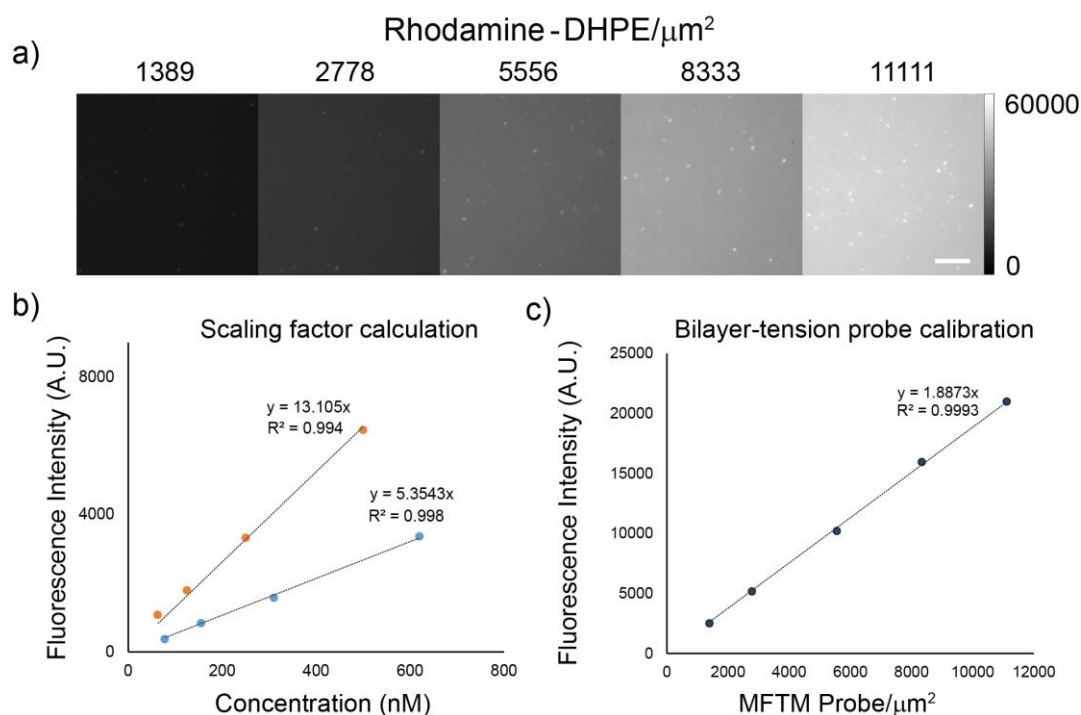


Figure 2.28 Surface crowding comparison between PEG and SBS passivation

Supported bilayers for calibration standards containing rhodamine-DHPE mixed with DOPC were formed in glass-bottom 96-well plates. a) Fluorescence images showed calibration bilayers with increasing amounts of rhodamine-DHPE (scale bar = $10 \mu\text{m}$). The fluorescence intensity of bilayers increases with increasing doping concentration (density) of rhodamine-DHPE. Each image corresponds to a single data point. b) The microscope was defocused into a solution of known lipid vesicle or tension probe, and the fluorescence intensity of the solution was recorded. The dotted lines represent linear regression fits, resulting in a scaling factor $F = k_{\text{probe}}/k_{\text{lipid}} = 2.44$. c) The calibrated tension probe surface density and fluorescence intensity were then plotted. The dotted line represents a linear regression fit of the five tension probe densities ($R^2 = 0.9993$).

defocused into a solution of lipid vesicle of known concentration and a solution of tension probes of known concentration. And the fluorescence intensity of the solution was recorded. The dotted lines represent linear regression fits, resulting in a scaling factor $F = k_{\text{probe}}/k_{\text{lipid}} = 2.44$. c) The calibrated tension probe surface density and fluorescence

intensity were then plotted. The dotted line represents a linear regression fit of the five tension probe densities ($R^2 = 0.9993$).

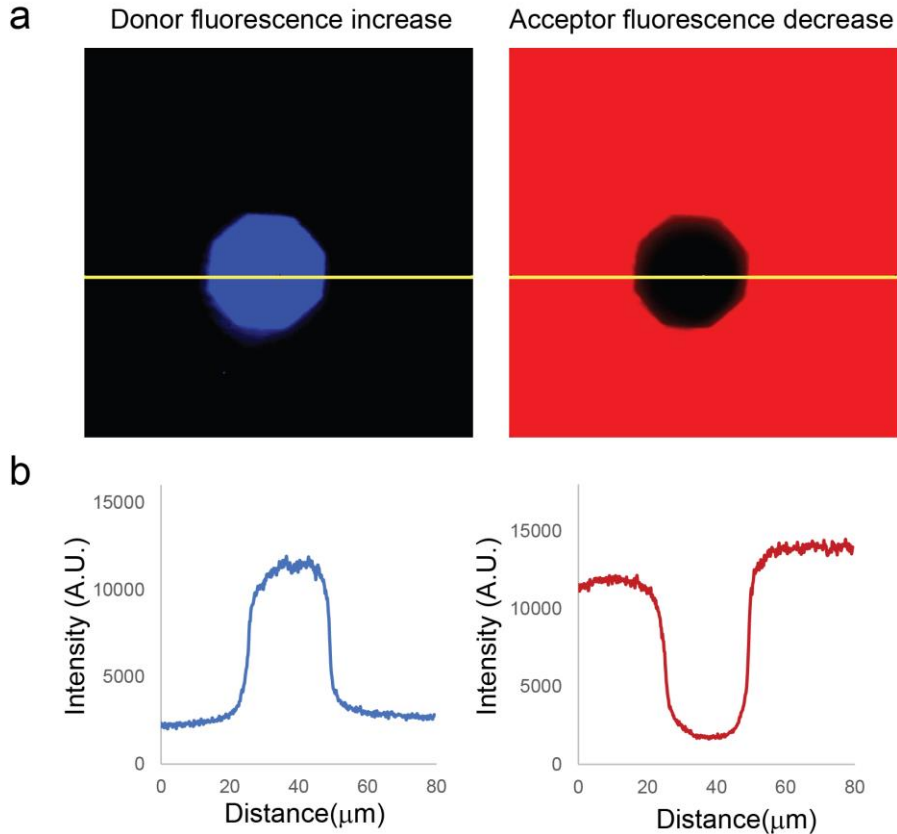


Figure 2.29 Determine quenching efficiency of MTFM sensor by photobleaching

Glass coverslips (as described in Materials and Methods) were passivated with SBS and modified with MTFM sensor 9a. a) A focused 561 nm laser was used to photobleach the TAMRA acceptor for a 5 min duration (center area in a). Representative images of the donor and acceptor channels is shown in the top panel. b) Line scan analysis of the images showed that the Alexa 488 donor increased in brightness by 83% (left), while the TAMRA acceptor intensity decreased by 85% (right). This result indicated that the quenching efficiency of the TAMRA-Alexa488 pair is at least 83%.

2.5.2 Determine the quenching efficiency of the MFTM sensor

To verify the quenching efficiency of the TAMRA-Alexa488/PEG24 tension probe, glass coverslips (as described in Materials and Methods) were passivated with SBS and modified with MTFM sensor 9a. A focused 561 nm laser was used to photobleach the TAMRA acceptor for a 5 min duration (center area in Figure 2.29 a) and a decrease in the acceptor channel TRITC was observed. Representative images of the donor and acceptor channels is shown in the top panel in Figure 2.28. At the same time, an increase in the donor channel FITC was also observed, which directly indicates the energy transfer between the donor and acceptor within the MTFM sensor on the glass slides. Line scan analysis of the images showed that the Alexa 488 donor increased in brightness by 83% (left), while the TAMRA acceptor intensity decreased by 85% (right). This result indicated that the quenching efficiency of the TAMRA-Alexa488 pair is at least 83%. The quenching efficiency of donor and quencher/acceptor was also determined by the measurement of fluorescence intensity of the biotinylated donor only molecule and donor-quencher/acceptor molecule on supported lipid bilayer (SLB). The biotinylated molecules are synthesized by coupling a small molecule biotin-azide through click chemistry onto the alkyne group of the probes. Eight lipid bilayer surfaces were functionalized with streptavidin and then incubated with either donor only or donor-acceptor molecules of different concentration (~50nM–400nM). The average fluorescence intensity for donor only surfaces was compared to the fluorescence intensity of surfaces containing both donor and acceptor in order to determine the quenching efficiency of the surfaces. The quenching efficiency is calculated to be $93.35\% \pm 0.05$ between TAMRA and QSY9 and $93.84\% \pm 0.04$ between Alexa 488 and TAMRA. All bilayer surfaces were tested for lateral mobility using FRAP experiments.

2.5.3 Integrin tension fluorescent map

To test the cRGDfK tension probe, NIH 3T3 fibroblast cells were plated onto TAMRA-QSY9 sensor modified surfaces for 1 hour to allow the cells to adhere. We used epifluorescence microscopy to image the live cell tension response and reflection interference contrast microscopy (RICM) to monitor cell-substrate binding.

Epifluorescence Microscopy is using a conventional compound microscope that has been equipped with a high-intensity mercury lamp light source that emits light in a broad spectrum from visible through ultraviolet.

Within one hour incubation, 3T3 cells strongly engaged these surfaces, as indicated by reflection interference

contrast microscopy

(RICM). A strong

fluorescence intensity

increase (up to 7 fold over

background) that was

strongly associated with the

cell-binding pattern in

RICM was observed in the

donor fluorescence channel

FITC. (Figure 2.30) The

signal to background ratio

at the brightest spots of the image was ~ 20 . This offers the advantage of allowing direct

and facile identification of areas of high tension. In some local regions, rod-like

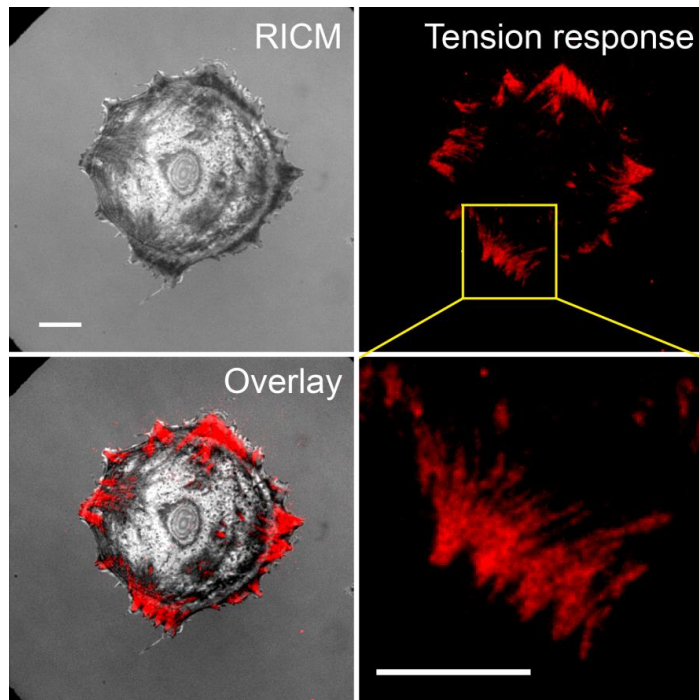


Figure 2.30. Fluorescence tension signals with fibril-like details at the cell protrusion leading edge

fluorescence patterns were formed (Figure 2.30), suggesting formation of mature focal adhesions. A dynamic increase in fluorescence in the tension channel (TAMRA) was observed in regions associated with the cell-binding pattern in RICM (Figure 2.31). The bright spots were diffraction limited, thus suggesting that the observed events are localized to punctate points that experience, which exclusively probes molecules within 100-150 nm of the substrate. The spatial distribution of tension was relatively dynamic, changing on a time scale of tens of minutes. The increase and decrease fluorescence fluctuation in the same location indicated that the fluorescent tension signal is dynamic and the cells are reusing the MTFM sensor meaning that it is robust and reversible.

2.5.4 Verifying tension reversibility by actin inhibitors

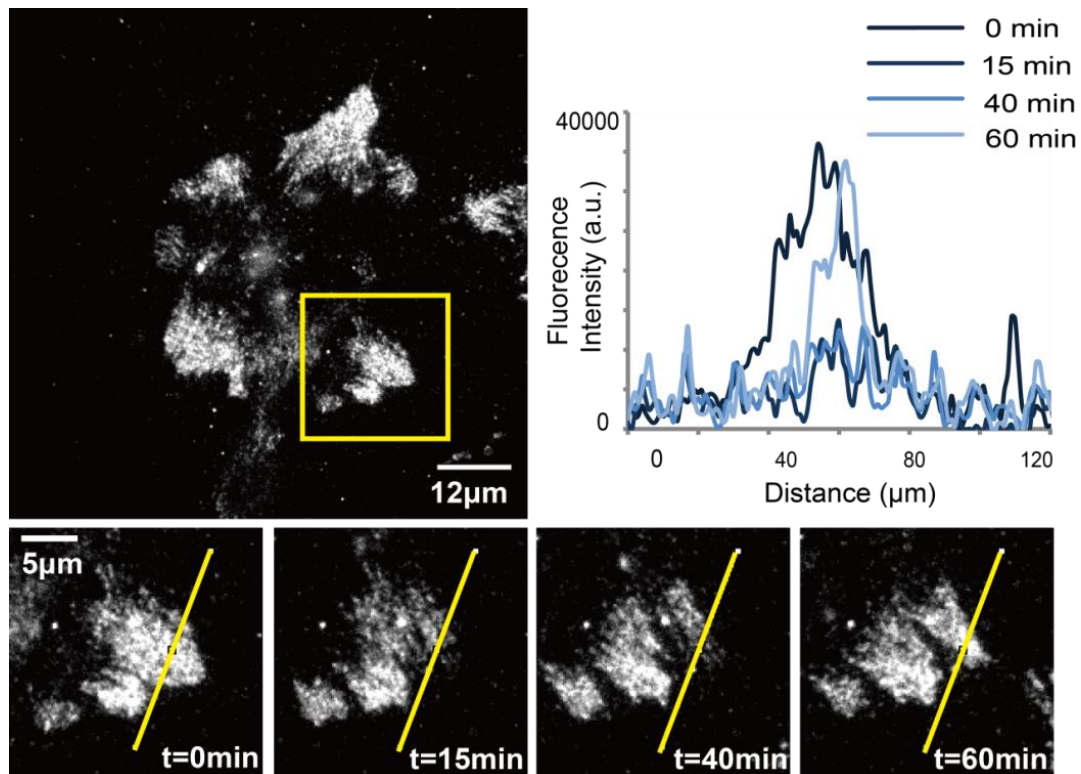


Figure 2.31 Dynamic tension signals

To verify that the tension response is reversible and actin dependent, the actin inhibitor Latrunculin B was applied to treat the cells incubated on the MTFM sensor surface. The drug latrunculin B (LatB) is commonly used to experimentally disrupt the actin cytoskeleton of cells.¹²⁶ LatB causes changes in cell shape and actin organization. It mainly works by sequestering G-actin and preventing F-actin assembly. It binds monomeric actin with 1:1 stoichiometry and can be used to block actin.

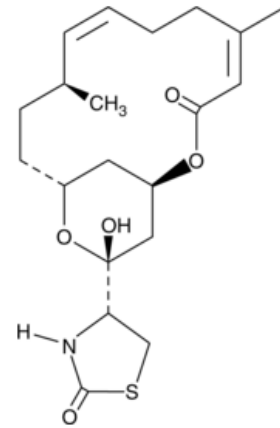


Figure 2.32 Chemical structure of Latrunculin B

Before being treated with the latB inhibitor, cells were strongly engaged with the surfaces as indicated by RICM, and fluorescence signals was as observed. At one hour incubation time point, cells were treated with latB and then imaged. The signal rapidly diminished and returned to background levels within 20 min of treatment of latB, indicating that the signal can be reduced by inhibiting the cellular cytoskeleton (Figure 2.32).

Taken together, the dynamic fluctuations in tension signal, live cell dual channel integrin/tension imaging, along with the latB experiment show that the reversible fluorescence response is due to mechanical tension exerted by integrin receptors engaged to the MTFM sensor.

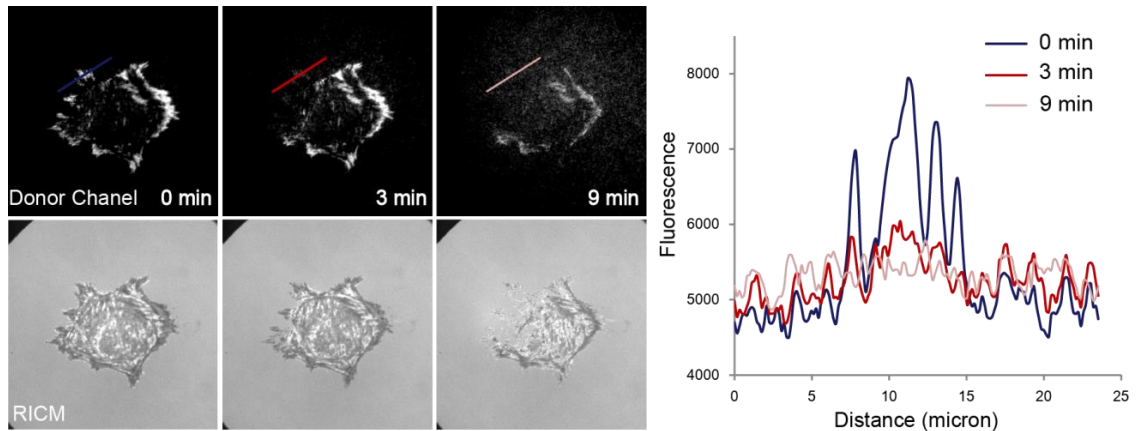


Figure 2.33 Tension signal is actin dependent

3T3 fibroblasts were treated with latrunculin B (latB). The signal rapidly diminished and returned to background levels within 20 min of treatment of latB. Scale bar = 10 μ m.

2.5.5 Tension causing by integrin mediated focal adhesion

Next, to verify that MTFM tension signal is through integrin mediated focal adhesions, NIH 3T3 cells were plated onto the cRGDfK tension sensor (10a) surface for 1 hr and then imaged in RICM and tension signal channels. Representative images are shown to the right (Before fixation). Subsequently, cells were fixed by incubation in 1 ml of 4% w/v paraformaldehyde (PFA) for 10 min. The PFA was subsequently rinsed off using 25 ml of 1 X PBS, and then cells were permeated by incubation with 0.1% (v/v) Triton X-100 for 5 min in PBS. The cells were then rinsed with 25 ml 1 X PBS, and then blocked for 1 hour using 1% w/v BSA. The tension signal following fixation (left) was weakened and more diffuse, in agreement with literature. The PEG polymer is not crosslinked by PFA and because the cellular cytoskeleton likely relaxes following PFA treatment, the tension signal typically becomes weaker following PFA treatment.

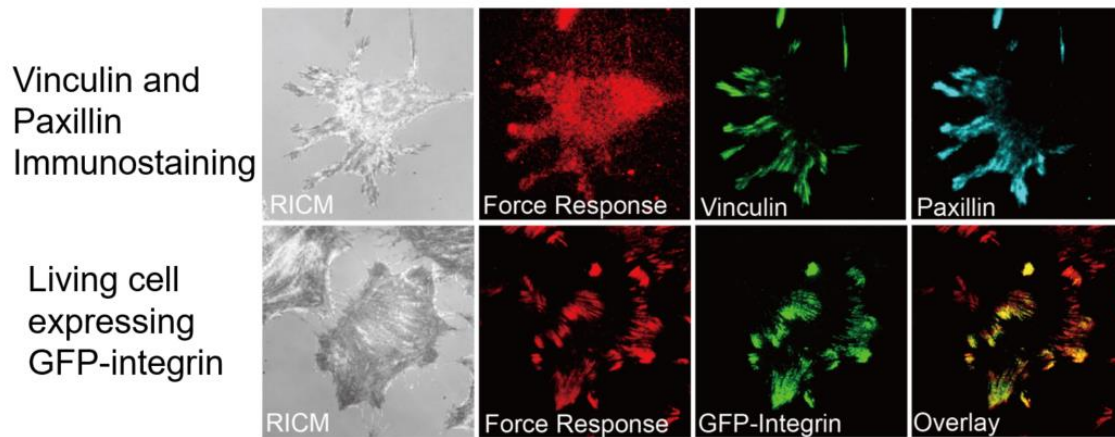


Figure 2.34 Tension is integrin mediated

3T3 fibroblasts were treated with latrunculin B (latB). The signal rapidly diminished and returned to background levels within 20 min of treatment of latB. Scale bar = 10 μ m.

Tension signal colocalized with GFP-tagged beta-3 integrin. To co-localize the tension signal with beta-3-integrin-GFP, rat embryonic fibroblast (REF) cells were transfected with GFP beta-3-integrins and plated on the cRGDfK-TAMRA-QSY9/PEG24 tension probe (10a) surface and imaged. At the 1 hour time point, the tension signal was highly co-localized with the GFP fluorescence, indicating that the 3-integrins are primarily associated with the observed tension. Manders' Colocalization test was performed for 8 cells and the Manders' Colocalization Coefficients (MCC) was calculated to be 0.88 ± 0.08 (beta-3-integrin-GFP over tension signal).¹²⁷ (Figure A2.7)

In summary, the dynamic fluctuations in tension signal, live cell dual channel integrin/tension imaging, as well as the latB inhibitor experiment demonstrate that the reversible fluorescence response is caused by mechanical tension exerted by integrin receptors acting on the MTFM sensor.

2.5.6 Quantification of tension

Our new class of stable and modular MTFM sensor design allows for precise quantification of the applied force required to extend the PEG linker from its resting state. The physical extension of the PEG polymer was calculated from the FRET relation, and this displacement was then used to estimate the mechanical tension using the extended worm-like chain (WLC) model.^{128,129}

2.5.6.1 Determination of the Förster Distance of Alexa 488-TAMRA FRET Pair and TAMRA-QSY9 FRET Pair

To convert the fluorescence signal to the distance between the fluorophores, we used the FRET equation where quenching efficiency depends on the donor-to-acceptor/quencher separation distance r with an inverse 6th power law due to the dipole-dipole coupling mechanism. $QE = \frac{1}{1+(r/R_0)^6}$,¹³⁰ in which R_0 is the Förster distance of this pair of donor and acceptor. To calculate the R_0 of the two donor and quencher/acceptor pairs (Alexa 488- TAMRA and TAMRA- QSY9), we measured the donor emission and acceptor/quencher absorption spectrum of these dyes. The R_0 was then calculated based on the overlap integral of the donor emission spectrum with the acceptor absorption spectrum and their mutual molecular orientation as expressed by

Eq

$$R_0^6 = \frac{9Q_0(\ln 10)\kappa^2 J}{128\pi^5 n^4 N_A}$$

where Q_0 is the fluorescence quantum yield of the donor in the absence of the acceptor, κ^2 is the dipole orientation factor, and $\kappa^2 = 2/3$ is assumed. n is the refractive index of the medium, N_A is Avogadro's number, and J is the spectral overlap integral as calculated by the following equation:

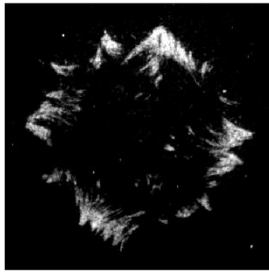
$$J = \int f_D(\lambda) \epsilon_A(\lambda) \lambda^4 d\lambda$$

Fit to the FRET equation, Förster distance (R_0) is determined to be 6.4 nm, and 488 and TAMRA pair to be 5.9 nm.

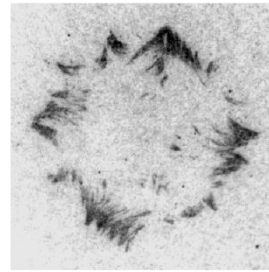
2.5.6.2 Measuring the quenching efficiency (QE) of Alexa 488-TAMRA FRET pair and QSY9 and TAMRA-QSY9 FRET pair

The quenching efficiency of donor and quencher/acceptor is determined by the measurement of fluorescence intensity of the biotinylated donor only molecule and donor-quencher/acceptor molecule on supported lipid bilayer (SLB). The biotinylated molecules were synthesized by coupling a small molecule biotin-azide through click chemistry onto the alkyne group of the probes. Eight lipid bilayer surfaces were functionalized with streptavidin and then incubated with either donor only or donor-acceptor molecules of different concentration (~50nM–400nM). The average fluorescence intensity for donor only surfaces was compared to the fluorescence intensity of surfaces containing both donor and acceptor in order to determine the quenching efficiency of the surfaces. The quenching efficiency is calculated to be $93.35\% \pm 0.05$ between TAMRA and QSY9 and $93.84\% \pm 0.04$ between Alexa 488 and TAMRA. All bilayer surfaces were tested for lateral mobility using FRAP experiments.

2.5.6.3 Stepwise image analysis of cellular tension

1). Effective fluorescence intensity (I_E)

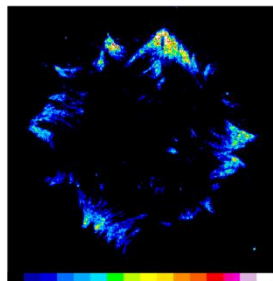
2). Quenching efficiency image (QE)



$$QE = 1 - \frac{I_E}{I_D}$$

$$z = R_0 * \left(\frac{1}{QE} - 1\right)^{\frac{1}{6}} - z_0$$

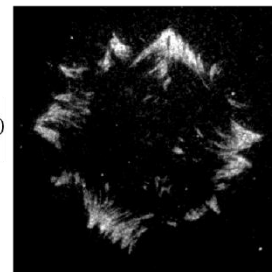
4). Tension map (F)



0 pN

20 pN

3). PEG extension image (z)



$$F = \frac{k_B T}{L_p} \left(\frac{z}{L_0} + \frac{1}{4 \left(1 - \frac{z}{L_0}\right)^2} - \frac{1}{4} + \sum_{i=2}^7 \alpha_i \left(\frac{z}{L_0}\right)^i \right)$$

I_E = Effective fluorescence intensity of the tension image, $I_E = I - I_B$ where I = fluorescence intensity of raw image, I_B = background produced by excess tension probes that cannot be used by limited numbers of integrins in unit area ($300/\mu\text{m}^2$).¹³¹

I_D = fluorescence intensity of donor only surface

R_0 = Förster radius, distance at which the energy transfer efficiency is 50%.

T = temperature (310 K)

L_p = persistence length (0.38 nm)

L_0 = contour length ($24 \times 0.35 = 8.40$ nm for PEG₂₄ and 16.8 for PEG₄₈)

z_0 = distance between donor and acceptor at the resting state.

z = PEG extension

k_B = Boltzmann constant (1.38×10^{-23} N*m/K)

The following image analysis steps were performed to estimate the magnitude of tension experienced by integrin receptors:

- 1) Collect raw fluorescence images of cells cultured on MTFM probes using indicated imaging parameters (see Optical Microscopy section in methods)
- 2) Subtract EMCCD instrumental background and acquire the raw tension image, I.
- 3) Determine the fluorescence intensity of the sensor at resting by averaging three regions of interest away from cells. Then divide this resting fluorescence intensity by (1- QE), thus yielding the fluorescence intensity of fully de-quenched surface (I_D). Given that the probe density was measured to be 1060 ± 31 sensors/ μm^2 ,⁵⁹ and beyond the maximum packing density of integrins of $300/\mu\text{m}^2$,¹³¹ we can estimate the background of non-accessible tension probes, which results in the background $I_B = I * (1 - \frac{300}{1060})$. Based on this estimation, we can calculate the effective fluorescence intensity image ($I_E = I - I_B$.)
- 4) Subsequently, convert I_E image to QE image by applying the equation $QE = 1 - I_E/I_D$.
- 5) Apply the FRET equation $z = R_0 * (\frac{1}{QE} - 1)^{\frac{1}{6}} - z_0$ thus converting the quenching efficiency map (QE map) to the PEG extension, z.
- 6) Apply the extended WLC model $F = \frac{k_b T}{L_p} (\frac{z}{L_0} + \frac{1}{4(1-\frac{z}{L_0})^2} - \frac{1}{4} + \sum_{i=2}^{i=7} \alpha_i (\frac{z}{L_0})^i)$,¹³² to convert the z map into a tension map.

2.5.6.4 Comparing PEG 24 and PEG 48 tension sensors

PEG is a well-characterized polymer. Given the predicted force-fluorescence curve for the PEG24 probes, we expect that the dynamic range of the probes is limited to ~ 15 pN; the stiffness of the probes increases drastically as the polymer approaches its contour length (Figure 2.35). To test this hypothesis, the extended WLC model was used to generate a plot of the applied forces as a function of PEG polymer linker displacement. The displacement or PEG extension is calculated from quenching efficiency. The zero-force state distance between the chromophores was determined experimentally and corresponds to the polymer length at maximum quenching efficiency. The PEG24 linker displays a wider dynamic range compared to PEG48 given the polymer conformations and the R_0 of the TAMRA and Alexa 488 pair. However, the PEG48-based tension probes have higher sensitivity at forces under 5 pN. The black lines in the fluorescence versus tension plot represent linear regression fits ($R^2=0.9$), which define the linear dynamic range of the PEG24 tension probes (<15 pN) and PEG48 tension probes (<5 pN).

To test this hypothesis, the TAMRA-QSY9 PEG₄₈-cRGDfK tension probe was manually synthesized using SPPS and coupled with cRGDfK ligand and quencher (QSY9) The synthesized construct (**12**) was purified by HPLC and its mass confirmed by MALDI-TOF MS. The TAMRA-QSY9 MTFM sensor with PEG 48 linker and RGD ligand was synthesized and coated on the glass coverslip. NIH 3T3 fibroblast cells were plated onto sensor modified surfaces for 1 hour to allow the cells to adhere. We used epifluorescence microscopy to image the live cell tension response and reflection interference contrast microscopy (RICM) to monitor cell-substrate binding. The tension map indicates that PEG48-based tension probes are active and perform similarly to the PEG24-based probes

despite the difference in dynamic range. This data supports the modularity of this approach in generating tension probes, allowing one to tune the dynamic range to appropriate levels that match the expected biophysical signaling system that employ a lower magnitude of tension, such as the Notch pathway.

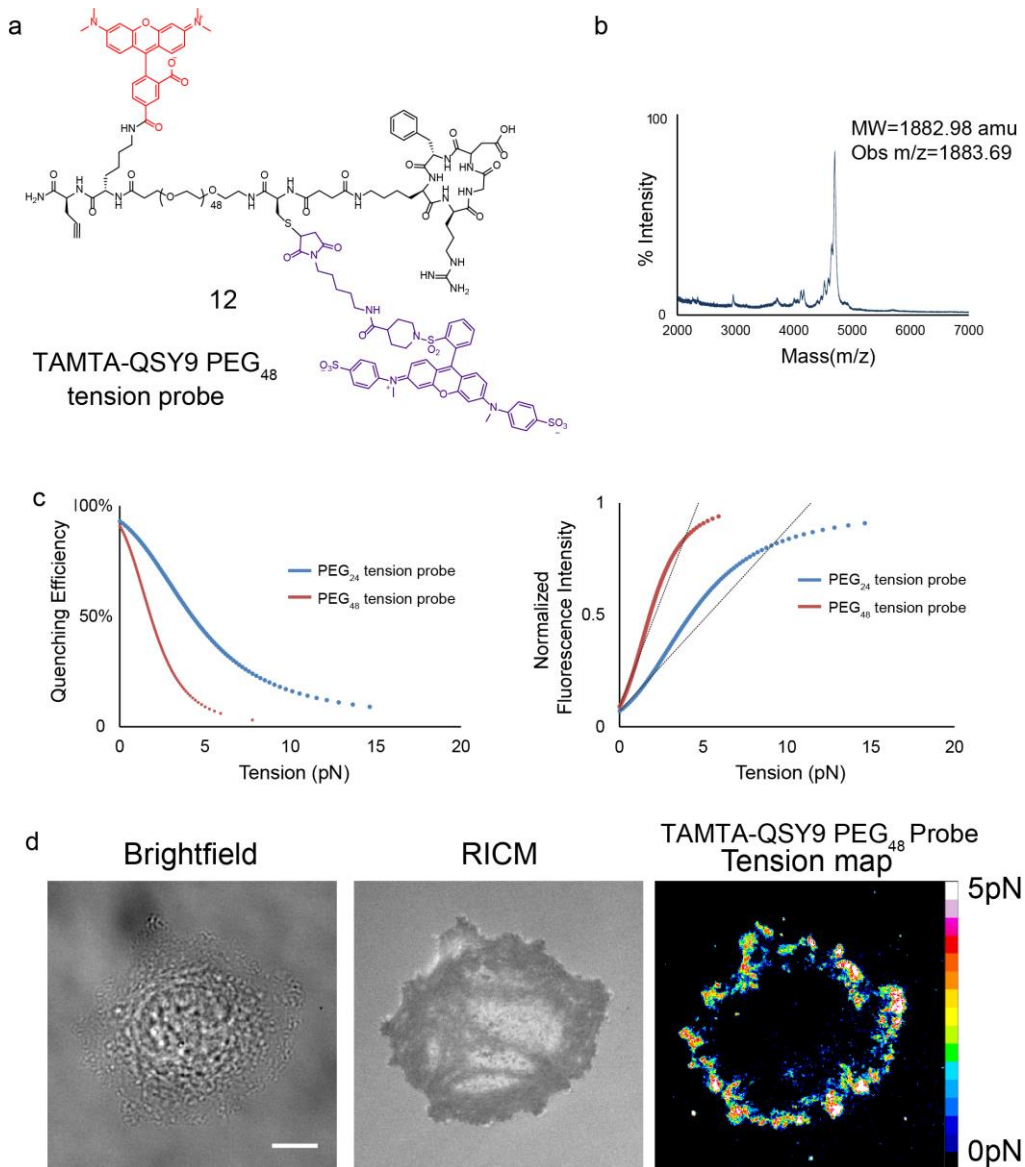


Figure 2.35 Tension mapping with PEG48 MTFM sensors

a) Chemical structure of PEG48 tension sensor; b) MALDI spectrum of PEG48 tension sensor;

c) theoretical plot of tension vs fluorescence intensity of PEG24 and PEG48 sensors; d)

Tension heat map generated by PEG48 MTFM sensors.

2.6 *Long term tension signal analysis*

To test the capability of the tension probes in long-term imaging, the FRET pair Alexa 488 and TAMRA was selected for their superior chemical- and photo-stability and insensitivity to the environment. We incubated NIH 3T3 fibroblasts on cRGDfK-Alexa488-TAMRA tension probes. Cells displayed tension patterns at the cell periphery similar to that of the FA markers (Figure 2.36a). After 20 min of incubation, the tension signal became more elongated as cells polarized. We followed the cRGDfK tension pattern for a period of 64 hrs. During this time, the average tension signal within FAs increased initially and then decreased as cells spread (Figure 2.36b). Note that the magnitude of integrin tension was correlated with the average size of FAs. As cells fully spread, FAs became slightly smaller in area, and this was accompanied by a decrease in integrin tension. This represents the longest imaging window for mapping receptor-ligand tension using a molecular probe. Minimal change was observed in the fluorescence background of both the donor and the acceptor during the 64-hour imaging window. The focal adhesion formation and progression observed by monitoring fluorescent tension signals is in agreement with the precedent literature describing this process.^{10,14} Nascent adhesions is the initiation of the adhesion of a protruding cell edge, and they are smaller than 0.25 μm in size. Some of these nascent adhesions disassemble within minutes as the leading-edge advances, but the remainder grow and mature into focal complexes, which is around 0.5 μm in size and continue into focal adhesions (FAs) which are as large as 1–5 μm . These FAs will either disassemble or mature further into stable fibrillar adhesions that do not promote migration but are involved in ECM remodeling. The process that FAs form from the initial nascent adhesion to matured FAs was observed through the size and geometry of the tension map.

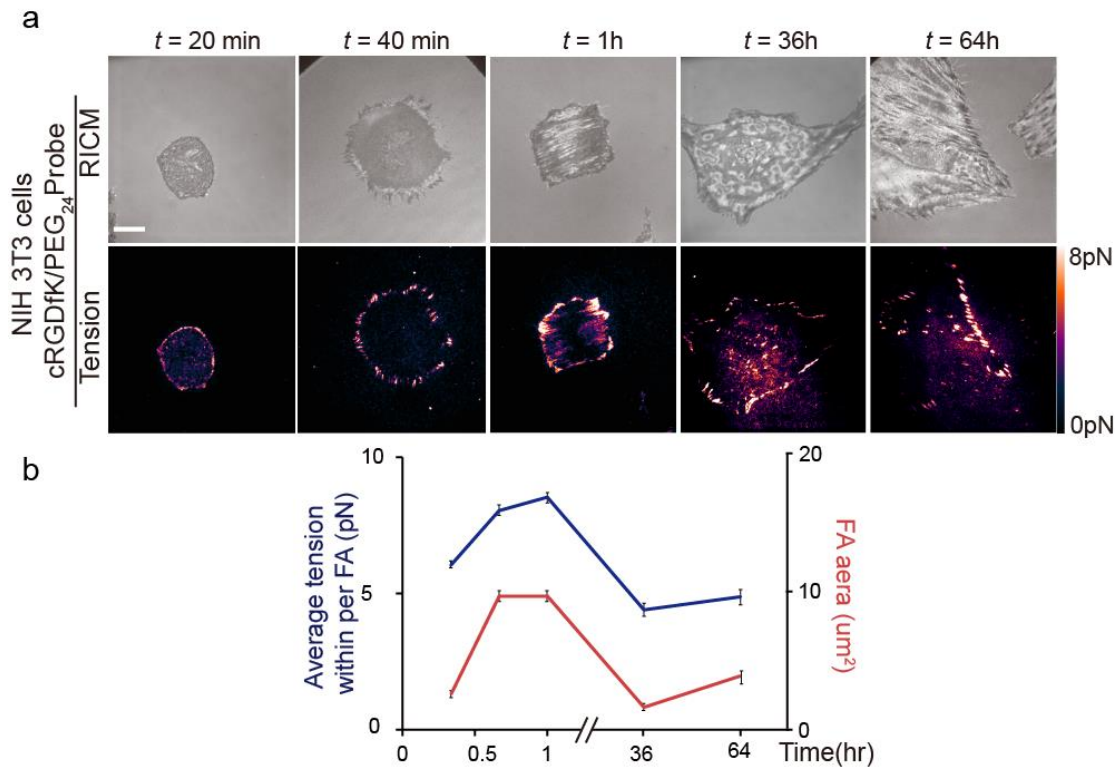


Figure 2.36 Long-term live cell mechano-imaging using TAMRA-Alexa 488

sensor. (a) RICM and fluorescence images showing the cell-substrate contact zone along with a map of integrin tension at the indicated time points that spanned from 20 min to 64 hrs. Note the changes in cell morphology and force pattern. Scale bar = 10 μm . (b) Plot showing the average tension within FAs (left y-axis), and average FA area (right y-axis) as a function of time over a period of 64 hrs. The error bars represent the SEM from $n=3-4$ cells, where 10-30 FAs were analyzed from each cell.

Note that the stability of the Alexa 488 and TAMRA sensor surfaces was tested by monitoring the fluorescence decay of donor and acceptor at cell culture condition (cell culture serum at 37 °C). Fluorescence intensity of the donor (Alexa 488) and acceptor (TAMRA) was measured before and after incubation, and minimal change was observed. Note that by $t=5$ days, the donor and acceptor signal decreased, indicating degradation of the dyes. Data was obtained from 10 different regions in two different samples. Figure A2.9.

2.7 Tension generated by binding fibronectin synergy ligand PHSRN

2.7.1 Fibronectin III 9th and 10th domain

The peptide PHSRN is found in the FN-III9, adjacent to the 10th domain that contains the RGD peptide.³⁸ PHSRN has been identified as a synergy ligand that enhances the spreading of cells on the RGD peptide.^{40,41,133} We asked whether PHSRN carries a mechanical load much like the RGD peptide that supports adhesion.

2.7.2 The effect of synergy site in cell mechanics

Tension probes with the PHSRN, cRGDfK, PHSRN(SG)4RGDS, and linear GRGDS peptides were immobilized on glass slides. Cells attached and spread inefficiently on PHSRN substrates (Figure 4a). In contrast, cells plated onto surfaces comprised a binary mixture of PHSRN and GRGDS/cRGDfK probes (1:1) spread efficiently. This is in agreement with recent reports showing that PHSRN enhances cell spreading with RGD but is inactive when presented exclusively.¹³⁴ The tension signals for cells cultured on PHSRN(SG)4RGDS, GRGDS, and cRGDfK were similar and greater than that of substrates with the binary mixture of GRGDS/cRGDfK and PHSRN (Figure 4b). Note that the samples modified with the binary mixture of RGD ligands and PHSRN display the same total density of MTFM probes but only 50% of the RGD ligand density as compared to the single component surfaces. Although the affinity of integrins for cRGDfK is greater than that of linear GRGDS, the signals were similar for both ligands, which is in agreement with results obtained using DNA-based tension probes.⁹ We were not able to detect tension signals on the substrates presenting PHSRN exclusively. These data indicate that mechanical tension is not transmitted through the PHSRN synergy ligand, but rather its role is most likely in enhancing integrin-ligand affinity. This conclusion clarifies a long-standing question regarding the mechanical role of the

PHSRN ligand in cell adhesion. We expect that MTFM probes generated using this modular approach will help elucidate the role of various ECM components in mediating mechanotransduction processes. A general caveat of this approach is that the dynamic range of the sensor is limited to ~ 15 pN; thus, while we are able to detect differences in the ensemble average tension signal, receptor forces that are $\gg 15$ pN are not distinguishable from lower magnitude signals. Therefore, the lack of statistical difference

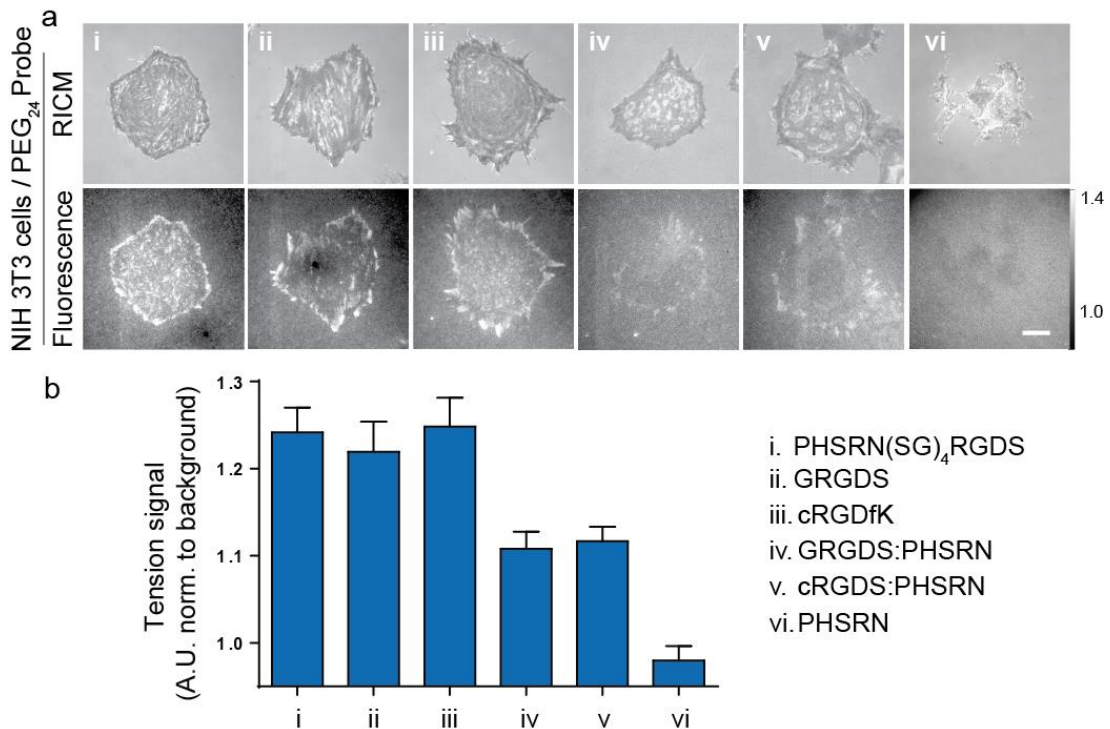


Figure 2.37 The role of RGD and PHSRN peptides in mediating integrin tension.

a) Representative RICM and fluorescence tension images of 3T3 fibroblasts cultured onto PHSRN(SG)₄RGDS, GRGDS, cRGDfK, 1:1 GRGDS: PHSRN, 1:1 cRGDfK: PHSRN, and PHSRN MTFM probes (TAMRA-Alexa 488). Scale bar = 10 μ m and contrasts are set identically. b) Bar graph showing the average tension normalized to the background for cells cultured onto the above substrates (a). Data obtained in triplicate from $n=8$ cells in each category for a total of 40 cells, where 10-30 FAs were analyzed from each cell. Note that the average tension for the PHSRN probe was $\sim 2\%$ below the background signal likely due to optical effects from cell adhesion.

in tension signal between the GRGDS, cRGDfK, and PHSRN(SG)₄RGDS probes may be due to probe sensitivity rather than the lack of biophysical difference.

2.8 *Cell-cell adhesion through Cadherin*

2.8.1 Tension map of cadherin

To study the tension generated by E-cadherin receptors, we plated endothelial cells (MDCK) on the SHAVSS peptide tension probes. In contrast to the FA tension patterns observed for the cRGDfK peptide sensor, we observed punctate tension across the cell-substrate junction. The intensity of tension signal was significantly lower for the SHAVSS peptide as compared to the cRGDfK peptide. The SHAVSS tension signal was abolished upon treating cells with latB, showing that the signal is generated by the cellular cytoskeleton (Figure 2.39). Immunostaining for the E-cadherin extracellular domain EC4 displayed puncta at the basal cell surface resembling the signal associated with E-cadherin tension in our assays (Figure 2.38). We also found that 3T3 fibroblasts did not adhere to the SHAVSS surface, confirming that E-cadherin expression is necessary for cell adhesion. Importantly, tension sensors specific to the N-cadherin ligand, LRAHAVDING, did not yield detectable signal when rat dorsal root ganglion (DRG) neurons were cultured onto substrates (data not shown). Taken together, these results indicate that E-cadherin-binding ligands experience lower values of tension than that of integrin ligands, which may reflect the mechanics of cadherin signaling or binding affinity and receptor density differences among these cell types.

2.8.2 Antibody mapping of cadherin

To validate that the E-cadherin signal is actin-dependent, MDCK cells were cultured onto SHAVSS probes modified surfaces for 6 hours, and then treated with 25 μ M latB. After 9 min, the fluorescence signal completely dissipated and returned to background levels for

all observed cells. b) To further validate that the tension signal is due to specific interaction of E-cadherin-SHAVSS ligand, MDCK cells were incubated on SHAVSS sensor modified surfaces for 6 hr and then fixed and immunostained for E-cadherin extracellular domain EC4. The results show the presence of E-cadherin puncta at the basal cell surface. These puncta resemble the signal observed for SHAVSS tension probe. Note that the tension signal significantly weakens once cells are fixed, likely due to nm scale cytoskeletal and PEG relaxation, and we are unable to obtain tension signals for fixed cells here. c) NIH 3T3 fibroblasts were cultured onto SHAVSS sensor substrate, and minimal cell attachment was observed under same experimental conditions. This is in agreement with published E-cadherin expression levels for fibroblasts.

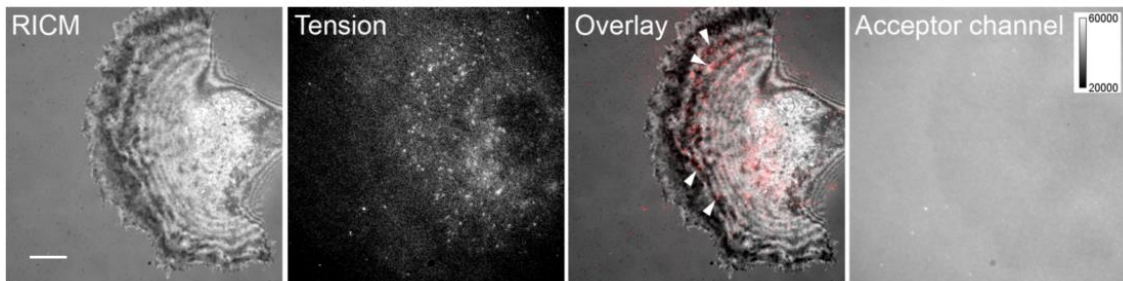


Figure 2.38 The Cadherin tension map

Representative RICM, fluorescence, overlay of fluorescence and RICM, and quantified heat map of tension for cells cultured on the SHAVSS (TAMRA-Alexa 488) tension probe surfaces. Figure shows an MDCK cell cultured on the SHAVSS peptide tension probe for 3 hrs. Raw fluorescence data were converted to a force map. Scale bar = 10 μm .

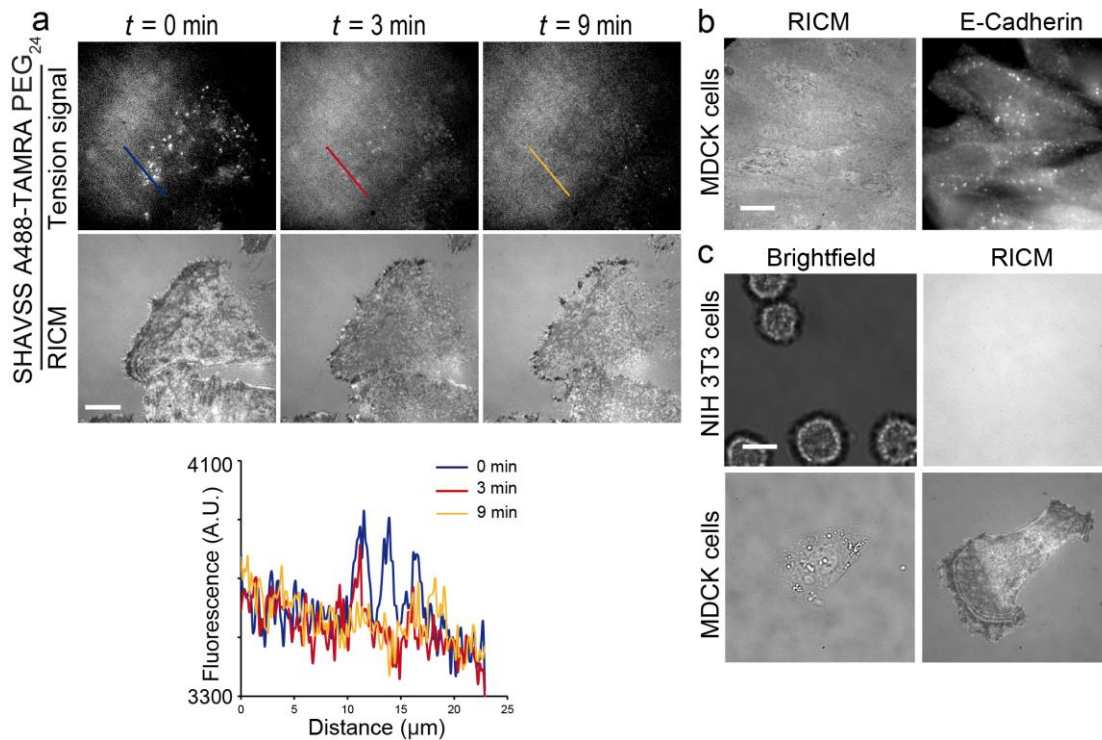


Figure 2.39 Fluorescent tension signal after treatment with actin inhibitor

a) To validate that the E-cadherin signal is actin-dependent, MDCK cells were cultured onto SHAVSS probes modified surfaces for 6 hours, and then treated with 25 μM latB. After 9 min, the fluorescence signal completely dissipated and returned to background levels for all observed cells. b) To further validate that the tension signal is due to specific interaction of E-cadherin-SHAVSS ligand, MDCK cells were incubated on SHAVSS sensor modified surfaces for 6 hr and then fixed and immunostained for E-cadherin extracellular domain EC4. The results show the presence of E-cadherin puncta at the basal cell surface. These puncta resemble the signal observed for SHAVSS tension probe. Note that the tension signal significantly weakens once cells are fixed, likely due to nm scale cytoskeletal and PEG relaxation, and we are unable to obtain tension signals for fixed cells here. c) NIH 3T3 fibroblasts were cultured onto SHAVSS sensor substrate, and minimal cell attachment was observed under same experimental conditions. This is in agreement with published E-cadherin expression levels for fibroblasts. Scale bar = 10 μm .

2.9 *Materials and Methods*

2.9.1 Reagents

(3-Aminopropyl) triethoxysilane (97%, APTES), triethylamine (99%, TEA), paraformaldehyde (95%, PFA), 1,3-Propanesultone (98%), N,N-Diisopropylethylamine(99.5%, DIEA), Hank's balanced salts (#H1387) and Triton X-100 were purchased from Sigma- Aldrich (St. Louis, MO) and used without further purification. All the Fmoc protected amino acids used in solid phase peptide synthesis and 5(6)-TAMRA, SE(# AS-81124-01), 5(6) - FAM, SE(#AS-81006) were purchased from Anaspec (Fremont, CA). The heterobifunctional linker azide-NHS (#88902) and azide-biotin (#10184) were purchased from Thermo Fisher Scientific (Rockford, IL). E-cadherin extracellular domain EC4 primary antibody was purchased from Santa Cruz Biotechnology (Dallas TX). The fluorescent dyes Alexa488-maleimide and Alexa647 labeled IgG1 secondary antibody were purchased from Life Technologies (Carlsbad, CA). Number two glass coverslips, ascorbic acid (>99.0%), and 96-well plates were purchased from Fisher Chemical & Scientific (Pittsburg, PA). DMF (>99.5%), DMSO (99.5%) and sodium bicarbonate (99.0%) were purchased from EMD chemicals (Philadelphia, PA)., mPEG-NHS (MW 2000) and mPEG-NHS (MW 5000) were purchased from Nanocs (New York, NY). Amine-PEG-SH (MW 3400) was purchased from Creative PEGworks (Winston Salem, NC). CuSO₄.5H₂O was purchased from Mallinckrodt (St. Louis, MO), and P4 gel size exclusion beads were acquired from BioRad (Hercules, CA). IgG1 paxillin-antibody was obtained from EMD Millipore (Billerica, MA). All DI water was obtained from a Nanopure water purification system with a UV sterilization unit and showed a resistivity of 18.2 MΩ.

2.9.2 Peptide synthesis

Peptides ligands 2-5 were synthesized following the standard procedure using a Liberty CEM Microwave Automated Peptide Synthesizer (NC, USA) and a Fmoc-Rink Amide MBHA Resin (AnaSpec, CA, USA).

2.9.3 HPLC

All PEG conjugated products were purified by using a C18 column (diameter: 4.6 mm; length: 250 mm) in a reverse phase binary pump HPLC that was coupled to a diode array detector (Agilent 1100).

2.9.4 MALDI-TOF Mass spectroscopy

A 10 mM solution of 2,5-dihydroxybenzoic acid (DHB) was prepared in 1% TFA water: Acetonitrile 1:1 solution as the MALDI matrix. All products were also pre-dissolved in matrix solution. 2 μ L of this mixture was added to each well on the MALDI plate. After allowing the solution to dry for 20 min, the sample was analyzed by a high performance MALDI time-of-flight mass spectrometer (Voyager STR).

2.9.5 Cu-TBTA preparation

1 mg CuBr was dissolved in 70 μ l DMSO/ t-BuOH 3:1 to obtain a 0.1 M solution. This solution must be freshly prepared and cannot be stored. 54 mg TBTA was dissolve in 1 ml DMSO/ t- BuOH 3:1 for 0.1M solution. This solution can be stored at -20°C.

1 volume of the 0.1 M CuBr solution was added quickly to 2 volumes of the 0.1 m TBTA solution to obtain click solution.

2.9.6 Fluorescence microscopy

Living cells were imaged in standard cell imaging buffer (Hank's balanced salt, pH 7.4, 10 mM HEPES without phenol red) at 37 °C, and fixed cells were imaged in 1% BSA in

1× PBS at room temperature. During imaging, physiological temperature was maintained with a warming apparatus consisting of a sample warmer and an objective warmer (Warner Instruments 641674D and 640375). The microscope was Nikon Eclipse Ti driven by the Elements software package. The microscope features an Evolve electron multiplying charge-coupled device (EMCCD; Photometrics), an Intensilight epifluorescence source (Nikon), a CFI Apo 100× (numerical aperture (NA) 1.49) objective (Nikon). This microscope also includes the Nikon Perfect Focus System, an interferometry-based focus lock that allowed the capture of multipoint and time-lapse images without loss of focus. The microscope was equipped with the following Chroma filter cubes: FITC, TRITC, Cy5, and reflection interference contrast microscopy (RICM). The FITC, TRITC, Cy5 images were taken using 500 ms exposure time while RICM images were acquired using 10-20 ms exposure time. One additional cutoff filter (product number: 86354, Edmund optics, USA) was included into the optical path to eliminate the bleed-through from acceptor TAMRA into the FITC channel.

2.9.7 Cell culture.

NIH 3T3 cells and rat embryonic fibroblast (REF) were cultured in DMEM medium (Mediatech) supplemented with 10% FBS (Mediatech), L-glutamine (2.1 mM, Mediatech), penicillin G (100 IU ml⁻¹, Mediatech) and streptomycin (100 µg ml⁻¹, Mediatech) and were incubated at 37 °C with 5% CO₂. Cells were passaged at 90–100% confluency and plated at a density of 50% using standard cell culture procedures.

2.9.8 Preparation of small unilamellar vesicles phospholipids

(1,2-dioleoyl- sn-glycero-3- phosphocholine, DOPC; and 1,2-dioleoyl- sn-glycero-3-phosphoethanolamine-N-(cap biotinyl), biotin-DPPE) were purchased from Avanti Polar

Lipids (Alabaster, AL). To prepare small unilamellar vesicles, lipids were combined in a round bottom flask at the desired molar ratio in chloroform and dried on a rotary evaporator to form a lipid film. The film was dried under a stream of N₂ for 15 min and then resuspended with Nanopure water to achieve a lipid concentration of 2 mg/ml. The lipid solution was frozen in a dry ice-acetone bath and thawed in a 40°C water bath three times. The vesicles were passed through a 100 nm polycarbonate filter (Whatman, Florham Park, NJ) 10 times using a high-pressure extruder (Northern Lipids, Burnaby, Canada) warmed to 45°C.

2.9.9 Assembly of supported lipid membranes

To prepare the glass surface, a 96-well plate with #1.5 glass (Greiner Bio-One, Monroe, NC) was etched with 1 M NaOH for 1 hr and rinsed with Nanopure water. A 0.5 mg/ml vesicle solution prepared in phosphate buffered saline (PBS) (for biotin-DPPE) and added to the glass for 20 min to form the bilayer. The surfaces were blocked with 0.1 mg/ml bovine serum albumin for 30 min. The membranes were then incubated with 36 nM streptavidin (Rockland Immunochemicals, Gilbertsville, PA) for 45 min. After rinsing unbound streptavidin, the surface was treated with 100 nM of biotinylated sample for 1 hr.

2.10 References

- (1) Bradshaw, R. A.; Dennis, E. A. *Handbook of cell signaling*, 2/e; 2010; Vol. 1–3.
- (2) Martin, G. S. *Cancer Cell* **2003**, 4 (3), 167–174.
- (3) Lai, E. C. *Development* **2004**, 131 (5), 965–973.
- (4) Eungdamrong, N. J.; Iyengar, R. *Biol. Cell* **2004**, 96 (5), 355–362.
- (5) Iskratsch, T.; Wolfenson, H.; Sheetz, M. P. *Nat. Rev. Mol. Cell Biol.* **2014**, 15 (12), 825–833.
- (6) SANFORD, K. K.; LIKELY, G. D.; EARLE, W. R. *J. Natl. Cancer Inst.* **1954**, 15 (2), 215–237.
- (7) Gauthier, N. C.; Fardin, M. A.; Roca-Cusachs, P.; Sheetz, M. P. *Proc. Natl. Acad. Sci.* **2011**, 108 (35), 14467–14472.
- (8) Sheetz, M. P.; Singer, S. J. *Proc. Natl. Acad. Sci.* **1974**, 71 (11), 4457–4461.
- (9) Liu, Z.; Tan, J. L.; Cohen, D. M.; Yang, M. T.; Sniadecki, N. J.; Alom, S.; Nelson, C. M.; Chen, C. S. **2010**.
- (10) Gardel, M. L.; Schneider, I. C.; Aratyn-Schaus, Y.; Waterman, C. M. *Annu. Rev. Cell Dev. Biol.* **2010**, 26 (1), 315–333.
- (11) Moy, V. T.; Florin, E. L.; Gaub, H. E. *Science* (80-.). **1994**, 266 (5183), 257–259.
- (12) Shah, N. H.; Muir, T. W. *Chem. Sci.* **2014**, 5 (1), 446–461.
- (13) Borghi, N.; Sorokina, M.; Shcherbakova, O. G.; Weis, W. I.; Pruitt, B. L.; Nelson, W. J.; Dunn, A. R. *Proc. Natl. Acad. Sci. U. S. A.* **2012**, 109 (31), 12568–12573.
- (14) Schwarz, U. S.; Gardel, M. L. *J. Cell Sci.* **2012**, 125 (Pt 13), 3051–3060.
- (15) Spudich, J. A. *Nat. Rev. Mol. Cell Biol.* **2001**, 2 (5), 387–392.

- (16) Lochter, a; Bissell, M. J. *Semin. Cancer Biol.* **1995**, *6*, 165–173.
- (17) Engler, A. J.; Sen, S.; Sweeney, H. L.; Discher, D. E. *Cell* **2006**, *126* (4), 677–689.
- (18) Chen, C. S.; Tan, J.; Tien, J. *Annu. Rev. Biomed. Eng.* **2004**, *6*, 275–302.
- (19) Plotnikov, S. V.; Pasapera, A. M.; Sabass, B.; Waterman, C. M. *Cell* **2012**, *151* (7), 1513–1527.
- (20) CURTIS, A. S. *J. Cell Biol.* **1964**, *20*, 199–215.
- (21) Izzard, C. S.; Lochner, L. R. *J. Cell Sci.* **1976**, *21* (1), 129–159.
- (22) Abercrombie, M.; Heaysman, J. E. M.; Pegrum, S. M. *Exp. Cell Res.* **1970**, *62* (2–3), 389–398.
- (23) Hynes, R. O. *Cell*. 2002, pp 673–687.
- (24) Giancotti, F. G. *Science* (80-.). **1999**, *285* (5430), 1028–1033.
- (25) Ludueña, M. A.; Wessells, N. K. *Dev. Biol.* **1973**, *30* (2), 427–440.
- (26) Kolega, J. *J. Cell Biol.* **1986**, *102* (4), 1400–1411.
- (27) LEVY, J. A.; DIAMENT, A. J.; SARAIVA, S. *Arq. Neuropsiquiatr.* **1960**, *18*, 259–264.
- (28) Hu, K.; Ji, L.; Applegate, K. T.; Danuser, G.; Waterman-Storer, C. M. *Science* (80-.). **2007**, *315* (5808), 111–115.
- (29) Aratyn-Schaus, Y.; Gardel, M. L. *Curr. Biol.* **2010**, *20* (13), 1143–1153.
- (30) del Rio, A.; Perez-Jimenez, R.; Liu, R.; Roca-Cusachs, P.; Fernandez, J. M.; Sheetz, M. P. *Science* **2009**, *323* (5914), 638–641.
- (31) Haque, F.; Lloyd, D. J.; Smallwood, D. T.; Dent, C. L.; Shanahan, C. M.; Fry, A. M.; Trembath, R. C.; Shackleton, S. *Mol. Cell. Biol.* **2006**, *26* (10), 3738–3751.
- (32) Jaalouk, D. E.; Lammerding, J. *Nat. Rev. Mol. Cell Biol.* **2009**, *10* (1), 63–73.

- (33) Tan, J. C. H. *Br. J. Ophthalmol.* **2006**, *90* (3), 383–388.
- (34) Johnstone, M. A. *J. Glaucoma* **2004**, *13* (5), 421–438.
- (35) Heydemann, A.; McNally, E. M. *Trends in Cardiovascular Medicine*. 2007, pp 55–59.
- (36) Zhong, C.; Chrzanowska-Wodnicka, M.; Brown, J.; Shaub, A.; Belkin, A. M.; Burrige, K. *J. Cell Biol.* **1998**, *141* (2), 539–551.
- (37) Wierzbicka-Patynowski, I.; Schwarzbauer, J. E. *J. Cell Sci.* **2003**, *116* (Pt 16), 3269–3276.
- (38) Aota, S.; Nomizu, M.; Yamada, K. M. *J. Biol. Chem.* **1994**, *269* (40), 24756–24761.
- (39) Kauf, A. C. W.; Hough, S. M.; Bowditch, R. D. *Biochemistry* **2001**, *40* (31), 9159–9166.
- (40) Redick, S. D. *J. Cell Biol.* **2000**, *149* (2), 521–527.
- (41) Li, F.; Redick, S. D.; Erickson, H. P.; Moy, V. T. *Biophys. J.* **2003**, *84* (2), 1252–1262.
- (42) le Duc, Q.; Shi, Q.; Blonk, I.; Sonnenberg, A.; Wang, N.; Leckband, D.; de Rooij, J. *J. Cell Biol.* **2010**, *189* (7), 1107–1115.
- (43) Le Duc, Q.; Shi, Q.; Blonk, I.; Sonnenberg, A.; Wang, N.; Leckband, D.; De Rooij, J. *J. Cell Biol.* **2010**, *189* (7), 1107–1115.
- (44) Harris, A.; Wild, P.; Stopak, D. *Science* (80-.). **1980**, *208* (4440), 177–179.
- (45) Oliver, T.; Jacobson, K.; Dembo, M. *Cell Motil. Cytoskeleton* **1995**, *31* (3), 225–240.
- (46) Chen, C. S.; Mrksich, M.; Huang, S.; Whitesides, G. M.; Ingber, D. E. *Science*

- (80-). **1997**, 276 (5317), 1425–1428.
- (47) Wang, N.; Butler, J.; Ingber, D. *Science* (80-). **1993**, 260 (5111), 1124–1127.
- (48) Rief, M. *Science* (80-). **1997**, 276 (5315), 1109–1112.
- (49) Merkel, R.; Nassoy, P.; Leung, A.; Ritchie, K.; Evans, E. *Nature* **1999**, 397 (6714), 50–53.
- (50) Ghassemi, S.; Meacci, G.; Liu, S.; Gondarenko, A. A.; Mathur, A.; Roca-Cusachs, P.; Sheetz, M. P.; Hone, J. *Proc. Natl. Acad. Sci.* **2012**, 109 (14), 5328–5333.
- (51) Galbraith, C. G.; Sheetz, M. P. *Proc. Natl. Acad. Sci.* **1997**, 94 (17), 9114–9118.
- (52) Singhvi, R.; Kumar, A.; Lopez, G. P.; Stephanopoulos, G. N.; Wang, D. I.; Whitesides, G. M.; Ingber, D. E. *Science* **1994**, 264 (5159), 696–698.
- (53) Choquet, D.; Felsenfeld, D. P.; Sheetz, M. P. *Cell* **1997**, 88 (1), 39–48.
- (54) Grashoff, C.; Hoffman, B. D.; Brenner, M. D.; Zhou, R.; Parsons, M.; Yang, M. T.; McLean, M. a; Sligar, S. G.; Chen, C. S.; Ha, T.; Schwartz, M. a. *Nature* **2010**, 466 (7303), 263–266.
- (55) Liu, Y.; Yehl, K.; Narui, Y.; Salaita, K. *J. Am. Chem. Soc.* **2013**, 135 (14), 5320–5323.
- (56) Meng, F.; Suchyna, T. M.; Sachs, F. *FEBS J.* **2008**, 275 (12), 3072–3087.
- (57) Stabley, D. R.; Jurchenko, C.; Marshall, S. S.; Salaita, K. S. *Nat. Methods* **2012**, 9 (1), 64–67.
- (58) Wang, X.; Ha, T. *Science* **2013**, 340 (6135), 991–994.
- (59) Zhang, Y.; Ge, C.; Zhu, C.; Salaita, K. *Nat. Commun.* **2014**, 5, 5167.
- (60) Hoffman, B. D.; Grashoff, C.; Schwartz, M. a. *Nature* **2011**, 475 (7356), 316–323.
- (61) Borghi, N.; Sorokina, M.; Shcherbakova, O. G.; Weis, W. I.; Pruitt, B. L.; Nelson,

- W. J.; Dunn, A. R. *Proc. Natl. Acad. Sci. U. S. A.* **2012**, *109* (31), 12568–12573.
- (62) Cai, D.; Chen, S. C.; Prasad, M.; He, L.; Wang, X.; Choesmel-Cadamuro, V.; Sawyer, J. K.; Danuser, G.; Montell, D. J. *Cell* **2014**, *157* (5), 1146–1159.
- (63) Conway, D. E.; Breckenridge, M. T.; Hinde, E.; Gratton, E.; Chen, C. S.; Schwartz, M. a. *Curr. Biol.* **2013**, *23* (11), 1024–1030.
- (64) Jurchenko, C.; Chang, Y.; Narui, Y.; Zhang, Y.; Salaita, K. S. *Biophys. J.* **2014**, *106* (7), 1436–1446.
- (65) Ma, V. P. Y.; Liu, Y.; Blanchfield, L.; Su, H.; Evavold, B. D.; Salaita, K. *Nano Lett.* **2016**, *16* (7), 4552–4559.
- (66) Morimatsu, M.; Mekhdjian, A. H.; Adhikari, A. S.; Dunn, A. R. *Nano Lett.* **2013**, *13* (9), 3985–3989.
- (67) Jurchenko, C.; Salaita, K. S. *Mol. Cell. Biol.* **2015**, *35* (15), 2570–2582.
- (68) Lakowicz, J. R. *Principles of fluorescence spectroscopy*; 2006.
- (69) Chapman-Smith, a; Cronan, J. E. *J. Nutr.* **1999**, *129* (Cronan 1990), 477S–484S.
- (70) Förster, T. *Ann Phys.* **1948**, *2*, 55–75.
- (71) Marko, J. F.; Siggia, E. D. *Macromolecules* **1995**, *28* (26), 8759–8770.
- (72) Bustamante, C.; Marko, J. F.; Siggia, E. D.; Smith, S. *Science* **1994**, *265* (1994), 1599–1600.
- (73) Wieland, T.; Bokelmann, E.; Bauer, L.; Lang, H. U.; Lau, H. *Justus Liebigs Ann. Chem.* **1953**, *583* (1), 129–149.
- (74) Dawson, P. E.; Muir, T. W.; Clark-Lewis, I.; Kent, S. B. *Science* **1994**, *266*, 776–779.
- (75) Liu, C. F.; Rao, C.; Tam, J. P. *J. Am. Chem. Soc.* **1996**, *118* (2), 307–312.

- (76) Shin, Y.; Winans, K. A.; Backes, B. J.; Kent, S. B. H.; Ellman, J. A.; Bertozzi, C. *R. J. Am. Chem. Soc.* **1999**, *121* (50), 11684–11689.
- (77) Xiao, J.; Chen, R.; Pawlicki, M. A.; Tolbert, T. J. *J. Am. Chem. Soc.* **2009**, *131* (38), 13616–13618.
- (78) Jurchenko, C.; Chang, Y.; Narui, Y.; Zhang, Y.; Salaita, K. S. *Biophys. J.* **2014**, *106* (7), 1436–1446.
- (79) Ghauharali, R. I.; Brakenhoff, G. J. *J. Microsc.* **2000**, *198* (2), 88–100.
- (80) Shi, H.; Liu, J.; Geng, J.; Tang, B. Z.; Liu, B. *J. Am. Chem. Soc.* **2012**, *134* (23), 9569–9572.
- (81) Chang, Y.; Liu, zheng; Zhang, Y.; Galior, K.; Yang, J.; Salaita, K. *J. Am. Chem. Soc.* **2016**, jacs.5b11602.
- (82) General, I. J.; Dragomirova, R.; Meirovitch, H. *J. Phys. Chem. B* **2012**, *116* (23), 6628–6636.
- (83) Yuan, C.; Chen, A.; Kolb, P.; Moy, V. T. *Biochemistry* **2000**, *39* (33), 10219–10223.
- (84) Smith, S.; Finzi, L.; Bustamante, C. *Science* (80-.). **1992**, *258* (5085), 1122–1126.
- (85) Hohng, S.; Zhou, R.; Nahas, M. K.; Yu, J.; Schulten, K.; Lilley, D. M. J.; Ha, T. *Science* **2007**, *318* (5848), 279–283.
- (86) Yu, C.; Law, J. B. K.; Suryana, M.; Low, H. Y.; Sheetz, M. P. *Proc. Natl. Acad. Sci. U. S. A.* **2011**, *108* (51), 20585–20590.
- (87) Pincet, F.; Husson, J. *Biophys. J.* **2005**, *89* (6), 4374–4381.
- (88) Choi, Y.; Kim, E.; Lee, Y.; Han, M. H.; Kang, I. C. *Proteomics* **2010**, *10* (1), 72–80.

- (89) Lehenkari, P. P.; Horton, M. a. *Biochem. Biophys. Res. Commun.* **1999**, 259 (3), 645–650.
- (90) Neuert, G.; Albrecht, C. H.; Gaub, H. E. *Biophys. J.* **2007**, 93 (4), 1215–1223.
- (91) Galush, W. J.; Nye, J. A.; Groves, J. T. *Biophys. J.* **2008**, 95 (5), 2512–2519.
- (92) Friedland, J. C.; Lee, M. H.; Boettiger, D. *Science* **2009**, 323 (5914), 642–644.
- (93) Kong, F.; García, A. J.; Mould, A. P.; Humphries, M. J.; Zhu, C. *J. Cell Biol.* **2009**, 185 (7), 1275–1284.
- (94) Kong, F.; Li, Z.; Parks, W. M.; Dumbauld, D. W.; García, A. J.; Mould, A. P.; Humphries, M. J.; Zhu, C. *Mol. Cell* **2013**, 49 (6), 1060–1068.
- (95) Schoen, I.; Pruitt, B. L.; Vogel, V. *Annu. Rev. Mater. Res.* **2013**, 43 (1), 589–618.
- (96) de Gennes, P. G. *Macromolecules* **1980**, 13 (19), 1069–1075.
- (97) Bell, G. I. *Science* **1978**, 200 (4342), 618–627.
- (98) Schwarz, U. S.; Balaban, N. Q.; Riveline, D.; Bershadsky, A.; Geiger, B.; Safran, S. A. *Biophys. J.* **2002**, 83, 1380–1394.
- (99) Klim, J. R.; Fowler, A. J.; Courtney, A. H.; Wrighton, P. J.; Sheridan, R. T. C.; Wong, M. L.; Kiessling, L. L. *ACS Chem. Biol.* **2012**, 7 (3), 518–525.
- (100) Song, L.; Hennink, E. J.; Young, I. T.; Tanke, H. J. *Biophys. J.* **1995**, 68 (6), 2588–2600.
- (101) Rajagopalan, P.; Marganski, W. a; Brown, X. Q.; Wong, J. Y. *Biophys. J.* **2004**, 87 (4), 2818–2827.
- (102) Ung, P.; Winkler; Winkler, D. A. *J. Med. Chem.* **2011**, 54 (5), 1–5.
- (103) Pfaff, M.; Tangemann, K.; Müller, B.; Gurrath, M.; Müller, G.; Kessler, H.; Timpl, R.; Engel, J. *J. Biol. Chem.* **1994**, 269 (32), 20233–20238.

- (104) Craig, J. a.; Rexeisen, E. L.; Mardilovich, A.; Shroff, K.; Kokkoli, E. *Langmuir* **2008**, *24* (18), 10282–10292.
- (105) Noë, V.; Willems, J.; Vandekerckhove, J.; Roy, F. Van; Bruyneel, E.; Mareel, M. *J. Cell Sci.* **1999**, *112*, 127–135.
- (106) Andrade, J. D.; Hlady, V.; Jeon, S.-I. In *Hydrophilic Polymers*; 1996; Vol. 248, pp 51–59.
- (107) Ratner, B. D.; Bryant, S. J. *Annu Rev Biomed Eng* **2004**, *6*, 41–75.
- (108) Horbett Thomas, A.; Brash John, L.; Horbett, T. A.; Brash, J. L. In *Proteins at Interfaces*; 1987; Vol. 343, pp 1–33.
- (109) Andrade, J. D.; Hlady, V. *Adv. Polym. Sci.* **1986**, *79*, 1–63.
- (110) Bronzino, E. J. D.; Park, J. B.; Kim, Y. K. *Biomed. Eng. (NY)*. **2000**.
- (111) Jeyachandran, Y. L.; Mielczarski, J. A.; Mielczarski, E.; Rai, B. *J. Colloid Interface Sci.* **2010**, *341* (1), 136–142.
- (112) Blawas, A. S.; Reichert, W. M. *Biomaterials*. 1998, pp 595–609.
- (113) Lee, J.; Joon Kim, M.; Lee, H. H. *Langmuir* **2006**, *22* (5), 2090–2095.
- (114) Visnapuu, M.-L.; Duzdevich, D.; Greene, E. C. *Mol. Biosyst.* **2008**, *4* (5), 394–403.
- (115) Estephan, Z. G. **2012**.
- (116) West, S. L.; Salvage, J. P.; Lobb, E. J.; Armes, S. P.; Billingham, N. C.; Lewis, A. L.; Hanlon, G. W.; Lloyd, A. W. *Biomaterials* **2004**, *25* (7–8), 1195–1204.
- (117) Holmlin, R. E.; Chen, X.; Chapman, R. G.; Takayama, S.; Whitesides, G. M. *Langmuir* **2001**, *17* (13), 2841–2850.
- (118) Matsuura, K.; Ohno, K.; Kagaya, S.; Kitano, H. *Macromol. Chem. Phys.* **2007**, *208*

- (8), 862–873.
- (119) Jia, G.; Cao, Z.; Xue, H.; Xu, Y.; Jiang, S. *Langmuir* **2009**, *25* (5), 3196–3199.
- (120) Backmann, N.; Kappeler, N.; Braun, T.; Huber, F.; Lang, H.-P.; Gerber, C.; Lim, R. Y. H. *Beilstein J. Nanotechnol.* **2010**, *1*, 3–13.
- (121) Streeter, H. B.; Rees, D. A. **1987**, *105* (July), 507–515.
- (122) Chiu, C.-S.; Jensen, K.; Sokolova, I.; Wang, D.; Li, M.; Deshpande, P.; Davidson, N.; Mody, I.; Quick, M. W.; Quake, S. R.; Lester, H. a. *J. Neurosci.* **2002**, *22* (23), 10251–10266.
- (123) Yang, T.; Baryshnikova, O. K.; Mao, H.; Holden, M. A.; Cremer, P. S. *J. Am. Chem. Soc.* **2003**, *125* (16), 4779–4784.
- (124) Sackmann, E. *Science* (80-.). **2007**, *271* (5245), 43–48.
- (125) Zwier, J. M.; Van Rooij, G. J.; Hofstraat, J. W.; Brakenhoff, G. J. *J. Microsc.* **2004**, *216* (1), 15–24.
- (126) Wakatsuki, T.; Schwab, B.; Thompson, N. C.; Elson, E. L. *J. Cell Sci.* **2001**, *114* (Pt 5), 1025–1036.
- (127) Dunn, K. W.; Kamocka, M. M.; McDonald, J. H. *Am. J. Physiol. Cell Physiol.* **2011**, *300* (4), C723–C742.
- (128) Oesterhelt, F.; Rief, M.; Gaub, H. E. *New J. Phys.* **1999**, *1*, 1–11.
- (129) Kienberger, F.; Kienberger, F.; Pastushenko, V. P.; Pastushenko, V. P.; Kada, G.; Kada, G.; Gruber, H. J.; Gruber, H. J.; Riener, C.; Riener, C.; Schindler, H.; Schindler, H.; Hinterdorfer, P.; Hinterdorfer, P. *Single Mol.* **2000**, *1* (2), 123–128.
- (130) *Introduction to Fluorescence Sensing*; Demchenko, A. P., Ed.; Springer Netherlands: Dordrecht, 2009.

- (131) Moore, S. W.; Roca-Cusachs, P.; Sheetz, M. P. *Dev. Cell* **2010**, *19* (2), 194–206.
- (132) Bouchiat, C.; Wang, M. D.; Allemand, J.; Strick, T.; Block, S. M.; Croquette, V. *Biophys. J.* **1999**, *76* (1), 409–413.
- (133) Petrie, T. a; Capadona, J. R.; Reyes, C. D.; García, A. J. *Biomaterials* **2006**, *27* (31), 5459–5470.
- (134) Feng, Y.; Mrksich, M. *Biochemistry* **2004**, *43* (50), 15811–15821.
- (135) Mano, J. F. *Advanced Engineering Materials*. 2008, pp 515–527.
- (136) Phillips, D. J.; Gibson, M. I. *Polym. Chem.* **2015**, *6* (7), 1033–1043.
- (137) Stuart, M. A. C.; Huck, W. T. S.; Genzer, J.; Müller, M.; Ober, C.; Stamm, M.; Sukhorukov, G. B.; Szleifer, I.; Tsukruk, V. V.; Urban, M.; Winnik, F.; Zauscher, S.; Luzinov, I.; Minko, S. *Nat. Mater.* **2010**, *9* (2), 101–113.
- (138) Liu, F.; Urban, M. W. *Prog. Polym. Sci.* **2010**, *35* (1–2), 3–23.
- (139) Yan, X.; Wang, F.; Zheng, B.; Huang, F. *Chem. Soc. Rev.* **2012**, *41* (18), 6042.
- (140) Jhaveri, S. J.; Hynd, M. R.; Dowell-Mesfin, N.; Turner, J. N.; Shain, W.; Ober, C. K. *Biomacromolecules* **2009**, *10* (1), 174–183.
- (141) Hoffman, A. S. *J. Control. Release* **2008**, *132* (3), 153–163.
- (142) Lim, H. L.; Hwang, Y.; Kar, M.; Varghese, S. *Biomater. Sci.* **2014**, *2* (5), 603.
- (143) Anker, J. N.; Hall, W. P.; Lyandres, O.; Shah, N. C.; Zhao, J.; Van Duyne, R. P. *Nat. Mater.* **2008**, *7* (6), 442–453.
- (144) Khokhlov, A. R. *Conformation-dependent design of sequences in copolymers*; 2006.
- (145) Forster, S. *Colloid Chem. 1* **2003**, *226*, 1–28.
- (146) Arotçaréna, M.; Heise, B.; Ishaya, S.; Laschewsky, A. *J. Am. Chem. Soc.* **2002**,

- 124 (14), 3787–3793.
- (147) Tokareva, I.; Minko, S.; Fendler, J. H.; Hutter, E. *J. Am. Chem. Soc.* **2004**, *126* (49), 15950–15951.
- (148) Burg, T. P.; Godin, M.; Knudsen, S. M.; Shen, W.; Carlson, G.; Foster, J. S.; Babcock, K.; Manalis, S. R. *Nature* **2007**, *446* (7139), 1066–1069.
- (149) Tu, Y.; Peng, F.; Sui, X.; Men, Y.; White, P. B.; van Hest, J. C. M.; Wilson, D. A. *Nat. Chem.* **2016**, *9* (5), 480–486.
- (150) MacKenzie, K. J.; Francis, M. B. *J. Am. Chem. Soc.* **2013**, *135* (1), 293–300.
- (151) Hoshino, K.; Yamasaki, H.; Chida, C.; Morohashi, S.; Sasakura, T.; Taniguchi, M.; Fujii, M. *J. Chem. Eng. Japan* **1997**, *30* (1), 30–37.
- (152) Lu, Y.; Mei, Y.; Ballauff, M.; Drechsler, M. *J. Phys. Chem. B* **2006**, *110* (9), 3930–3937.
- (153) Lu, Y.; Proch, S.; Schrunner, M.; Drechsler, M.; Kempe, R.; Ballauff, M. *J. Mater. Chem.* **2009**, *19* (23), 3955.
- (154) Blankschien, M. D.; Pretzer, L. a.; Huschka, R.; Halas, N. J.; Gonzalez, R.; Wong, M. S. *ACS Nano* **2013**, *7* (1), 654–663.
- (155) Kim, Y. S.; Liu, M.; Ishida, Y.; Ebina, Y.; Osada, M.; Sasaki, T.; Hikima, T.; Takata, M.; Aida, T. *Nat. Mater.* **2015**, *14* (10), 1002–1007.
- (156) Cowie, J. M. G.; Arrighi, V. *Polym. Chem. Phys. Mod. Mater.* **2007**, 463.
- (157) Atkins, P.; Paula, J. De. *Atkins' physical chemistry*; 2009.
- (158) Fujishige, S.; Kubota, K.; Ando, I. *J. Phys. Chem.* **1989**, *93* (8), 3311–3313.
- (159) Roy, D.; Brooks, W. L. A.; Sumerlin, B. S. *Chem. Soc. Rev.* **2013**, *42* (17), 7214.
- (160) Scarpa, J. S.; Mueller, D. D.; Klotz, I. M. *J. Am. Chem. Soc.* **1967**, *89* (24), 6024–

6030.

- (161) Bankar, S. B.; Bule, M. V.; Singhal, R. S.; Ananthanarayan, L. *Biotechnology Advances*. 2009, pp 489–501.
- (162) Singh, J.; Verma, N. *Adv. Appl. Sci. Res.* **2013**, 4 (3), 250–257.
- (163) Wilson, R.; Turner, A. P. F. *Biosensors and Bioelectronics*. 1992, pp 165–185.
- (164) Liu, Z.; Liu, Y.; Chang, Y.; Seyf, H. R.; Henry, A.; Mattheyses, A. L.; Yehl, K.; Zhang, Y.; Huang, Z.; Salaita, K. *Nat. Methods* **2015**, 13 (december), 1–8.
- (165) Fors, B. P.; Poelma, J. E.; Menyo, M. S.; Robb, M. J.; Spokoyny, D. M.; Kramer, J. W.; Waite, J. H.; Hawker, C. J. *J. Am. Chem. Soc.* **2013**, 135 (38), 14106–14109.
- (166) Rechenmacher, F.; Neubauer, S.; Polleux, J.; Mas-Moruno, C.; De Simone, M.; Cavalcanti-Adam, E. A.; Spatz, J. P.; Fässler, R.; Kessler, H. *Angew. Chemie - Int. Ed.* **2013**, 52, 1572–1575.
- (167) Rahmouni, S.; Lindner, A.; Rechenmacher, F.; Neubauer, S.; Sobahi, T. R. A.; Kessler, H.; Cavalcanti-Adam, E. A.; Spatz, J. P. *Adv. Mater.* **2013**, 25, 5869–5874.
- (168) Laughlin, S. T.; Baskin, J. M.; Amacher, S. L.; Bertozzi, C. R. *Science* (80-.). **2008**, 320 (5876), 664–667.

Chapter 3: Thermo-responsive enzymatic nanoreactor to regulate reaction rate

3.1. Motivation and designing the thermo-regulated enzymatic nanoreactor

3.1.1 Introduction

Stimulus-responsive polymers are a class of polymers which undergo drastic changes in properties (usually molecular conformational changes) upon external stimulation. This type of material has garnered a lot of attention in a variety of research and applications due to their versatility and facile controllability. The stimuli in the environment include temperature, pH, light, ionic strength, mechanical force, redox potential, concentration of certain chemicals, magnetic field, etc.^{135–139} Among these stimuli, temperature has remained a popular choice for a broad-range of biomedical studies ranging from drug delivery to surface coating and tissue engineering.^{140–143} For these type of materials, the change in conformations with temperature is based on the property of changing solubility in aqueous solutions. The changes are either the precipitation of a polymer solution at a lower critical solution temperature (LCST) or the dissolution of a polymer precipitate at an upper critical solution temperature (UCST). On a molecular level, a reversible conformational transition occurs from a random coil state (hydrated, soluble) to a compact globule state (dehydrated, insoluble) when transitioning at the LCST.^{144,145} LCSTs have been demonstrated to commonly exist in (co)polymers, and many have measurable transitions temperatures. On the other hand, polymers that have a UCST in water are less common, and they are usually hydrophobic polymers that have strong attraction between polymer chains.¹⁴⁶ This interaction is broken by water molecule above UCSTs. Such observed “smart” temperature-dependent behavior of these polymers have inspired the research and development of biosensors,^{147,148} actuators,¹⁴⁹ biocatalysts^{150,151} etc.

Currently, the control of biochemical pathways is largely achieved by the addition of chemicals or constituents that are difficult to remove once added. Biomaterials can be designed to be responsive to external or internal stimuli and provide an easy way of controlling a biochemical reaction in a less invasive manner. The application of smart polymers in the biocatalyst field is less commonly explored. However, the stimulus-responsive regulatory mechanism enables the external control over the efficiency of catalysts, which makes them a “smart” tool and has opened new directions in chemical and biochemical catalysis. The regulation of catalyst reactivation could be based on exposing or hiding the active site of enzymes or catalytic surfaces on metal nanoparticles or changing the polarity/hydrophobicity of the polymer, and thus regulating the solubility of the substrates. For example, Lu et al.^{152,153} described a tunable catalyst that was made by embedding a number of 10-nm metal nanoparticles inside a thermo-responsive polymer shell of a much larger polystyrene particle. Swelling and shrinking of the shell regulated by external temperature change were used to alternatively expose and hide the

catalytic nanoparticles embedded in the colloids, and therefore modulating the catalytic activity. (Figure 3.1)

The shell was composed of cross-linked poly N-isopropylacrylamide (PNIPAM) polymer and undergoes a volume transition at around 30°C. The microgel particles exhibit a weak positive charge due to the cationic initiator. The reduction of 4-nitrophenol to 4-aminophenol by sodium borohydride was chosen to be the model reaction. It was demonstrated that the oxidation activity of the metal nanocomposite can be modulated by the volume transition of microgels. The change of the rate constants k with temperature can be divided into two sections. When the reaction temperature approaches the LCST, the PNIPAM network shrinks with an increase in temperature. The shrinking of the network is followed by a decrease in the diffusion of substrates within the network. This process lowered the rate of the reaction and overcompensated the increase in k by the rise in temperature. Hence, the reaction rate must reach its minimum at the transition

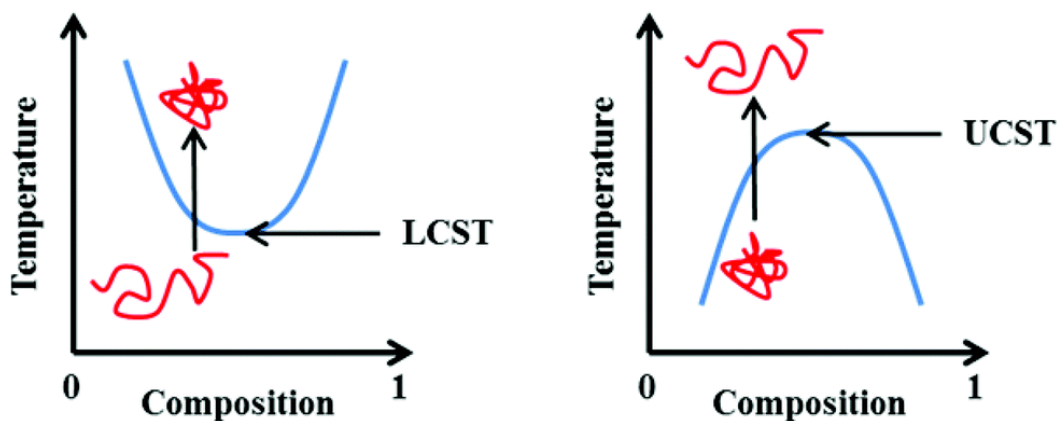


Figure 3.1 Phase transition associated with the LCST (left) and UCST (right). Blue line represents the phase separation boundary at which a cloud point is observed. Adapted from (1) Phillips, D. J.; Gibson, M. I. *Polym. Chem.* 2015, 6 (7), 1033–1043.

temperature. While the density of the network stays constant when the temperature was

increased further, the strong increase in k with temperature dominates, and the reaction rate rises again.

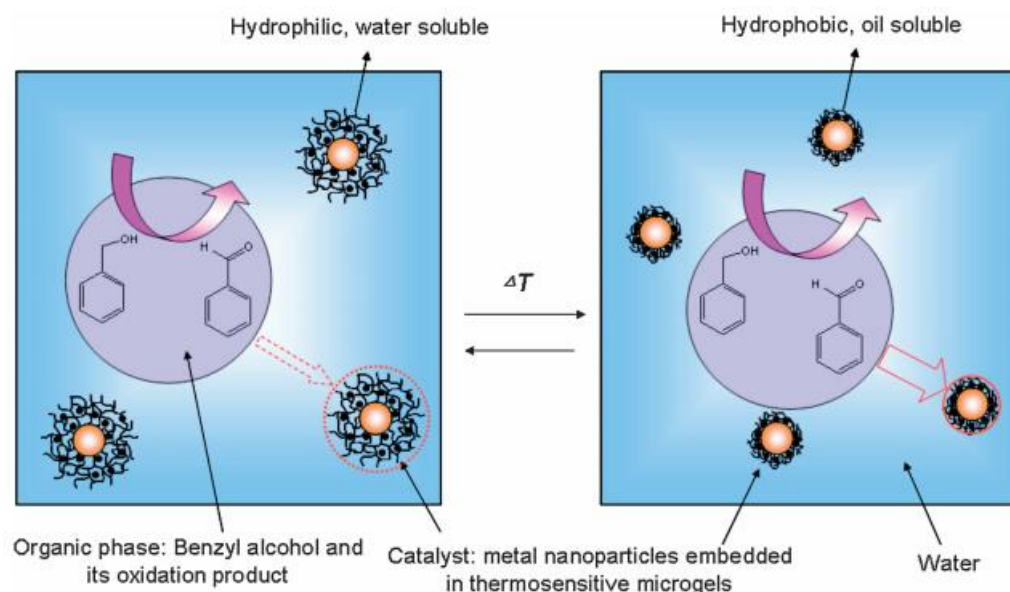
On another note, the reaction oxidation of benzyl alcohol in the presence of metal nanoparticles behaved differently. When the temperature is higher than LCST, the network shrinks and becomes hydrophobic, thus presenting a steric barrier for the substrate molecules to diffuse to the surface of the metal catalysts. However, this process is overcompensated by the increase in hydrophobicity of the hydrogel after LCST, which favors more of the diffusion of hydrophobic substrates. Therefore, the catalytic activity of the metal-microgel is increased by the polarity change of the microgel induced by its LCST transition.

Another example is the work by Tu et al. A temperature-sensitive polymer brush is covalently grown onto a bowl-shaped polymeric vesicles, in which catalytic platinum nanoparticles were entrapped. The narrow opening of the vesicles served as an entrance for the substrate H_2O_2 , as well as an outlet for the O_2 generated during the decomposition of the H_2O_2 catalyzed by Pt particles. This access of the hydrogen peroxide substrate was regulated by the opening and closing of the temperature-responsive valve. When the temperature is higher than the LCST, the valve was closed, which rejects the access of H_2O_2 , thus shutting down the catalyzed reaction. (Figure 3.2)

In the biocatalysis field, the control over enzymatic reaction rate has also been explored using light.¹⁵⁴ Blankschien et al. has demonstrated the application of plasmonic gold nanoparticle to activate enzymatic reactions. The gold particles were conjugated with a thermophilic enzyme *Aeropyrum pernix*, the key enzyme for the decomposition of glucose via the glycolysis pathway, onto Au nanorods. Upon resonant optical

illumination, optical energy was converted to thermal energy and a 60% increase in the reaction rate was achieved with light activation. However, applications of smart polymers in biocatalysis have been limited to using metal catalysts since protein enzymes have intrinsic restrictions, including 1) the conjugation of enzymes to the polymer, 2) the stability of enzymes attached to the polymer, and 3) the characterization of the material with enzymes. However, owing to the limited catalytic ability of metal particles, it is imperative to develop new methods or carriers to apply the precise control of smart polymers on natural enzymes.

a)



b)

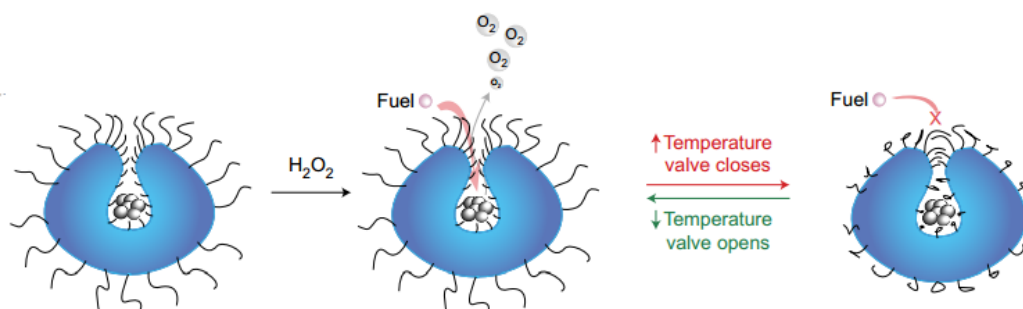


Figure 3.2 (adapted from *J. Mater. Chem.*, 2009,19, 3955-3961 and *Nature Chemistry* 9, 480–486 (2017))

a) Schematic representation of the catalytic reaction in the presence of metal nanoparticles immobilized in thermosensitive microgel at different temperatures. The microgel particles in which the metal catalyst are embedded will take up more of the substrate when shrunken and hydrophobic, causing the catalytic activity of the metal-microgel composites to be increased. b) Schematic representation of stomatocyte nanoreactors with temperature-responsive speed regulation. Access of the substrate hydrogen peroxide is controlled by the opening and closing of the valve. The collapse of pNIPAM brushes takes place, and so the opening of the stomatocytes is covered when the temperature is increased above the LCST of pNIPAM.

3.1.2 *Design and mechanism of the thermo-regulated nanoenzyme reactor*

Recent advances in stimuli responsive materials have made it an attractive candidate in biomedical science. These materials have been playing an increasingly important part in a diverse range of applications, including biocatalysis. However, the research and application of smart polymers in controlling biocatalysis has been limited to using metal catalysts since protein enzymes have their intrinsic challenges when combined with the stimuli-responsive polymers.^{153,155} These challenges, such as the chemistry of conjugation, the characterization of modification, and the stability of enzymes, have impeded the implementation of enzymes in biomaterial catalysis. Currently, the rate of enzymatic reactions is largely regulated by chemically inhibiting the catalytic enzymatic system. Herein, we report an enzymatic nanoreactor carrier system that allows the modulation of the activity of enzymes through a thermodynamic transition that takes place within the carrier system. In this system, enzymes are homogeneously and covalently conjugated to the interior of the pNIPAM hydrogel nano-sized particles. Drastic polymer volume transition produced by environmental stimuli causes the collapse of the polymer. The collapsed polymer creates a hydrophobic layer on top of the enzymes which significantly restricts substrate access to the embedded enzyme molecule and results in the ceasing of enzymatic reaction (Figure 3.3). The LCST behavior of pNIPAM is reversible, hence the collapse of the pNIPAM can be switched on and off by adjusting the temperature, which in turn functions as a regulatory mechanism to control the rate of the enzymatic reaction. The covalent linkage of the enzyme to the hydrogel can largely prevent the dissociation of the enzymes, and thus eliminating the contribution of reactivity of soluble enzymes. This regulation is counterintuitive since the majority of

enzymatic activities are thermophilic. To the best of our knowledge, this represents the first nano-sized, reversible, thermo-controlled enzyme reactor carrier. We envision that

such stimuli-responsive nanosystems with a wide range of adaptability could have potential applications in biomedical science.

3.1.3 Thermoresponsive polymers

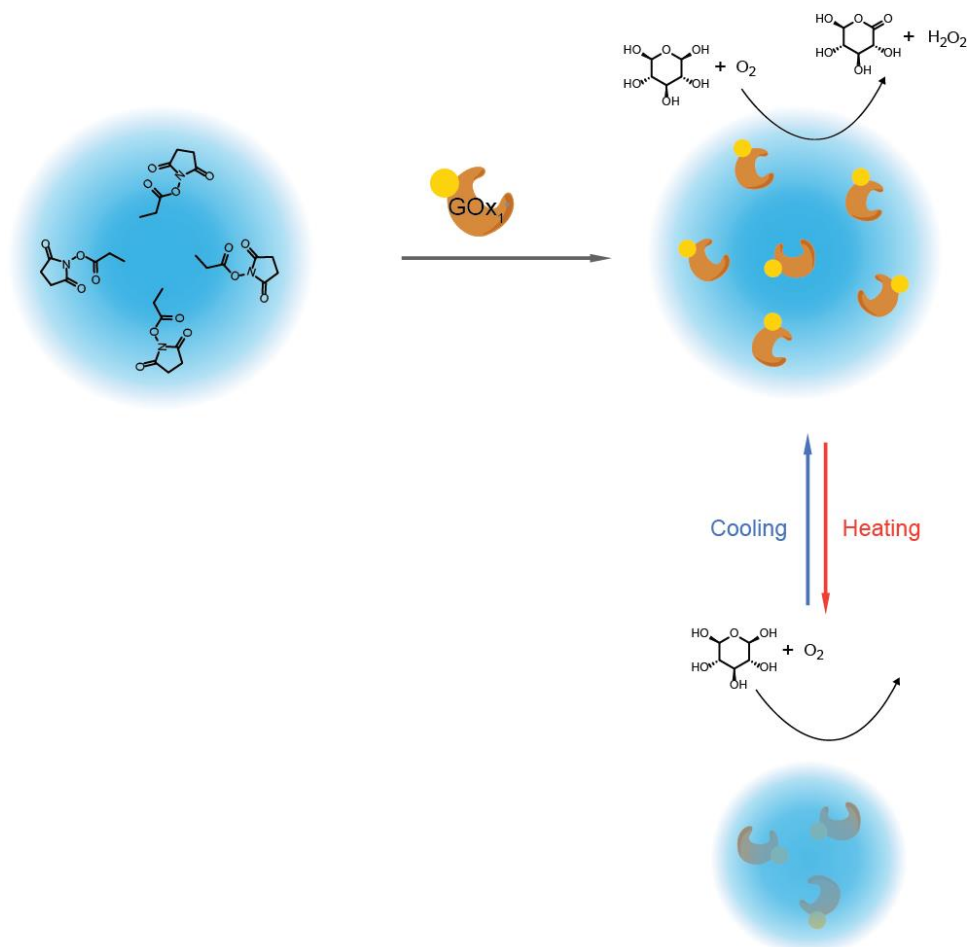


Figure 3.3 Schematic representation of thermo-regulated nanoenzyme reactor

NHS modified thermoresponsive polymer particles reacts with the amine residue on natural enzymes, which creates a covalent linkage between enzymes and hydrogel. By adjusting the external temperature, the hydrogel particles change in volume as well as hydrophobicity, which alternatively switches the accessibility of the substrate to the embedded enzymes. This will result in the modulation of the rate of the enzymatic reaction.

3.1.3.1 LCST

The above-mentioned lower critical solution temperature (LCST) is also often referred as phase or volume transition temperature.^{156,157} Beyond this temperature, the polymer undergoes changes of precipitation of a polymer solution at a lower critical solution temperature (LCST). On a molecular level, a reversible conformational transition occurs from a random coil state (hydrated, soluble) to a compact globule state (dehydrated, insoluble) when transitioning at the LCST. This is due to the hydrogen bonding disruption at higher temperatures (Figure 3.4). In aqueous solution, the polymer forms extensive hydrogen bonding interactions with the surrounding H₂O molecules but limited intra- and intermolecular hydrogen bonding within polymer molecules. When temperature reaches or higher than LCST, hydrogen bonding with H₂O is disrupted, and intra- and intermolecular hydrogen bonding/hydrophobic interactions dominate. This in turn results in a transition in volume and solubility.¹⁵⁸ Notably, it is a common misannotation that the LCST usually is referred to as a single “transition temperature”,

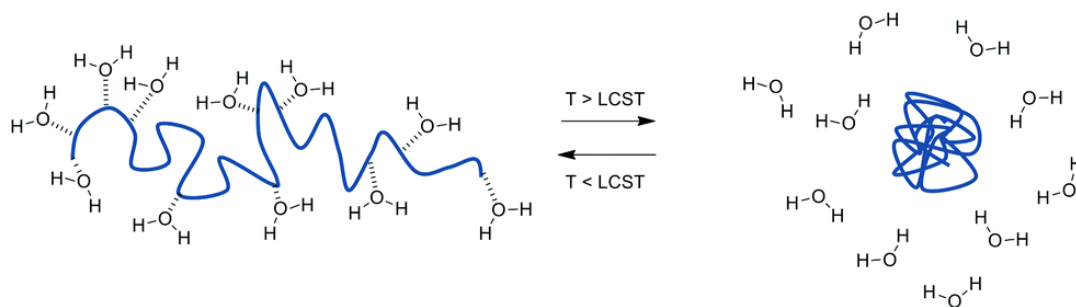


Figure 3.4 Dehydration mechanism of polymer with LCST

Polymers with a lower critical solution temperature (LCST) phase separate upon heating based on a loss of entropically unfavorable “hydrophobic hydration” of hydrophobic segments at the critical temperature.

even though this term is originally derived from the temperature vs. composition phase

diagram. The lowest point of the temperature vs. composition phase diagram is defined as the LCST when it is a concave curve. However, at a fixed composition, the transition temperature of the polymer from soluble to insoluble is more appropriately termed as the “cloud point”. For the purpose of consistency with most of the references, the terms “LCST”, “transition temperature” and “cloud point” will be used interchangeably.

The transition temperature of a polymer in solution is one of the most important parameters to take into consideration under a given set of conditions. LCSTs have been demonstrated to commonly exist in (co)polymers, and many have very sharp transition temperatures due to the dispersity of the polymer. This phase transition behavior of polymer solutions is a critical property related to the development and design of biotech applications. There are two main types of temperature responsiveness in water-UCST and LCST. Polymers with a LCST undergo a phase/volume transition upon heating based on a loss of entropically unfavorable “hydrophobic hydration” of hydrophobic segments at the critical temperature. This temperature can be modified or tuned by adjusting the hydrophilic–hydrophobic balance on a molecular level within the polymer molecule, and this easy adaptability makes it a versatile candidate for a wide range of research.

3.1.3.2 pNIPAM and pNIPMAM

A large number of polymers have been found to have LCST behavior. These polymers include poly(lactam)s, poly(alkoxide)s, poly(N-vinylalkylamide)s, poly(pyrrolidone)s, poly(N-substituted(meth)acrylamide)s, poly(2-alkyl-2-oxazoline)s, and poly(oligo ethylene glycol) methyl ether(meth)acrylates (pOEG(M)A).¹⁵⁹ The most commonly used thermos-responsive polymer is still pNIPAM since it was the earliest reported polymer that has the thermal phase transition behavior (1967, by Scarpa et al).¹⁶⁰ More

importantly, pNIPAM has a sharp phase transition around 32 °C, which is conveniently between room temperature and body temperatures, making it an ideal candidate for biomedical applications. The LCST also could easily be adjusted to near ~37°C (or physiological temperature) through the incorporation of hydrophilic groups such as acrylic acid. Doped co-polymers containing acrylic acid in small concentrations (~3 mol %) will result in a marked shift to higher phase-transition temperature LCST. This LCST behavior of pNIPAM allows for the control of the collapse of the polymer by adjusting the temperature, which produces a hydrophobic layer on the outside of the embedded enzymes. This layer restricts the access of the substrate (hydrogen peroxide) to the interior of the nanomotor. Owing to the lack of substrates, the enzymatic reaction will decelerate or cease.

3.1.3.3 Glucose oxidase and horse radish peroxidase

In this study, the enzyme pair glucose oxidase (GOx) and horseradish peroxidase (HRP) is the model enzyme systems that were conjugated on the pNIPAM hydrogel nanoparticles. Glucose oxidase catalyzes the oxidation of β -D-glucose to gluconic acid by utilizing molecular oxygen as an electron acceptor with simultaneous production of hydrogen peroxide. It is widely used and usually coupled with an HRP reaction that colorimetrically visualizes the product hydrogen peroxide. Hydrogen peroxide reacts with 2',2'-azino-bis(3-ethylbenzothiazoline-6-sulphonic acid (ABTS) in the presence of horse radish peroxidase (HRP) to form a green colored product, ABTS cation radical. The GOx reaches its maximum reactivity of V_{max} and K_m value 17 U/mg and 7.1 mM, respectively, at 25-30°C and pH 5.5-6.0 for the oxidation of D-glucose.¹⁶¹⁻¹⁶³ The stability of HRP and GOx at high temperature makes it an ideal candidate for use in thermo-stimulations. The

enzyme is stable at 50 °C for 1 h without any prior stabilization.¹⁶² On the other hand, HRP also has a high turnover rate of $\sim 400\text{-}600\text{ s}^{-1}$ which allows the rapid formation of product to be monitored. The reaction scheme of GOx and HRP is depicted in Figure 3.5.

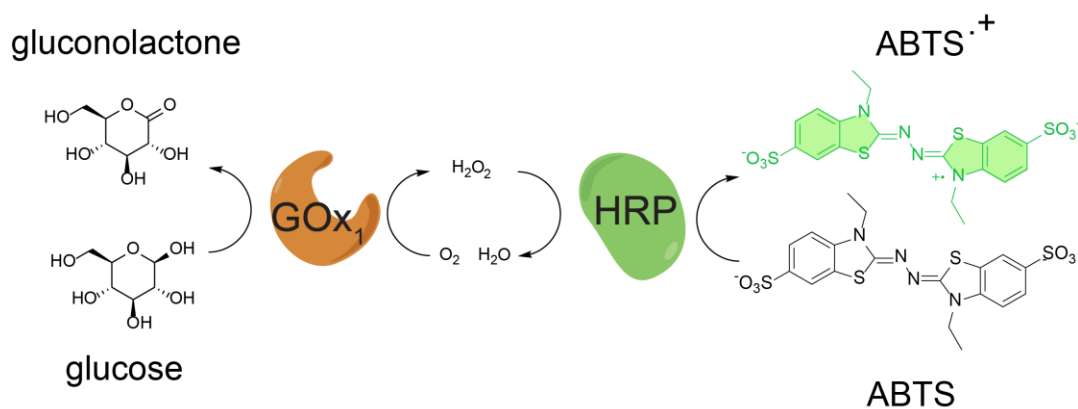


Figure 3.5 Reaction of GOX and HRP in the nanoenzymes

Glucose oxidase catalyzes the oxidation of β -D-glucose to gluconic acid by utilizing molecular oxygen as an electron acceptor with simultaneous production of hydrogen peroxide. The latter product acts as the substrate for HRP, mediating the oxidation of ABTS²⁻ to the colored product, ABTS^{•+}.

3.2. Synthesis of enzymatic nanoreactors

3.2.1 *Synthesis of polyNIPAM and polyNIPMAM nanoparticles with alkyne functional groups*

0.1 g of N-isopropylacrylamide and 0.01 g of the cross-linking agent N,N'-methylenebisacrylamide were dissolved in 15 ml Milli-Q water in a three-neck flask. The mixture was heated to 70 °C under continuous stirring and purged with continuous N₂ flow. After 1 min, pNIPMAM polymerization was initiated with the addition of 80 µl (0.1 M) of the free radical initiator 2,2'-azobis(2-methylpropionamidine) dihydrochloride (AAPH) and the polymerization was allowed to proceed for 2 h at 70 °C. To decorate the particles with the alkyne functional group, 30 µl of propargyl methacrylate monomer dissolved in 1 mL ethanol was added at the 10 min, 30 min, and 100 min time point of

the reaction for the different distributions within the nanoparticle (Figure 3.6). The free-radical polymerization was allowed to proceed for the full 2 h. Note that vigorous stirring (1,200 rpm) was used in every step in the particle synthesis, and no additional detergent was used in the protocol. After the reaction was complete, the sample was allowed to gradually cool to room temperature while stirring. To achieve particle size homogeneity

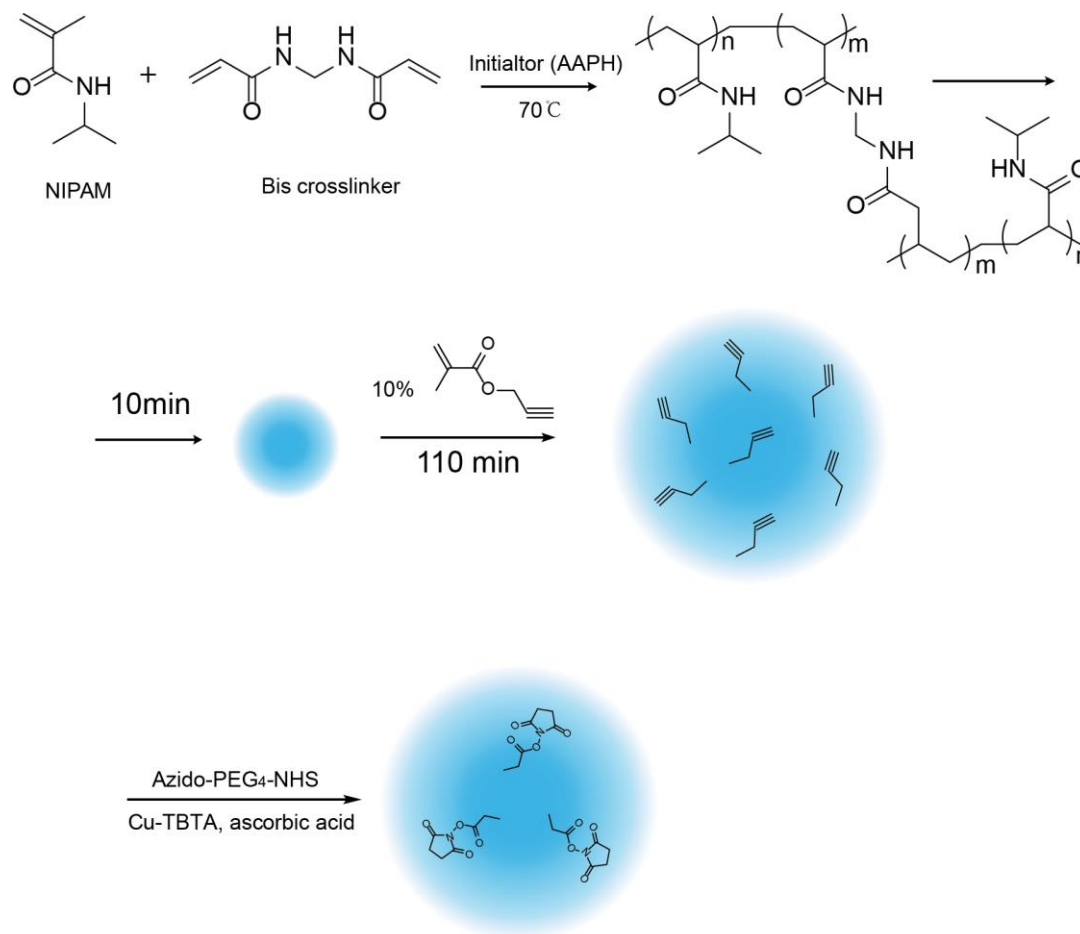


Figure 3.6 The synthesis and modification of pNIPAM nanoparticles

NIPAM monomer and BIS cross linker was mixed in aqueous solution with initiator. propargyl methacrylate monomer was added accordingly at different time point to functionalize the particles. NHS ester was then modified on the particle though click chemistry

and remove smaller size particles, the dispersion was diluted with water and centrifuged, then the supernatant was removed, and the resulting pellet was redispersed in water. The procedure was repeated at least three times. The synthesis of the control pNIPAM particles with N-isopropylmethacrylamide was identical to the protocol described above for the pNIPAM particles.

3.2.2 Modification of nanoparticles with NHS ester functional groups

To further modify particles with the NHS ester functional group, standard Copper assisted click chemistry was carried out with the freshly synthesized pNIPAM nanoparticles. 300 mM NHS PEG4-Azide (Thermo Fisher 26130) was prepared and 2 μL was added into a 50 μL solution containing 5 μL of 10 mM ascorbic acid (Thermo Fisher), 5 μL of 10 mM Cu(II)-TBTA (55% DMSO), and 40 μL of 55% (by volume) DMSO. This reaction was allowed to proceed at room temperature for 1 hour with shaking at 500 rpm.

3.2.3 Characterization of nanoparticles

3.2.3.1 TEM

Negative staining transmission electron microscopy (TEM) was carried out on a Hitachi H-7500 transmission electron microscope at an accelerating voltage of 75 kV. TEM images showed the presence of pNIPAM nanoparticles with monodispersion and diameter \sim 400-500nm (Figure 3.7).

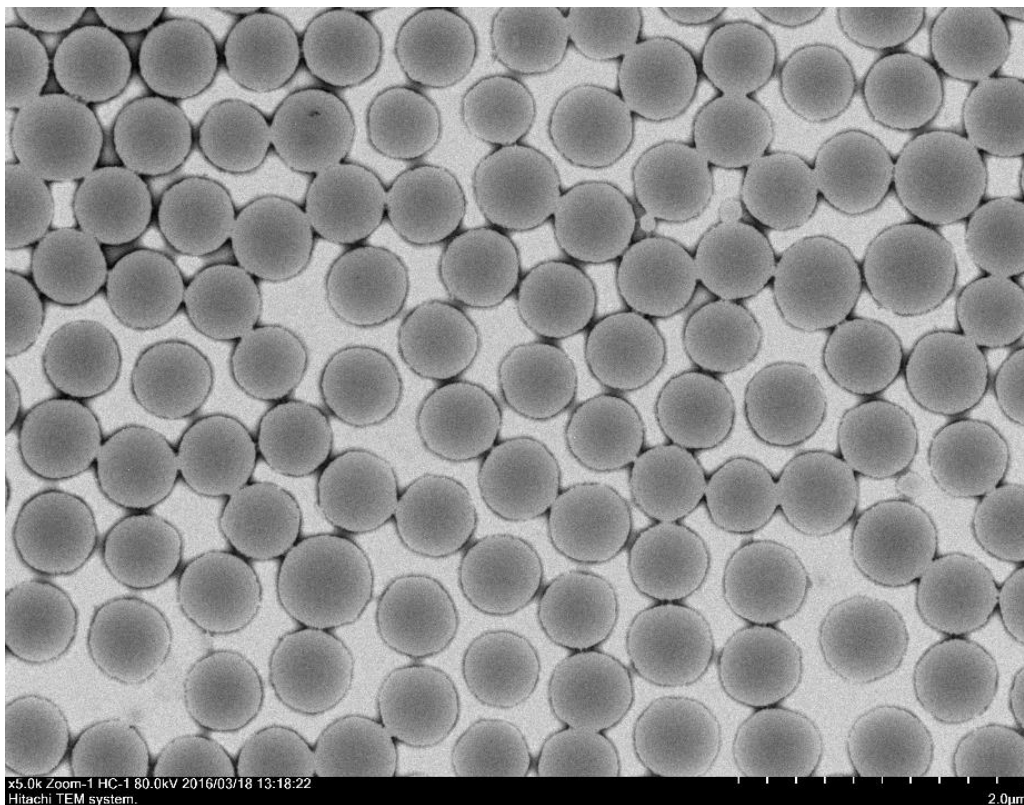


Figure 3.7 TEM image with negative staining of pNIPAM nanoparticles
Scale bar: 2μm

3.2.4 *Conjugation of enzymes on the nanoparticles*

3.2.4.1 Fluorescent modification of enzyme for quantification purpose

To quantify the implantation efficiency of enzymes in the pNIPAM particles, the enzymes were labeled with organic fluorescent dye Alexa 400 NHS ester (Life Technology). General protocol for labeling of proteins with NHS-ester dyes was followed. 1 mg of NHS ester fluorescent dye was dissolved in 50μl DMSO to reach a final concentration of approx. 25nmol/μl). Glucose oxidase was in 1X PBS buffer, pH 7.45. For optimal labeling, the protein concentration should usually be between 5-20 mg/ml. Transfer an appropriate volume of the NHS ester stock prepared in step 1 above

dropwise under stirring to the protein solution. 5 molar excess of dye was added to the protein solution for the dye to protein ratio to be between 1 and 2. The reaction was allowed to proceed at room temperature for 1 h, and then the unreacted dye was separated from labeled protein using BioGel P-4 and gel filtration Eppendorf tubes by centrifugation. UV-Vis was used to characterize the labeled product. The absorption peak at 280nm represents the protein absorbance and the maximum at 488nm represents the dye (Figure 3.8). The ratio of dye to protein was calculated by using the extinction coefficients at the absorption maximums. Note that the 280 nm absorption of the Alexa 488 dye was subtracted during the calculation.

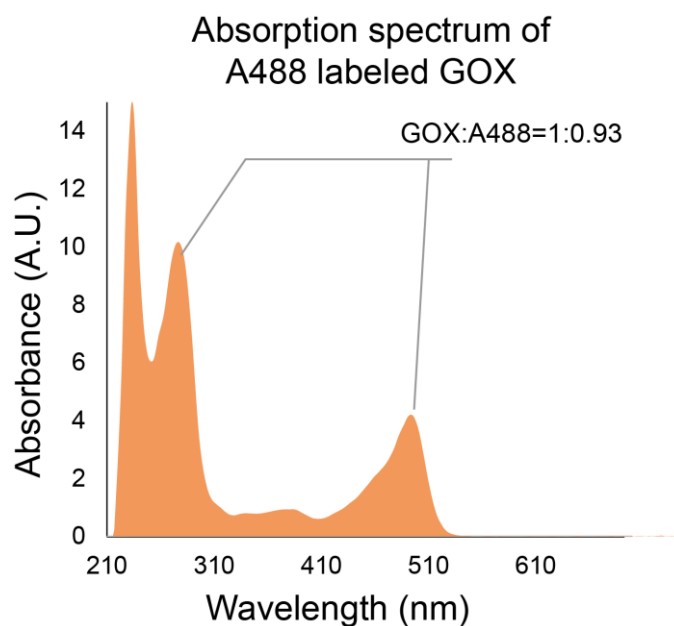


Figure 3.8 Absorption spectrum of Alexa 488 labeled GOx

3.2.4.2 Covalent conjugation of enzymes

To immobilize the enzymes onto the pNIPAM nanoparticles that had already been modified with the NHS ester functional group, the Alexa 488 labeled enzyme glucose oxidase (5mg/ml) was mixed with the NHS-pNIPAM nanoparticles at a one to one ratio. The reaction was allowed to proceed for at least 3 h with shaking at 700-800 rpm (Figure 3.9). To remove the unbounded GOX protein, the reaction mixture was diluted to 1 mL with PBS buffer and centrifuged down. The supernatant was removed and this procedure was repeated 5 times.

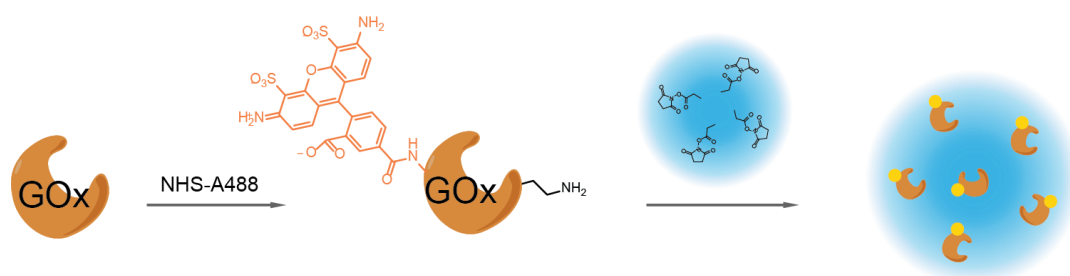


Figure 3.9 Modification with pNIPAM nanoparticles with Alexa 488 labeled GOx

3.2.4.3 Fluorescent image of nanoactuators

To confirm the immobilization of GOx on the pNIPAM nanoparticles, the particles were suspended in PBS, and of which 50 μ l was added in between two sandwiched glass coverslips. After a 30 min incubation, each glass coverslip was rinsed with 30mL of PBS buffer and then imaged using conventional fluorescent microscope in a chamber containing PBS buffer. Particles are clearly visualized in both RICM and Fluorescence channel (FITC). The RICM images and FITC images showed high level of colocalization which indicates the successful immobilization (Figure 3.10).

The microscope was Nikon Eclipse Ti driven by the Elements software package. The microscope features an Evolve electron multiplying charge coupled device (EMCCD;

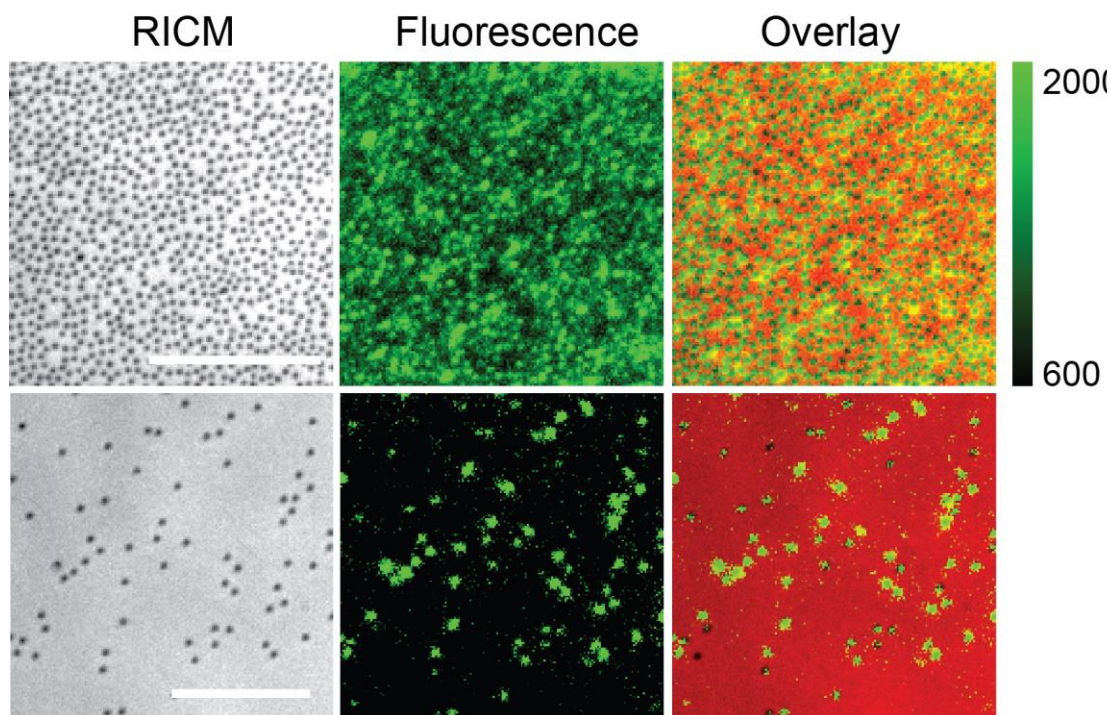


Figure 3.10 The fluorescence image of Alexa 488-GOX on PNIPAM nanoparticles

Scale bar (12 μ m)

Photometrics), an Intensilight epifluorescence source (Nikon), and a CFI Apo 100 \times (numerical aperture (NA) 1.49) objective (Nikon). The experiments used the following Chroma filter cubes: TRITC, FITC, and reflection interference contrast microscopy (RICM)

3.2.4.4 Mapping the distribution of enzymes in the particle using 5nm gold

To map the location of the immobilized GOx enzymes in the pNIPAM nanoparticles, 5nm gold nanoparticles were used since it could be easily visualized using transmission electron microscopy (TEM). First the alkyne functionalized NIPAM particles were

reacted with NHS-PEG4-Azide through standard copper assisted click chemistry procedure (see section 3.3.2). Streptavidin (5mg/mL) in PBS was then added to the particle solution at a one to one volume ratio. The reaction was allowed to proceed at room temperature for at least 3 hours with shaking followed by the centrifuge removal of unreacted streptavidin. The reaction mixture was diluted to 1 mL with PBS buffer and centrifuged down. The supernatant was removed and this procedure was repeated 5 times. Next, 5nm biotinylated gold nanoparticles (Cytodiagnosics) were added to the NIPAM-streptavidin particles. This mixture was incubated for 1 hour at room temperature to allow the binding of biotin to streptavidin. Negative staining transmission electron microscopy (TEM) was carried out on a Hitachi H-7500 transmission electron

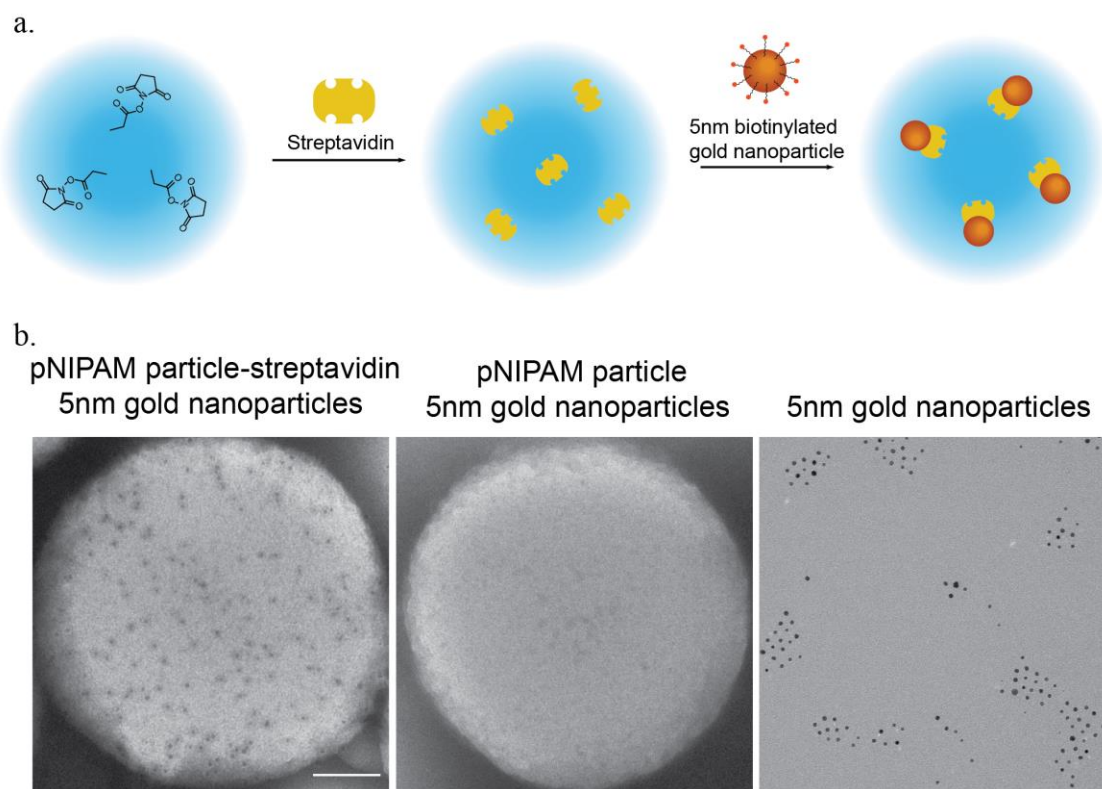


Figure 3.11 The TEM image of streptavidin-bound biotinylated gold nanoparticles on pNIPAM particles

Scale bar (100 nm)

microscope at an accelerating voltage of 75 kV. TEM images showed the presence of 5nm gold nanoparticles within the pNIPAM particle. The distribution of 5nm gold particles is homogenous within the NIPAM hydrogel, which provided a map of the potential GOx locations (Figure 3.11). The dimensions of the gold particle inside the hydrogel matched that of the free unbounded 5nm gold nanoparticles in solution. Note that the reaction incubation of the 5nm gold particles with NIPAM with no NHS functionalities showed no binding of gold inside of the particles.

3.2.5 Determination of the number of enzymes on the hydrogel particle by fluorescence

To quantify the GOx enzyme density on the pNIPAM hydrogel particle, it is necessary to identify both the concentration of the enzyme and the particle in solution. It has been challenging to determine the concentration of the hydrogel particle since there is no standard extinction coefficient. Previously, our lab has reported a pNIPMAM coated gold nanoparticle as an optical molecular actuator (OMA particles).¹⁶⁴ These particles contain a single gold nanorod embedded in the center of the hydrogel shell, which allows the direct quantification of the particles. By modifying the OMA particles the same way as the nanoenzymes mentioned previously, both the concentration of the NIPAM hydrogels and the GOx enzymes will be acquired. (Figure 3.12) The procedure of synthesizing the OMA nanoparticles was adapted from Zheng *et al.*¹⁶⁴ The Alexa 488 labeled GOX was immobilized onto the OMAs after the NHS modification. (procedure see 3.2.2 and 3.2.2). The concentration of the gold nanorod was determined using the UV-Vis spectrometer (Agilent 8453 Spectrophotometer), and the concentration of GOx was determined by fluorescence (Horiba, Kyoto, Japan Dual FI fluorimeter). To test if the gold nanorod is

causing fluorescence quenching of the dye labeled GOx due to nanometal surface energy transfer (NSET), the gold nanorod was dissolved, and fluorescence was compared to the control group. No considerable fluorescence change was observed after the OMA solution was treated with KCN 50 mM (200 μ final concentration) which indicated that

the NSET effect is negligible in this experiment. A gold nanorod to GOx ratio of 1 to 32.5 was determined. This result is in agreement with the TEM image of the mapping of the enzyme docking sites using 5 nm gold nanoparticles.

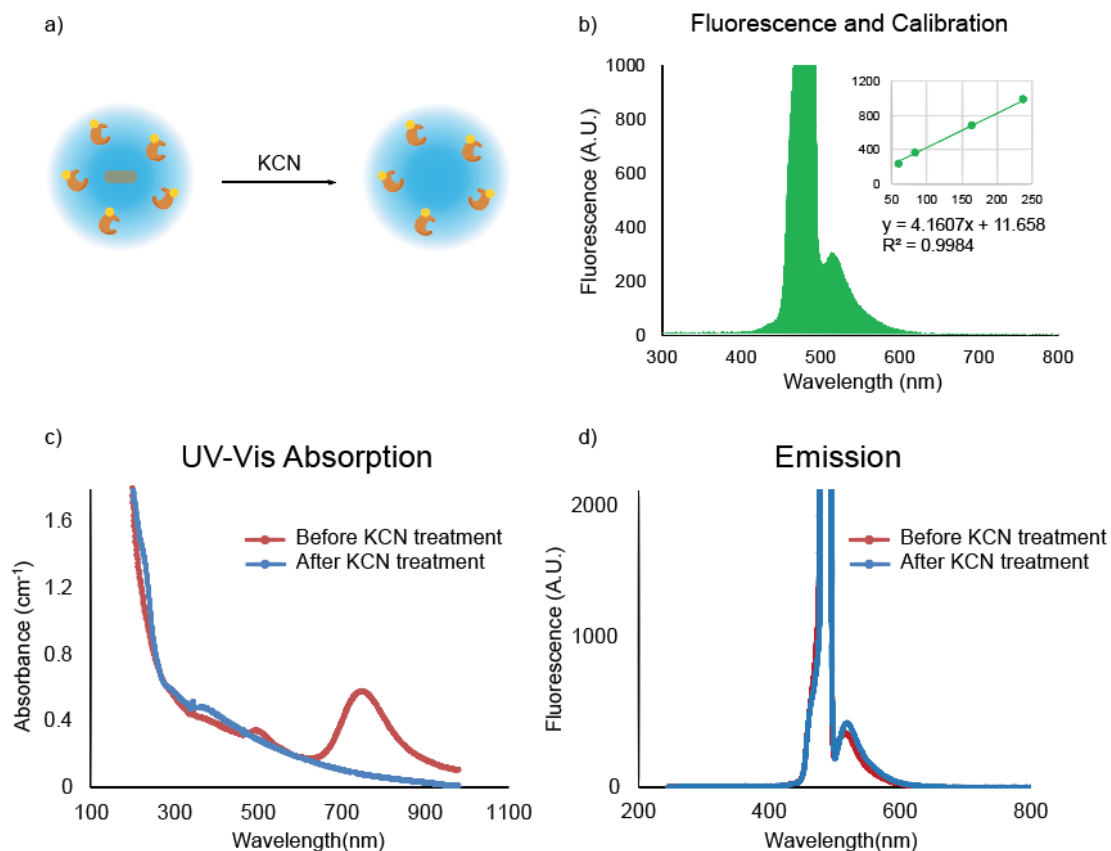


Figure 3.12 Determination of number of GOX enzymes on the NIPAM nanoparticles

a) Schematic representation of dissolving gold nanorod in the OMA particles. b) fluorescence measurement of the sample OMA particles with GOx-Alexa 488, inserted was the fluorescence standard curve using free enzymes. c) UV-Vis showing the OMA particles absorption before and after etching gold. d) Fluorescence spectra of OMA particles before and after etching.

3.2.5.1 DLS analysis of particle volume transition with temperature

Temperature controlled dynamic light scattering (DLS) was performed on a Zetasizer Nano ZS90 (Malvern Instruments, Malvern, UK). Figure 3.13 is a representative plot of nanoparticle size distribution of the PNIPAM. Note that the diameter in the DLS plot refers to the hydrodynamic diameter, which is usually larger than the actual polymer size observed by TEM. The sharpness of the distribution peak indicated a monodispersed population of nanoparticles.

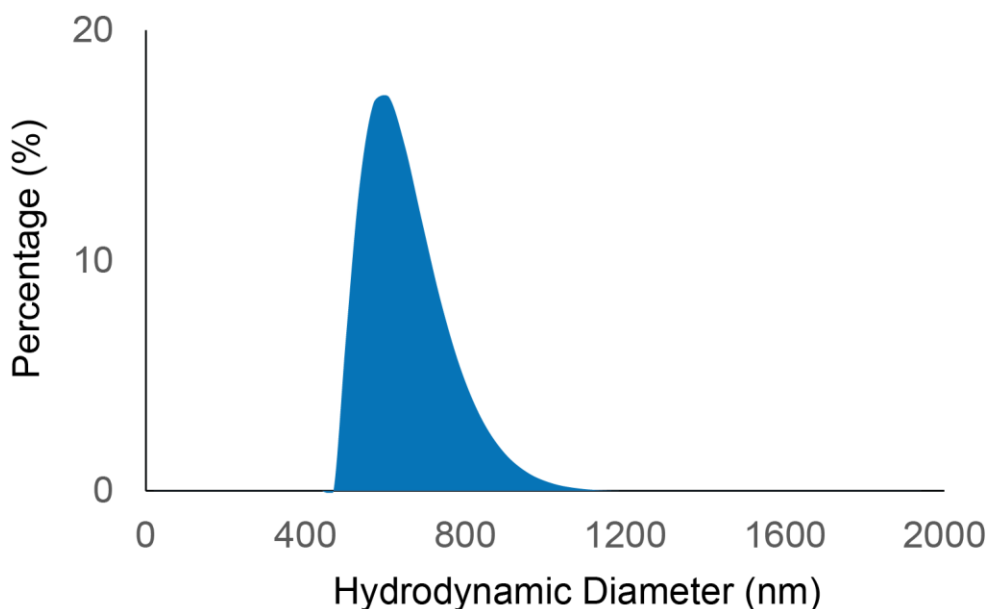


Figure 3.13 DLS size distribution of NIPAM nanoparticles

A program of measuring the particle diameter with an increasing and decreasing temperature revealed the sharp phase transition at LCST, as well as the temperature at which the particle shrunk to the minimal size. By decreasing the temperature gradually, the particles rehydrated and swelled back to the original size, which indicated that the phase transition is reversible. Figure 3.14 showed the phase transition curve of pNIPAM and pNIPMAM particles, where pNIPMAM showed a higher LCST of 44.5 ± 0.6 °C than

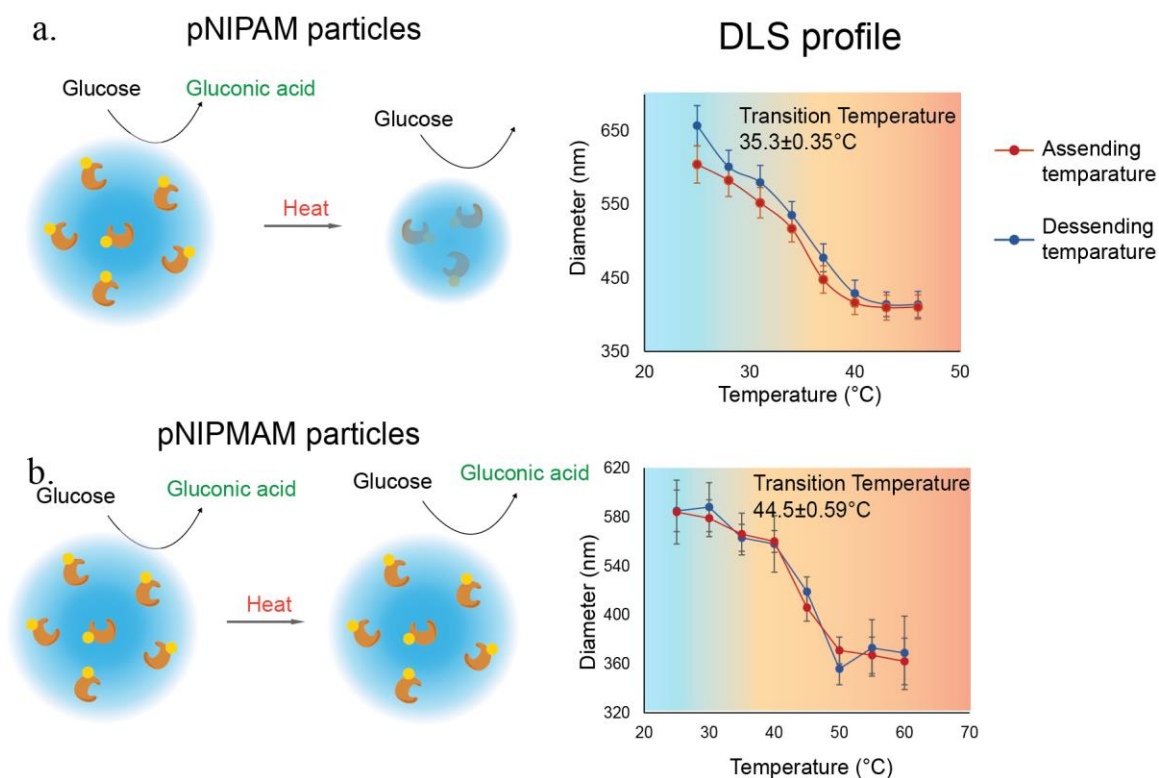


Figure 3.14 DLS phase transition curve of PNIPAM and PNIPMAM particles.

the LCST of 35.3 ± 0.4 for pNIPAM (Figure 3.14). Therefore, we hypothesized that at 35°C , only the pNIPAM particles will collapse in size and exclude the access of glucose substrates of GOx, which in turn will cause the slowdown of the enzymatic reaction.

3.3. Kinetics of enzymatic reaction actuation

3.3.1 Results and discussion

To demonstrate that the pNIPAM particles are capable of regulating the enzymatic reaction rate, the above-mentioned Alexa 488 GOx modified pNIPAM nanoparticles was prepared and tested. The nanoparticles (containing ~ 10 nM of GOx enzyme) were resuspended in a PBS buffered (pH 7.45) solution containing 1 mM of Glucose (Sigma

Aldrich), 1 mM of MgCl₂ (Sigma Aldrich), 2 mM of ABTS (Sigma Aldrich), and 1 μM of HRP (Sigma Aldrich). The HRP enzymes were not bound to the nanoparticles. The UV-Vis spectrometer was used to monitor the kinetics by monitoring the 403nm ABTS absorption. At 25 °C, the pNIPAM network is completely swollen with water, in which case the enzymes embedded in the network are fully accessible to the substrate glucose and oxygen. Here, the kinetics plot displayed a conventional linear regime since the consumption of substrate can be ignored initially (<500 s). However, when the reaction temperature is 37 °C, the temperature at which the particles shrink to the smallest in size according to the DLS, a remarkable decrease in reaction rate was observed. (Figure 3.15) This is owing to the shrinking of the network resulting from the expulsion of water and is followed by a concomitant slowing down of the diffusion of reactants within the network. This process will in turn lower the rate of the reaction catalyzed by the embedded GOx. Another possible mechanism is that below LCST, the hydrogel network is in loose random coil state, the polymer chains interfere minimally with the substrate binding to the enzymes. When phase transition is triggered at higher temperature, the collapsed polymers could block the active site of the enzymes, which would prevent the catalysis of the substrates. Note that the concentration of the product ABTS cation radical went down first and then remained stable at a low level. This could be caused by the instability of the molecule, which gets broken down or reduced at that condition.

In a control experiment, free Alexa 488 labeled enzymes were added to the reaction mixture without binding to the NIPAM particles (Figure 3.15). No observable difference

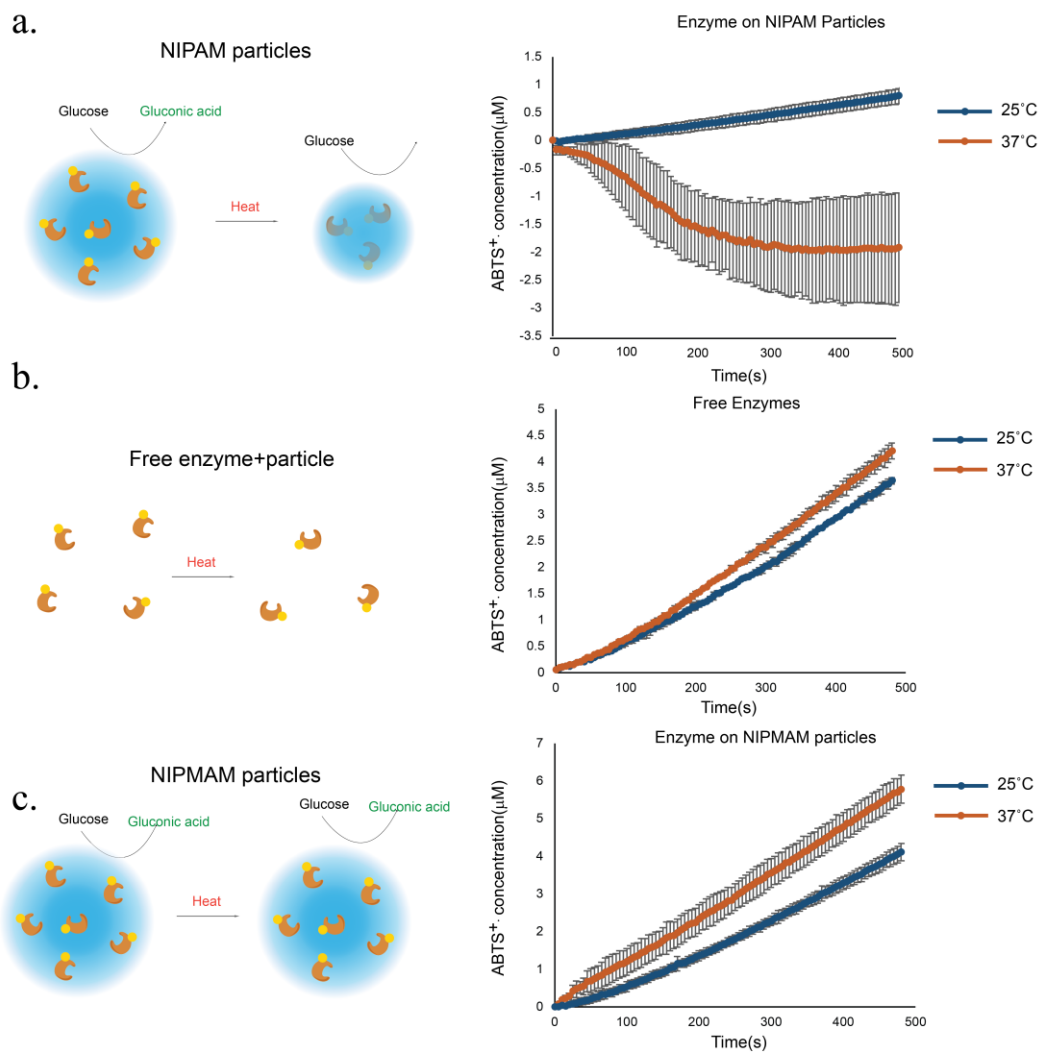


Figure 3.15 Kinetics of the GOx enzymatic reaction by monitoring ABTS²⁻ using UV-Vis

a) Free enzyme at 25°C and 37 °C. b) pNIPAM nanoparticles with GOx at 25°C and 37 °C. c) pNIPAM nanoparticles with GOx at 25°C and 37 °C

in reaction rate was observed at 25°C and 37 °C, which indicated that temperature does not have an effect on the reaction rate of the enzymes independent of the NIPAM particles. Note that this result also suggested that diffusion is no longer affected by

temperature at this certain substrate concentration. Next, pNIPMAM particles modified with Alexa 488-GOX were prepared and tested in the substrate solution. As expected, no remarkable differences in reaction rate was observed, which indicated that the existence of the polymer itself did not cause the ceasing of the reaction.

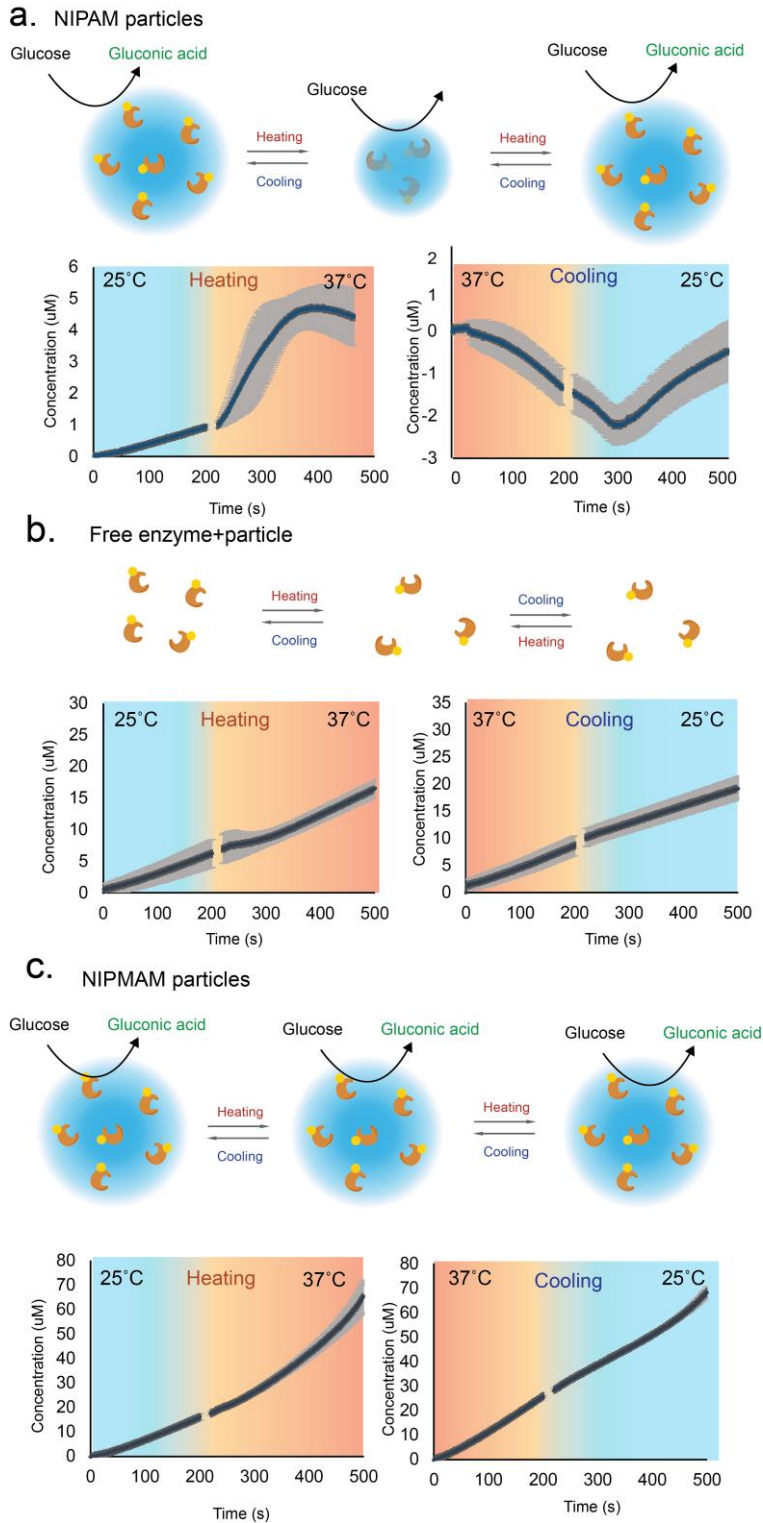


Figure 3.16. Real-time heating and cooling of the thermoresponsive nanoparticle catalyzed relations

3.3.2 Real-time recording of enzymatic reaction inhibition

In a separate experiment, the pNIPAM nanoparticles-catalyzed reaction was monitored with the temperature change after the reaction started, and the reaction underwent both heating and cooling processes (Figure 3.16). For the reactions with free enzymes and NIPMAM particles, the heating and cooling did not cause a dramatic change in the reaction rate. However, for pNIPAM particles-catalyzed reactions, it is clear that the heating from 25 °C to 37 °C caused the reaction to cease and cooling revived the reaction.

3.4. Conclusion and outlook

In summary, this is a demonstration of control over reaction rate via a stimulus-responsive regulatory mechanism. A thermoresponsive nano-reactor was developed to control the enzymatic activities. The particles were covalently modified with enzymes, and the regulation was achieved by adjusting the temperature to trigger the phase transition of the polymer, which impeded the access to the substrate. The reaction rate constant k was observed to decrease at temperature above LCST. This general approach could theoretically be applied to any enzymes since the covalent modification is facile and nonspecific. The thermoresponsive particle can act as a universal enzyme carrier or reactor to provide thermal regulation of reaction rate. By changing the component of the polymer, the regulation could be tuned to a wide temperature range. Moreover, the addition of a gold nanorod inside the hydrogel particles could allow the optical control of the phase transition of the nanoparticles, which opens a new door to the non-invasive control of the enzymatic reactions. This approach could significantly improve control of biochemical pathways for in vitro and quite possibly, in vivo applications.

3.5. References

- (1) Bradshaw, R. A.; Dennis, E. A. *Handbook of cell signaling*, 2/e; 2010; Vol. 1–3.
- (2) Martin, G. S. *Cancer Cell* **2003**, 4 (3), 167–174.
- (3) Lai, E. C. *Development* **2004**, 131 (5), 965–973.
- (4) Eungdamrong, N. J.; Iyengar, R. *Biol. Cell* **2004**, 96 (5), 355–362.
- (5) Iskratsch, T.; Wolfenson, H.; Sheetz, M. P. *Nat. Rev. Mol. Cell Biol.* **2014**, 15 (12), 825–833.
- (6) SANFORD, K. K.; LIKELY, G. D.; EARLE, W. R. *J. Natl. Cancer Inst.* **1954**, 15 (2), 215–237.
- (7) Gauthier, N. C.; Fardin, M. A.; Roca-Cusachs, P.; Sheetz, M. P. *Proc. Natl. Acad. Sci.* **2011**, 108 (35), 14467–14472.
- (8) Sheetz, M. P.; Singer, S. J. *Proc. Natl. Acad. Sci.* **1974**, 71 (11), 4457–4461.
- (9) Liu, Z.; Tan, J. L.; Cohen, D. M.; Yang, M. T.; Sniadecki, N. J.; Alom, S.; Nelson, C. M.; Chen, C. S. **2010**.
- (10) Gardel, M. L.; Schneider, I. C.; Aratyn-Schaus, Y.; Waterman, C. M. *Annu. Rev. Cell Dev. Biol.* **2010**, 26 (1), 315–333.
- (11) Moy, V. T.; Florin, E. L.; Gaub, H. E. *Science* (80-.). **1994**, 266 (5183), 257–259.
- (12) Shah, N. H.; Muir, T. W. *Chem. Sci.* **2014**, 5 (1), 446–461.
- (13) Borghi, N.; Sorokina, M.; Shcherbakova, O. G.; Weis, W. I.; Pruitt, B. L.; Nelson, W. J.; Dunn, A. R. *Proc. Natl. Acad. Sci. U. S. A.* **2012**, 109 (31), 12568–12573.
- (14) Schwarz, U. S.; Gardel, M. L. *J. Cell Sci.* **2012**, 125 (Pt 13), 3051–3060.
- (15) Spudich, J. A. *Nat. Rev. Mol. Cell Biol.* **2001**, 2 (5), 387–392.
- (16) Lochter, a; Bissell, M. J. *Semin. Cancer Biol.* **1995**, 6, 165–173.
- (17) Engler, A. J.; Sen, S.; Sweeney, H. L.; Discher, D. E. *Cell* **2006**, 126 (4), 677–689.

- (18) Chen, C. S.; Tan, J.; Tien, J. *Annu. Rev. Biomed. Eng.* **2004**, *6*, 275–302.
- (19) Plotnikov, S. V.; Pasapera, A. M.; Sabass, B.; Waterman, C. M. *Cell* **2012**, *151* (7), 1513–1527.
- (20) CURTIS, A. S. *J. Cell Biol.* **1964**, *20*, 199–215.
- (21) Izzard, C. S.; Lochner, L. R. *J. Cell Sci.* **1976**, *21* (1), 129–159.
- (22) Abercrombie, M.; Heaysman, J. E. M.; Pegrum, S. M. *Exp. Cell Res.* **1970**, *62* (2–3), 389–398.
- (23) Hynes, R. O. *Cell*. 2002, pp 673–687.
- (24) Giancotti, F. G. *Science* (80-.). **1999**, *285* (5430), 1028–1033.
- (25) Ludueña, M. A.; Wessells, N. K. *Dev. Biol.* **1973**, *30* (2), 427–440.
- (26) Kolega, J. *J. Cell Biol.* **1986**, *102* (4), 1400–1411.
- (27) LEVY, J. A.; DIAMENT, A. J.; SARAIVA, S. *Arq. Neuropsiquiatr.* **1960**, *18*, 259–264.
- (28) Hu, K.; Ji, L.; Applegate, K. T.; Danuser, G.; Waterman-Storer, C. M. *Science* (80-.). **2007**, *315* (5808), 111–115.
- (29) Aratyn-Schaus, Y.; Gardel, M. L. *Curr. Biol.* **2010**, *20* (13), 1143–1153.
- (30) del Rio, A.; Perez-Jimenez, R.; Liu, R.; Roca-Cusachs, P.; Fernandez, J. M.; Sheetz, M. P. *Science* **2009**, *323* (5914), 638–641.
- (31) Haque, F.; Lloyd, D. J.; Smallwood, D. T.; Dent, C. L.; Shanahan, C. M.; Fry, A. M.; Trembath, R. C.; Shackleton, S. *Mol. Cell. Biol.* **2006**, *26* (10), 3738–3751.
- (32) Jaalouk, D. E.; Lammerding, J. *Nat. Rev. Mol. Cell Biol.* **2009**, *10* (1), 63–73.
- (33) Tan, J. C. H. *Br. J. Ophthalmol.* **2006**, *90* (3), 383–388.
- (34) Johnstone, M. A. *J. Glaucoma* **2004**, *13* (5), 421–438.

- (35) Heydemann, A.; McNally, E. M. *Trends in Cardiovascular Medicine*. 2007, pp 55–59.
- (36) Zhong, C.; Chrzanowska-Wodnicka, M.; Brown, J.; Shaub, A.; Belkin, A. M.; Burridge, K. *J. Cell Biol.* **1998**, *141* (2), 539–551.
- (37) Wierzbicka-Patynowski, I.; Schwarzbauer, J. E. *J. Cell Sci.* **2003**, *116* (Pt 16), 3269–3276.
- (38) Aota, S.; Nomizu, M.; Yamada, K. M. *J. Biol. Chem.* **1994**, *269* (40), 24756–24761.
- (39) Kauf, A. C. W.; Hough, S. M.; Bowditch, R. D. *Biochemistry* **2001**, *40* (31), 9159–9166.
- (40) Redick, S. D. *J. Cell Biol.* **2000**, *149* (2), 521–527.
- (41) Li, F.; Redick, S. D.; Erickson, H. P.; Moy, V. T. *Biophys. J.* **2003**, *84* (2), 1252–1262.
- (42) le Duc, Q.; Shi, Q.; Blonk, I.; Sonnenberg, A.; Wang, N.; Leckband, D.; de Rooij, J. *J. Cell Biol.* **2010**, *189* (7), 1107–1115.
- (43) Le Duc, Q.; Shi, Q.; Blonk, I.; Sonnenberg, A.; Wang, N.; Leckband, D.; De Rooij, J. *J. Cell Biol.* **2010**, *189* (7), 1107–1115.
- (44) Harris, A.; Wild, P.; Stopak, D. *Science* (80-.). **1980**, *208* (4440), 177–179.
- (45) Oliver, T.; Jacobson, K.; Dembo, M. *Cell Motil. Cytoskeleton* **1995**, *31* (3), 225–240.
- (46) Chen, C. S.; Mrksich, M.; Huang, S.; Whitesides, G. M.; Ingber, D. E. *Science* (80-.). **1997**, *276* (5317), 1425–1428.
- (47) Wang, N.; Butler, J.; Ingber, D. *Science* (80-.). **1993**, *260* (5111), 1124–1127.

- (48) Rief, M. *Science* (80-.). **1997**, 276 (5315), 1109–1112.
- (49) Merkel, R.; Nassoy, P.; Leung, A.; Ritchie, K.; Evans, E. *Nature* **1999**, 397 (6714), 50–53.
- (50) Ghassemi, S.; Meacci, G.; Liu, S.; Gondarenko, A. A.; Mathur, A.; Roca-Cusachs, P.; Sheetz, M. P.; Hone, J. *Proc. Natl. Acad. Sci.* **2012**, 109 (14), 5328–5333.
- (51) Galbraith, C. G.; Sheetz, M. P. *Proc. Natl. Acad. Sci.* **1997**, 94 (17), 9114–9118.
- (52) Singhvi, R.; Kumar, A.; Lopez, G. P.; Stephanopoulos, G. N.; Wang, D. I.; Whitesides, G. M.; Ingber, D. E. *Science* **1994**, 264 (5159), 696–698.
- (53) Choquet, D.; Felsenfeld, D. P.; Sheetz, M. P. *Cell* **1997**, 88 (1), 39–48.
- (54) Grashoff, C.; Hoffman, B. D.; Brenner, M. D.; Zhou, R.; Parsons, M.; Yang, M. T.; McLean, M. a; Sligar, S. G.; Chen, C. S.; Ha, T.; Schwartz, M. a. *Nature* **2010**, 466 (7303), 263–266.
- (55) Liu, Y.; Yehl, K.; Narui, Y.; Salaita, K. *J. Am. Chem. Soc.* **2013**, 135 (14), 5320–5323.
- (56) Meng, F.; Suchyna, T. M.; Sachs, F. *FEBS J.* **2008**, 275 (12), 3072–3087.
- (57) Stabley, D. R.; Jurchenko, C.; Marshall, S. S.; Salaita, K. S. *Nat. Methods* **2012**, 9 (1), 64–67.
- (58) Wang, X.; Ha, T. *Science* **2013**, 340 (6135), 991–994.
- (59) Zhang, Y.; Ge, C.; Zhu, C.; Salaita, K. *Nat. Commun.* **2014**, 5, 5167.
- (60) Hoffman, B. D.; Grashoff, C.; Schwartz, M. a. *Nature* **2011**, 475 (7356), 316–323.
- (61) Borghi, N.; Sorokina, M.; Shcherbakova, O. G.; Weis, W. I.; Pruitt, B. L.; Nelson, W. J.; Dunn, A. R. *Proc. Natl. Acad. Sci. U. S. A.* **2012**, 109 (31), 12568–12573.
- (62) Cai, D.; Chen, S. C.; Prasad, M.; He, L.; Wang, X.; Choesmel-Cadamuro, V.;

- Sawyer, J. K.; Danuser, G.; Montell, D. J. *Cell* **2014**, *157* (5), 1146–1159.
- (63) Conway, D. E.; Breckenridge, M. T.; Hinde, E.; Gratton, E.; Chen, C. S.; Schwartz, M. a. *Curr. Biol.* **2013**, *23* (11), 1024–1030.
- (64) Jurchenko, C.; Chang, Y.; Narui, Y.; Zhang, Y.; Salaita, K. S. *Biophys. J.* **2014**, *106* (7), 1436–1446.
- (65) Ma, V. P. Y.; Liu, Y.; Blanchfield, L.; Su, H.; Evavold, B. D.; Salaita, K. *Nano Lett.* **2016**, *16* (7), 4552–4559.
- (66) Morimatsu, M.; Mekhdjian, A. H.; Adhikari, A. S.; Dunn, A. R. *Nano Lett.* **2013**, *13* (9), 3985–3989.
- (67) Jurchenko, C.; Salaita, K. S. *Mol. Cell. Biol.* **2015**, *35* (15), 2570–2582.
- (68) Lakowicz, J. R. *Principles of fluorescence spectroscopy*; 2006.
- (69) Chapman-Smith, a; Cronan, J. E. *J. Nutr.* **1999**, *129* (Cronan 1990), 477S–484S.
- (70) Förster, T. *Ann Phys.* **1948**, *2*, 55–75.
- (71) Marko, J. F.; Siggia, E. D. *Macromolecules* **1995**, *28* (26), 8759–8770.
- (72) Bustamante, C.; Marko, J. F.; Siggia, E. D.; Smith, S. *Science* **1994**, *265* (1994), 1599–1600.
- (73) Wieland, T.; Bokelmann, E.; Bauer, L.; Lang, H. U.; Lau, H. *Justus Liebigs Ann. Chem.* **1953**, *583* (1), 129–149.
- (74) Dawson, P. E.; Muir, T. W.; Clark-Lewis, I.; Kent, S. B. *Science* **1994**, *266*, 776–779.
- (75) Liu, C. F.; Rao, C.; Tam, J. P. *J. Am. Chem. Soc.* **1996**, *118* (2), 307–312.
- (76) Shin, Y.; Winans, K. A.; Backes, B. J.; Kent, S. B. H.; Ellman, J. A.; Bertozzi, C. R. *J. Am. Chem. Soc.* **1999**, *121* (50), 11684–11689.

- (77) Xiao, J.; Chen, R.; Pawlicki, M. A.; Tolbert, T. J. *J. Am. Chem. Soc.* **2009**, *131* (38), 13616–13618.
- (78) Jurchenko, C.; Chang, Y.; Narui, Y.; Zhang, Y.; Salaita, K. S. *Biophys. J.* **2014**, *106* (7), 1436–1446.
- (79) Ghauharali, R. I.; Brakenhoff, G. J. *J. Microsc.* **2000**, *198* (2), 88–100.
- (80) Shi, H.; Liu, J.; Geng, J.; Tang, B. Z.; Liu, B. *J. Am. Chem. Soc.* **2012**, *134* (23), 9569–9572.
- (81) Chang, Y.; Liu, zheng; Zhang, Y.; Galior, K.; Yang, J.; Salaita, K. *J. Am. Chem. Soc.* **2016**, jacs.5b11602.
- (82) General, I. J.; Dragomirova, R.; Meirovitch, H. *J. Phys. Chem. B* **2012**, *116* (23), 6628–6636.
- (83) Yuan, C.; Chen, A.; Kolb, P.; Moy, V. T. *Biochemistry* **2000**, *39* (33), 10219–10223.
- (84) Smith, S.; Finzi, L.; Bustamante, C. *Science* (80-.). **1992**, *258* (5085), 1122–1126.
- (85) Hohng, S.; Zhou, R.; Nahas, M. K.; Yu, J.; Schulten, K.; Lilley, D. M. J.; Ha, T. *Science* **2007**, *318* (5848), 279–283.
- (86) Yu, C.; Law, J. B. K.; Suryana, M.; Low, H. Y.; Sheetz, M. P. *Proc. Natl. Acad. Sci. U. S. A.* **2011**, *108* (51), 20585–20590.
- (87) Pincet, F.; Husson, J. *Biophys. J.* **2005**, *89* (6), 4374–4381.
- (88) Choi, Y.; Kim, E.; Lee, Y.; Han, M. H.; Kang, I. C. *Proteomics* **2010**, *10* (1), 72–80.
- (89) Lehenkari, P. P.; Horton, M. a. *Biochem. Biophys. Res. Commun.* **1999**, *259* (3), 645–650.

- (90) Neuert, G.; Albrecht, C. H.; Gaub, H. E. *Biophys. J.* **2007**, *93* (4), 1215–1223.
- (91) Galush, W. J.; Nye, J. A.; Groves, J. T. *Biophys. J.* **2008**, *95* (5), 2512–2519.
- (92) Friedland, J. C.; Lee, M. H.; Boettiger, D. *Science* **2009**, *323* (5914), 642–644.
- (93) Kong, F.; García, A. J.; Mould, A. P.; Humphries, M. J.; Zhu, C. *J. Cell Biol.* **2009**, *185* (7), 1275–1284.
- (94) Kong, F.; Li, Z.; Parks, W. M.; Dumbauld, D. W.; García, A. J.; Mould, A. P.; Humphries, M. J.; Zhu, C. *Mol. Cell* **2013**, *49* (6), 1060–1068.
- (95) Schoen, I.; Pruitt, B. L.; Vogel, V. *Annu. Rev. Mater. Res.* **2013**, *43* (1), 589–618.
- (96) de Gennes, P. G. *Macromolecules* **1980**, *13* (19), 1069–1075.
- (97) Bell, G. I. *Science* **1978**, *200* (4342), 618–627.
- (98) Schwarz, U. S.; Balaban, N. Q.; Rivelino, D.; Bershadsky, A.; Geiger, B.; Safran, S. A. *Biophys. J.* **2002**, *83*, 1380–1394.
- (99) Klim, J. R.; Fowler, A. J.; Courtney, A. H.; Wrighton, P. J.; Sheridan, R. T. C.; Wong, M. L.; Kiessling, L. L. *ACS Chem. Biol.* **2012**, *7* (3), 518–525.
- (100) Song, L.; Hennink, E. J.; Young, I. T.; Tanke, H. J. *Biophys. J.* **1995**, *68* (6), 2588–2600.
- (101) Rajagopalan, P.; Marganski, W. a; Brown, X. Q.; Wong, J. Y. *Biophys. J.* **2004**, *87* (4), 2818–2827.
- (102) Ung, P.; Winkler; Winkler, D. A. *J. Med. Chem.* **2011**, *54* (5), 1–5.
- (103) Pfaff, M.; Tangemann, K.; Müller, B.; Gurrath, M.; Müller, G.; Kessler, H.; Timpl, R.; Engel, J. *J. Biol. Chem.* **1994**, *269* (32), 20233–20238.
- (104) Craig, J. a.; Rexeisen, E. L.; Mardilovich, A.; Shroff, K.; Kokkoli, E. *Langmuir* **2008**, *24* (18), 10282–10292.

- (105) Noë, V.; Willems, J.; Vandekerckhove, J.; Roy, F. Van; Bruyneel, E.; Mareel, M. *J. Cell Sci.* **1999**, *112*, 127–135.
- (106) Andrade, J. D.; Hlady, V.; Jeon, S.-I. In *Hydrophilic Polymers*; 1996; Vol. 248, pp 51–59.
- (107) Ratner, B. D.; Bryant, S. J. *Annu Rev Biomed Eng* **2004**, *6*, 41–75.
- (108) Horbett Thomas, A.; Brash John, L.; Horbett, T. A.; Brash, J. L. In *Proteins at Interfaces*; 1987; Vol. 343, pp 1–33.
- (109) Andrade, J. D.; Hlady, V. *Adv. Polym. Sci.* **1986**, *79*, 1–63.
- (110) Bronzino, E. J. D.; Park, J. B.; Kim, Y. K. *Biomed. Eng. (NY)*. **2000**.
- (111) Jeyachandran, Y. L.; Mielczarski, J. A.; Mielczarski, E.; Rai, B. *J. Colloid Interface Sci.* **2010**, *341* (1), 136–142.
- (112) Blawas, A. S.; Reichert, W. M. *Biomaterials*. 1998, pp 595–609.
- (113) Lee, J.; Joon Kim, M.; Lee, H. H. *Langmuir* **2006**, *22* (5), 2090–2095.
- (114) Visnapuu, M.-L.; Duzdevich, D.; Greene, E. C. *Mol. Biosyst.* **2008**, *4* (5), 394–403.
- (115) Estephan, Z. G. **2012**.
- (116) West, S. L.; Salvage, J. P.; Lobb, E. J.; Armes, S. P.; Billingham, N. C.; Lewis, A. L.; Hanlon, G. W.; Lloyd, A. W. *Biomaterials* **2004**, *25* (7–8), 1195–1204.
- (117) Holmlin, R. E.; Chen, X.; Chapman, R. G.; Takayama, S.; Whitesides, G. M. *Langmuir* **2001**, *17* (13), 2841–2850.
- (118) Matsuura, K.; Ohno, K.; Kagaya, S.; Kitano, H. *Macromol. Chem. Phys.* **2007**, *208* (8), 862–873.
- (119) Jia, G.; Cao, Z.; Xue, H.; Xu, Y.; Jiang, S. *Langmuir* **2009**, *25* (5), 3196–3199.

- (120) Backmann, N.; Kappeler, N.; Braun, T.; Huber, F.; Lang, H.-P.; Gerber, C.; Lim, R. Y. H. *Beilstein J. Nanotechnol.* **2010**, *1*, 3–13.
- (121) Streeter, H. B.; Rees, D. A. **1987**, *105* (July), 507–515.
- (122) Chiu, C.-S.; Jensen, K.; Sokolova, I.; Wang, D.; Li, M.; Deshpande, P.; Davidson, N.; Mody, I.; Quick, M. W.; Quake, S. R.; Lester, H. a. *J. Neurosci.* **2002**, *22* (23), 10251–10266.
- (123) Yang, T.; Baryshnikova, O. K.; Mao, H.; Holden, M. A.; Cremer, P. S. *J. Am. Chem. Soc.* **2003**, *125* (16), 4779–4784.
- (124) Sackmann, E. *Science* (80-.). **2007**, *271* (5245), 43–48.
- (125) Zwier, J. M.; Van Rooij, G. J.; Hofstraat, J. W.; Brakenhoff, G. J. *J. Microsc.* **2004**, *216* (1), 15–24.
- (126) Wakatsuki, T.; Schwab, B.; Thompson, N. C.; Elson, E. L. *J. Cell Sci.* **2001**, *114* (Pt 5), 1025–1036.
- (127) Dunn, K. W.; Kamocka, M. M.; McDonald, J. H. *Am. J. Physiol. Cell Physiol.* **2011**, *300* (4), C723–C742.
- (128) Oesterhelt, F.; Rief, M.; Gaub, H. E. *New J. Phys.* **1999**, *1*, 1–11.
- (129) Kienberger, F.; Kienberger, F.; Pastushenko, V. P.; Pastushenko, V. P.; Kada, G.; Kada, G.; Gruber, H. J.; Gruber, H. J.; Riener, C.; Riener, C.; Schindler, H.; Schindler, H.; Hinterdorfer, P.; Hinterdorfer, P. *Single Mol.* **2000**, *1* (2), 123–128.
- (130) *Introduction to Fluorescence Sensing*; Demchenko, A. P., Ed.; Springer Netherlands: Dordrecht, 2009.
- (131) Moore, S. W.; Roca-Cusachs, P.; Sheetz, M. P. *Dev. Cell* **2010**, *19* (2), 194–206.
- (132) Bouchiat, C.; Wang, M. D.; Allemand, J.; Strick, T.; Block, S. M.; Croquette, V.

- Biophys. J.* **1999**, 76 (1), 409–413.
- (133) Petrie, T. a; Capadona, J. R.; Reyes, C. D.; García, A. J. *Biomaterials* **2006**, 27 (31), 5459–5470.
- (134) Feng, Y.; Mrksich, M. *Biochemistry* **2004**, 43 (50), 15811–15821.
- (135) Mano, J. F. *Advanced Engineering Materials*. 2008, pp 515–527.
- (136) Phillips, D. J.; Gibson, M. I. *Polym. Chem.* **2015**, 6 (7), 1033–1043.
- (137) Stuart, M. A. C.; Huck, W. T. S.; Genzer, J.; Müller, M.; Ober, C.; Stamm, M.; Sukhorukov, G. B.; Szleifer, I.; Tsukruk, V. V.; Urban, M.; Winnik, F.; Zauscher, S.; Luzinov, I.; Minko, S. *Nat. Mater.* **2010**, 9 (2), 101–113.
- (138) Liu, F.; Urban, M. W. *Prog. Polym. Sci.* **2010**, 35 (1–2), 3–23.
- (139) Yan, X.; Wang, F.; Zheng, B.; Huang, F. *Chem. Soc. Rev.* **2012**, 41 (18), 6042.
- (140) Jhaveri, S. J.; Hynd, M. R.; Dowell-Mesfin, N.; Turner, J. N.; Shain, W.; Ober, C. K. *Biomacromolecules* **2009**, 10 (1), 174–183.
- (141) Hoffman, A. S. *J. Control. Release* **2008**, 132 (3), 153–163.
- (142) Lim, H. L.; Hwang, Y.; Kar, M.; Varghese, S. *Biomater. Sci.* **2014**, 2 (5), 603.
- (143) Anker, J. N.; Hall, W. P.; Lyandres, O.; Shah, N. C.; Zhao, J.; Van Duyne, R. P. *Nat. Mater.* **2008**, 7 (6), 442–453.
- (144) Khokhlov, A. R. *Conformation-dependent design of sequences in copolymers*; 2006.
- (145) Forster, S. *Colloid Chem. 1* **2003**, 226, 1–28.
- (146) Arotçaréna, M.; Heise, B.; Ishaya, S.; Laschewsky, A. *J. Am. Chem. Soc.* **2002**, 124 (14), 3787–3793.
- (147) Tokareva, I.; Minko, S.; Fendler, J. H.; Hutter, E. *J. Am. Chem. Soc.* **2004**, 126

- (49), 15950–15951.
- (148) Burg, T. P.; Godin, M.; Knudsen, S. M.; Shen, W.; Carlson, G.; Foster, J. S.; Babcock, K.; Manalis, S. R. *Nature* **2007**, *446* (7139), 1066–1069.
- (149) Tu, Y.; Peng, F.; Sui, X.; Men, Y.; White, P. B.; van Hest, J. C. M.; Wilson, D. A. *Nat. Chem.* **2016**, *9* (5), 480–486.
- (150) MacKenzie, K. J.; Francis, M. B. *J. Am. Chem. Soc.* **2013**, *135* (1), 293–300.
- (151) Hoshino, K.; Yamasaki, H.; Chida, C.; Morohashi, S.; Sasakura, T.; Taniguchi, M.; Fujii, M. *J. Chem. Eng. Japan* **1997**, *30* (1), 30–37.
- (152) Lu, Y.; Mei, Y.; Ballauff, M.; Drechsler, M. *J. Phys. Chem. B* **2006**, *110* (9), 3930–3937.
- (153) Lu, Y.; Proch, S.; Schrunner, M.; Drechsler, M.; Kempe, R.; Ballauff, M. *J. Mater. Chem.* **2009**, *19* (23), 3955.
- (154) Blankschien, M. D.; Pretzer, L. a.; Huschka, R.; Halas, N. J.; Gonzalez, R.; Wong, M. S. *ACS Nano* **2013**, *7* (1), 654–663.
- (155) Kim, Y. S.; Liu, M.; Ishida, Y.; Ebina, Y.; Osada, M.; Sasaki, T.; Hikima, T.; Takata, M.; Aida, T. *Nat. Mater.* **2015**, *14* (10), 1002–1007.
- (156) Cowie, J. M. G.; Arrighi, V. *Polym. Chem. Phys. Mod. Mater.* **2007**, 463.
- (157) Atkins, P.; Paula, J. De. *Atkins' physical chemistry*; 2009.
- (158) Fujishige, S.; Kubota, K.; Ando, I. *J. Phys. Chem.* **1989**, *93* (8), 3311–3313.
- (159) Roy, D.; Brooks, W. L. A.; Sumerlin, B. S. *Chem. Soc. Rev.* **2013**, *42* (17), 7214.
- (160) Scarpa, J. S.; Mueller, D. D.; Klotz, I. M. *J. Am. Chem. Soc.* **1967**, *89* (24), 6024–6030.
- (161) Bankar, S. B.; Bule, M. V.; Singhal, R. S.; Ananthanarayan, L. *Biotechnology*

Advances. 2009, pp 489–501.

- (162) Singh, J.; Verma, N. *Adv. Appl. Sci. Res.* **2013**, *4* (3), 250–257.
- (163) Wilson, R.; Turner, A. P. F. *Biosensors and Bioelectronics*. 1992, pp 165–185.
- (164) Liu, Z.; Liu, Y.; Chang, Y.; Seyf, H. R.; Henry, A.; Mattheyses, A. L.; Yehl, K.; Zhang, Y.; Huang, Z.; Salaita, K. *Nat. Methods* **2015**, *13* (december), 1–8.
- (165) Fors, B. P.; Poelma, J. E.; Menyo, M. S.; Robb, M. J.; Spokoyny, D. M.; Kramer, J. W.; Waite, J. H.; Hawker, C. J. *J. Am. Chem. Soc.* **2013**, *135* (38), 14106–14109.
- (166) Rechenmacher, F.; Neubauer, S.; Polleux, J.; Mas-Moruno, C.; De Simone, M.; Cavalcanti-Adam, E. A.; Spatz, J. P.; Fässler, R.; Kessler, H. *Angew. Chemie - Int. Ed.* **2013**, *52*, 1572–1575.
- (167) Rahmouni, S.; Lindner, A.; Rechenmacher, F.; Neubauer, S.; Sobahi, T. R. A.; Kessler, H.; Cavalcanti-Adam, E. A.; Spatz, J. P. *Adv. Mater.* **2013**, *25*, 5869–5874.
- (168) Laughlin, S. T.; Baskin, J. M.; Amacher, S. L.; Bertozzi, C. R. *Science* (80-.). **2008**, *320* (5876), 664–667.

Chapter 4: Summary and future directions

In this thesis, two major projects were detailed and highlighted. Chapter 1 and Chapter 2 provided an overview of the field of studying mechanical signal transduction and reported the development of a synthetic strategy to generate modular tension probes combining the native chemical ligation (NCL) reaction with solid phase peptide synthesis (SPPS). In principle, this approach accommodates virtually any peptide or expressed protein amenable to NCL. A small library of tension probes displaying different ligands was generated for mapping integrin and cadherin tension. It was also a first demonstration of a long-term (~3 days) molecular tension imaging paradigm. Mechanical forces between cells and their extracellular matrix (ECM) are mediated by hundreds of different receptors. These biophysical interactions play fundamental roles in processes ranging from cellular development to tumor progression. However, mapping the spatial and temporal dynamics of tension among various receptor-ligand pairs remains a significant challenge. In Chapter 3, the development of a thermo-responsive enzymatic nanoreactor for the regulation of reaction rate was described. Enzymes were embedded into hydrogel nanoparticles that are sensitive to external temperature changes. By controlling the temperature, the hydrophobicity of the polymer could be regulated, causing the collapse of the nanoparticles, which in turn controls the enzymatic reaction rate. This approach provides a tool to modulate enigmatic interactions using external stimuli and could significantly improve biochemical pathways and can be implemented for greater control for in vitro and quite possibly, in vivo applications.

The development of the synthetic MTFM sensor has built a platform that allows the investigation of mechanical behaviors of living cells on a bio-mimicking nonliving surface. The conversion of fluorescent signal to the magnitude of tension was based on

two mathematic models, FRET and worm-like-chain model. Yet there is a need to calibrate the system using magnetic tweezers or optical tweezers. The calibration method was once described by Grashoff et al.⁶⁰ to calibrate the genetically encoded tension sensor TSMoD. Single molecule fluorescence imaging was coupled with optical tweezers to calibrate the system (fluorescence vs tension). In order to facilitate the fluorescence measurement, the fluorescent proteins at the ends of the linker were replaced with the organic dyes Cy3 and Cy5, and by using optical tweezers, this construct was stretched and subsequently the fluorescence changes were recorded. Our system could be calibrated the same by modifying beads with integrin receptors and incubating the beads with the sensor coated surfaces.

There are many biological questions that can be answered using this system. For example, to study the impact of geometry on cell mechanobiology, our MTFM sensor could be covalently modified on the surface with varying design patterns. The patterning technique is described by Fors et al. using a photo-mediated ATRA reaction and a photo mask to spatially control the functionalization of surfaces with visible light.¹⁶⁵ This method could be used to print a well-defined chemically differentiated monolayer of MTFM tension sensors, which provides varied geometry information along with different modulus, etc. It has been discovered that integrin $\alpha v\beta 3$ and $\alpha 5\beta 1$ plays distinctively roles in establishing adhesion. $\alpha 5\beta 1$ integrin mediates adhesion strength, whereas $\alpha v\beta 3$ integrin participate in adhesion reinforcement and mechanotransduction. Meanwhile, Rechenmacher and coworkers have reported the design and synthesis of integrin antagonists specifically targeting either $\alpha 5\beta 1$ or $\alpha v\beta 3$.^{166,167} Functioning our MTFM sensor with these integrin antagonists allows the investigation of ligand specificity impact

on mechanotransduction, and it can provide richer information about how a cell functions, and how responses are regulated by a single integrin subtype.

A third direction would be the use of MTFM sensors to investigate mechanotransduction within the cell-cell adhesion. Modifying cell surfaces with functional groups/molecules has become a more mature technique which requires the feeding of cells with Azide-mannose.¹⁶⁸ The mannose will be displayed on the cell surface and this allows for the covalent conjugation of MTFM sensors on the cell surface. Since the MTFM tension sensor is highly modular, cadherin reactive ligands could be modified on the sensor. Tension transduction mediated by cadherin between cells could thus be mapped and reported by monitoring the fluorescence change at cell-cell junctions.

For the thermoresponsive nanoreactors, it provides a strategy to regulate enzymatic rate using external stimuli. Although temperature has been the most standard way to regulate

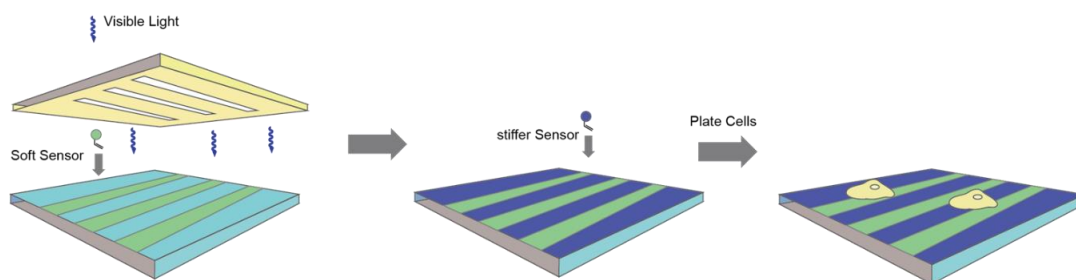


Figure 4.1 Photo-printing MTFM sensors on the glass coverslip with defined patterns

reaction rate, the thermoresponsive nanoreactors allow an inhibitory control of reaction rate with an increased temperature. This temperature could also be adjusted higher or lower by changing the hydrogel polymer component, which accommodates more needs to control the reaction rate. On another note, the combination of exothermic enzymatic reactions (with high ΔH) with the thermoresponsive nanoreactors could generate a built-

in reaction-regulating mechanism. The thermal energy released by the reaction will accumulate and ultimately lead to the collapse of the polymer which in turn slows down the reaction. Once the heat is exchanged with the environment, the polymer will be rehydrated and allow the exothermic reaction to proceed again. This cycle will create a chemical-thermal oscillation system with chemical fuel, which brings the potential for the design of artificial muscle system.

References:

- (1) Bradshaw, R. A.; Dennis, E. A. *Handbook of cell signaling*, 2/e; 2010; Vol. 1–3.
- (2) Martin, G. S. *Cancer Cell* **2003**, 4 (3), 167–174.
- (3) Lai, E. C. *Development* **2004**, 131 (5), 965–973.
- (4) Eungdamrong, N. J.; Iyengar, R. *Biol. Cell* **2004**, 96 (5), 355–362.
- (5) Iskratsch, T.; Wolfenson, H.; Sheetz, M. P. *Nat. Rev. Mol. Cell Biol.* **2014**, 15 (12), 825–833.
- (6) SANFORD, K. K.; LIKELY, G. D.; EARLE, W. R. *J. Natl. Cancer Inst.* **1954**, 15 (2), 215–237.
- (7) Gauthier, N. C.; Fardin, M. A.; Roca-Cusachs, P.; Sheetz, M. P. *Proc. Natl. Acad. Sci.* **2011**, 108 (35), 14467–14472.
- (8) Sheetz, M. P.; Singer, S. J. *Proc. Natl. Acad. Sci.* **1974**, 71 (11), 4457–4461.
- (9) Liu, Z.; Tan, J. L.; Cohen, D. M.; Yang, M. T.; Sniadecki, N. J.; Alom, S.; Nelson, C. M.; Chen, C. S. **2010**.

- (10) Gardel, M. L.; Schneider, I. C.; Aratyn-Schaus, Y.; Waterman, C. M. *Annu. Rev. Cell Dev. Biol.* **2010**, *26* (1), 315–333.
- (11) Moy, V. T.; Florin, E. L.; Gaub, H. E. *Science (80-.)*. **1994**, *266* (5183), 257–259.
- (12) Shah, N. H.; Muir, T. W. *Chem. Sci.* **2014**, *5* (1), 446–461.
- (13) Borghi, N.; Sorokina, M.; Shcherbakova, O. G.; Weis, W. I.; Pruitt, B. L.; Nelson, W. J.; Dunn, A. R. *Proc. Natl. Acad. Sci. U. S. A.* **2012**, *109* (31), 12568–12573.
- (14) Schwarz, U. S.; Gardel, M. L. *J. Cell Sci.* **2012**, *125* (Pt 13), 3051–3060.
- (15) Spudich, J. A. *Nat. Rev. Mol. Cell Biol.* **2001**, *2* (5), 387–392.
- (16) Lochter, a; Bissell, M. J. *Semin. Cancer Biol.* **1995**, *6*, 165–173.
- (17) Engler, A. J.; Sen, S.; Sweeney, H. L.; Discher, D. E. *Cell* **2006**, *126* (4), 677–689.
- (18) Chen, C. S.; Tan, J.; Tien, J. *Annu. Rev. Biomed. Eng.* **2004**, *6*, 275–302.
- (19) Plotnikov, S. V.; Pasapera, A. M.; Sabass, B.; Waterman, C. M. *Cell* **2012**, *151* (7), 1513–1527.
- (20) CURTIS, A. S. *J. Cell Biol.* **1964**, *20*, 199–215.
- (21) Izzard, C. S.; Lochner, L. R. *J. Cell Sci.* **1976**, *21* (1), 129–159.
- (22) Abercrombie, M.; Heaysman, J. E. M.; Pegrum, S. M. *Exp. Cell Res.* **1970**, *62* (2–3), 389–398.
- (23) Hynes, R. O. *Cell*. 2002, pp 673–687.
- (24) Giancotti, F. G. *Science (80-.)*. **1999**, *285* (5430), 1028–1033.
- (25) Ludueña, M. A.; Wessells, N. K. *Dev. Biol.* **1973**, *30* (2), 427–440.
- (26) Kolega, J. *J. Cell Biol.* **1986**, *102* (4), 1400–1411.
- (27) LEVY, J. A.; DIAMENT, A. J.; SARAIVA, S. *Arq. Neuropsiquiatr.* **1960**, *18*, 259–264.

- (28) Hu, K.; Ji, L.; Applegate, K. T.; Danuser, G.; Waterman-Storer, C. M. *Science* (80- .). **2007**, *315* (5808), 111–115.
- (29) Aratyn-Schaus, Y.; Gardel, M. L. *Curr. Biol.* **2010**, *20* (13), 1143–1153.
- (30) del Rio, A.; Perez-Jimenez, R.; Liu, R.; Roca-Cusachs, P.; Fernandez, J. M.; Sheetz, M. P. *Science* **2009**, *323* (5914), 638–641.
- (31) Haque, F.; Lloyd, D. J.; Smallwood, D. T.; Dent, C. L.; Shanahan, C. M.; Fry, A. M.; Trembath, R. C.; Shackleton, S. *Mol. Cell. Biol.* **2006**, *26* (10), 3738–3751.
- (32) Jaalouk, D. E.; Lammerding, J. *Nat. Rev. Mol. Cell Biol.* **2009**, *10* (1), 63–73.
- (33) Tan, J. C. H. *Br. J. Ophthalmol.* **2006**, *90* (3), 383–388.
- (34) Johnstone, M. A. *J. Glaucoma* **2004**, *13* (5), 421–438.
- (35) Heydemann, A.; McNally, E. M. *Trends in Cardiovascular Medicine*. 2007, pp 55–59.
- (36) Zhong, C.; Chrzanowska-Wodnicka, M.; Brown, J.; Shaub, A.; Belkin, A. M.; Burridge, K. *J. Cell Biol.* **1998**, *141* (2), 539–551.
- (37) Wierzbicka-Patynowski, I.; Schwarzbauer, J. E. *J. Cell Sci.* **2003**, *116* (Pt 16), 3269–3276.
- (38) Aota, S.; Nomizu, M.; Yamada, K. M. *J. Biol. Chem.* **1994**, *269* (40), 24756–24761.
- (39) Kauf, A. C. W.; Hough, S. M.; Bowditch, R. D. *Biochemistry* **2001**, *40* (31), 9159–9166.
- (40) Redick, S. D. *J. Cell Biol.* **2000**, *149* (2), 521–527.
- (41) Li, F.; Redick, S. D.; Erickson, H. P.; Moy, V. T. *Biophys. J.* **2003**, *84* (2), 1252–1262.

- (42) le Duc, Q.; Shi, Q.; Blonk, I.; Sonnenberg, A.; Wang, N.; Leckband, D.; de Rooij, J. *J. Cell Biol.* **2010**, *189* (7), 1107–1115.
- (43) Le Duc, Q.; Shi, Q.; Blonk, I.; Sonnenberg, A.; Wang, N.; Leckband, D.; De Rooij, J. *J. Cell Biol.* **2010**, *189* (7), 1107–1115.
- (44) Harris, A.; Wild, P.; Stopak, D. *Science (80-.)*. **1980**, *208* (4440), 177–179.
- (45) Oliver, T.; Jacobson, K.; Dembo, M. *Cell Motil. Cytoskeleton* **1995**, *31* (3), 225–240.
- (46) Chen, C. S.; Mrksich, M.; Huang, S.; Whitesides, G. M.; Ingber, D. E. *Science (80-.)*. **1997**, *276* (5317), 1425–1428.
- (47) Wang, N.; Butler, J.; Ingber, D. *Science (80-.)*. **1993**, *260* (5111), 1124–1127.
- (48) Rief, M. *Science (80-.)*. **1997**, *276* (5315), 1109–1112.
- (49) Merkel, R.; Nassoy, P.; Leung, A.; Ritchie, K.; Evans, E. *Nature* **1999**, *397* (6714), 50–53.
- (50) Ghassemi, S.; Meacci, G.; Liu, S.; Gondarenko, A. A.; Mathur, A.; Roca-Cusachs, P.; Sheetz, M. P.; Hone, J. *Proc. Natl. Acad. Sci.* **2012**, *109* (14), 5328–5333.
- (51) Galbraith, C. G.; Sheetz, M. P. *Proc. Natl. Acad. Sci.* **1997**, *94* (17), 9114–9118.
- (52) Singhvi, R.; Kumar, A.; Lopez, G. P.; Stephanopoulos, G. N.; Wang, D. I.; Whitesides, G. M.; Ingber, D. E. *Science* **1994**, *264* (5159), 696–698.
- (53) Choquet, D.; Felsenfeld, D. P.; Sheetz, M. P. *Cell* **1997**, *88* (1), 39–48.
- (54) Grashoff, C.; Hoffman, B. D.; Brenner, M. D.; Zhou, R.; Parsons, M.; Yang, M. T.; McLean, M. a; Sligar, S. G.; Chen, C. S.; Ha, T.; Schwartz, M. a. *Nature* **2010**, *466* (7303), 263–266.
- (55) Liu, Y.; Yehl, K.; Narui, Y.; Salaita, K. *J. Am. Chem. Soc.* **2013**, *135* (14), 5320–

5323.

- (56) Meng, F.; Suchyna, T. M.; Sachs, F. *FEBS J.* **2008**, *275* (12), 3072–3087.
- (57) Stabley, D. R.; Jurchenko, C.; Marshall, S. S.; Salaita, K. S. *Nat. Methods* **2012**, *9* (1), 64–67.
- (58) Wang, X.; Ha, T. *Science* **2013**, *340* (6135), 991–994.
- (59) Zhang, Y.; Ge, C.; Zhu, C.; Salaita, K. *Nat. Commun.* **2014**, *5*, 5167.
- (60) Hoffman, B. D.; Grashoff, C.; Schwartz, M. a. *Nature* **2011**, *475* (7356), 316–323.
- (61) Borghi, N.; Sorokina, M.; Shcherbakova, O. G.; Weis, W. I.; Pruitt, B. L.; Nelson, W. J.; Dunn, A. R. *Proc. Natl. Acad. Sci. U. S. A.* **2012**, *109* (31), 12568–12573.
- (62) Cai, D.; Chen, S. C.; Prasad, M.; He, L.; Wang, X.; Choessel-Cadamuro, V.; Sawyer, J. K.; Danuser, G.; Montell, D. J. *Cell* **2014**, *157* (5), 1146–1159.
- (63) Conway, D. E.; Breckenridge, M. T.; Hinde, E.; Gratton, E.; Chen, C. S.; Schwartz, M. a. *Curr. Biol.* **2013**, *23* (11), 1024–1030.
- (64) Jurchenko, C.; Chang, Y.; Narui, Y.; Zhang, Y.; Salaita, K. S. *Biophys. J.* **2014**, *106* (7), 1436–1446.
- (65) Ma, V. P. Y.; Liu, Y.; Blanchfield, L.; Su, H.; Evavold, B. D.; Salaita, K. *Nano Lett.* **2016**, *16* (7), 4552–4559.
- (66) Morimatsu, M.; Mekhdjian, A. H.; Adhikari, A. S.; Dunn, A. R. *Nano Lett.* **2013**, *13* (9), 3985–3989.
- (67) Jurchenko, C.; Salaita, K. S. *Mol. Cell. Biol.* **2015**, *35* (15), 2570–2582.
- (68) Lakowicz, J. R. *Principles of fluorescence spectroscopy*; 2006.
- (69) Chapman-Smith, a; Cronan, J. E. *J. Nutr.* **1999**, *129* (Cronan 1990), 477S–484S.
- (70) Förster, T. *Ann Phys.* **1948**, *2*, 55–75.

- (71) Marko, J. F.; Siggia, E. D. *Macromolecules* **1995**, *28* (26), 8759–8770.
- (72) Bustamante, C.; Marko, J. F.; Siggia, E. D.; Smith, S. *Science* **1994**, *265* (1994), 1599–1600.
- (73) Wieland, T.; Bokelmann, E.; Bauer, L.; Lang, H. U.; Lau, H. *Justus Liebigs Ann. Chem.* **1953**, *583* (1), 129–149.
- (74) Dawson, P. E.; Muir, T. W.; Clark-Lewis, I.; Kent, S. B. *Science* **1994**, *266*, 776–779.
- (75) Liu, C. F.; Rao, C.; Tam, J. P. *J. Am. Chem. Soc.* **1996**, *118* (2), 307–312.
- (76) Shin, Y.; Winans, K. A.; Backes, B. J.; Kent, S. B. H.; Ellman, J. A.; Bertozzi, C. *R. J. Am. Chem. Soc.* **1999**, *121* (50), 11684–11689.
- (77) Xiao, J.; Chen, R.; Pawlicki, M. A.; Tolbert, T. J. *J. Am. Chem. Soc.* **2009**, *131* (38), 13616–13618.
- (78) Jurchenko, C.; Chang, Y.; Narui, Y.; Zhang, Y.; Salaita, K. S. *Biophys. J.* **2014**, *106* (7), 1436–1446.
- (79) Ghauharali, R. I.; Brakenhoff, G. J. *J. Microsc.* **2000**, *198* (2), 88–100.
- (80) Shi, H.; Liu, J.; Geng, J.; Tang, B. Z.; Liu, B. *J. Am. Chem. Soc.* **2012**, *134* (23), 9569–9572.
- (81) Chang, Y.; Liu, zheng; Zhang, Y.; Galior, K.; Yang, J.; Salaita, K. *J. Am. Chem. Soc.* **2016**, jacs.5b11602.
- (82) General, I. J.; Dragomirova, R.; Meirovitch, H. *J. Phys. Chem. B* **2012**, *116* (23), 6628–6636.
- (83) Yuan, C.; Chen, A.; Kolb, P.; Moy, V. T. *Biochemistry* **2000**, *39* (33), 10219–10223.

- (84) Smith, S.; Finzi, L.; Bustamante, C. *Science* (80-.). **1992**, 258 (5085), 1122–1126.
- (85) Hohng, S.; Zhou, R.; Nahas, M. K.; Yu, J.; Schulten, K.; Lilley, D. M. J.; Ha, T. *Science* **2007**, 318 (5848), 279–283.
- (86) Yu, C.; Law, J. B. K.; Suryana, M.; Low, H. Y.; Sheetz, M. P. *Proc. Natl. Acad. Sci. U. S. A.* **2011**, 108 (51), 20585–20590.
- (87) Pincet, F.; Husson, J. *Biophys. J.* **2005**, 89 (6), 4374–4381.
- (88) Choi, Y.; Kim, E.; Lee, Y.; Han, M. H.; Kang, I. C. *Proteomics* **2010**, 10 (1), 72–80.
- (89) Lehenkari, P. P.; Horton, M. a. *Biochem. Biophys. Res. Commun.* **1999**, 259 (3), 645–650.
- (90) Neuert, G.; Albrecht, C. H.; Gaub, H. E. *Biophys. J.* **2007**, 93 (4), 1215–1223.
- (91) Galush, W. J.; Nye, J. A.; Groves, J. T. *Biophys. J.* **2008**, 95 (5), 2512–2519.
- (92) Friedland, J. C.; Lee, M. H.; Boettiger, D. *Science* **2009**, 323 (5914), 642–644.
- (93) Kong, F.; García, A. J.; Mould, A. P.; Humphries, M. J.; Zhu, C. *J. Cell Biol.* **2009**, 185 (7), 1275–1284.
- (94) Kong, F.; Li, Z.; Parks, W. M.; Dumbauld, D. W.; García, A. J.; Mould, A. P.; Humphries, M. J.; Zhu, C. *Mol. Cell* **2013**, 49 (6), 1060–1068.
- (95) Schoen, I.; Pruitt, B. L.; Vogel, V. *Annu. Rev. Mater. Res.* **2013**, 43 (1), 589–618.
- (96) de Gennes, P. G. *Macromolecules* **1980**, 13 (19), 1069–1075.
- (97) Bell, G. I. *Science* **1978**, 200 (4342), 618–627.
- (98) Schwarz, U. S.; Balaban, N. Q.; Rivelino, D.; Bershadsky, A.; Geiger, B.; Safran, S. A. *Biophys. J.* **2002**, 83, 1380–1394.
- (99) Klim, J. R.; Fowler, A. J.; Courtney, A. H.; Wrighton, P. J.; Sheridan, R. T. C.;

- Wong, M. L.; Kiessling, L. L. *ACS Chem. Biol.* **2012**, 7 (3), 518–525.
- (100) Song, L.; Hennink, E. J.; Young, I. T.; Tanke, H. J. *Biophys. J.* **1995**, 68 (6), 2588–2600.
- (101) Rajagopalan, P.; Marganski, W. a; Brown, X. Q.; Wong, J. Y. *Biophys. J.* **2004**, 87 (4), 2818–2827.
- (102) Ung, P.; Winkler; Winkler, D. A. *J. Med. Chem.* **2011**, 54 (5), 1–5.
- (103) Pfaff, M.; Tangemann, K.; Müller, B.; Gurrath, M.; Müller, G.; Kessler, H.; Timpl, R.; Engel, J. *J. Biol. Chem.* **1994**, 269 (32), 20233–20238.
- (104) Craig, J. a.; Rexeisen, E. L.; Mardilovich, A.; Shroff, K.; Kokkoli, E. *Langmuir* **2008**, 24 (18), 10282–10292.
- (105) Noë, V.; Willems, J.; Vandekerckhove, J.; Roy, F. Van; Bruyneel, E.; Mareel, M. *J. Cell Sci.* **1999**, 112, 127–135.
- (106) Andrade, J. D.; Hlady, V.; Jeon, S.-I. In *Hydrophilic Polymers*; 1996; Vol. 248, pp 51–59.
- (107) Ratner, B. D.; Bryant, S. J. *Annu Rev Biomed Eng* **2004**, 6, 41–75.
- (108) Horbett Thomas, A.; Brash John, L.; Horbett, T. A.; Brash, J. L. In *Proteins at Interfaces*; 1987; Vol. 343, pp 1–33.
- (109) Andrade, J. D.; Hlady, V. *Adv. Polym. Sci.* **1986**, 79, 1–63.
- (110) Bronzino, E. J. D.; Park, J. B.; Kim, Y. K. *Biomed. Eng. (NY)*. **2000**.
- (111) Jeyachandran, Y. L.; Mielczarski, J. A.; Mielczarski, E.; Rai, B. *J. Colloid Interface Sci.* **2010**, 341 (1), 136–142.
- (112) Blawas, A. S.; Reichert, W. M. *Biomaterials*. 1998, pp 595–609.
- (113) Lee, J.; Joon Kim, M.; Lee, H. H. *Langmuir* **2006**, 22 (5), 2090–2095.

- (114) Visnapuu, M.-L.; Duzdevich, D.; Greene, E. C. *Mol. Biosyst.* **2008**, *4* (5), 394–403.
- (115) Estephan, Z. G. **2012**.
- (116) West, S. L.; Salvage, J. P.; Lobb, E. J.; Armes, S. P.; Billingham, N. C.; Lewis, A. L.; Hanlon, G. W.; Lloyd, A. W. *Biomaterials* **2004**, *25* (7–8), 1195–1204.
- (117) Holmlin, R. E.; Chen, X.; Chapman, R. G.; Takayama, S.; Whitesides, G. M. *Langmuir* **2001**, *17* (13), 2841–2850.
- (118) Matsuura, K.; Ohno, K.; Kagaya, S.; Kitano, H. *Macromol. Chem. Phys.* **2007**, *208* (8), 862–873.
- (119) Jia, G.; Cao, Z.; Xue, H.; Xu, Y.; Jiang, S. *Langmuir* **2009**, *25* (5), 3196–3199.
- (120) Backmann, N.; Kappeler, N.; Braun, T.; Huber, F.; Lang, H.-P.; Gerber, C.; Lim, R. Y. H. *Beilstein J. Nanotechnol.* **2010**, *1*, 3–13.
- (121) Streeter, H. B.; Rees, D. A. **1987**, *105* (July), 507–515.
- (122) Chiu, C.-S.; Jensen, K.; Sokolova, I.; Wang, D.; Li, M.; Deshpande, P.; Davidson, N.; Mody, I.; Quick, M. W.; Quake, S. R.; Lester, H. a. *J. Neurosci.* **2002**, *22* (23), 10251–10266.
- (123) Yang, T.; Baryshnikova, O. K.; Mao, H.; Holden, M. A.; Cremer, P. S. *J. Am. Chem. Soc.* **2003**, *125* (16), 4779–4784.
- (124) Sackmann, E. *Science (80-.)*. **2007**, *271* (5245), 43–48.
- (125) Zwier, J. M.; Van Rooij, G. J.; Hofstraat, J. W.; Brakenhoff, G. J. *J. Microsc.* **2004**, *216* (1), 15–24.
- (126) Wakatsuki, T.; Schwab, B.; Thompson, N. C.; Elson, E. L. *J. Cell Sci.* **2001**, *114* (Pt 5), 1025–1036.

- (127) Dunn, K. W.; Kamocka, M. M.; McDonald, J. H. *Am. J. Physiol. Cell Physiol.* **2011**, *300* (4), C723–C742.
- (128) Oesterhelt, F.; Rief, M.; Gaub, H. E. *New J. Phys.* **1999**, *1*, 1–11.
- (129) Kienberger, F.; Kienberger, F.; Pastushenko, V. P.; Pastushenko, V. P.; Kada, G.; Kada, G.; Gruber, H. J.; Gruber, H. J.; Riener, C.; Riener, C.; Schindler, H.; Schindler, H.; Hinterdorfer, P.; Hinterdorfer, P. *Single Mol.* **2000**, *1* (2), 123–128.
- (130) *Introduction to Fluorescence Sensing*; Demchenko, A. P., Ed.; Springer Netherlands: Dordrecht, 2009.
- (131) Moore, S. W.; Roca-Cusachs, P.; Sheetz, M. P. *Dev. Cell* **2010**, *19* (2), 194–206.
- (132) Bouchiat, C.; Wang, M. D.; Allemand, J.; Strick, T.; Block, S. M.; Croquette, V. *Biophys. J.* **1999**, *76* (1), 409–413.
- (133) Petrie, T. a; Capadona, J. R.; Reyes, C. D.; García, A. J. *Biomaterials* **2006**, *27* (31), 5459–5470.
- (134) Feng, Y.; Mrksich, M. *Biochemistry* **2004**, *43* (50), 15811–15821.
- (135) Mano, J. F. *Advanced Engineering Materials*. 2008, pp 515–527.
- (136) Phillips, D. J.; Gibson, M. I. *Polym. Chem.* **2015**, *6* (7), 1033–1043.
- (137) Stuart, M. A. C.; Huck, W. T. S.; Genzer, J.; Müller, M.; Ober, C.; Stamm, M.; Sukhorukov, G. B.; Szleifer, I.; Tsukruk, V. V.; Urban, M.; Winnik, F.; Zauscher, S.; Luzinov, I.; Minko, S. *Nat. Mater.* **2010**, *9* (2), 101–113.
- (138) Liu, F.; Urban, M. W. *Prog. Polym. Sci.* **2010**, *35* (1–2), 3–23.
- (139) Yan, X.; Wang, F.; Zheng, B.; Huang, F. *Chem. Soc. Rev.* **2012**, *41* (18), 6042.
- (140) Jhaveri, S. J.; Hynd, M. R.; Dowell-Mesfin, N.; Turner, J. N.; Shain, W.; Ober, C. K. *Biomacromolecules* **2009**, *10* (1), 174–183.

- (141) Hoffman, A. S. *J. Control. Release* **2008**, *132* (3), 153–163.
- (142) Lim, H. L.; Hwang, Y.; Kar, M.; Varghese, S. *Biomater. Sci.* **2014**, *2* (5), 603.
- (143) Anker, J. N.; Hall, W. P.; Lyandres, O.; Shah, N. C.; Zhao, J.; Van Duyne, R. P. *Nat. Mater.* **2008**, *7* (6), 442–453.
- (144) Khokhlov, A. R. *Conformation-dependent design of sequences in copolymers*; 2006.
- (145) Forster, S. *Colloid Chem. 1* **2003**, *226*, 1–28.
- (146) Arotçaréna, M.; Heise, B.; Ishaya, S.; Laschewsky, A. *J. Am. Chem. Soc.* **2002**, *124* (14), 3787–3793.
- (147) Tokareva, I.; Minko, S.; Fendler, J. H.; Hutter, E. *J. Am. Chem. Soc.* **2004**, *126* (49), 15950–15951.
- (148) Burg, T. P.; Godin, M.; Knudsen, S. M.; Shen, W.; Carlson, G.; Foster, J. S.; Babcock, K.; Manalis, S. R. *Nature* **2007**, *446* (7139), 1066–1069.
- (149) Tu, Y.; Peng, F.; Sui, X.; Men, Y.; White, P. B.; van Hest, J. C. M.; Wilson, D. A. *Nat. Chem.* **2016**, *9* (5), 480–486.
- (150) MacKenzie, K. J.; Francis, M. B. *J. Am. Chem. Soc.* **2013**, *135* (1), 293–300.
- (151) Hoshino, K.; Yamasaki, H.; Chida, C.; Morohashi, S.; Sasakura, T.; Taniguchi, M.; Fujii, M. *J. Chem. Eng. Japan* **1997**, *30* (1), 30–37.
- (152) Lu, Y.; Mei, Y.; Ballauff, M.; Drechsler, M. *J. Phys. Chem. B* **2006**, *110* (9), 3930–3937.
- (153) Lu, Y.; Proch, S.; Schrinner, M.; Drechsler, M.; Kempe, R.; Ballauff, M. *J. Mater. Chem.* **2009**, *19* (23), 3955.
- (154) Blankschien, M. D.; Pretzer, L. a.; Huschka, R.; Halas, N. J.; Gonzalez, R.; Wong,

- M. S. *ACS Nano* **2013**, 7 (1), 654–663.
- (155) Kim, Y. S.; Liu, M.; Ishida, Y.; Ebina, Y.; Osada, M.; Sasaki, T.; Hikima, T.; Takata, M.; Aida, T. *Nat. Mater.* **2015**, 14 (10), 1002–1007.
- (156) Cowie, J. M. G.; Arrighi, V. *Polym. Chem. Phys. Mod. Mater.* **2007**, 463.
- (157) Atkins, P.; Paula, J. De. *Atkins' physical chemistry*; 2009.
- (158) Fujishige, S.; Kubota, K.; Ando, I. *J. Phys. Chem.* **1989**, 93 (8), 3311–3313.
- (159) Roy, D.; Brooks, W. L. A.; Sumerlin, B. S. *Chem. Soc. Rev.* **2013**, 42 (17), 7214.
- (160) Scarpa, J. S.; Mueller, D. D.; Klotz, I. M. *J. Am. Chem. Soc.* **1967**, 89 (24), 6024–6030.
- (161) Bankar, S. B.; Bule, M. V.; Singhal, R. S.; Ananthanarayan, L. *Biotechnology Advances*. 2009, pp 489–501.
- (162) Singh, J.; Verma, N. *Adv. Appl. Sci. Res.* **2013**, 4 (3), 250–257.
- (163) Wilson, R.; Turner, A. P. F. *Biosensors and Bioelectronics*. 1992, pp 165–185.
- (164) Liu, Z.; Liu, Y.; Chang, Y.; Seyf, H. R.; Henry, A.; Mattheyses, A. L.; Yehl, K.; Zhang, Y.; Huang, Z.; Salaita, K. *Nat. Methods* **2015**, 13 (december), 1–8.
- (165) Fors, B. P.; Poelma, J. E.; Menyo, M. S.; Robb, M. J.; Spokoyny, D. M.; Kramer, J. W.; Waite, J. H.; Hawker, C. J. *J. Am. Chem. Soc.* **2013**, 135 (38), 14106–14109.
- (166) Rechenmacher, F.; Neubauer, S.; Polleux, J.; Mas-Moruno, C.; De Simone, M.; Cavalcanti-Adam, E. A.; Spatz, J. P.; Fässler, R.; Kessler, H. *Angew. Chemie - Int. Ed.* **2013**, 52, 1572–1575.
- (167) Rahmouni, S.; Lindner, A.; Rechenmacher, F.; Neubauer, S.; Sobahi, T. R. A.; Kessler, H.; Cavalcanti-Adam, E. A.; Spatz, J. P. *Adv. Mater.* **2013**, 25, 5869–5874.

- (168) Laughlin, S. T.; Baskin, J. M.; Amacher, S. L.; Bertozzi, C. R. *Science* (80-.).
2008, 320 (5876), 664–667.

Appendix

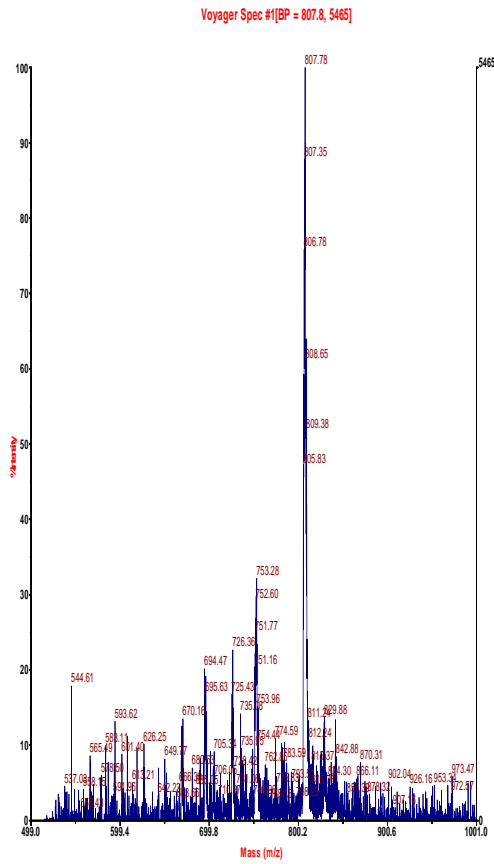
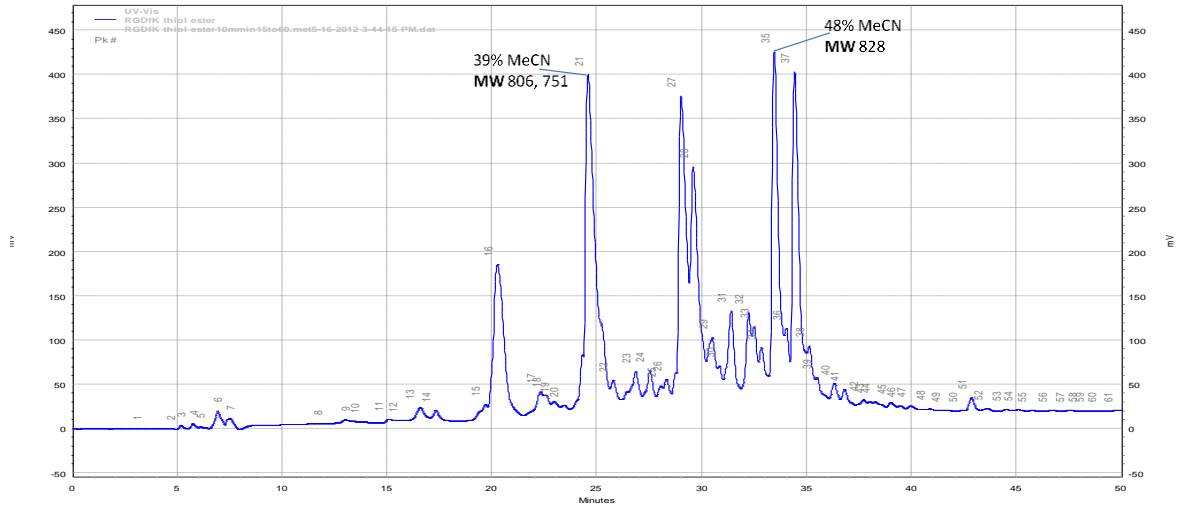


Figure A2.1 HPLC and MALDI cyclic RGD thioester

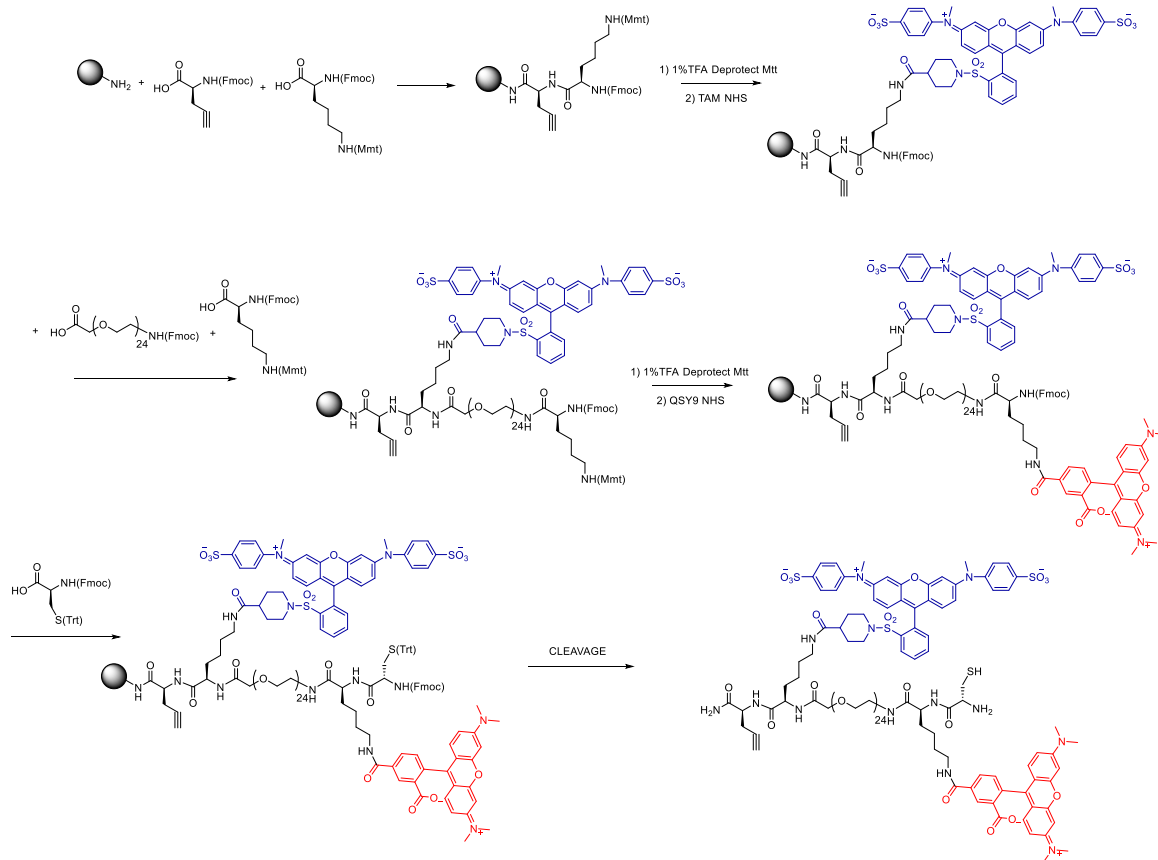


Figure A2.2 Synthesis of the two-step MTFM sensor precursor

C-terminal alkyne-modified amino acid followed by lysine, discrete PEG24, and the lysine was deprotected coupled to a QSY9 NHS ester. Another lysine was coupled to the solid support and was deprotected then coupled with NHS-ester modified tetramethylrhodamine (TAMRA) fluorophore. The lysine was then coupled with a terminal cysteine. The peptide conjugate was then cleaved and purified using reverse phase HPLC (RP-HPLC) and verified using MALDI-TOF.

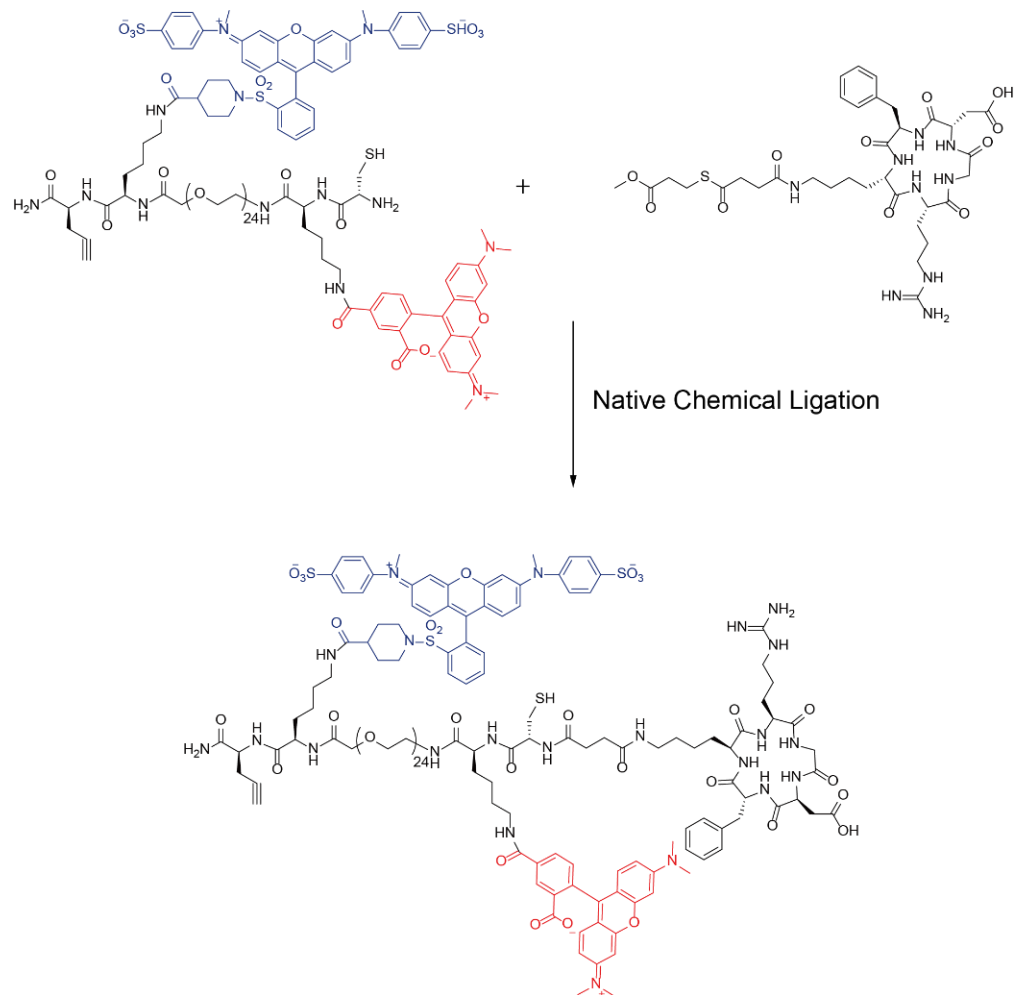


Figure A2.3 Synthesis of MTFM sensor using two step strategy

The native chemical ligation (NCL) reaction was used to conjugate peptide α -thioesters to the tension probe. The NCL reaction was carried out by mixing sensor precursor (10 mM) with 5 mM cRGD peptide thioester in 20 mM sodium phosphate buffer (pH 7.5) containing 5 mM betaine and 30 mM sodium 2-mercaptoethanesulfonic acid (MPAA). The reaction mixture was incubated for 24 hrs at room temperature.

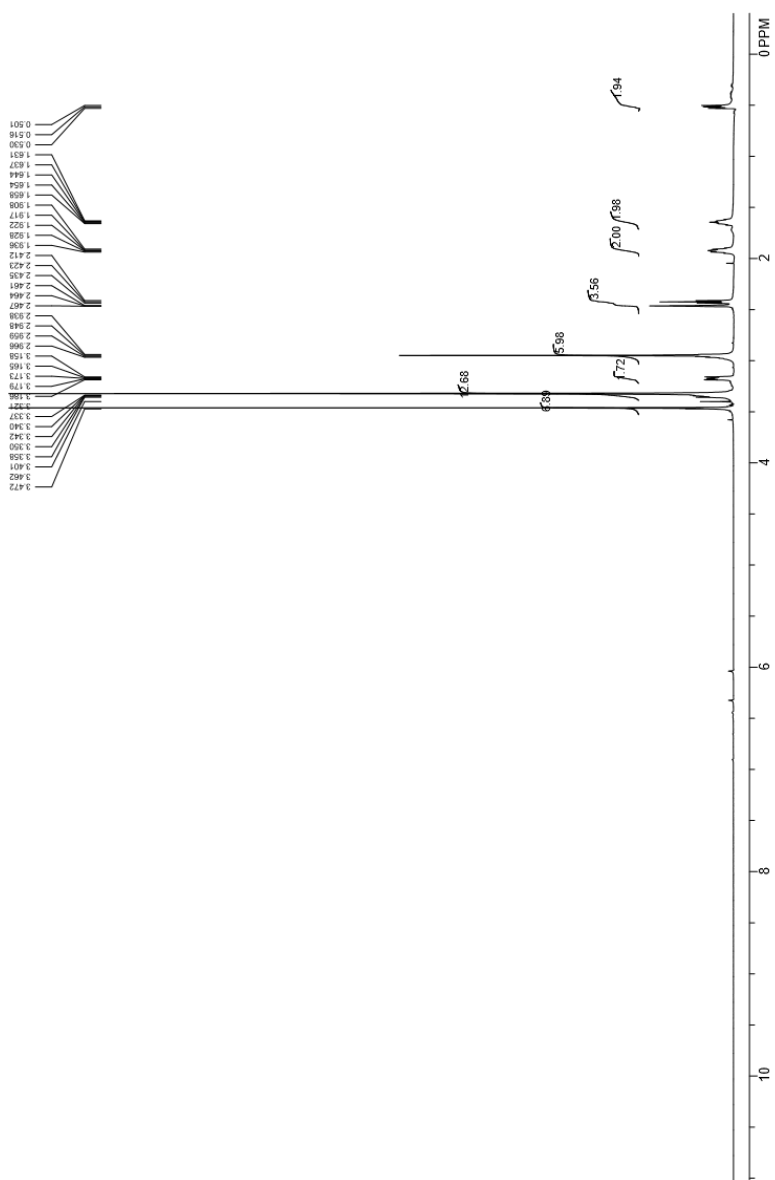


Figure A2.4 $^1\text{H-NMR}$ of SBS silane (3-(dimethyl-(3-(trimethoxysilyl)propyl)ammonio) propane-1-sulfonate)

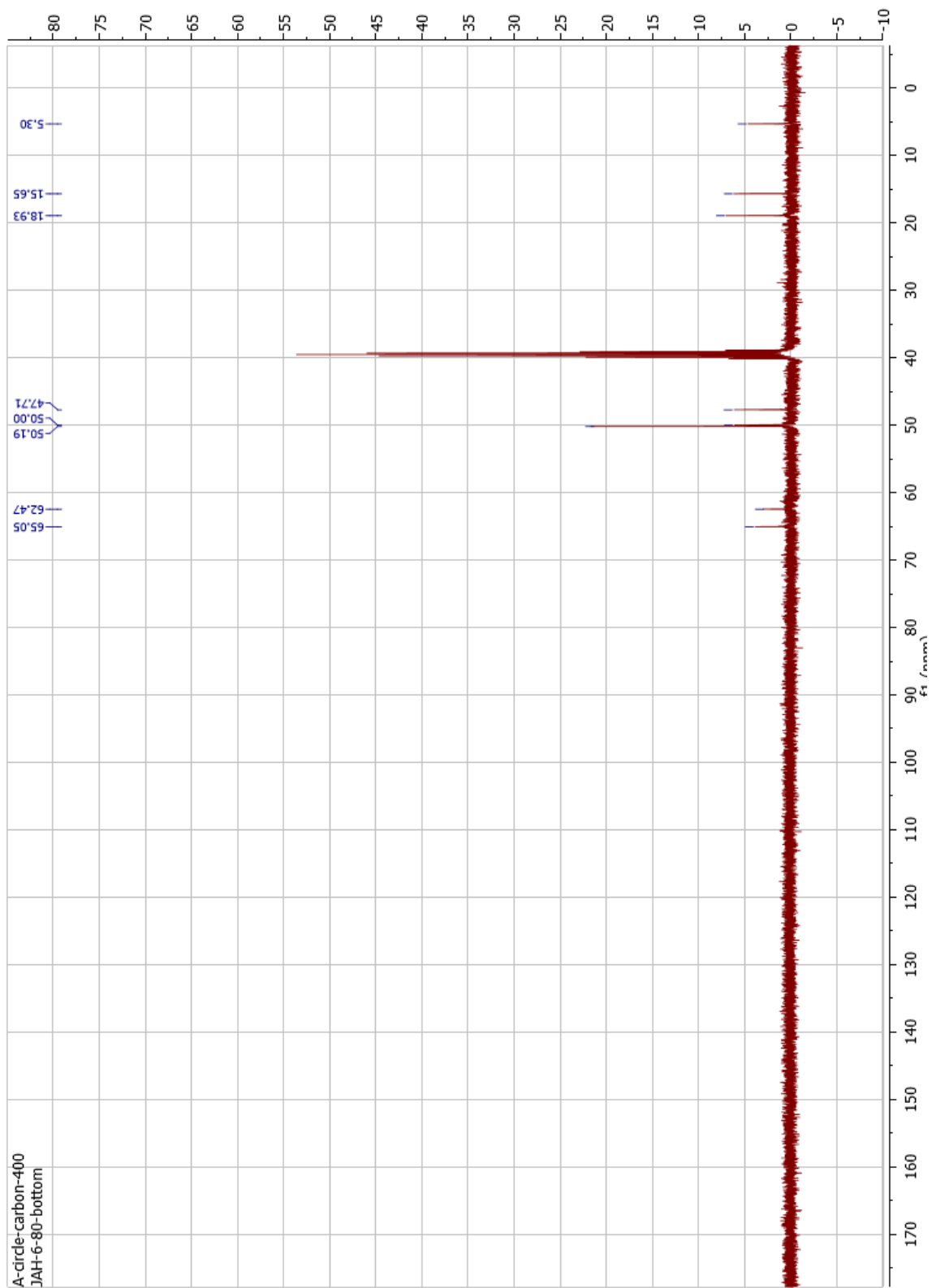


Figure A2.5 ^1H -NMR of SBS silane (3-(dimethyl-(3-(trimethoxysilyl)propyl)ammonio) propane-1-sulfonate)

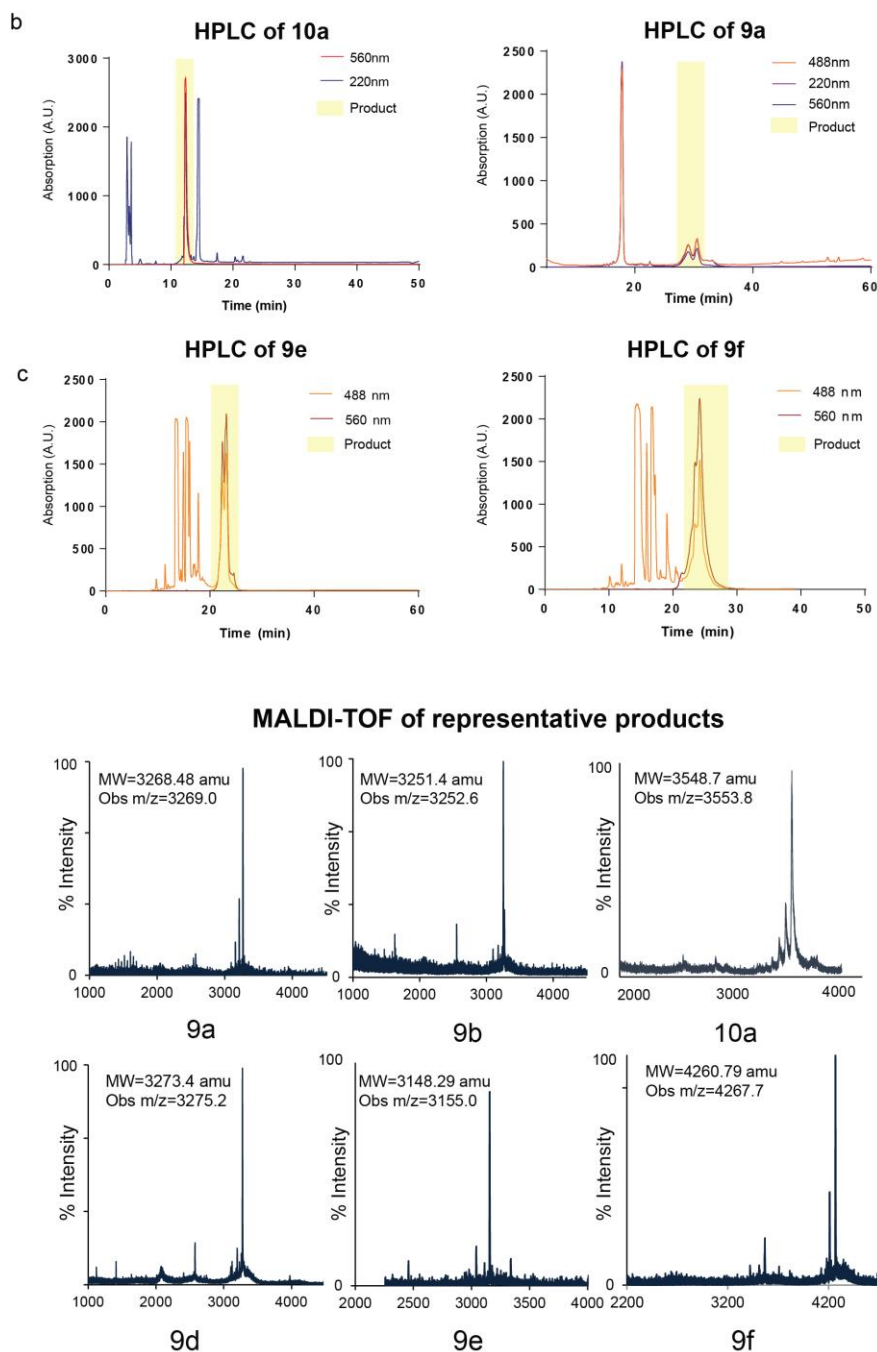


Figure A2.6 Characterization of MTFM sensor final products

b) The final product was purified by HPLC and analyzed by MALDI-TOF MS.

Reverse phase HPLC chromatogram of compound 9a, 9e, 9f and 10a are shown in SI Figure S4 b. The absorbance was measured at 220nm, 488nm and 560 nm. 1 ml fractions were collected as they eluted off the column (flow rate = 1 ml/min from 8% to 100%).

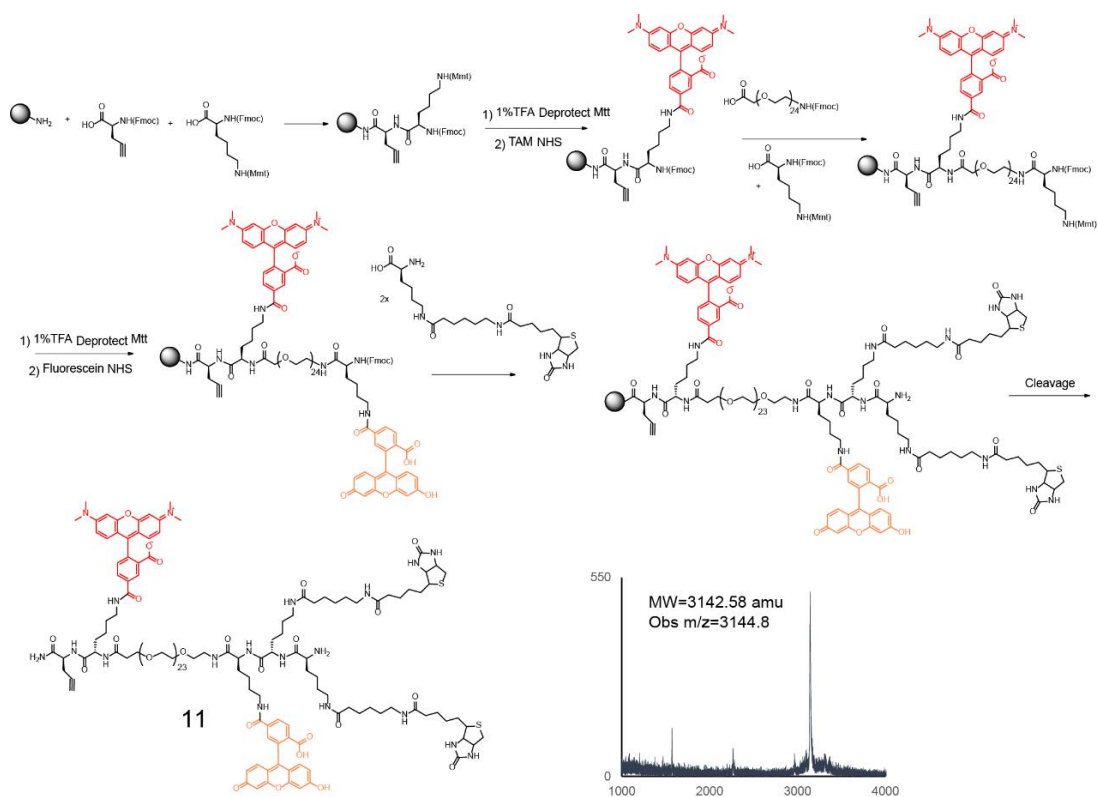


Figure A2.6 Synthesis, purification, and characterization of the tandem biotin probe for measuring PEG extension as a function of passivation

The tandem biotin probe was synthesized using manual SPPS and on-resin dye labeling in concordance with a procedure similar to that used for compound **1**. Briefly, Fmoc-L-propargylglycine and Fmoc-Lys(Mtt)-OH were coupled sequentially following standard Fmoc peptide synthesis procedures in a syringe. The Mtt protecting group of the lysine was selectively deprotected with 1% TFA in CH₂Cl₂. The resin was then treated with excess TAMRA succinimidyl ester in DMF. After deprotecting the Fmoc on the terminal Lys residue, Fmoc-PEG₂₄-OH and Fmoc-Lys(Mtt)-OH residues were coupled to the peptide. The Mtt protecting group on the terminal Lys residue was then deprotected and treated with excess fluorescein succinimidyl ester with 5 molar excess of DIEA. Following this step, two Fmoc Lys(LC-LC-biotin)-OH residues were coupled to the peptide chain N-terminus. The tandem biotin probe was then cleaved from the resin with 95% TFA, using triisopropylsilane (TIS) as a scavenger. 1 ml fractions were collected as they eluted off the column (flow rate = 1 ml/min from 8% to 100% Acetonitrile/water). The synthesized construct, **11**, was characterized by HPLC and MALDI-TOF MS. The yield of the products was >40%.

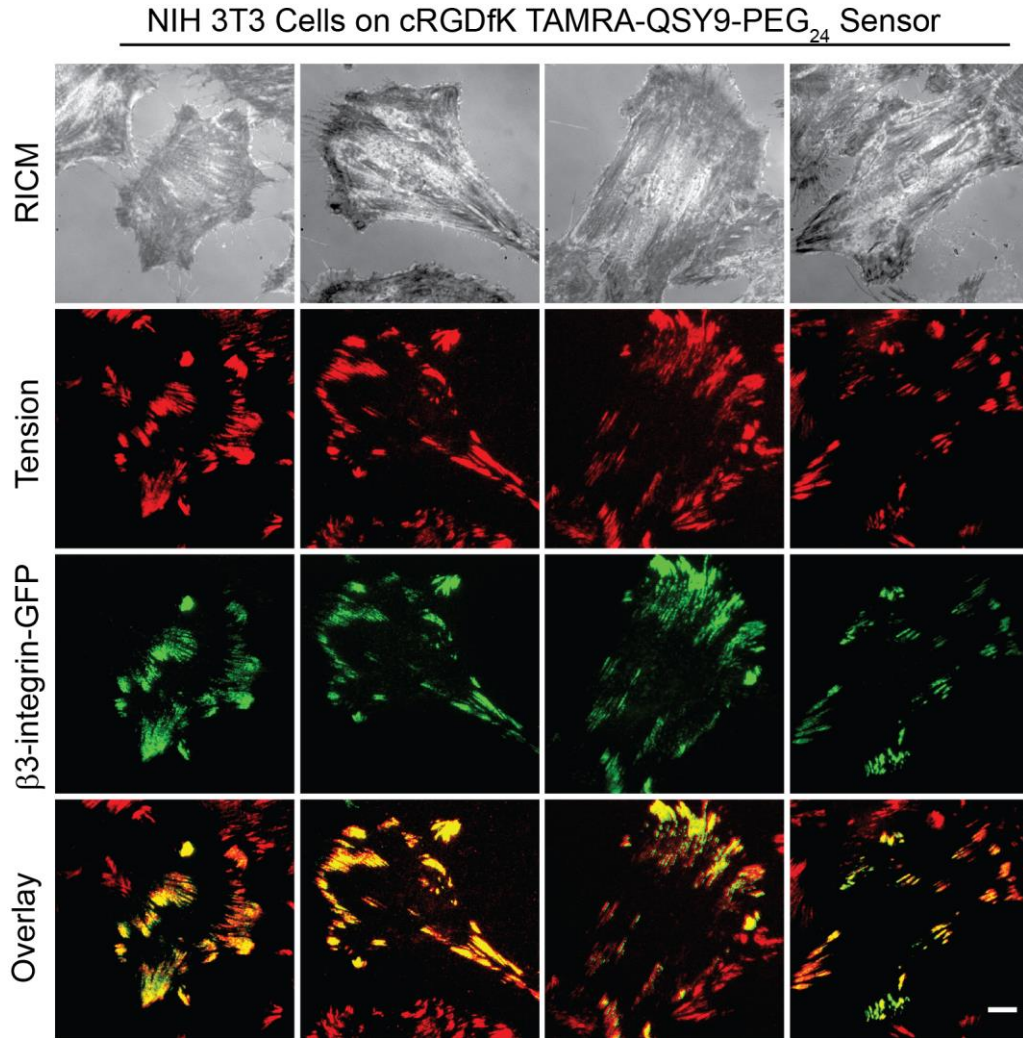


Figure A2.7 Co-localization analysis of tension signal and beta3-integrin-GFP

To co-localize the tension signal with beta-3-integrin-GFP, rat embryonic fibroblast (REF) cells were transfected with GFP beta-3-integrins and plated on the cRGDfK-TAMRA-QSY9/PEG₂₄ tension probe (**10a**) surface and imaged. At the 1 hour time point, the tension signal was highly co-localized with the GFP fluorescence, indicating that the beta-3-integrins are primarily associated with the observed tension. Manders' Colocalization test was performed for 8 cells and the Manders' Colocalization Coefficients (MCC) was calculated to be 0.88 ± 0.08 (beta-3-integrin-GFP over tension signal). (Scale bar 10 μm)

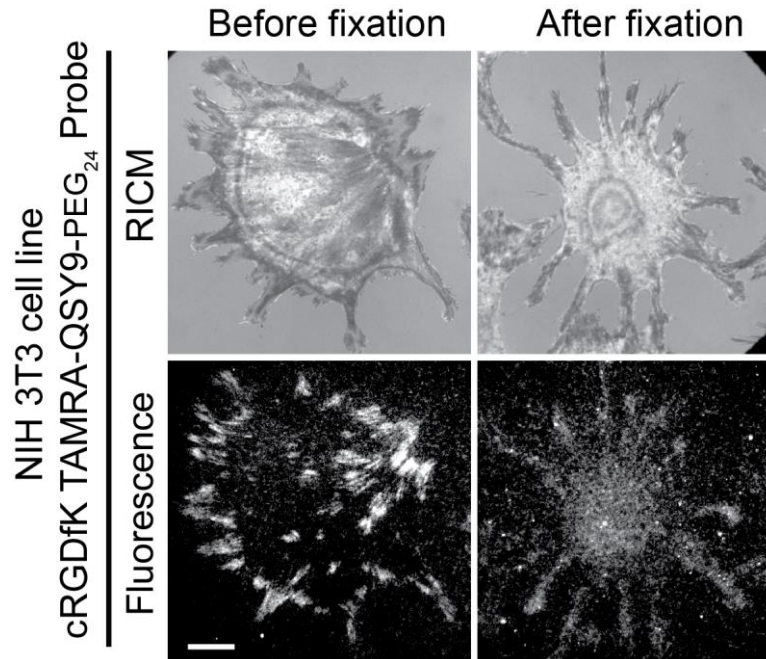


Figure A2.8 Tension signal dissipates following PFA fixation

NIH 3T3 cells were plated onto the cRGDfK tension sensor (**10a**) surface for 1 hr and then imaged in RICM and tension signal channels. Representative images are shown to the right (Before fixation). Subsequently, cells were fixed by incubation in 1 ml of 4% w/v paraformaldehyde (PFA) for 10 min. The PFA was subsequently rinsed off using 25 ml of 1 X PBS, and then cells were permeated by incubation with 0.1% (v/v) Triton X-100 for 5 min in PBS. The cells were then rinsed with 25 ml 1 X PBS, and then blocked for 1 hr using 1% w/v BSA. The tension signal following fixation (left) was weakened and more diffuse, in agreement with literature. The PEG polymer is not crosslinked by PFA and because the cellular cytoskeleton likely relaxes following PFA treatment, the tension signal typically becomes weaker following PFA treatment.⁵⁵ (Scale bar 10 μm).

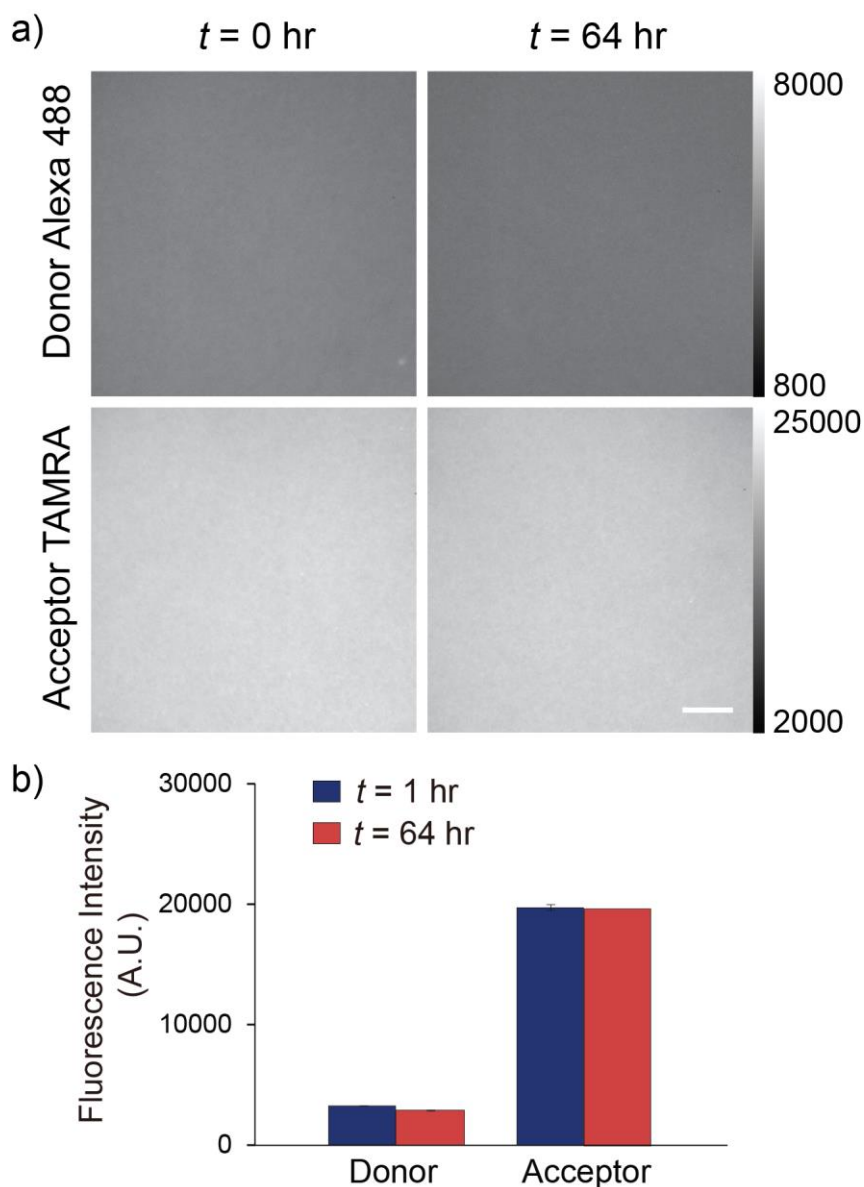


Figure A2.9 Fluorescence intensity change of MTFM probes over 64 hours

To test the stability of the MTFM probes, coverslips modified with TAMRA-Alexa488-PEG₂₄ probes were stored in cell culture media for 64 hours at 37 °C. Fluorescence intensity of donor (Alexa 488) and acceptor (TAMRA) was measured before and after incubation, and minimal change was observed (a and b). Note that by $t=5$ days, the donor and acceptor signal decreased, indicating degradation of the dyes. Data was obtained from 10 different regions in two different samples. Scale bar = 10 μ m.

